

# Monolayer and Multilayer Water & Mixed OH/Water on Pd(111)



UNIVERSITY OF  
LIVERPOOL

Thesis submitted in accordance with the requirements of the University of Liverpool for the  
degree of Doctor in Philosophy

By

Linda Cummings

Surface Science Research Centre, Department of Chemistry

January 2013

*Aerodynamically, the bumble bee shouldn't be able to fly, but the bumble  
bee doesn't know it so it goes on flying anyway.*

*Mary Kay Ash*

## Abstract

An extensive amount of literature can be found containing experimental and theoretical studies of water adsorption on metal surfaces, yet an understanding of the water – metal interface remains far from complete. The binding energy of the water – metal interface determines whether water wets a metal surface to form a complete hydrogen bonded network, forms 3-dimensional ice clusters on a non-wetting surface or dissociates to form hydroxyl, hydrogen and sometimes oxygen on the surface. All of these structures are seen depending on the growth conditions and reactivity of the metal surface.

In this thesis it is shown that submonolayer water adsorbs intact on Pd(111) to form a structure with  $(\sqrt{3} \times \sqrt{3})R30^\circ$  periodicity. As the first layer saturates the spots in the  $\sqrt{3}$  position split due to the formation of dense domain boundaries. Although the first layer of water covers the Pd surface, subsequent layer-by-layer growth does not occur. Instead, an extended superstructure forms by attaching 3D clusters of ice and areas of bare monolayer remain exposed. The formation of an ordered oxygen network results in detection of an intense LEED pattern, even at a coverage of 80 layers. As the first layer of water compresses, it stabilises the growth of the larger superstructure. Further investigation shows the hydrogen network formed during multilayer growth is weakly bonded and helium atom scattering shows that there is disorder on a local scale.

Co-adsorption of oxygen alters the structure and stability of water overlayers and on Pd(111) a stable mixed (OH + H<sub>2</sub>O) layer forms with  $(\sqrt{3} \times \sqrt{3})R30^\circ$  periodicity but is unreactive towards hydrogen, therefore the low temperature reaction between hydrogen and oxygen cannot be catalysed.

## Acknowledgements

It's been a long journey and it's not been easy but I couldn't have done it without a great support network. I would like to thank the following people for providing help, support and friendship over the years;

Firstly, my supervisor Prof. Andrew Hodgson and co-supervisor Dr. Martin Volk for setting up a project and providing invaluable contributions to the work undertaken. To Chris, for teaching me the ropes and introducing me to the world of surface science.

Sam Haq, without whom this work could not have been completed. It has been a pleasure to work with you and I appreciate all the time spent helping me in the lab. Also, thanks to the dynamics group for being tall – without Mark and Chris I would have had to do my work on stilts.

Rasmita for making the centre a good place to work and making us all feel welcome. Also, thanks to everyone in the centre for making it an enjoyable experience. A special thanks to Teresa for being a good friend – the tea room won't be the same without us.

A big thank-you goes to my Mum and Dad for putting up with me over the years and letting me be a student into their retirement. I've finally left school to enter the big wide world of work so the hard work was definitely worth it. Thank-you for supporting me in so many ways – without your encouragement and positivity I could never have achieved half as much.

Thanks to my new team for taking me in and making me feel welcome – as one chapter ends, another one begins and I look forward to the new challenges ahead.

Last, but by no means least, thank-you to David for being there for me throughout the ups and downs. Thanks for correcting my grammar and always wanting to help. More importantly, thank-you for always making me smile and encouraging me to get where I am today – I couldn't have done it without you.

<b>Chapter 1: Introduction</b>	<b>1</b>
1. Introduction	2
1.1 The Structure of Water and Ice	2
1.2 Surface Tension and wetting	5
1.3 Water adsorption at metal surfaces	6
1.4 Palladium	16
1.5 Thesis outline	17
1.6 References	19
<b>Chapter 2: Experimental Techniques</b>	<b>21</b>
2. Experimental Techniques	22
2.1 Ultra-High Vacuum Chambers	22
2.2 Sputter and Anneal Cycles	24
2.3 Dosing Gases	24
2.4 Temperature Programmed Desorption (TPD)	26
2.5 Quadrupole Mass Spectrometer	30
2.6 Low Energy Electron Diffraction (LEED)	31
2.7 Reflection Absorption Infra-Red Spectroscopy (RAIRS)	37
2.8 Helium atom scattering (HAS)	41
2.9 Kelvin Probe Measurements	44
2.10 References	46
<b>Chapter 3: Monolayer water adsorption on Pd(111)</b>	<b>47</b>
3. Monolayer water adsorption on Pd(111)	48
3.1 Introduction	48
3.2 Temperature Programmed Desorption & Low Energy Electron Diffraction	51
3.2.1 Introduction	51
3.2.2 Experimental Procedures	51
3.2.3 Results and Discussion	52
3.3 RAIRS, Work function and DFT calculations	57
3.3.1 Introduction	57
3.3.2 Experimental Procedures	57
3.3.3 Results and Discussion	58

3.4 Collaborative Work:	
Work Function measurements & DFT Calculations	60
3.5 Helium atom scattering	71
3.5.1 Introduction	71
3.5.2 Experimental	72
3.5.3 Results and discussion	73
3.6 Conclusions: Monolayer water adsorption on Pd(111)	83
3.7 References	85
<b>Chapter 4: Multilayer water growth on Pd(111)</b>	<b>87</b>
4. Multilayer water growth on Pd(111)	88
4.1 Introduction	88
4.2 Temperature programmed desorption & low energy electron diffraction	88
4.2.1 LEED : Chamber 1	91
4.2.2 LEED : Chamber 2	97
4.2.3 Summary of LEED from two chambers	103
4.3 Chloroform Adsorption and Isothermal Desorption	105
4.3.1 Introduction	105
4.3.2 Experimental	106
4.3.3 Results and Discussion : Chloroform Adsorption	106
4.4 Helium atom scattering	114
4.5 Concluding Remarks	118
4.5 References	120
<b>Chapter 5: Mixed OH/water structures on Pd(111)</b>	<b>122</b>
5. Mixed OH/water structures on Pd(111)	123
5.1 Introduction to the paper	123
5.2 Mixed water/OH structures on Pd(111)	124
5.2.1 Abstract	124
5.2.2 Introduction	124
5.2.3. Experimental	126
5.2.4. Results	127
5.2.5. Discussion	137

5.2.6. Conclusion	138
5.2.7. References	139
<b>Chapter 6: Ultrafast surface dynamic</b>	<b>141</b>
6. Ultrafast surface dynamics	142
6.1 Introduction	142
6.1.1 Femtochemistry	142
6.1.2 Surface Reactions Initiated by Femtosecond Laser Pulses	145
6.1.3 Hydrogen Recombination	147
6.1.4 Resonance Enhanced Multiphoton Ionisation (REMPI)	148
6.2. Experimental Techniques	149
6.2.1 Atom Beam Source	149
6.2.2 Nd:YAG and Dye Lasers	152
6.2.3 Femtosecond Laser	154
6.2.4 Ion Detection	157
6.3 Results and Discussion	158
6.3.1 Deuterium	158
6.3.2 Hydrogen REMPI	160
6.3.3 Hydrogen Recombination: Femtosecond Laser Excitation	164
6.4 Concluding Remarks	167
6.5 References	172

## List of figures

- Figure 1.1:** a) Lewis dot-cross diagram showing the bonding between hydrogen and oxygen atoms. Oxygen has two lone pairs of electrons.  
b) Schematic to show the preferred tetrahedral geometry of water molecules. O – H bond lengths are 0.96 Å, hydrogen bond lengths (---) are 1.86 Å and the H – O – H angle is 109.47°.
- Figure 1.2:** phase diagram for ice showing 12 known phases. The area of main interest shows hexagonal ( $I_h$ ) and cubic ( $I_c$ ) ice<sup>1</sup>.  
Reprinted by permission from Macmillan Publishers Ltd: [NATURE] (C. Lobban, J. L. Finney and W. F. Kuhs, *Nature*, 1998, **391**, 268-270), copyright (1998)
- Figure 1.3:** Schematic to show the hexagonal network of water molecules. The oxygen atoms lie 0.5 Å above and below the plane of ice (depicted by red and blue oxygen atoms).  
— Oxygen – hydrogen covalent bond  
- - - Hydrogen bond
- Figure 1.4:** Schematic to show the lattices of a) cubic ice and b) hexagonal ice.
- Figure 1.5:** Schematic to illustrate wetting and non-wetting of surfaces. This process is determined by Young's Equation given in equation 1.1.
- Figure 1.6:** Schematic to depict the parameters of Young's equation (equation 1.1).
- Figure 1.7:** A schematic of water adsorbed on a close packed metal surface. The oxygen atoms adsorb on atop sites in a hexagonal structure.
- Figure 1.8:** LEED images to show the (1 x 1) structure formed when water is adsorbed on NaCl(100) (left hand side) and the c(4 x 2) reconstructed structure formed after irradiation with electrons for 1000 s (right hand side).  
Reprinted with permission from [J. P. Toennies, F. Traeger, J. Vogt and H. Weiss, *Journal of Chemical Physics*, 2004, 120, 11347-11350]. Copyright [2004], American Institute of Physics
- Figure 1.9:** STM image taken at 100 K. The water chains are shown growing along the [001] direction (120 x 140Å, V=-196 mV, I=-0.34 nA).  
Reprinted by permission from Macmillan Publishers Ltd: [NATURE MATERIALS] (J. Carrasco, A. Michaelides, M. Forster, S. Haq, R. Raval, A. Hodgson, *Nature Materials*, 2009, 8, 427-431), copyright (2009).
- Figure 2.1:** Schematic of UHV chamber. IG refers to the ion gauges.
- Figure 2.2:** Schematic representation of a square uptake profile showing the King and Wells technique for sticking probability.
- Figure 2.3:** Schematic representation of a desorption profile showing the rise and fall in the intensity of desorbing gases with increasing temperature. In this example the x axis displays temperature but data can also show time in seconds.
- Figure 2.4:** Ideal temperature programmed desorption profile for an adsorbate exhibiting zero order kinetics (n=0).
- Figure 2.5:** Ideal temperature programmed desorption profile for an adsorbate exhibiting first order kinetics (n=1).

- Figure 2.6:** Ideal temperature programmed desorption profile for an adsorbate exhibiting second order kinetics ( $n=2$ ).
- Figure 2.7:** Schematic of a quadrupole mass spectrometer
- Figure 2.8:** The universal curve for mean electron escape depth. Reproduced with permission from [S. S. Perry and G. A. Somorjai, *Surfaces. Encyclopedia of Inorganic Chemistry; John Wiley & Sons, Inc., New York, 2006. Copyright (2206).*
- Figure 2.9:** Schematic representation of the back scattering of a wave of electrons (red arrows) from a 1D plane of atoms (black circles). The green lines represent the wavelength of electrons and the path difference between the scattered waves.
- Figure 2.10:** Schematic representation of LEED optics.  $E_r$ : retarding voltage;  $E_p$ : primary energy
- Figure 2.11:** Schematic to represent Wood's notation along with a descriptive equation containing the parameters required
- Figure 2.12:** Schematic representation of LEED patterns on fcc metals in real space (left hand side) and reciprocal space (right hand side).
- Figure 2.13:** Schematic to show the surface selection rules for CO adsorbed on a metal surface.
- Figure 2.14:** Normal modes of water adsorption with  $C_{2v}$  symmetry on a flat metal surface. Arrows represent vibrations in the plane of the paper + / - represent vibrations perpendicular to the plane of paper.
- Figure 2.15:** Schematic representation of the RAIRS experiment.
- Figure 2.16:** Diagram to show the difference in penetration depth between a) helium atom scattering and b) low energy electron diffraction.
- Figure 3.1:** LEED image observed by Yamada *et al.* and reported in reference 9; analogous to the results described in this thesis. Reprinted (adapted) with permission from (T. Yamada, H. Okuyama, T. Aruga and M. Nishijima, *Journal of Physical Chemistry B*, 2003, 107, 13962-13968). Copyright (2003) American Chemical Society.
- Figure 3.2:** Temperature programmed desorption profile of water desorbing from Pd(111) after being dosed at 150 K. The peak at 170 - 175 K saturates with a coverage of one monolayer (all coverages are quoted in reference to this).
- Figure 3.3:** A plot of  $\ln[I(T)]$  against  $\ln[\theta_{rel}]$  giving a gradient and therefore value for  $n$ , of 0.987 with an  $R^2$  value of 0.996. This implies that monolayer water desorbs from Pd(111) with close to first order desorption kinetics.
- Figure 3.4:** Low energy electron diffraction pattern for submonolayer water adsorbed on a Pd(111) surface at 150 K. a) shows a halo around the (0,0) position and b) clearly shows sharp singular spots in the  $\sqrt{3}$  positions. Beam current = 2.20 A, beam energy = 25 eV, drain current = 50 nA, water coverage = 0.71. Data from chamber 1.
- Figure 3.5:** Low energy electron diffraction pattern for 1.5 layers of water. The sample is rotated away from the surface normal to allow the ring around the (0,0) beam to be observed more clearly (right of the central optics). 2 metal spots are evident on the left hand side and the diffuse triangular  $\sqrt{3}$  beams are shown above and below the centre.

Reproduced with permission from [F. McBride, A. Omer, C. M. Clay, L. Cummings, G. R. Darling, A. Hodgson *Journal of Physics: Condensed Matter*, 2012, 24, 124102]. Copyright (2012), IOP.

- Figure 3.6:** a) Low energy electron diffraction pattern for water adsorbed on a Rh(111) surface. The images show a halo around the (0,0) spot and additional features around the spots in the  $\sqrt{3}$  position. These features are attributed to an extended superstructure. b) STM images showing the small islands form into a larger hexagonal network. Reprinted with permission from [A. Beniya, Y. Sakaguchi, T. Narushima, K. Mukai, Y. Yamashita, S. Yoshimoto and J. Yoshinobu, *Journal of Chemical Physics*, 2009, 130, 034706]. Copyright [2009], American Institute of Physics.
- Figure 3.7:** RAIR spectra for water adsorbed on Pd(111). The bands at  $830\text{ cm}^{-1}$ ,  $1620\text{ cm}^{-1}$  and  $3414\text{ cm}^{-1}$  are due to the librational, scissors and stretching modes of water respectively. Completion of the first layer of water gives rise to a weak band at  $3685\text{ cm}^{-1}$ , attributed to non hydrogen-bonded hydroxyl groups.
- Figure 3.8:** Schematic of the double layer at an atomically smooth metal surface.
- Figure 3.9:** Data to show the change in work function for water films grown at 140 K. The change in work function for one layer of water was found to be 0.7 eV. The solid line shows the linear decrease in  $\Delta\Phi$  as the first layer completes. The inset shows the full data set as  $\Delta\Phi$  saturates. Figure reproduced with permission from Dr. Ahmed Omer.
- Figure 3.10:** Schematic of the chain model for water adsorption. Red and orange spheres represent oxygen molecules along chains of water molecules. The chains form a hexagonal superstructure of water molecules. The white spheres represent hydrogen and the grey ones are atoms on the metal surface.  
a) A side view of the chain structure suggests disorder in the water structure whereas b) show the ordered chains and extended hexagonal network.
- Figure 3.11:** A single hexamer  $1.6 \times 1.6\text{ nm}^2$ . Hexamers were found to be the most stable water clusters.  
STM conditions: 120 mV, 175 pA.  
Reprinted (adapted) with permission from (M. Tatarkhanov, D. F. Ogletree, F. Rose, T. Mitsui, E. Fomin, S. Maier, M. Rose, J. I. Cerda and M. Salmeron, *Journal of the American Chemical Society*, 2009, 131, 18425-18434). Copyright (2009) American Chemical Society.
- Figure 3.12:** a) Elongated water clusters grown on Pd(111) at 45 K. The clusters are made up of side sharing hexamers up to a few cells in width as shown in more detail in b) and c). Reprinted (adapted) with permission from (M. Tatarkhanov, D. F. Ogletree, F. Rose, T. Mitsui, E. Fomin, S. Maier, M. Rose, J. I. Cerda and M. Salmeron, *Journal of the American Chemical Society*, 2009, 131, 18425-18434). Copyright (2009) American Chemical Society.
- Figure 3.13:** With increasing growth temperature, the chains of hexagons are shown to form structures with greater lateral size giving rise to an extended honeycomb structure. Reprinted (adapted) with permission from (M. Tatarkhanov, D. F. Ogletree, F. Rose, T. Mitsui, E. Fomin, S. Maier, M. Rose, J. I. Cerda and M. Salmeron, *Journal of the American Chemical Society*, 2009, 131, 18425-18434). Copyright (2009) American Chemical Society.
- Figure 3.14:** Schematics of calculated structures (left hand side) and the corresponding LEED simulations (right hand side) expected for a  $(7 \times 7)$  structure (top) and a  $(\sqrt{52} \times \sqrt{52}R14^\circ)$  structure (bottom). The simulations assume that water is bound flat lying above Pd. Intensity less than 5 % of the (0,0) beam is omitted.

Reproduced with permission from [F. McBride, A. Omer, C. M. Clay, L. Cummings, G. R. Darling, A. Hodgson *Journal of Physics: Condensed Matter*, 2012, 24, 124102]. Copyright (2012), IOP.

- Figure 3.15:** Helium atom scattering from clean Pd(111). Angular scans were performed immediately after cleaning and cooling the sample.
- Figure 3.16:** Reverse scan of figure 3.11. Helium atom scattering was carried out on clean Pd(111) immediately after the previous scan. A drop in the specular reflectivity is observed along with additional features with a parallel momentum transfer of  $\pm 1.5 \text{ \AA}^{-1}$  close to the (1/3, 1/3) diffraction positions due to contamination with gases from the background. This specular peak for this scan is 70 % lower than the forward scan in figure 3.15 and is only 5 % of the optimised beam value.
- Figure 3.17:** Close up of the broad maxima at approximately  $\pm 1.5 \text{ \AA}^{-1}$  observed in figure 3.16. Although small in relation to the specular, the adsorption of background hydrogen is responsible for this peak due to the long scan time used for these experiments.
- Figure 3.18:** HAS of 1 BL of water adsorbed on Rh(111) at 140 K <sup>26</sup>. The 2 sharp peaks either side of the specular are due to the  $\sqrt{3}$  structure. Additional features close to the specular are attributed to an extended superstructure.
- Figure 3.19:** Helium atom scattering from approximately 0.86 ML water grown at 140 K. The specular reflectivity peak has an intensity of 15,000 counts/second and additional features are observed at  $\Delta K_{\parallel} \pm 1.5 \text{ \AA}^{-1}$  which are shown in more detail in figure 3.20.
- Figure 3.20:** Close up of the features with parallel momentum transfer of  $\pm 1.5 \text{ \AA}^{-1}$ . Taken from data shown in figure 3.19. Inset shows figure 3.19 for reference.
- Figure 3.21:** The helium atom reflectivity remains close to zero during multilayer water desorption and begins to increase as the monolayer desorbs reaching a maximum once all of the water has desorbed from the surface.
- Figure 3.22:** The helium reflectivity is shown as a function of water and hydrogen desorption. As the water monolayer begins to desorb from the surface, the helium reflectivity increases but does not return to a maximum reflectivity value until hydrogen desorbs. The left hand side of the line shows water desorbing followed by thermal desorption of hydrogen on the right hand side of the line.
- Figure 3.23:** Helium atom scattering traces for coverages just below and just over 1ML. It can be seen that the main specular peak is almost completely masked at 0.97 ML and as the water layer saturates, the peak disappears completely. This is in agreement with my results shown in figure 3.24. Reproduced with permission from [F. McBride, A. Omer, C. M. Clay, L. Cummings, G. R. Darling, A. Hodgson *Journal of Physics: Condensed Matter*, 2012, 24, 124102]. Copyright (2012), IOP.
- Figure 3.24:** Helium atom scattering traces for coverages just below and just over 1ML. For a water coverage of 0.86 ML, the intensity of the specular is reduced to only 1.5 % of that for the optimised beam on a clean surface. The intensity rapidly reduces with increasing coverage until it is masked completely as the multilayer begins to grow.
- Figure 4.1:** Temperature programmed desorption profile of water desorbing from Pd(111) after being dosed at 150 K. The peak at approximately 175 K saturates with a coverage of one monolayer (all coverages are quoted in reference to this). Onset of multilayer growth is shown with desorption at  $\sim 155$ -165 K. Data recorded using chamber 1.

- Figure 4.2:** Temperature programmed desorption profile showing multilayer water desorption from Pd(111). The peak at ~ 165 K is indicative of multilayer growth and continues to grow with increasing water coverage. Data recorded using chamber 1.
- Figure 4.3:** Low energy electron diffraction pattern for water adsorbed on Pd(111) at 150 K. The drain current for the images shown here was in the region 50 – 100 nA. Images a-c show 0.8, 1.2 and 4 layers of water respectively. All images recorded in chamber 1.
- Figure 4.4:** Low energy electron diffraction pattern for water adsorbed on Pd(111) at 150 K. These images show the triangle pattern of spots in the  $\sqrt{3}$  position due to multilayer water adsorption and also show the (1 x 1) spots of the Pd(111) surface. This image was recorded reproducibly for coverages ranging between 1 – 80 layers of water suggesting that water does not undergo layer-by-layer growth on the Pd(111) surface. Images recorded in chamber 1.
- 2 layers of water, 54 eV, 50 nA
  - 10 layers of water, 55 eV, 50 nA
  - 20 layers of water, 50 eV, 45 nA
- Figure 4.5:** Low energy electron diffraction pattern for water adsorbed on Pd(111) at 150 K. Images were recorded at 26 eV with a drain current of 50 nA in chamber 1. Images here show how electron damage causes restructuring over time.
- LEED image recorded as soon as the electron beam was switched on. A bright spot in the  $\sqrt{3}$  position is surrounded by a faint triangle
  - LEED image recorded during the same experiment after increased exposure to the electron beam. The  $\sqrt{3}$  spots have split into three spots and form a triangle pointing inwards towards the (0,0) position.
- Figure 4.6:** Low energy electron diffraction pattern for water adsorbed on Cu(110) at 140 K
- (7 x 8) superstructure taken at 14 eV
  - (7 x 8) superstructure taken at 47 eV
  - (2 x 2) structure formed after electron damage occurs to the (7 x 8) structure
- Images from Schiros *et al.*<sup>1</sup>  
 Reprinted from T. Schiros, S. Haq, H. Ogasawara, O. Takahashi, H. Ostrom, K. Andersson, L. G. M. Pettersson, A. Hodgson and A. Nilsson, *Chemical Physics Letters*, 2006, 429, 415-419., Copyright (2006), with permission from Elsevier.
- Figure 4.7:** Water desorption from Pd(111). The high temperature shoulder is much more prominent after irradiation with the electron beam during LEED experiments. Data from chamber 1. Water coverage here was less than one monolayer but this behaviour is observed at all coverages. The LEED was recorded at 26 eV with a drain current of 50 nA in chamber 1.
- Figure 4.8:** Total ionization cross sections for e-H<sub>2</sub>O scattering in various phases.  
 Reprinted from M. Vinodkumar, K. N. Joshipura, C. G. Limbachiya and B. K. Antony, *Nuclear Instruments and Methods in Physics Research Section B: Beam Interactions with Materials and Atoms*, 2003, 212, 63-66., Copyright (2003), with permission from Elsevier.
- Figure 4.9:** Water desorption from Pd(111) after adsorption at 150 K in a second UHV chamber. There is a long trailing edge on each desorption profile but no evidence of a distinct shoulder as seen previously. As the multilayer grows, the monolayer peak remains saturated.
- Figure 4.10:** Hydrogen desorption from Pd(111) after the desorption of water. The size of the profiles indicates that the amount of hydrogen desorbed is not directly related to the amount of water adsorbed on the surface.

- Figure 4.11:** Water desorption from Pd(111) after adsorption at 150 K in a second UHV chamber. There is a long trailing edge on each desorption profile but no evidence of a distinct shoulder as seen previously.
- Figure 4.12:** Low energy electron diffraction pattern for water adsorbed on Pd(111) at 150 K in the second vacuum chamber with the low current LEED system. A diffuse triangular diffraction pattern was observed and upon closer inspection, the three split spots can be observed although they are not as distinct as the ones observed in the first chamber (figure 4.4). These images were recorded at 30 eV with a drain current of 1-4 nA with a water coverage of 1.5 (a) and 3.0 (b).
- Figure 4.13:** Low energy electron diffraction pattern for water adsorbed on Pd(111) at 150 K in the second vacuum chamber. Images were recorded at 28 eV with a drain current of 3 nA. These images were recorded after exposing the water layer to the electron beam for approximately 30 seconds. The spot slitting can be observed although the resolution is not as clear as for the first chamber. These images show that electron damage is not responsible for the spot splitting and that the unusual pattern is reproducibly observed on a freshly grown water layer. The coverage of water was approximately 1.5 layers.
- Figure 4.14:** Low energy electron diffraction pattern for 1.5 layers of water adsorbed on Pd(111) at 140 K. Taken at 53 eV. Reproduced with permission from [F. McBride, A. Omer, C. M. Clay, L. Cummings, G. R. Darling, A. Hodgson *Journal of Physics: Condensed Matter*, 2012, 24, 124102]. Copyright (2012), IOP.
- Figure 4.15:** Change on workfunction ( $\Delta\Phi$ ) as water adsorbs on Pd(111). The saturation of the first layer occurs at  $\Delta\Phi = -0.7$  eV and is discussed in chapter 3.  $\Delta\Phi$  saturates at -1.06 eV between 10 and 13 layers of water.
- Figure 4.16:** Chloroform desorption from Pd(111). Submonolayer coverages of  $\text{CHCl}_3$  desorb at 185 K and a multilayer peak grows at 140 K following saturation of the high temperature feature.
- Figure 4.17:** The blue trace indicates the chloroform dose used for dosing on top of water films. A coverage of just less than one monolayer was used and care was taken to ensure multilayer coverages were not dosed.
- Figure 4.18:** Chloroform desorption from amorphous solid water films of varying coverage, grown at 115 K. The  $\alpha$  peak is due to water desorbing from the metal surface and diminishes between 2-3 layers of water. The  $\beta$  peak is due to water desorbing from underlying water layers. A small shoulder can be seen on the  $\beta$  peak which is attributed to water desorbing from the first layer of water and also disappears with a coverage of 2 layers of water.
- Figure 4.19:** Chloroform desorption from crystalline ice layers of varying coverage, grown at 140 K. The  $\alpha$  peak is due to water desorbing from the metal surface and is observed for up to 10 layers of water. The  $\beta$  peak is due to water desorbing from the first monolayer of ice and exists for up to 80 layers of water. The  $\gamma$  peak grows with increasing coverage and is due to water adsorbed on multilayer ice. As the surface adsorption sites become blocked, this peak becomes the only feature in the desorption profiles for coverages of ice exceeding 80 layers.
- Figure 4.20:** Water desorption from Pd(111) after chloroform desorption experiments. The water monolayer desorbs at 160 K; 15 K lower than water desorption from the sample without probing with chloroform. At the point of saturating this peak, the multilayer

grows at a similar temperature as seen previously (165 K) and continues to grow with increasing water coverage. Desorption recorded simultaneously with chloroform desorption.

- Figure 4.21:** Water desorption from Pd(111) after chloroform desorption experiments. The water monolayer desorbs at 160 K; 15 K lower than water desorption from the sample without probing with chloroform (black trace). At the point of saturating this peak, the multilayer grows at a similar temperature as seen previously (165 K) and continues to grow with increasing water coverage. These traces are taken from figure 4.20 to show the desorption peaks more clearly.
- Figure 4.22:** Isothermal desorption profiles for 30 – 120 layers of water grown at 115 K. Crystallisation of the water occurs before the multilayer desorbs followed by sublimation of the water film. This behaviour suggests that water does not wet by layer-by-layer growth, instead islands of ice clusters form.
- Figure 4.23:** Helium atom scattering from multilayer water grown at 140 K. The intensity of the specular reflectivity peak is weak with a maximum of 700 counts/second. Two weak side bands appear at  $\pm 3 \text{ \AA}^{-1}$  with a maximum reflectivity just above the noise level. This image was taken just as the multilayer began to grow but the specular peak completely disappeared as the coverage was increased further.
- Figure 4.24:** Helium atom scattering from a complete  $(\sqrt{3} \times \sqrt{3})R30^\circ$  mixed OH/water layer. Reproduced with permission from [F. McBride, A. Omer, C. M. Clay, L. Cummings, G. R. Darling, A. Hodgson *Journal of Physics: Condensed Matter*, 2012, 24, 124102]. Copyright (2012), IOP.
- Figure 5.1**
- a) Desorption of water from Pd(111) after growth of an ordered ice film at 150 K showing the monolayer peak near 175 K and initial stages of growth of the multilayer peak, ~158 K, for a coverage of 0.17, 0.26, 0.35, 0.44, 0.52, 0.61, 0.70, 0.79 ML.
  - b) Multilayer TPD of 1.0, 1.3, 1.5, 1.7 and 1.9 ML water.
  - c) TPD spectrum of H<sub>2</sub>O following the adsorption of water (0.70-0.80 ML) onto clean and O pre-covered Pd(111) at 143 K. As the total oxygen coverage is increased towards 0.16 ML the intact water monolayer peak near 176 K disappears and water desorbs from a multilayer peak or from the mixed OH/H<sub>2</sub>O phase near 193 K. Heating rate 2 K s<sup>-1</sup>.
- Figure 5.2**
- Saturation uptake of H<sub>2</sub>O on to oxygen pre-covered Pd(111) at 170 K as a function of oxygen coverage (solid points). The dotted lines indicate H<sub>2</sub>O/O ratio of 4, 3 and 2. Above an H<sub>2</sub>O/O ratio of ~2 the LEED pattern shows only  $\sqrt{3}$  spots. For an H<sub>2</sub>O/O ratio of <2 extra LEED spots are observed in the (2 x 2) positions along with the  $\sqrt{3}$  spots (shaded regime).
- Figure 5.3**
- a) Thermal desorption spectra of H<sub>2</sub>O from Pd(111) following adsorption of H<sub>2</sub>O on clean Pd (at 150 K) and O pre-covered surfaces at 170 K.
  - b) TPD curves showing the thermal desorption spectra of H<sub>2</sub>O from the same total OH<sub>x</sub> coverage, 0.64 ML, but with varying total amounts of hydrogen – shown in the legend by the water/oxygen ratio.
  - c) Detail showing the shift in TPD peak for OH/H<sub>2</sub>O structures formed at 170 K by saturating different O coverage with water as a function of the water/oxygen ratio. Heating rate 2 K s<sup>-1</sup>.
- Figure 5.4**
- Plot of the <sup>18</sup>O and <sup>16</sup>O coverage left on the surface after adsorption of different doses of H<sub>2</sub><sup>18</sup>O onto a saturated (2 x 2)<sup>16</sup>O–Pd surface at 165 K, followed by thermal decomposition of the product. The oxygen coverage is calculated from CO titration at 273 K by integrating the CO<sub>2</sub> signal at masses 44 and 46.

- Figure 5.5** Plot showing the partial pressure of H<sub>2</sub> and H<sub>2</sub>O during the exposure of a) (2 x 2)O layer and b) 0.60 ML (OH + H<sub>2</sub>O) to a H<sub>2</sub> beam (left hand frame) and then the desorption of the products (right hand frame). The increase in partial pressure of H<sub>2</sub> (left hand frame) shows where the beam is admitted to the chamber, while the arrows indicate where a flag in the chamber is moved to expose the sample. The corresponding H<sub>2</sub>O partial pressure is shown below and does not change as the surface is exposed to H<sub>2</sub>. the surface is then heated (right hand frame) to desorb water and H<sub>2</sub> from the surface.
- Figure 6.1:** Schematic to show femtosecond laser pulse induced energy flow at a metal surface. The fs laser pulse excites electrons to a higher energy state before they equilibrate back to their original state as a function of electron – phonon coupling time. Figure adapted from reference 4
- Figure 6.2:** Schematic to illustrate the two temperature model with typical temperature transients for electron and phonon heat baths with temperatures T<sub>el</sub> and T<sub>ph</sub> respectively. For the example shown, the substrate metal is Ru and a 120 fs laser pulse was used with 50 mJ/cm<sup>2</sup> at 800 nm centre wavelength.  
Reprinted (adapted) with permission from (C. Frischkorn and M. Wolf, *Chemical Reviews*, 2006, 106, 4207-4233). Copyright (2006) American Chemical Society.
- Figure 6.3:** Schematic to illustrate the thermal and fs-laser excitation of carbon monoxide and oxygen co-adsorbed on ruthenium.  
a) Thermal excitation leads to the desorption of CO only due to the lower energy required for the desorption in comparison to O activation.  
b) Femtosecond laser excitation also leads to the desorption of CO<sub>2</sub> due to coupling of the adsorbate to the phonon bath of the ruthenium substrate. The oxidation reaction is initiated by hot substrate electrons, occurring on a sub-picosecond time scale.  
From [M. Bonn, S. Funk, C. Hess, D. N. Denzler, C. Stampfl, M. Scheffler, M. Wolf and G. Ertl, *Science*, 1999, 285, 1042-1045]. Reprinted with permission from AAAS.
- Figure 6.4:** a) A femtosecond laser pulse excites electrons in the metal resulting in a unequal population distribution.  
b) Thermalisation occurs on a time scale of 10-100 fs, resulting in a hot electron distribution that has a high energy tail.  
c) Electron flow enables an adsorbate-derived affinity level to be populated by electrons from the substrate. A changed charge distribution initiates adsorbate motion. Electron flow between the metal and substrate is subject to friction /damping.  
Reprinted (adapted) with permission from (C. Frischkorn and M. Wolf, *Chemical Reviews*, 2006, 106, 4207-4233). Copyright (2006) American Chemical Society.
- Figure 6.5:** Non adiabatic energy coupling between electronic and nuclear degrees of freedom. Electrons are repeatedly transferred from the high energy tail of the electronically excited occupied state of the substrate to an unoccupied molecular orbital of the adsorbate-substrate complex.  
The hashed region depicts a population of cold electrons that do not have enough energy to reach the unoccupied levels.  
Reprinted (adapted) with permission from (C. Frischkorn and M. Wolf, *Chemical Reviews*, 2006, 106, 4207-4233). Copyright (2006) American Chemical Society.
- Figure 6.6** Schematic of a (2+1) REMP scheme for hydrogen and deuterium.
- Figure 6.7:** a) A photograph of the lit microwave discharge of hydrogen. Image shows a view of the atom beam source looking towards the air and hydrogen inlets.  
b) Schematic of the atom beam source fitted in place of the molecular beam shown in figure 2.1. The tuning rod enabled tuning of the microwave cavity in order to light the discharge. The nozzle at the end of the gas delivery tube was aligned to the

skimmer allowing a directional beam of H/D atoms to enter the main vacuum chamber. Air was circulated through the cooling tube to prevent melting of the pyrex body.

Dimensions used for the atom beam source:  
 Gas delivery tube : 6 mm internal diameter  
 Nozzle of gas delivery tube : 0.5 mm  
 Cooling jacket - front section : 32 mm diameter

- Figure 6.8:** Schematic of the laser set-up used to generate VUV light with a wavelength of ~ 201 - 205 nm.
- Figure 6.9:** Schematic of the laser path from the femtosecond laser unit to the UHV chamber.
1. various prisms and mirrors used to direct the beam into the autocorrelator
  2. Autocorrelator used to split the beam into two components for a 2PC experiment
  3. Silver mirror used to direct the beam into the vacuum chamber through a window at the back of the chamber.
  4. Gold mirror used to direct the beam into the vacuum chamber through a window at the back of the chamber.
- Figure 6.10:** Schematic of the chirped pulse amplification technique. The seed pulse has low energy and a short wavelength. This is stretched and amplified before being compressed, resulting in a pulse with the same wavelength as the seed pulse but higher energy.
- Figure 6.11:** Autocorrelation traces of the femtosecond laser pulses at a) 1 kHz and b) 100 Hz.
- Figure 6.12:** Schematic of the time-of-flight optics used for ion detection. The red spot represents the laser focal point, 12 mm in front of the Cu(111) crystal.
- Figure 6.13:** Temperature programmed desorption profiles for deuterium desorbing from Cu(111) by heating the sample. The peak on the right hand side corresponds to deuterium desorbing from the surface at ~ 300 K. The lower temperature feature is due to subsurface D.
- Figure 6.14:** Schematic of the experimental set-up.
- Figure 6.15:** Recorded data showing the flight times of hydrogen ions with an applied extract voltage of 0 – 60 V.
- Figure 6.16:** Ideal curves showing the calculated time scales for the flight times of hydrogen atoms with extract voltages of 10 – 60 V.
- Figure 6.17:** Time-of-flight recorded experimentally for hydrogen ions desorbing from Cu(111) with extract voltages of 10 – 60 V.
- Figure 6.18:** Temperature programmed desorption profile for hydrogen desorbing from Cu(111) at approximately 300 K.
- Figure 6.19:** REMPI – TOF ion detection for experiments carried out using only the UV laser spot (green), hydrogen atom with the UV laser spot (red) and hydrogen, the UV laser and the femtosecond laser pulse (blue). This shows that there is no significant difference in the number of ions detected with the femtosecond laser pulse is used. No hydrogen recombination is induced by the femtosecond laser under the experimental conditions used. Ions are detected when the UV laser spot is used alone due to residual hydrogen in the chamber and the creation of ions as the laser spot scatters from objects inside the vacuum chamber.

- Figure 6.20:** High-collection efficiency quadrupole mass spectrometer. The photograph on the left shows the glass Feulner cup and the position of the crystal & fs laser pulse path. The figure on the right hand side shows a schematic of the set up.  
Reprinted (adapted) with permission from (D. N. Denzler, C. Frischkorn, M. Wolf and G. Ertl, *Journal of Physical Chemistry B*, 2004, 108, 14503-14510.). Copyright (2004) American Chemical Society.
- Figure 6.21:** Hydrogen TPD recorded with and without using the Feulner cup, highlighting the improvement in signal-noise ratio.  
Reprinted (adapted) with permission from (D. N. Denzler, C. Frischkorn, M. Wolf and G. Ertl, *Journal of Physical Chemistry B*, 2004, 108, 14503-14510.). Copyright (2004) American Chemical Society.
- Figure 6.22:** Schematic of the experimental set up used by Funk *et al.* and later by Denzler *et al.*. Solid lines show the beam path for desorption experiments and dashed lines show the SFG setup.

### List of tables

- Table 1.1:** Spacing of different metal close packed surfaces (D) compared to a commensurate bulk ice film.  $\Delta X$  is the lateral expansion required to form a commensurate ( $\sqrt{3} \times 3R30^\circ$  hexagonal ice layer on the close packed face).  
Adapted from reference 7.
- Table 1.2:** A summary of the wetting behaviour observed on different metal surfaces. Adapted from reference 7, where additional references can be found for the original sources of information
- Table 1.3:** A summary of chemical and physical properties of palladium.
- Table 3.1:** Calculated binding energies for various structures of water formed on Pd(111) (adapted from reference 7)
- Table 3.2:** Calculated binding energies and values for the change in workfunction for various structures formed on Pd(111). Table adapted from reference 17. Figures reproduced with permission from [F. McBride, A. Omer, C. M. Clay, L. Cummings, G. R. Darling, A. Hodgson *Journal of Physics: Condensed Matter*, 2012, 24, 124102]. Copyright (2012), IOP.

## List of Acronyms

ASW	Amorphous solid water
CI	Crystalline ice
CPA	Chirped pulse amplification
DFT	Density functional theory
HAS	Helium atom scattering
IR	Infrared
LEED	Low energy electron diffraction
ML	Monolayer
STM	Scanning tunnelling microscopy
RAIRS	Reflection-absorption infrared spectroscopy
REMPI	Resonance enhanced multiphoton ionisation
SHG	Second harmonic generation
THG	Third harmonic generation
TPD	Temperature programmed desorption
TPRS	Temperature programmed reaction spectroscopy
TSP	Titanium sublimation pump
UHV	Ultra-high vacuum
UV	Ultra-violet

## List of Publications

Mixed OH/water structures on Pd(111).

C. Clay, L. Cummings and A. Hodgson, *Surface Science*, 2007, **601**, 562-568

Strain relief and disorder in commensurate water layers formed on Pd(111).

F. McBride, A. Omer, C. M. Clay, L. Cummings, G. R. Darling, A. Hodgson *Journal of Physics: Condensed Matter*, 2012, **24**, 124102

# Chapter 1

## Introduction

## 1. Introduction

### 1.1 The Structure of Water and Ice

Water is the most abundant molecule on the Earth's surface occupying approximately 70 % in its three states (gas, liquid and solid). The structure of water consists of intermolecular covalent bonding between hydrogen and oxygen atoms as well as highly directional hydrogen bonds between adjacent water molecules. This gives a preferred tetrahedral geometry as shown in figure 1.1.

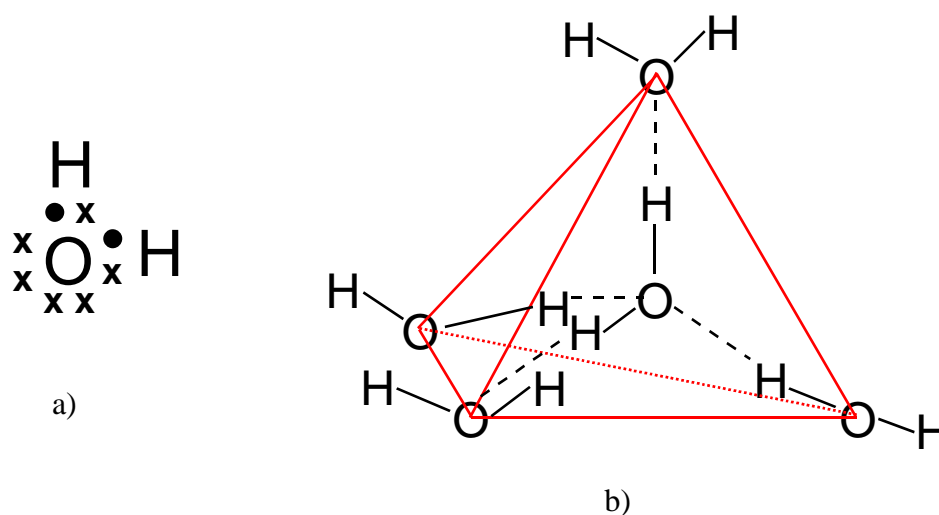


**Figure 1.1:** a) Lewis dot-cross diagram showing the bonding between hydrogen and oxygen atoms. Oxygen has two lone pairs of electrons.  
b) Schematic to show the preferred tetrahedral geometry of water molecules. O – H bond lengths are 0.96 Å, hydrogen bond lengths (---) are 1.86 Å and the H – O – H angle is 109.47°.

At atmospheric pressure and temperature, water exists as a liquid but below 270 K, at standard pressure, water becomes ice and the H bond network freezes to form a crystalline network with each molecule being held in place by up to four bonds. As the network freezes, the hydrogen bonds can distort from the tetrahedral geometry resulting in different O-O bond lengths, which leads to a complex phase diagram (figure 1.2). The phase diagram shows 12 known phases of ice <sup>1</sup>.

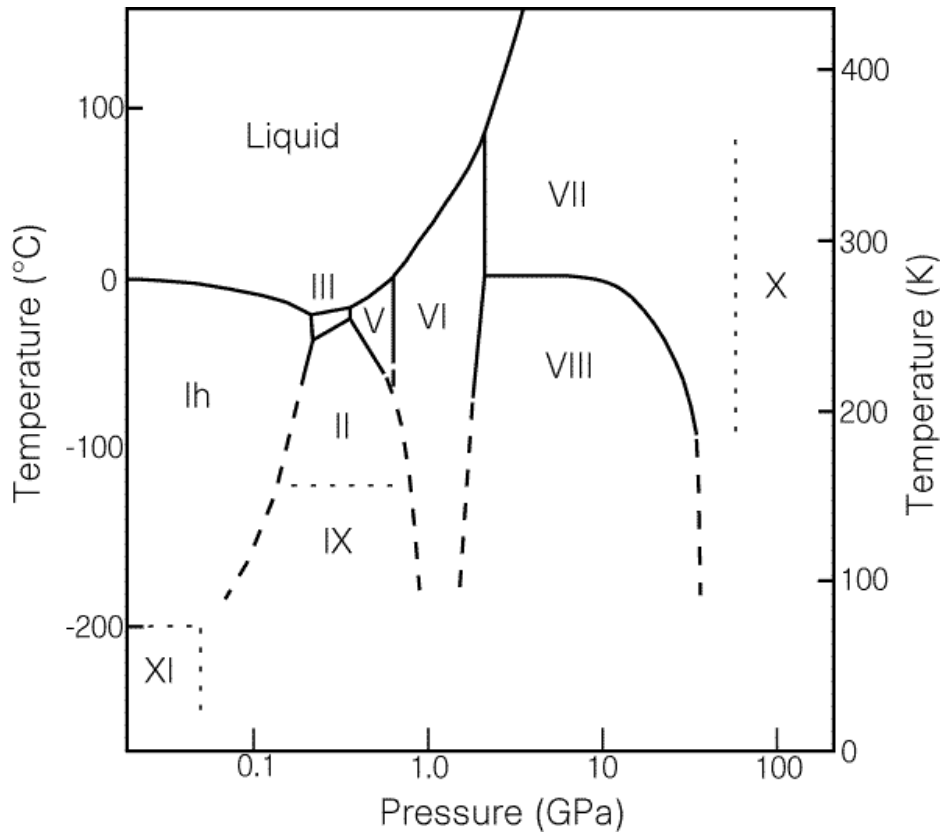


**Figure 1.2:** Phase diagram for ice showing 12 known phases. The area of main interest shows hexagonal ( $I_h$ ) and cubic ( $I_c$ ) ice<sup>1</sup>. Reprinted by permission from Macmillan Publishers Ltd: [NATURE] (C. Lobban, J. L. Finney and W. F. Kuhs, *Nature*, 1998, **391**, 268-270), copyright (1998)

The structure of ice according to the Bernal and Fowler<sup>2</sup> and Pauling<sup>3</sup> rules for bulk ice consists of hexagonal rings of water molecules hydrogen bonded together (figure 1.3). Puckered rings are formed in order to maintain the preferred tetrahedral geometry with each oxygen atom being displaced by  $0.97 \text{ \AA}$  from its next nearest neighbour.

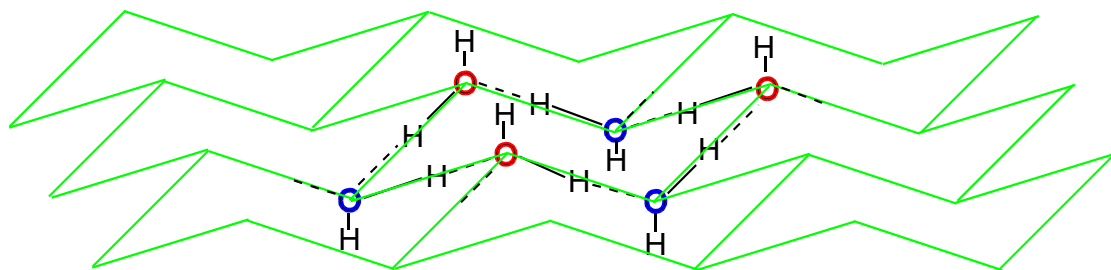


**Figure 1.3:** Schematic to show the hexagonal network of water molecules. The oxygen atoms lie  $0.5 \text{ \AA}$  above and below the plane of ice (depicted by red and blue oxygen atoms).  
 — Oxygen – hydrogen covalent bond  
 - - - Hydrogen bond

The ice we see in everyday life (snowflakes, hail, glaciers) is primarily hexagonal ice ( $I_h$ ) with a lower percentage of the metastable cubic ice ( $I_c$ ). Hexagonal ice has a crystal structure consisting of hexagonal rings of water molecules stacked in layers of ABAB with B being a reflection of A. It is stable down to  $-200\text{ }^\circ\text{C}$  (73 K) and has a density lower than liquid water ( $0.917\text{ g/cm}^3$  versus  $0.99704\text{ g/cm}^3$ ) due to the low density of its crystal lattice. Cubic ice forms between 130 – 150 K and is stable up to 200 K at which point it converts to the hexagonal form. The crystal structure of this metastable form consists of water molecules being stacked in an ABCABC pattern. In addition to crystalline ice, amorphous solid water forms at temperatures less than 140 K. This form of ice is metastable compared to crystalline ice and has no long range order in the hydrogen bond structure. Figure 1.4 shows a schematic of the cubic and hexagonal lattices of ice <sup>4</sup>. Other forms of amorphous ice include low-density amorphous ice (LDA), high density amorphous ice (HDA) and hyper-quenched glassy water (HGW).

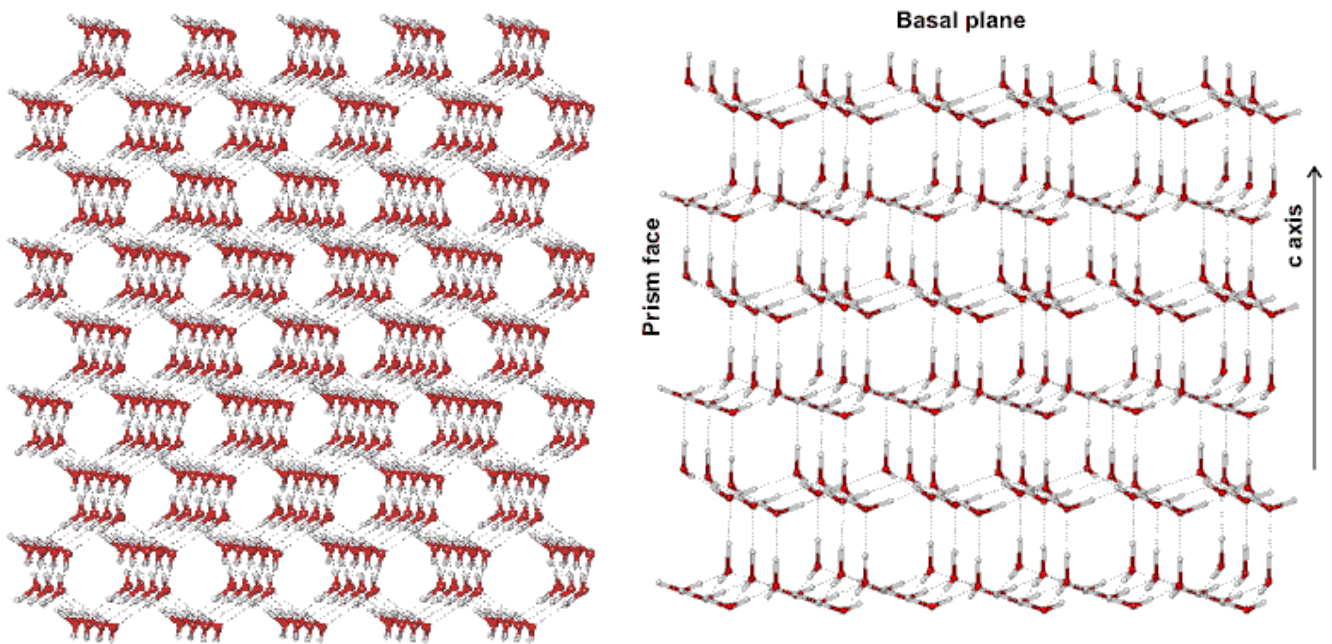


**Figure 1.4 <sup>4</sup>:** Schematic to show the lattices of a) cubic ice and b) hexagonal ice.

## 1.2 Surface Tension and wetting

In preparation for looking at how water adsorbs on metal surfaces in UHV studies, it is important to understand the fundamental principle of surface tension. Surface tension is a measure of the cohesive energy present at an interface and at the liquid – solid interface, the strength of adhesive forces (liquid – solid) and cohesive forces (liquid – liquid molecules) determines whether the liquid wets the surface or not. A liquid will wet the underlying surface when the adhesive forces are greater than the cohesive ones. This can be quantified by measuring the contact angle between the liquid in solid as depicted in figure 1.5. Wetting occurs for contact angles less than  $90^\circ$  and complete wetting is observed when the contact angle is zero.

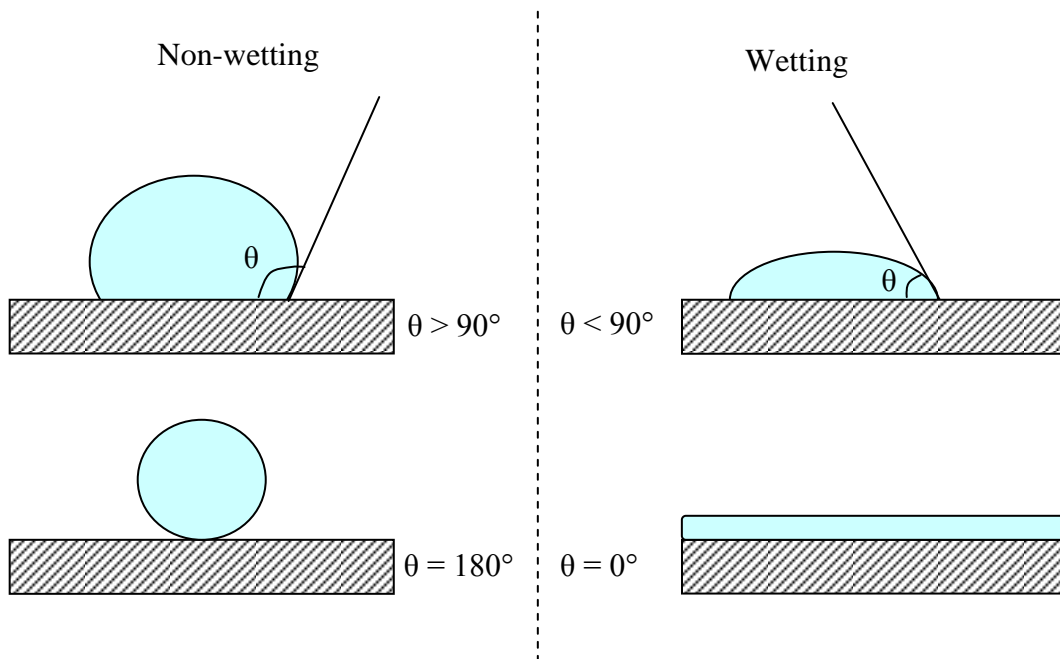


**Figure 1.5:** Schematic to illustrate wetting and non-wetting of surfaces. This process is determined by Young's Equation given in equation 1.1.

The contact angle between the liquid and solid is a function of the surface energies for the solid – gas interface, liquid – gas interface and solid – liquid interface as related by Young's equation (equation 1.1) and the given parameters are illustrated in figure 1.6.

$$\gamma_{LV} \cos \theta = \gamma_{SV} - \gamma_{SL} \quad \text{Equation 1.1}$$

$\gamma_{LV}$  = liquid – vapour interfacial tension

$\gamma_{SV}$  = solid – vapour interfacial tension

$\gamma_{SL}$  = solid – liquid interfacial tension

$\theta$  = contact angle between liquid and solid

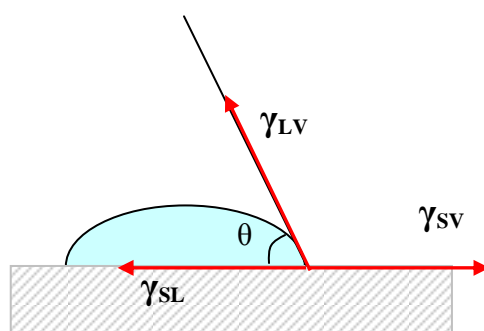


**Figure 1.6:** Schematic to depict the parameters of Young's equation (equation 1.1).

### 1.3 Water adsorption at metal surfaces

The importance of water in nature is unquestionable and unravelling the chemistry of metal surface – water interfaces is of great importance in many areas of science, for example heterogeneous catalysis, corrosion studies and electrochemistry. Much literature can be found containing experimental and theoretical studies of water adsorption on metal surfaces yet an understanding of the water – metal interface remains far from complete.

On close packed metal surfaces water adsorbs with a binding energy comparable to the hydrogen bond strength between water molecules (~23 kJ/mol) so in order for stable adsorption structures to form, optimisation of both metal – water and water – water interactions are required. It is the binding energy of water to the metal surface

that determines whether it wets to form a complete hydrogen bonded network, aggregates to form non-wetting ice clusters or dissociates to form hydroxyl, hydrogen and sometimes oxygen on the surfaces. All of these structures have been reported for various growth conditions on surfaces with different reactivity<sup>5-8</sup>.

The conventional model for wetting of metal surfaces involves the adsorption of intact water molecules in the formation of a puckered bilayer, consisting of a hexagonal network of water molecules hydrogen bonded to each other<sup>9</sup>. This network is believed to resemble the basal plane of hexagonal ice,  $I_h(0001)$ , with corrugation of the bilayer enabling water molecules to remain in their preferred tetrahedral coordination. The original model was modified when molecules in the first layer were reported to chemisorb directly to the surface via the O atom<sup>10</sup>. Alternate molecules are raised and lowered out of the plane of the structure allowing hydrogen bonds to form between consecutive halves of the bilayer structure. To retain  $\sqrt{3}$  registry, the lattice parameter of the metal substrate should match the intermolecular separation of ice, varying with bucking of the bilayer structure. Structures maintaining long-range order have previously been observed on several surfaces with completion of the bilayer forming a  $(\sqrt{3} \times \sqrt{3})R30^\circ$  LEED pattern<sup>6-8</sup>.

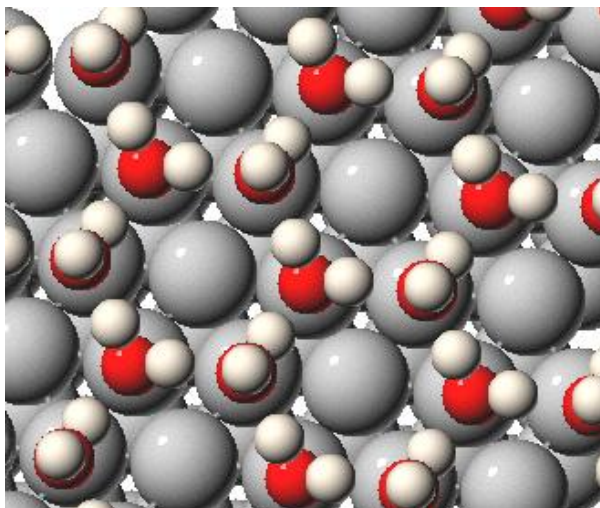


**Figure 1.7:** A schematic of water adsorbed on a close packed metal surface. The oxygen atoms adsorb on atop sites in a hexagonal structure.

Recent work has re-examined the bilayer explanation of water adsorption on metal surfaces and shows a much richer behaviour. Studies of water adsorption on Pt(111) show that at 40 K, water has a low diffusion rate resulting in the formation of monomers on the surface. These monomers begin to cluster, forming stable dimers and trimers<sup>11, 12</sup>. An amorphous solid water (ASW) phase forms upon further dosing of water at temperatures below 110 K<sup>13</sup>. Annealing the ASW to above 150 K causes the water to reform, giving a crystalline ice (CI) phase which can also be formed by dosing water on Pt(111) at 135 K. The water adsorbed at 135 K, desorbs intact near 160 K with zero-order desorption kinetics. As the surface saturates with water, this peak saturates and a second, lower temperature peak continues to grow with increasing coverage indicating multilayer water growth on Pt(111). Initial LEED investigations proposed a commensurate  $(\sqrt{3} \times \sqrt{3})R30^\circ$  structure for water adsorbed on Pt(111)<sup>14</sup>. Formation of a  $(\sqrt{3} \times \sqrt{3})R30^\circ$  structure would enable water to adsorb preferentially in the atop site of the metal, however, it would reduce the density of water adsorbed on the surface and therefore distort the hydrogen bonded network. Further evidence shows that instead of the simple  $(\sqrt{3} \times \sqrt{3})R30^\circ$  structure, water adsorbs with a slightly distorted registry from the Pt(111) surface, firstly forming islands with  $(\sqrt{37} \times \sqrt{37})R25.3^\circ$  registry. As the water coverage increases water preferentially binds to the metal surface rather than on the first layer of water, causing the  $\sqrt{37}$  phase to compress and form a structure with  $(\sqrt{39} \times \sqrt{39})R16.1^\circ$  periodicity as the surface becomes saturated with water. These structures are seen by helium atom scattering<sup>15</sup> and by LEED<sup>16-18</sup>. A  $(\sqrt{3} \times \sqrt{3})R30^\circ$  LEED pattern has been observed due to electron damage to the water layer and by coadsorption with oxygen.

When carrying experimental studies involving water films on metal surfaces, the damage that could be caused by electron damage must be taken into consideration. Electrons in the range 20 – 1000 eV are used for LEED studies and can cause changes to the overlayer structure or even result in water dissociation. For example, on some metals, including Pt(111) a high temperature peak is present in the desorption profiles of water after exposure to the electron beam (features which are not present without electron damage). For Ru(0001) this behaviour is true for D<sub>2</sub>O desorption only due to the dissociation of water at temperatures greater than 150 K in the absence of any

exposure to electrons. Electron damage has also been reported for the water monolayer grown on NaCl(100)<sup>19</sup>. Water adsorbs on NaCl(100) to form an ordered (1 x 1) structure but when this structure is exposed to an electron beam at 90 eV (approximately two electrons per water molecule) the water overlayer reconstructs to form a stable c(4 x 2) structure as shown in figure 1.8<sup>19</sup>.

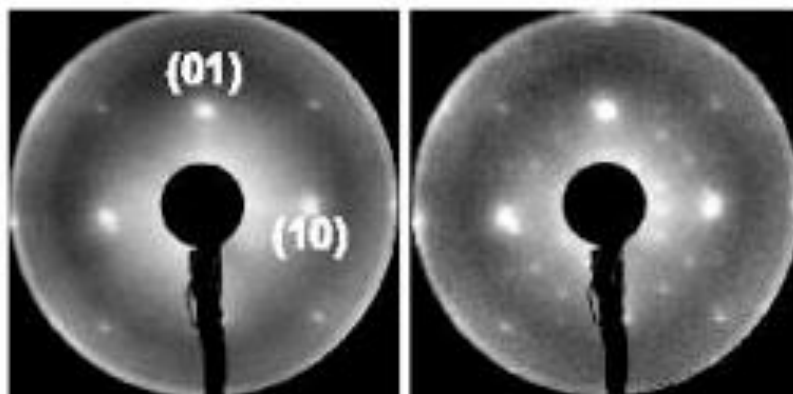


**Figure 1.8<sup>19</sup>:** LEED images to show the (1 x 1) structure formed when water is adsorbed on NaCl(100) (left hand side) and the c(4 x 2) reconstructed structure formed after irradiation with electrons for 1000 s (right hand side). Reprinted with permission from [J. P. Toennies, F. Traeger, J. Vogt and H. Weiss, *Journal of Chemical Physics*, 2004, 120, 11347-11350]. Copyright [2004], American Institute of Physics

STM studies remain controversial with suggestions that the tip causes the water structure to change. The closest agreement comes from a study by Thurmer *et al.*<sup>20</sup> who report that the corrugation seen has spacings almost in agreement with  $\sqrt{39}$  spacing but have reduced order in comparison to the LEED studies. RAIR experiments carried out by Haq *et al.* find a broad OH/OD stretching band 2700 – 2000  $\text{cm}^{-1}$ <sup>16</sup> attributed to H<sub>2</sub>O and D<sub>2</sub>O monolayers with a  $\sqrt{39}$  structure. A change in the vibrational spectra is observed as the multilayer begins to grow at which point a weak band is present at 2720  $\text{cm}^{-1}$  due to free OH groups. This is consistent with the formation of islands with increased water coverage.

Water adsorption on Ni(111) shows similar characteristics to Pt(111) as the monolayer structure contains a large unit cell with hydrogen bonding taking preference over atop adsorption as seen on various other metals surfaces. At coverages of 0.67 – 1.0 layers, the wetting layer forms an extended H-bonded

network with  $(2\sqrt{7} \times 2\sqrt{7})R19^\circ$  periodicity, which reforms with adsorption above one monolayer <sup>21</sup>. As the water coverage reaches two layers an incommensurate structure with hexagonal periodicity becomes visible by LEED with diffraction spots situated close to the  $\sqrt{3}$  position. An ordered multilayer forms on Ni(111) due to reconstruction of the monolayer which is not held in tight registry to the Ni(111) surface. Desorption of the multilayer at 150 K sees the hexagonal pattern disappear and the initial  $(2\sqrt{7} \times \sqrt{7})R19^\circ$  structure to reform as the coverage reaches one monolayer of water. This behaviour suggests that water forms islands with  $(2\sqrt{7} \times \sqrt{7})R19^\circ$  periodicity up to the point where the first layer saturates, followed by more ordered multilayer growth with a honeycomb structure. It has been shown that water does not form a simple commensurate  $(\sqrt{3} \times \sqrt{3})R30^\circ$  structure on Ni(111) and further highlights the need to re-assess the modes of water adsorption on metal surfaces in comparison to the originally proposed bilayer structure.

The bilayer structure was reported experimentally for D<sub>2</sub>O on Ru(0001) <sup>22-24</sup> but these experiments did not agree with theoretical studies of the same system. In 2002, DFT calculations by Feibelman re-addressed how water adsorbs to metal surfaces when he discovered that the binding energy of intact water was too low to wet the Ru(0001) surface. Instead, he proposed a partially dissociated layer on the surface consisting of hexagonal rings with half of the sites occupied by intact water and half with hydroxyl fragments <sup>25</sup>. Theoretical calculations suggest that the formation of 3-D ice crystals is more energetically favoured than a complete monolayer yet a wetting layer is found. This layer is believed to form a hexagonal superstructure containing disordered chains of H-down and flat water molecules. Excess water in the structure increases the density and disturbs the  $(\sqrt{3} \times \sqrt{3})R30^\circ$  periodicity. Below 145 K, water adsorbs on Ru(0001) to form clusters <sup>26</sup> and further increasing the water coverage results in multilayer growth. Annealing the adlayer to 145 K causes the multilayer to desorb at which point a structure with  $(\sqrt{3} \times \sqrt{3})R30^\circ$  periodicity is observed <sup>20, 26</sup>. The  $(\sqrt{3} \times \sqrt{3})R30^\circ$  pattern was initially interpreted as an intact bilayer but interestingly, it has been shown experimentally that an isotope effect exists on Ru(0001) with D<sub>2</sub>O desorbing intact at 175 K and water adsorbing with two peaks in the temperature programmed desorption spectrum <sup>20, 22, 27</sup>, leaving trace amounts of hydrogen and

oxygen on the surface<sup>28</sup>. The two peaks in the TPD profile exist at 165 K and 205 K and these findings provide evidence in agreement with Feibelman's hypothesis for a partially dissociated water structure. RAIR spectra taken at adsorption temperatures below 145 K show bands for the OH stretching mode and H<sub>2</sub>O bending mode characteristic of intact water adsorption. These bands disappear as the adsorption temperature is increased above 150 K suggesting partial dissociation of water with the remaining water molecules forming a mixed OH/water structure reinforced by hydrogen bonding.

Rh(111) was expected to be a good template to study water adsorption on metal surfaces due to a small lattice mismatch of 3% and the large adsorption energy of water to Rh(111) of 60 kJ/mol<sup>29-32</sup>. Experiments show that water adsorbs intact forming a  $(\sqrt{3} \times \sqrt{3})R30^\circ$  structure when adsorbed at 20 K and annealed to 145 K. STM studies reveal that at low coverages, water forms islands on Rh(111) that arrange randomly on the surface. Aggregation of these islands results in a commensurate structure with  $(\sqrt{3} \times \sqrt{3})R30^\circ$  periodicity with the  $\sqrt{3}$  spots becoming more intense at a water coverage of 0.25<sup>33</sup>. As the water coverage is increased to 0.56, additional features are observed in the LEED images, forming an intense halo around the (0,0) position and additional spots appearing around the spots in the  $\sqrt{3}$  position. These features become more intense at a coverage of 0.89 as a superlattice structure forms. Further adsorption of water results in the formation of 3D crystallites suggesting water growth by the Stranski-Krastanov (SK) mode. The SK method for water growth occurs when the initial water forms a 2D layer and 3D islands grow on top of this layer due to its hydrophobic nature.

Isothermal desorption studies of water adsorption on Au(111) reveal a hydrophobic surface with non-zero desorption kinetics due to the formation of ice clusters by means of Volmer-Weber film growth<sup>34</sup>. TPD experiments show a single desorption feature at 157 K which does not saturate with increasing water coverage<sup>35</sup>. The maximum desorption temperature increases as more water is dosed due to the stronger nature of the interaction between water molecules than the bonding between water and the Au(111) surface. Similar desorption behaviour has been reported on Cu(111) and Ag(111) where non-wetting of the metal substrate occurs in preference to

formation of the wetting bilayer<sup>36</sup>. This is due to the weak interaction between the metal surface and water, which is indicated by a relatively low temperature peak in TPD spectra at 160 K. Michaelides *et al.* carried out a low temperature STM study and confirmed their results using DFT calculations. They find that water adsorption at low temperature (17 K) yields similar results on Ag(111) and Cu(111) with no significant differences noted between H<sub>2</sub>O and D<sub>2</sub>O. On Ag (111), water does not form a continuous wetting layer, instead it forms 3D clusters with areas of metal remaining exposed<sup>36</sup>. The clusters are formed even at low temperatures, the adsorption temperature only altering the size of the clusters, not the way in which water adsorbs. 3D ice clusters were also found to form on Cu(111) but areas of bare metal were not left exposed, instead, other water molecules adsorbed in the spaces to form a (2 × 1) superstructure. On both surfaces, large amorphous structures form containing more than ten water molecules and arrange themselves in no particular order. In addition to these clusters, a small amount of water particles exist which do not aggregate to form larger 1-D or 2-D structures as reported for Pd(111) and Cu(110) and they do not form a commensurate ( $\sqrt{3} \times \sqrt{3}$ )R30° structure as seen on various other metal surfaces. The smallest structure formed by the water particles is a water hexamer aligned in the close packed direction of the surface. DFT calculations confirm that the cyclic hexamer is the lowest energy arrangement of cluster containing six water molecules on both Cu(111) and Ag(111). The water particles also form heptamers, octamers and nonmers on the two surfaces in preference to a complete wetting layer.

The variation in growth mode for water adsorption on a range of metal surfaces illuminates the need to resolve the chemistry of the metal surface – water interface on close packed metal surfaces. In addition to the brief review given here, many extensive reviews of water adsorption at metal surfaces have been published<sup>6, 8</sup>. The more recent review from Hodgson *et al.*<sup>7</sup> provides a comprehensive review of the literature to date and includes a table summarising the equilibrium adsorption phases observed on different close packed metal surfaces. In addition, the lattice spacing of different metals has been compared to that of bulk ice to provide a value for the lateral expansion required to form a ( $\sqrt{3} \times \sqrt{3}$ )R30° structure on the close packed face. These values highlight the strain that structures would be put under in order to

form the commensurate structure and provide insight into why so many different water structures exist depending on the underlying substrate.

**Table 1.1:** Spacing of different metal close packed surfaces (D) compared to a commensurate bulk ice film.  $\Delta X$  is the lateral expansion required to form a commensurate  $(\sqrt{3} \times \sqrt{3})R30^\circ$  hexagonal ice layer on the close packed face. Adapted from reference 7.

Metal	D (Å)	$\Delta X$ (%)
Ni	2.49	-4.5
Cu	2.56	-2.1
Rh	2.69	3.1
Ru	2.71	3.7
Pd	2.75	5.4
Pt	2.77	6.3
Ag	2.89	10.7

More recent developments found an interesting growth mode for water adsorbed on a Cu(110) surface. Carrasco *et al.*<sup>37</sup> show that on Cu(110), ice does not form the usual well documented hexagonal structure but instead it forms chains, approximately 1 nm in width, made up from face sharing pentagons of water. They combine STM and IR spectroscopy with DFT to explain how the pentagonal structure forms a strong H-bonded network while maintaining a strong bond between the water and the metal substrate. Figure 1.9 shows an STM image of the chains of pentagons formed on Cu(110). The novel pentagon based structure is reported for the first time on a metal surface and reveals a model that suggests that water structures are able to optimise bonding within the overlayer and to the surface. As the characterisation of water structures formed at metal surfaces remains difficult to resolve, the authors provide a recommendation for future studies to concentrate on looking for structures that provide an optimum balance between water – water and water – metal bonding rather than solely relying on finding a hexagonal model that fits.

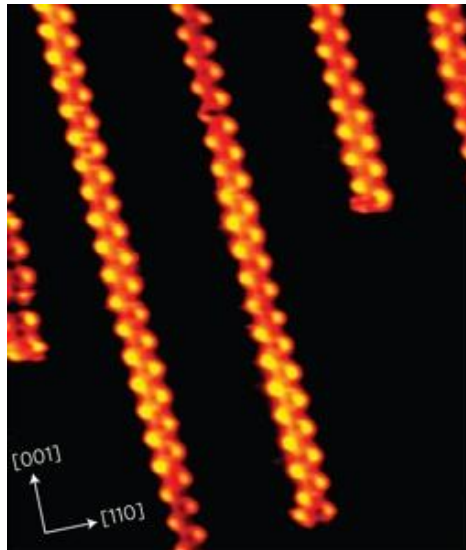


**Figure 1.9<sup>37</sup>:** STM image taken at 100 K. The water chains are shown growing along the [001] direction ( $120 \times 140 \text{ \AA}$ ,  $V=-196 \text{ mV}$ ,  $I=-0.34 \text{ nA}$ ). Reprinted by permission from Macmillan Publishers Ltd: [NATURE MATERIALS] (J. Carrasco, A. Michaelides, M. Forster, S. Haq, R. Raval, A. Hodgson, *Nature Materials*, 2009, 8, 427-431), copyright (2009).

**Table 1.2:** A summary of the wetting behaviour observed on different metal surfaces. Adapted from reference 7, where additional references can be found for the original sources of information

	<b>Sub-monolayer</b>	<b>Monolayer</b>	<b>Multilayer</b>
<b>Ni</b>	Extended islands of a $(2\sqrt{7} \times 2\sqrt{7})R19^\circ$ structure	$(2\sqrt{7} \times 2\sqrt{7})R19^\circ$ structure, presumed to be a disordered hexagonal water network	First layer reorders after adsorption of second layer to form an incommensurate hexagonal bulk ice (0001) film oriented to the surface
<b>Cu</b>	Does not wet, 3D ice clusters several layers thick form, with the buckled bilayer structure, oriented to the substrate		Multilayer adsorption stabilised by OH at higher temperatures
<b>Rh</b>	Small clusters of interlinked hexagons	$\sqrt{3}$ diffraction pattern but additional structure present. Water layer contains uncoordinated OH groups oriented both H-down and H-up	Multilayer water preferentially decorates the H-up free OH groups to form 3-D ice crystallites on the first layer
<b>Ru</b>	Small clusters consisting of water adsorbed flat to form interlinked water hexagons of limited size	Intact and $\sqrt{3}$ structure forms, with long range order near 0.67 ML. The $\sqrt{3}$ layer compresses at saturation, probably by forming domain boundaries. Intact layer is metastable with respect to dissociation, with $H_2O$ partially dissociating above 160 K but $D_2O$ desorbing intact. Water adopts a well defined lateral registry in the $\sqrt{3}$ structure, with no H-up water until the coverage $\geq 0.67$ ML. The O height is disordered and does not follow the simple $\sqrt{3}$ periodicity	First layer does not wet, 3-D ice clusters form on top of the first layer
<b>Pd</b>	Small clusters of interlinked hexagons with water adsorbed flat	$\sqrt{3}$ diffraction pattern, but additional structure present	Non-wetting first layer, 3-D ice clusters grow on top of the first layer water
<b>Pt</b>	Highly ordered extended $(\sqrt{37} \times \sqrt{37})R25^\circ$ islands form even at $< 0.1$ ML coverage	$\sqrt{37}$ islands compress to form a $(\sqrt{39} \times \sqrt{39})R16^\circ$ structure at saturation. Structure contains flat or H-down water molecules, with few free OH groups pointing into the vacuum	Multilayer water reconstructs first layer, forming an incommensurate bulk ice (0001) film, oriented to the metal surface. Multilayer clusters coexist with the first layer and do not cover the surface until the film is more than ca. 50 layers thick. Cluster growth is limited by nucleation of new layers. Growth of thick films proceeds rapidly at screw dislocations to form cubic ice. OH coadsorption inhibits wetting

## 1.4 Palladium

The experiments discussed in this thesis were all carried out on a Pd(111) crystal. Pd is one of the platinum group metals along with iridium, osmium, platinum, rhodium and ruthenium. Palladium was discovered in 1803 by William Hyde Wollaston and named after the asteroid Pallas. Table 1.1 summarises some physical and chemical properties of palladium.

**Table 1.3:** A summary of chemical and physical properties of palladium<sup>38</sup>.

Property	Value
Atomic number	46
Group	10
Period	5
Appearance	White malleable metal
Atomic radius (metallic)	1.37 Å
Atomic volume	8.9 cm <sup>3</sup> mol <sup>-1</sup>
Covalent radius	1.28 Å
Electron configuration	1s <sup>2</sup> 2s <sup>2</sup> p <sup>6</sup> 3s <sup>2</sup> p <sup>6</sup> d <sup>10</sup> 4s <sup>2</sup> p <sup>6</sup> d <sup>10</sup>
Crystal structure	Face centred cubic
Ionic radius	0.86 Å
Oxidation states	+2, 4
Atomic mass (average)	106.42 g mol <sup>-1</sup>
Boiling point	3237 K
Melting point	1825 K
Density	12.02 g cm <sup>-3</sup> at 20°C
Physical state at 20°C and 1 atm	Solid
Electron work function	5.12 eV
Electronegativity (Pauling)	2.20

## 1.5 Thesis outline

In this thesis, the growth of thin ice films and thick multilayers is investigated on a Pd(111) substrate. Temperature programmed desorption experiments are used to assess the initial growth behaviour before probing the system further with a range of surface science techniques. A low energy electron diffraction study into submonolayer, saturation coverage and multilayer growth of water films provides a discussion about the change in structure from an initial commensurate  $(\sqrt{3} \times \sqrt{3})R30^\circ$  configuration to a change structure evident from the splitting of the initial LEED spots. The change in structure occurs at the point where the first layer saturates and may be attributed to the onset of the growth of 3D ice clusters in preference to the ideal layer-by-layer growth. DFT and LEED simulations are used alongside workfunction calculations and experiments to provide evidence for an initial wetting layer which is bound tightly to the Pd surface through oxygen atoms (atop Pd) and forms the foundation for multilayer cluster growth. A growth mode consisting of a largely flat/H-down network is proposed.

Chapter 3 focuses on (sub)monolayer water adsorption on Pd(111) to draw initial conclusions of a wetting layer forming a structure with  $(\sqrt{3} \times \sqrt{3})R30^\circ$  periodicity but provides an evidence for an extended superstructure, due to the appearance of additional features in LEED patterns. Helium atom scattering is used to provide an indication of the disorder in the H network of adsorbed water overlayers. The interference of hydrogen adsorption from background gases proves to be an issue when trying to keep the surface clean. At the point where the first layer saturates, a change in growth mode is observed, characteristic of Stranski-Krastnow growth. A decrease in helium reflectivity occurs with increasing coverage, providing evidence to suggest that layer-by-layer multilayer growth does not occur and therefore no order is detected with coverages of water above the point where the first layer saturates. However, the order in the oxygen structure can be detected, even for coverages of 80 layers of water and it is shown that the first layer of water remains intact, stabilising the growth of ice clusters on top. The possibility of a  $(7 \times 7)$  or  $(\sqrt{52} \times \sqrt{52})R14^\circ$  structure is presented in chapter 3 with supporting evidence for an extended water superstructure on Pd(111). The model proposed has a large unit cell and disordered

H-down protons account for the absence of ordered diffraction peaks in the HAS spectra.

Chapter 4 focuses on multilayer water growth on Pd(111) and utilises chloroform adsorption to investigate the characteristics of multilayer growth further and also presents differences between crystalline ice (CI), grown at 140 K and amorphous solid water (ASW) grown at the lower temperature of 115 K. This section outlines significant differences in growth behaviour depending on adsorption temperature, with ASW covering the Pd(111) surface completely after the adsorption of two layers of water. In contrast, areas of bare monolayer remain exposed for up to 80 layers of crystalline ice adsorbed on the surface.

In chapter 5, a publication from the journal *Surface Science* is included, for which I was co-author and participated in all experimentation and analysis. TPD, LEED and CO titration experiments were used to show how oxygen and water are co-adsorbed to form a stable mixed OH/water phase at temperatures between 150 and 220 K on Pd(111). The  $(\sqrt{3} \times \sqrt{3})R30^\circ$  structure is stabilised by a hydrogen bonded network but, unlike behaviour reported for a similar structure on Pt(111), this phase does not catalyse the water formation reaction on Pd(111).

Chapter 6 outlines a different project carried out, using ultrafast surface dynamics to investigate the recombinative desorption of hydrogen on Cu(111). It is shown how a femtosecond laser is synchronised with a REMPI-TOF system to set-up an experiment to act as a pump-probe technique. The recombinative desorption of hydrogen is not detected at low fluence and further experiments are suggested in order to complete the project alongside suggestions for why laser induced desorption was not detected.

## 1.6 References

1. C. Lobban, J. L. Finney and W. F. Kuhs, *Nature*, 1998, **391**, 268-270.
2. J. D. Bernal and R. H. Fowler, *Journal of Chemical Physics*, 1933, **1**, 515-548
3. L. Pauling, *Journal of the American Chemical Society*, 1935, **57**, 2680-2684.
4. M. Chaplin, *Water Structure and Science*, [www.Isbu.ac.uk/water/index.html](http://www.Isbu.ac.uk/water/index.html).
5. C. Clay and A. Hodgson, *Current Opinion in Solid State & Materials Science*, 2005, **9**, 11-18.
6. M. A. Henderson, *Surface Science Reports*, 2002, **46**, 1-308
7. A. Hodgson and S. Haq, *Surface Science Reports*, 2009, **64**, 381-451.
8. P. A. Thiel and T. E. Madey, *Surface Science Reports*, 1987, **7**, 211-385.
9. D. L. Doering and T. E. Madey, *Surface Science*, 1982, **123**, 305-337.
10. A. Michaelides, V. A. Ranea, P. L. de Andres and D. A. King, *Physical Review Letters*, 2003, **90**, 216102.
11. A. L. Glebov, A. P. Graham and A. Menzel, *Surface Science*, 1999, **428**, 22-26.
12. H. Ogasawara, J. Yoshinobu and M. Kawai, *Journal of Chemical Physics*, 1999, **111**, 7003-7009.
13. K. P. Stevenson, G. A. Kimmel, Z. Dohnalek, R. S. Smith and B. D. Kay, *Science*, 1999, **283**, 1505-1507.
14. L. E. Firment and G. A. Somorjai, *Surface Science*, 1979, **84**, 275-294.
15. A. Glebov, A. P. Graham, A. Menzel and J. P. Toennies, *Journal of Chemical Physics*, 1997, **106**, 9382-9385.
16. S. Haq, J. Harnett and A. Hodgson, *Surface Science*, 2002, **505**, 171,
17. J. Harnett, S. Haq and A. Hodgson, *Surface Science*, 2003, **528**, 15-19.
18. G. Zimbitas, S. Haq and A. Hodgson, *Journal of Chemical Physics*, 2005, **123**, 174701.
19. J. P. Toennies, F. Traeger, J. Vogt and H. Weiss, *Journal of Chemical Physics*, 2004, **120**, 11347-11350.
20. K. Thurmer and N. C. Bartelt, *Physical Review Letters*, 2008, **100**, 186101.
21. M. E. Gallagher, S. Haq, A. Omer and A. Hodgson, *Surface Science*, 2007, **601**, 268-273.
22. G. Held and D. Menzel, *Surface Science*, 1994, **316**, 92-102.
23. G. Held and D. Menzel, *Surface Science*, 1995, **327**, 301-320.

24. G. Held and D. Menzel, *Physical Review Letters*, 1995, **74**, 4221-4224.
25. P. J. Feibelman, *Science*, 2002, **295**, 99-102.
26. P. A. Thiel, F. M. Hoffmann and W. H. Weinberg, *Journal of Chemical Physics*, 1981, **75**, 5556-5572.
27. P. J. Schmitz, J. A. Polta, S. L. Chang and P. A. Thiel, *Journal of Vacuum Science & Technology a-Vacuum Surfaces and Films*, 1987, **5**, 1086-1088.
28. D. N. Denzler, S. Wagner, M. Wolf and G. Ertl, *Surface Science*, 2003, **532**, 113-119.
29. A. Beniya, K. Mukai, Y. Yamashita and J. Yoshinobu, *Journal of Chemical Physics*, 2007, **126**, 141102.
30. A. Beniya, K. Mukai, Y. Yamashita and J. Yoshinobu, *Journal of Chemical Physics*, 2008, **129**, 016101.
31. A. Beniya, Y. Sakaguchi, T. Narushima, K. Mukai, Y. Yamashita, S. Yoshimoto and J. Yoshinobu, *Journal of Chemical Physics*, 2009, **130**, 034706.
32. A. Beniya, S. Yamamoto, K. Mukai, Y. Yamashita and J. Yoshinobu, *Journal of Chemical Physics*, 2006, **125**, 054717.
33. K. D. Gibson, D. R. Killelea and S. J. Sibener, *Journal of Physical Chemistry C*, 2009, **113**, 13325-13330.
34. R. S. Smith, C. Huang, E. K. L. Wong and B. D. Kay, *Surface Science*, 1996, **367**, L13-L18.
35. B. D. Kay, K. R. Lykke, J. R. Creighton and S. J. Ward, *The Journal of Chemical Physics*, 1989, **91**, 5120-5121.
36. A. Michaelides and K. Morgenstern, *Nature Materials*, 2007, **6**, 597-601.
37. J. Carrasco, A. Michaelides, M. Forster, S. Haq, R. Raval, A. Hodgson, *Nature Materials*, 2009, **8**, 427-431.
38. C. E. Housecroft and E. C. Constable, *Chemistry: An Introduction to Organic, Inorganic and Physical Chemistry*, 4<sup>th</sup> ed. 2010.

# **Chapter 2**

## **Experimental Techniques**

## 2. Experimental Techniques

All experimental work was carried out in one of four ultra-high vacuum chambers designed by V.S.W Scientific Instruments Ltd. The majority of experiments were carried out in a large vacuum chamber equipped with a molecular beam for controlled dosing of gases, a quadrupole mass spectrometer to monitor gas desorption via temperature programmed desorption and isothermal desorption techniques and a low energy electron diffraction unit for probing surface structure. Helium atom scattering experiments were performed in a second chamber further equipped with a helium nozzle, a supersonic nozzle for dosing gases, a VG smart IQ<sup>+</sup> mass spectrometer for TPD measurements and a Hiden mass spectrometer situated in a side arm used to detect helium atoms scattered from the surface. Additional chambers were used to collect RAIRS data and work function measurements under similar vacuum conditions. This chapter outlines the theory behind the procedures used to collect the data in this thesis and more detailed information about specific experiments will be provided in subsequent chapters.

### 2.1 Ultra-High Vacuum Chambers

The chamber of main focus in this thesis (figure 2.1) consisted of three stages pumped by water-cooled oil diffusion pumps and backed by rotary vane pumps of various sizes. Diffusion pumps were used in preference to turbomolecular pumps as they have been proven to pump hydrogen more efficiently. When first pumped down, the chamber would reach  $1 \times 10^{-8}$  mbar but once baked at temperatures greater than 150 °C, working pressures reached less than  $1 \times 10^{-10}$  mbar. A liquid nitrogen cold trap was filled in order to limit the flow of unwanted gases back into the main chamber. Extra pumping was obtained from a titanium sublimation pump (TSP) by means of a titanium film reacting to remove active gases such as oxygen, nitrogen and hydrogen.

The experimental analysis equipment was all located in the main section of the chamber which was fitted with an x,y,z ( $\theta$ ) manipulator which had the Pd(111) crystal mounted on it. The Pd(111) crystal was cut and polished to within  $0.25^\circ$  of the

crystallographic plane and spot-welded to Ta posts with Ta wire. The posts were connected to a copper feedthrough using barrel connectors, which enabled cooling to 100 K to be achieved. A K-type thermocouple was spot-welded to the edge of the crystal allowing the sample to be resistively heated to 1000 K with a DC power supply and the temperature to be monitored. The main chamber was fitted with a leak valve, to which gases could be attached and background dosed and argon was regularly used in this way for repeated cleaning cycles. For more accurate dosing, an effusive molecular beam was employed for steady control over gas flux.

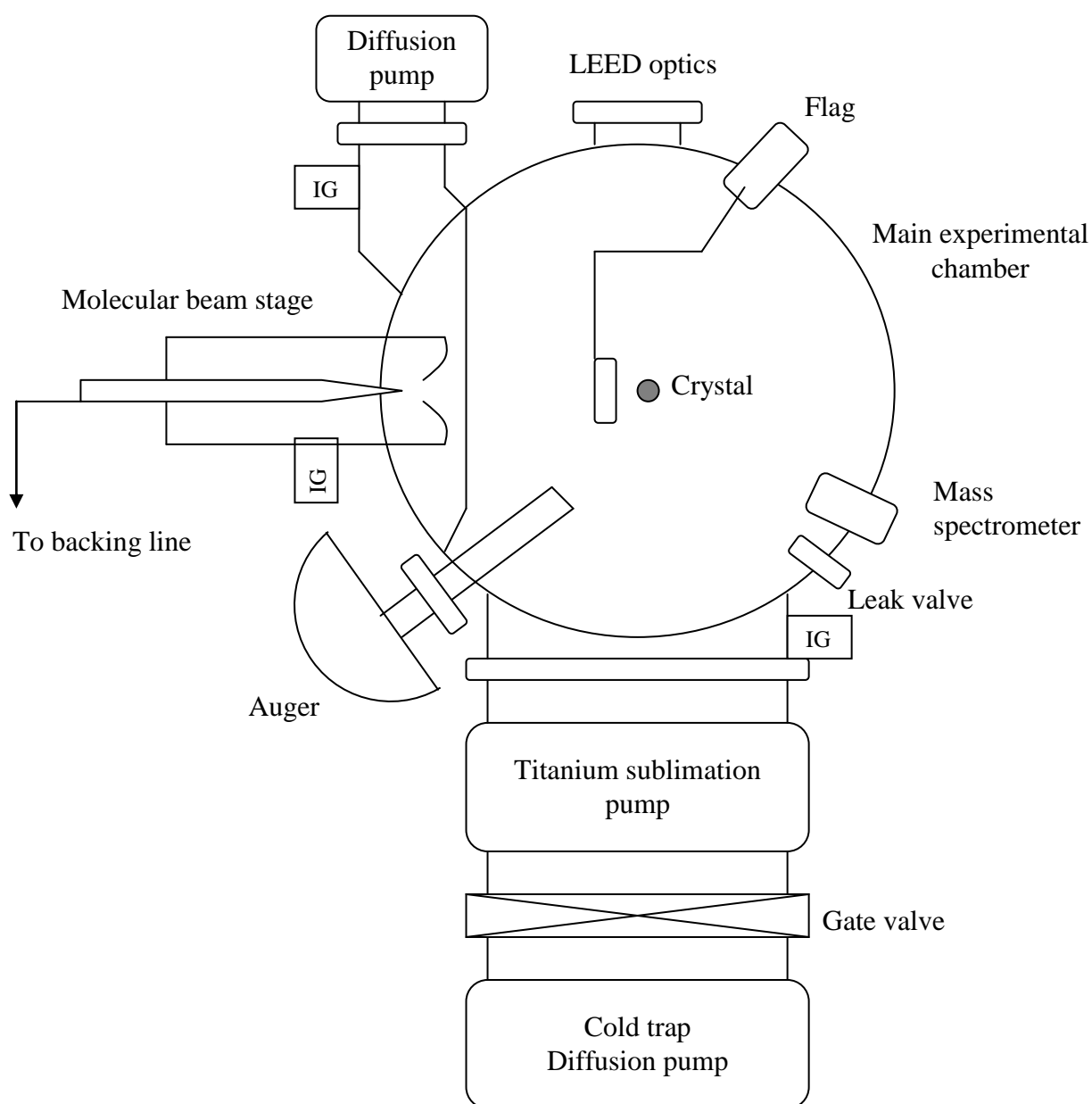


**Figure 2.1:** Schematic of UHV chamber. IG refers to the ion gauges.

## 2.2 Sputter and Anneal Cycles

Argon ion sputtering cycles were used to clean the crystal. Argon gas was leaked into the main chamber at a pressure of  $1 \times 10^{-6}$  mbar and an ion gun (VSW AS10) was used to bombard the surface with 500 eV of argon ions (drain current of  $5.2 \mu\text{Acm}^{-2}$ ) for 10 – 15 minutes. Following each cycle, the crystal was annealed to 1000 K to reorder the surface.

## 2.3 Dosing Gases

Gases were dosed onto the surface by means of an effusive molecular beam comprising a 0.25 mm glass capillary and skimmer to collimate the beam which results in a beam with a spot diameter of approximately 5 mm. The beam was differentially pumped and had a backing pressure of a few torr. The use of an effusive molecular beam allowed high control over the flux of gases in comparison to a leak valve and minimised excess gases being dosed into the chamber. Gases were dosed according to the well acclaimed King and Wells technique for sticking probabilities<sup>1</sup>. This involved letting the molecular beam into the chamber at time  $t_0$ , with a flag placed between the incoming beam and the surface. This caused an increase of water (or other dosing gas) pressure in the chamber,  $p_0$ , which remained constant with a set pressure of the beam. At time  $t_1$ , the flag was moved out of the path of the beam, resulting in a pressure drop,  $p_1$ , as the gas adsorbed on the surface. With conditions of constant flux, surface temperature and number of adsorption sites,  $p_1$  remains steady. As the number of adsorption sites decreases (as the surface becomes saturated),  $p_1$  begins to increase back to the background level (figure 2.2).

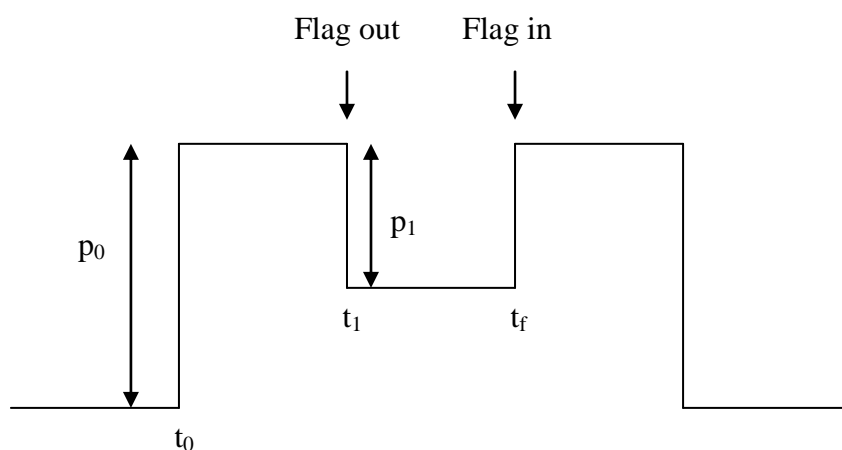


**Figure 2.2:** Schematic representation of a square uptake profile showing the King and Wells technique for sticking probability <sup>1</sup>.

The time taken for a surface to saturate can be measured at a particular pressure. If the given adsorbate only forms one layer (eg. oxygen) then the sticking probability becomes 0 at the point where that layer saturates because there are no more adsorption sites available. However, if the adsorbate forms a multilayer (eg. water), then adsorption remains constant with time and in this case the flux can be determined by the onset of multilayer growth (ie, saturation of the first layer).

The Kings and Wells technique to determine sticking probabilities involves integrating the partial pressure of the adsorbed gas (recorded on the QMS) as a function of time (equation 2.1) and the value can be calibrated against the integral of the corresponding desorption profile. The relationship between sticking probability and partial pressures is shown in Equation 2.1.

$$S = \frac{P_0 - P_1}{P_0} \quad \text{Equation 2.1}$$

## 2.4 Temperature Programmed Desorption (TPD)

Gases are dosed into a vacuum chamber and adsorb onto a given surface to form an adlayer. Heating at a steady rate causes the adsorbed gas to desorb at a temperature characteristic to both the surface and species involved. The desorption process occurs when the energy barrier for the metal-gas bond is overcome. As the gas desorbs, a pressure increase is observed before dropping back to base pressure once the desorption is complete. This behaviour gives a plot of pressure versus time which yields information about surface coverage (area underneath the curve) and the binding energy of the gas to the surface (from the maximum peak temperature). A schematic is given in figure 2.3

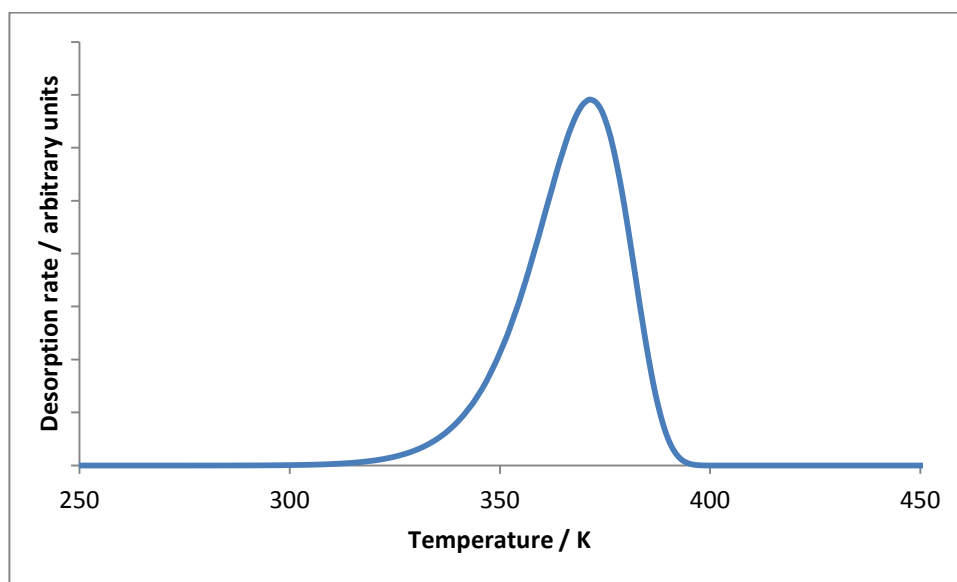


**Figure 2.3:** Schematic representation of a desorption profile showing the rise and fall in the intensity of desorbing gases with increasing temperature. In this example the x axis displays temperature but data can also show time in seconds.

The rate of desorption can be determined by using the Polanyi-Wigner equation. The desorption signal recorder by the mass spectrometer is proportional to the rate of desorption ( $r_{\text{des}}$ ) under conditions with a sufficiently high and constant pumping speed to prevent re-adsorption onto the surface. The activation parameters are dependent on surface coverage and the resulting Polanyi-Wigner expression is given in Equation 2.2.

$$r_{des} = -\frac{d\theta_{A(ads)}}{dt} = \nu_n \cdot \theta_{A(ads)}^n \cdot \exp\left[\frac{-E_{des}}{RT}\right] \quad \text{Equation 2.2}$$

The parameters in equation 2.2 are defined below:

- $r_{des}$  desorption rate in molecules  $\text{cm}^{-2} \text{s}^{-1}$
- $\theta_{A(ads)}$  surface concentration of adsorbate A
- $\nu_n$  pre-exponential factor
- $n$  desorption order
- $E_{des}$  activation energy for desorption

The maximum desorption temperature ( $T_{\max}$ ) is affected by the activation energy of desorption. The frequency factor, the heating rate and the coverage and the order of reaction when  $n \neq 0$ . The overall shape of the peak is affected by the frequency factor, heating rate and order of reaction. Finally, the peak area is determined by the coverage.

In equation 2.2,  $n$  refers to the order of reaction and is a value between zero and two. The shape of the desorption profile provides information regarding reaction kinetics and is discussed in more detail below.

### Zero order kinetics ( $n=0$ )

$$-\frac{d\theta}{dt} = \nu \cdot \exp\left[-\frac{E_a^{des}}{RT}\right] \quad \text{Equation 2.3}$$

Because  $n = 0$ , the coverage term from equation 2.3 disappears, therefore the rate of desorption for zero order reactions is independent of coverage and an exponential increase occurs with temperature (figure 2.4). For a given ramp rate, the leading edge of the desorption curve remains the same and there is a rapid decline once all molecules have desorbed. Zero order desorption can be expected for thick layers of

adsorbates due to the high amount of desorbing molecules. This behaviour can also be observed for pseudo first order reactions involving strong interactive attractions between adsorbates.

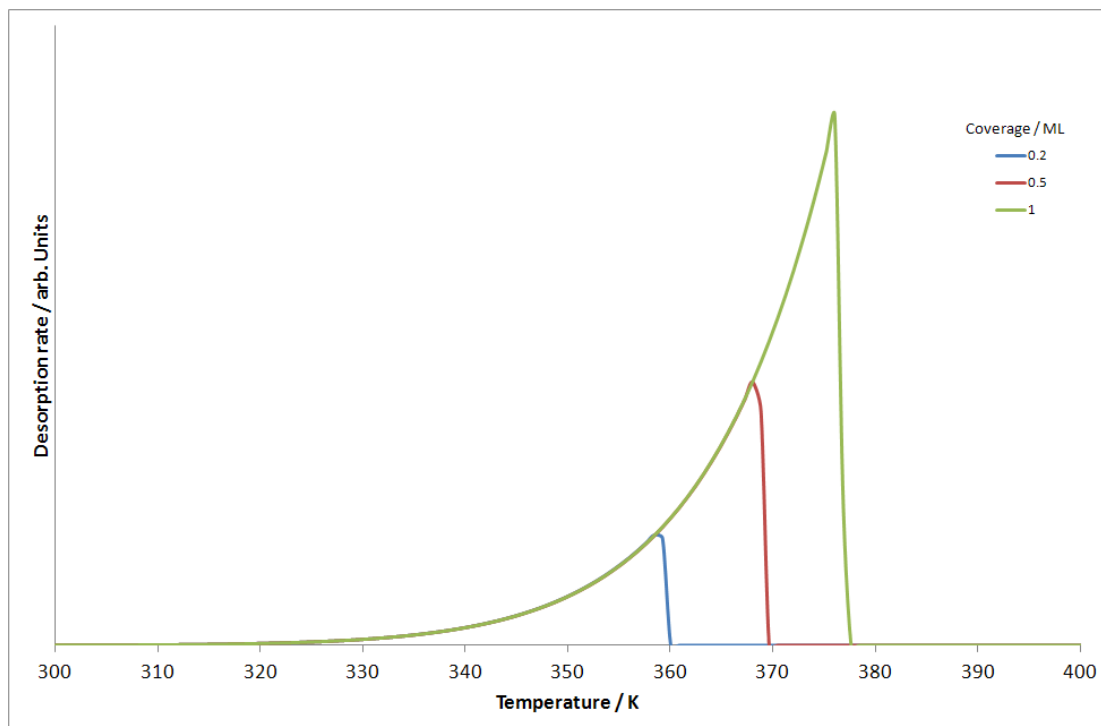


**Figure 2.4:** Ideal temperature programmed desorption profile for an adsorbate exhibiting zero order kinetics ( $n=0$ ).

### First order kinetics ( $n=1$ )

$$-\frac{d\theta}{dt} = \nu \cdot \theta \cdot \exp\left[-\frac{E_a^{des}}{RT}\right] \quad \text{Equation 2.4}$$

Reactions with first order rate kinetics are expected for non-dissociative molecular adsorption and atomic adsorption. The desorption rate is proportional to the instantaneous coverage and presents a balance between coverage and exponential terms. The desorption peak remains at a constant temperature as the coverage increases and this desorption temperature is determined by the binding energy of the adsorbate to the surface. The resulting peak is asymmetric and an example is given in figure 2.5.

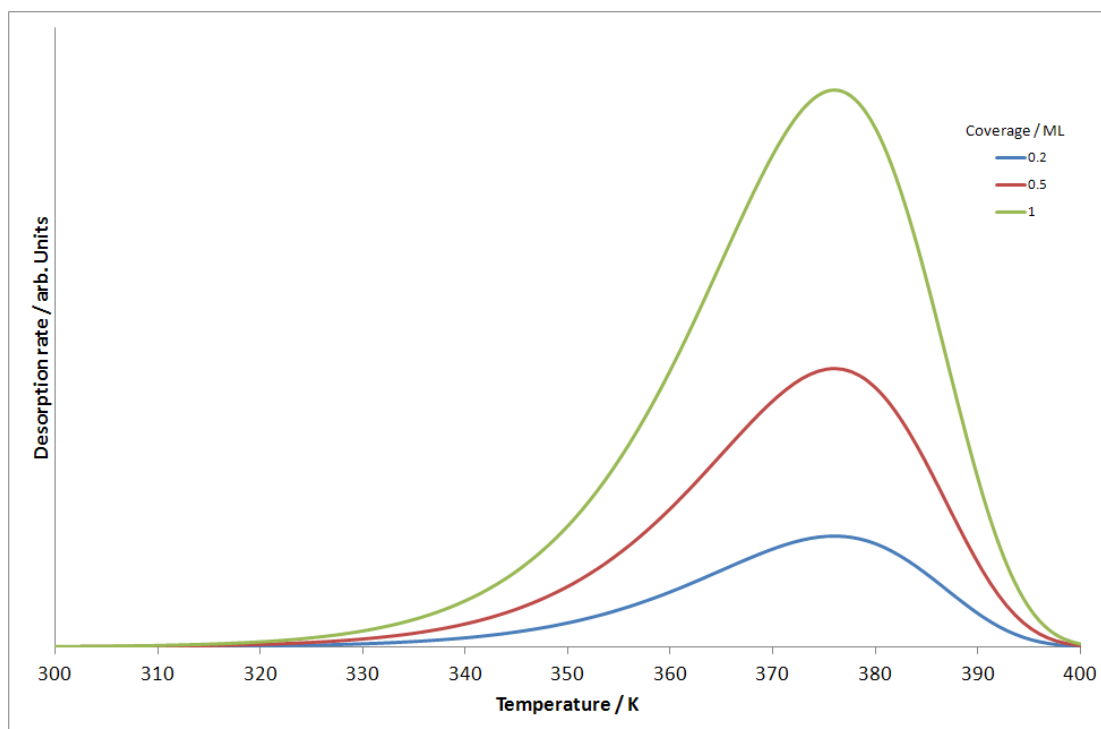


**Figure 2.5:** Ideal temperature programmed desorption profile for an adsorbate exhibiting first order kinetics ( $n=1$ ).

### Second order kinetics ( $n=2$ )

$$-\frac{d\theta}{dt} = \nu \cdot \theta^2 \cdot \exp\left[-\frac{E_a^{des}}{RT}\right] \quad \text{Equation 2.5}$$

Second order kinetics are observed for recombinative desorption reactions and the desorption rate is proportional to the square of instantaneous coverage. The maximum desorption temperature moves to a lower value with increasing coverage and for a specific ramp rate, the desorption traces have a common trailing edge and peaks that are almost symmetrical (figure 2.6).

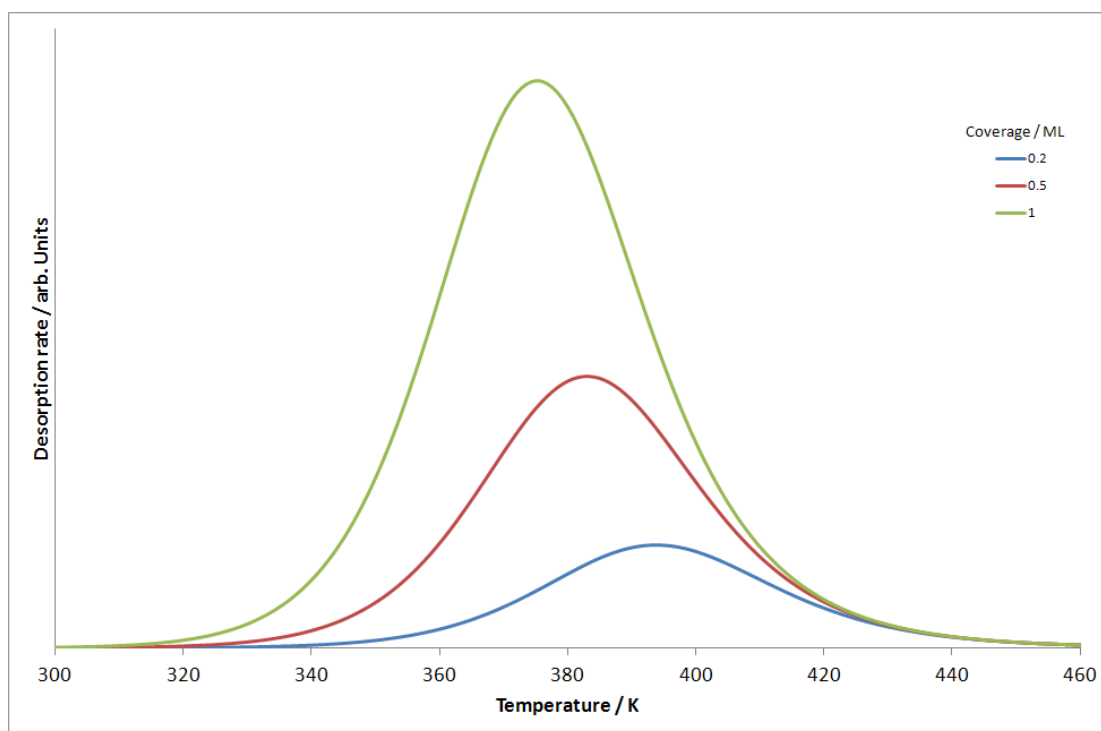


**Figure 2.6:** Ideal temperature programmed desorption profile for an adsorbate exhibiting second order kinetics ( $n=2$ ).

## 2.5 Quadrupole Mass Spectrometer

Mass spectrometry is an analytical technique used to record the elemental composition of samples to deduce chemical structures, determine background gases present or to record desorption products. The main concept of mass spectrometry involves using an electron impact ioniser with a high energy electron beam (70 eV) to bombard molecules and ionise them. The resulting charged particles are accelerated towards a detector and the relative abundances of masses present are recorded.

Desorption experiments discussed in this thesis were carried out using a quadrupole mass spectrometer (figure 2.7) consisting of an ion source, quadrupole analyser and ion detector (electron multiplier). A quadrupole mass spectrometer contains extraction and acceleration ion optics which separate ions with a specific mass to charge ratio ( $m/z$ ) and discard the others. The voltage applied affects the trajectory of the ions travelling between the quadrupole analyser rods, therefore, to detect a specific mass, a specific voltage must be applied.

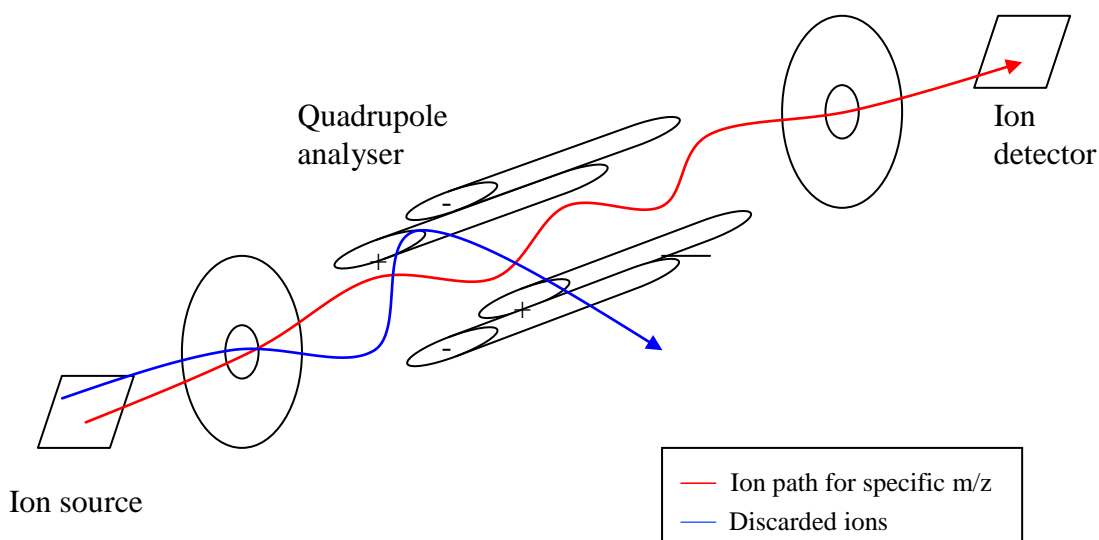


**Figure 2.7:** Schematic of a quadrupole mass spectrometer

The mass spectrometer was used to run an analogue scan before each experiment in order to monitor the background gases present in the chamber. This was used to detect a full range of masses rather than individual fragments. During desorption experiments, the mass spectrometer was used to detect water, oxygen and hydrogen as the temperature of the sample was increased. A temperature calibration was carried out by measuring the voltage on the mass spectrometer as the temperature was ramped at a steady rate. This allowed desorption profiles to be plotted against temperature rather than time.

## 2.6 Low Energy Electron Diffraction (LEED)

LEED is used to probe the first few layers of a structure by analysing elastically back scattered electrons in the range of 20 – 1000 eV. This energy range equates to a mean free path for the electrons of between 1 and 20 Å which is how far the electrons can travel into the surface. LEED is good for surface analysis because the de Broglie wavelength of the electrons used is comparable to the inter-atomic spacings between atoms in metal surfaces. If atoms are arranged in a periodic structure, electron diffraction patterns can be recorded. The curve shown in figure 2.8 is referred to as

the universal curve and combines escape depth data for electrons with a kinetic energy between 2 – 1500 eV.

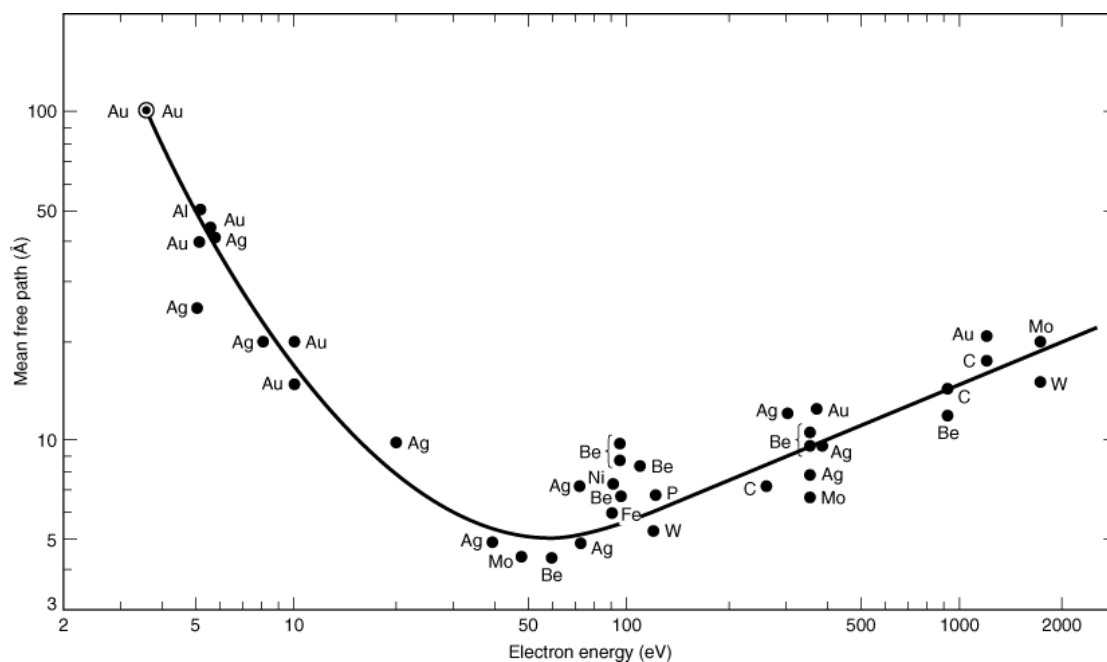


**Figure 2.8:** The universal curve for mean electron escape depth<sup>2</sup>.  
Reproduced with permission from [S. S. Perry and G. A. Somorjai, *Surfaces. Encyclopedia of Inorganic Chemistry*; John Wiley & Sons, Inc., New York, 2006. Copyright (2206).

The electron beam can be seen as a plane wave at normal incidence to the surface and has a De Broglie wavelength:

$$\lambda = \frac{h}{p} = \frac{h}{mv} \quad \text{Equation 2.6}$$

For an electron this becomes:

$$\lambda / \text{\AA} = \sqrt{\frac{150}{E_0 / \text{eV}}} \quad \text{Equation 2.7}$$

In the above equations;

$v$  : velocity

$\lambda$  : wavelength

$p$  : momentum

$h$  : Planck's constant

$E$  : kinetic energy

Therefore, as an example an electron beam at 50 eV will give a wavelength of 1.73 Å.

For constructive interference:

$$d = a \sin \theta = n\lambda \quad \text{Equation 2.8}$$

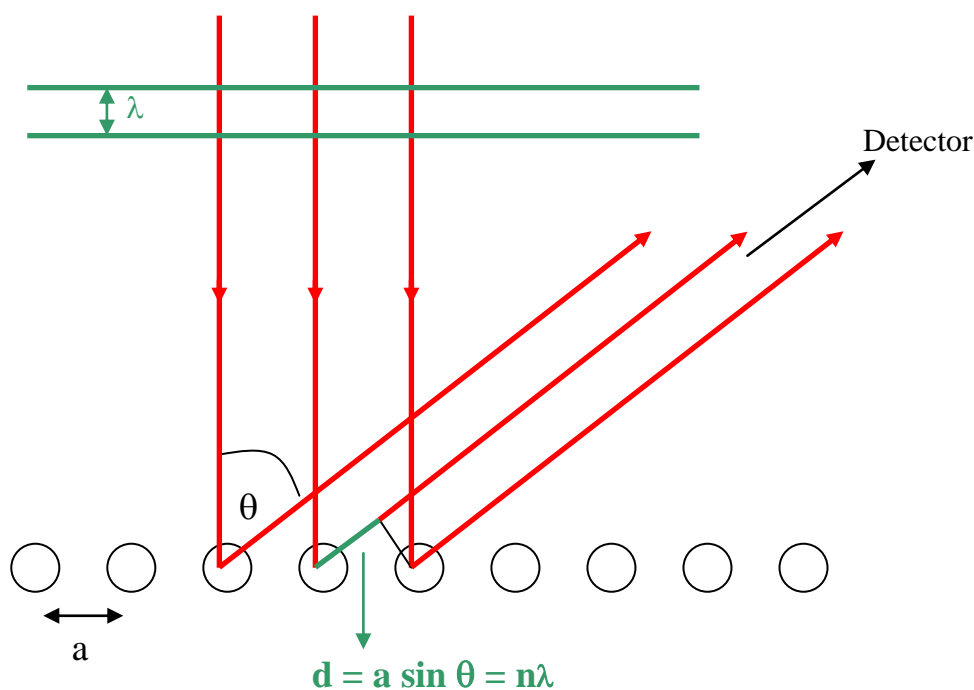


**Figure 2.9:** Schematic representation of the back scattering of a wave of electrons (red arrows) from a 1D plane of atoms (black circles). The green lines represent the wavelength of electrons and the path difference between the scattered waves.

The single crystal sample was positioned inside the UHV chamber in front of the LEED optics. A monochromatic beam of electrons with variable energy was generated by an electron gun and lined up to be incident with the sample. Before carrying out experiments, the sample was grounded in order to prevent charging. Elastically scattered electrons do not lose energy and back-scatter from a periodic

surface towards a set of grids as shown in figure 2.10. The outer grid is earthed and forms a field free region for electrons to travel through. The grids in the middle are held at a negative potential just lower than the kinetic energy of electrons produced by the electron gun and act as a filter, only allowing elastically scattered electrons to pass through to the detector and removing secondary electrons with lower energies. The detector is held at a positive high voltage ( $\sim 6$  kV) in order to accelerate the elastically scattered electrons resulting in light emission from the fluorescent phosphor screen – this pattern takes the form of brightly coloured spots on a black background and yields information about the surface structure and symmetry. The resulting pattern is in reciprocal space and as the lattice constants increase, the scattering angle for the beam decreases. Figure 2.12 gives examples of LEED patterns for adlayers on fcc surfaces.

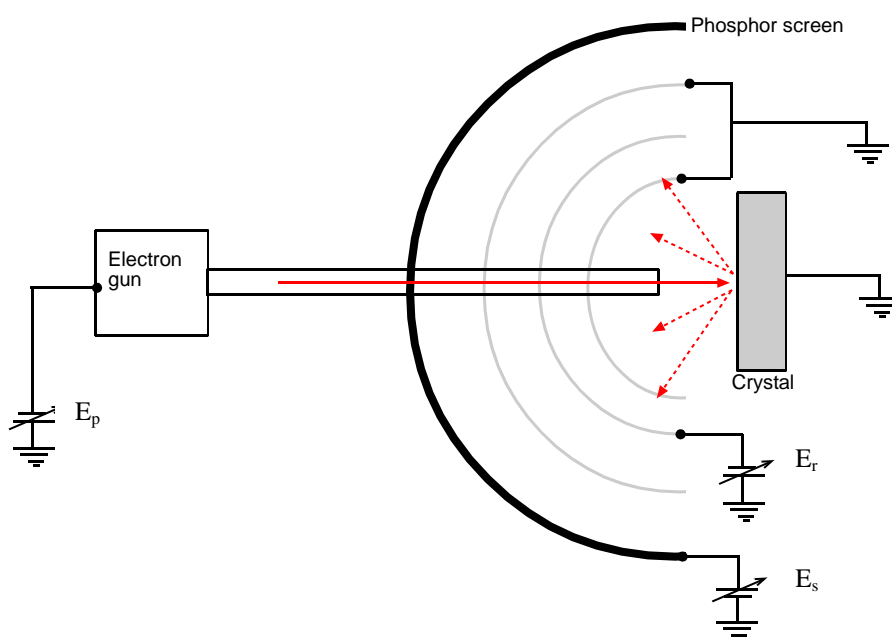


**Figure 2.10:** Schematic representation of LEED optics.  $E_r$ : retarding voltage;  $E_p$ : primary energy

In figure 2.12 there are two notations given to describe the LEED schematics. One is the matrix notation (top) and the other is Wood's notation (bottom) which is more commonly employed. The definition of Wood's notation comes from the use of

vectors as shown in figure 2.12 and can only be used when  $\mathbf{b}_1$  and  $\mathbf{b}_2$  are rotated through the same angle,  $\theta$ , with respect to vectors  $\mathbf{a}_1$  and  $\mathbf{a}_2$ . When describing LEED images, Wood's notation is often abbreviated to the format  $(p \times q)R\theta^\circ$  as will be seen throughout this document with the  $(\sqrt{3} \times \sqrt{3})R30^\circ$  structure amongst others. The matrix notation is similar to Wood's notation but instead of  $(p \times q)R\theta^\circ$ , a  $2 \times 2$  matrix is used to map the overlayer structure onto the surface. For example,  $(2 \times 2)R0^\circ$  would be equivalent to writing  $\begin{bmatrix} 2 & 0 \\ 0 & 2 \end{bmatrix}$ . More examples are given in more detail in figure 2.11.

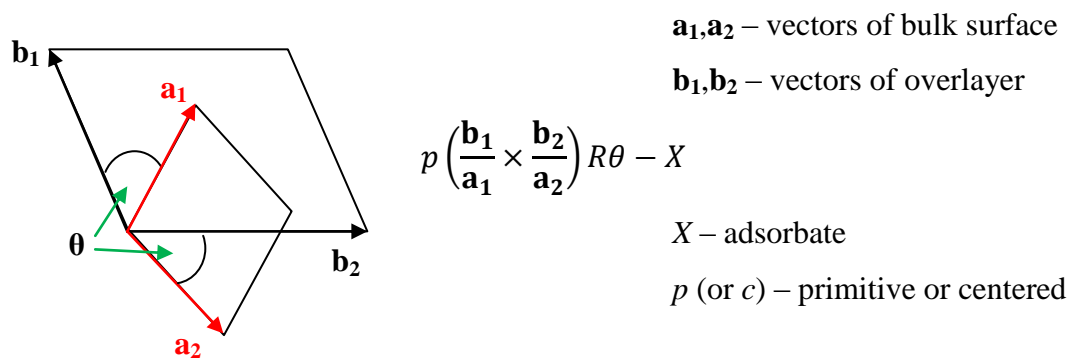


**Figure 2.11:** Schematic to represent Wood's notation along with a descriptive equation containing the parameters required

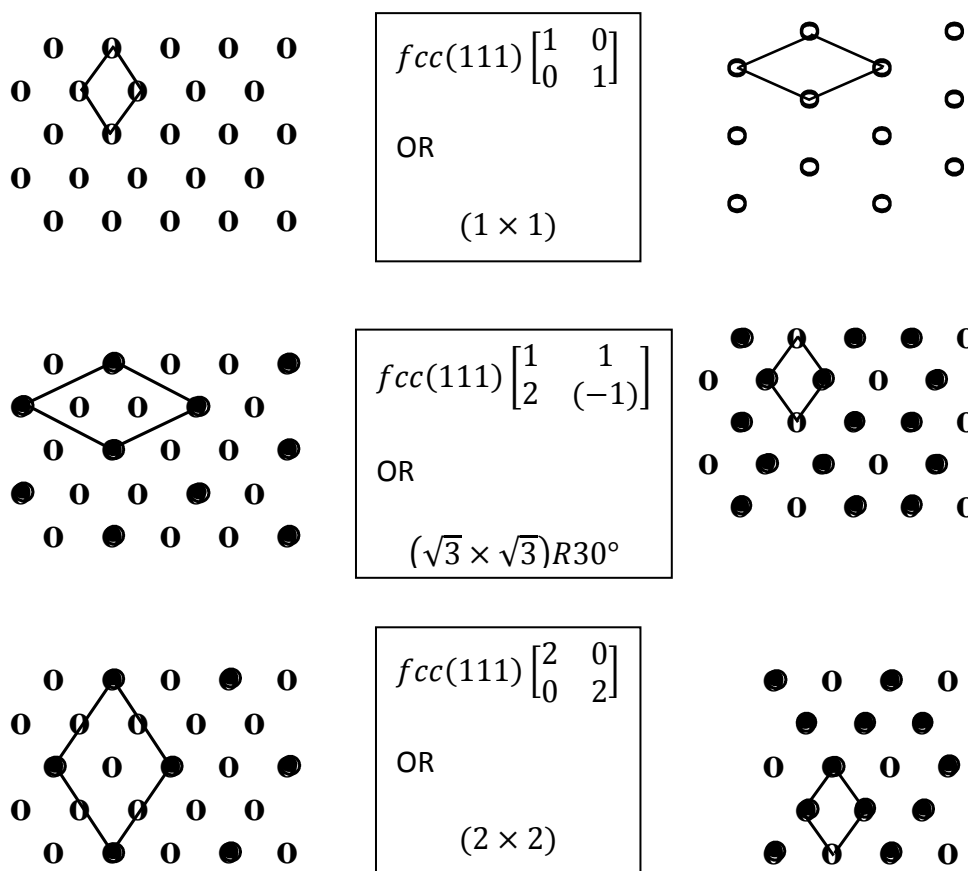


**Figure 2.12:** Schematic representation of LEED patterns on fcc metals in real space (left hand side) and reciprocal space (right hand side).

Using LEED allows us to monitor the cleanliness of a surface – for example, for a clean Pd(111) surface, a sharp (1 x 1) pattern should be observed with additional spots indicating impurities adsorbed on the surface. Images obtained of water layers adsorbed on metal surfaces provide an indication of the order present in the adlayer in addition to information regarding the growth mechanism from changes observed due to different growth conditions. Difficulties arise because of the sensitivity of water films to electron damage and therefore, care must be taken to minimise exposure time to the electron beam and emission currents need to remain as low as possible.

In summary, LEED is a useful probe which helps to analyse the periodicity of gases adsorbed onto metal substrates. Quantitative and qualitative data can be obtained from LEED experiments. Quantitative analysis involves producing LEED IV curves, which

show the intensity of diffracted electron beams as a function of the incident beam. However, only qualitative analysis will be discussed further with respect to LEED investigations on Pd(111). For experiments described in this thesis, LEED will be used to determine the periodicity of water and mixed OH/water overlayers on the Pd(111) surface. Initial LEED images of the clean Pd(111) surface were used to provide confirmation of the surface cleanliness after Ar<sup>+</sup> ion sputter and anneal cycles.

## **2.7 Reflection Absorption Infra-Red Spectroscopy (RAIRS)**

RAIRS can be used to investigate molecular vibrations of surface adsorbates to characterise the composition of water overlayers and yields results characteristic of the molecule and the method of bonding to the surface. An absorption band can only be detected if molecules are infra-red active and observe two selection rules. The first rule states that for adsorption of infra-red light to occur, there must be a change in dipole moment. The second rule is additional for surface adsorbates and states that there must be an oscillating dipole moment normal to the surface for the vibrations to be observed using RAIRS. Figure 2.13 illustrates the selection rules by using carbon monoxide as an example. The orientation lying normal to the surface is IR active and would be observed in RAIRS because the net dipole is maximised. The dipole moment for the molecule lying parallel to the surface is cancelled out by an image dipole formed at the surface.

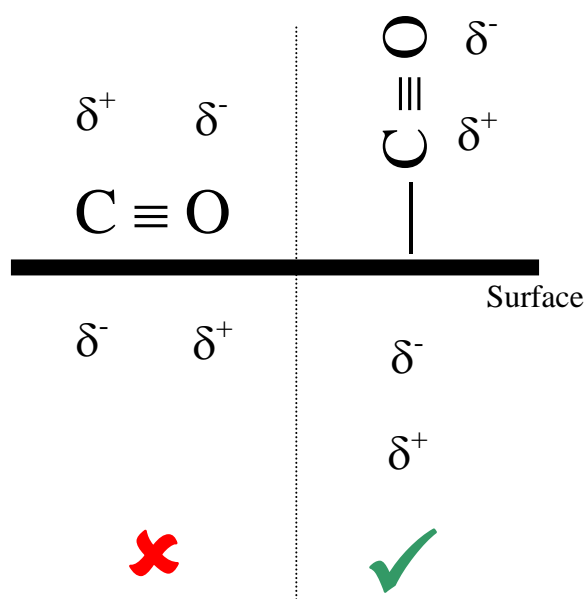
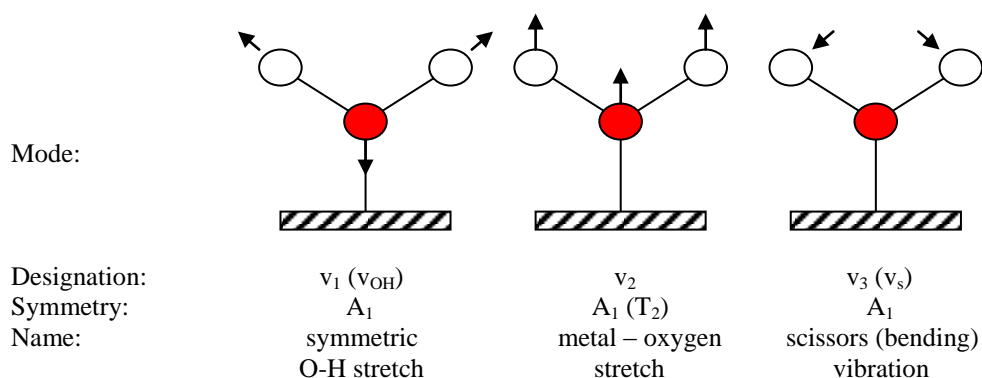


**Figure 2.13:** Schematic to show the surface selection rules for CO adsorbed on a metal surface.

Different orientations of water on the surface show up with absorption bands at various wavenumbers. An individual water molecule has  $C_{2v}$  symmetry and water adsorbed to a surface via the oxygen atom has nine vibrational modes as shown in figure 2.14<sup>3</sup>. For an upright water molecules, the three dipole allowed transitions would be observed in the vibrational spectra (the symmetric O-H stretching mode, metal-oxygen stretch and scissors mode). The literature contains theoretical DFT calculations that find single water molecules preferring to adsorb on a metal surface with the plane of the H-O-H bond lying parallel to the surface. Therefore, for flat lying water molecules, these vibrational modes become IR inactive and the librational modes and frustrated translation dipole-forbidden transitions become IR active. For a situation involving the adsorption of a tilted water molecule (neither upright nor flat), a combination of the dipole allowed and dipole forbidden transitions would become IR active. The IR transitions described here are applicable to single water molecules and the vibrational spectra become more complicated with the addition of hydrogen bonding between adjacent molecules. Water cluster formation causes the dipoles to interact resulting in coupling between water vibrations. This coupling can cause broadening of the IR spectra and an increase in the interaction between dipoles as reported in the literature for CO adsorption on Cu(111)<sup>4</sup>. For low coverage water adsorption (only a few films thick), figure 2.14 summarises the dominant vibrations

that will be observed in the IR spectra. The exact position of absorption bands, along with their width, depends on the geometry of the adsorbed water molecules, the strength of the hydrogen bond interactions and the strength of the interaction to the metal surface.

### Dipole allowed transitions



### Dipole forbidden transition

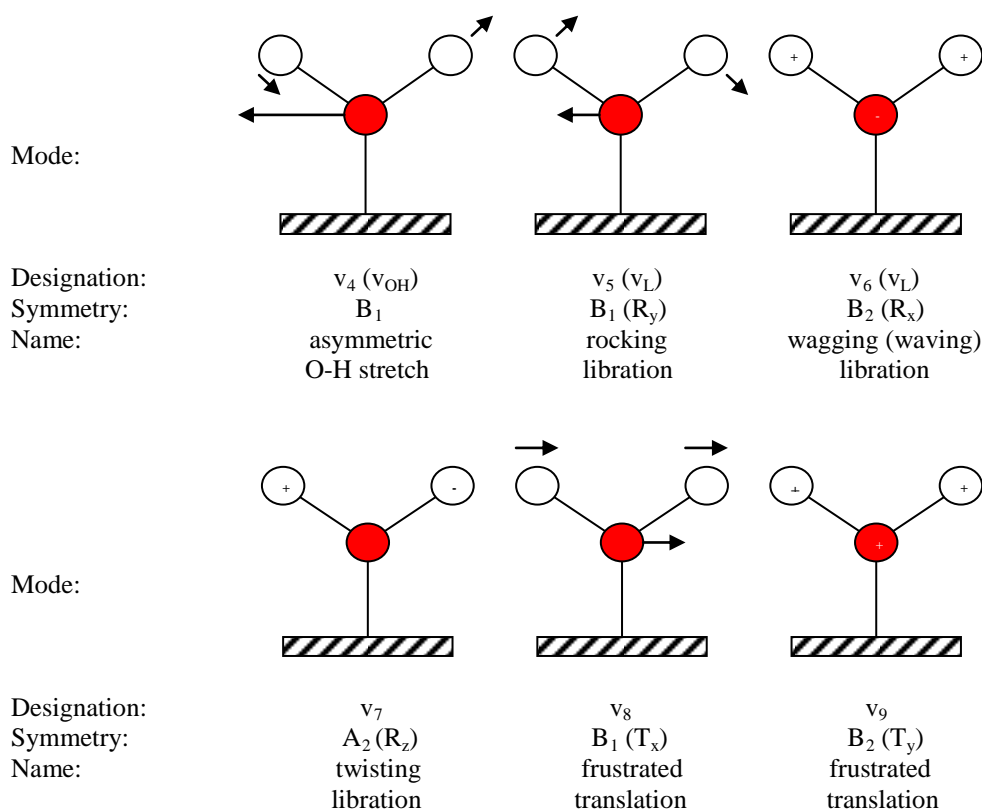


**Figure 2.14:** Normal modes of water adsorption with  $C_{2v}$  symmetry on a flat metal surface. Arrows represent vibrations in the plane of the paper + / - represent vibrations perpendicular to the plane of paper.

There are two types of infrared spectrometers, dispersive IR instruments which operate in the frequency domain and fourier transform (FT) spectrometers that allow the advantage of measuring in the time domain and using a computer to transform the data into the frequency domain. A typical dispersive IR spectrometer operates with radiation from a broad-band source passing through a sample to a monochromator. The monochromator disperses the radiation into component frequencies using prisms or gratings in conjunction with variable slit mechanisms, mirrors and filters. For example, the grating would rotate to focus a narrow band of frequency on to a mechanical slit and the narrower the slit, the better the resolution. The beams reach a detector which records the output in the frequency domain. A FTIR spectrometer can use the same radiation source as the dispersive IR but the monochromator is replaced by an interferometer. This divides and recombined the radiation from the broad-band source, after the split beams have travelled different optical paths to generate constructive and destructive interference. The resulting beam passes through the sample and is recorded in the time domain by the detector. Computer processing can then be used to transform the data into the frequency domain. The FTIR technique provides many advantages over dispersive IR and these are summarised below:

- FTIR provides better sensitivity in a much faster time period (Felgett advantage).
- All frequencies are recorded simultaneously meaning that only one scan is required to gain a complete spectrum in comparison to dispersive IR where the individual frequencies are recorded sequentially.
- FTIR data is recorded with higher resolution (improved signal / noise ratio) for an equivalent time period.
- There is increased optical throughput (Jaquinot advantage) due to the elimination of energy wasting slits.
- The amount of stray light is significantly reduced or eliminated when using FTIR.
- The instrumentation used for FTIR has a simpler mechanical design than that used for dispersive IR.
- The computer associated with FTIR provides advantages in data processing.

For experiments described in this thesis, a Mattson 6020 FTIR spectrometer was used to produce an infra-red beam that could be focused onto the crystal using a KBr lens ( $f = 280$  mm) at an incidence grazing angle of  $\theta = 82^\circ$  to the surface normal. The reflected light was focused onto a liquid nitrogen cooled detector and the absorbance spectra recorded. A wide band mercury cadmium telluride (MCT) detector was used to detect light in the range  $6000 - 400$   $\text{cm}^{-1}$ . The RAIRS data was taken in a chamber with a background pressure below  $1 \times 10^{-10}$  mbar and  $\text{H}_2\text{O} / \text{D}_2\text{O}$  films were grown by backfilling the chamber through a leak valve and background dosing the gas onto the sample.

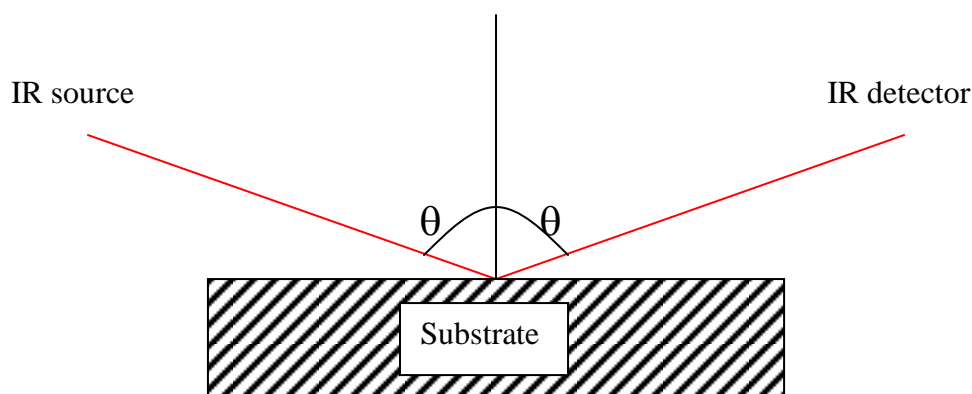


**Figure 2.15:** Schematic representation of the RAIRS experiment.

## 2.8 Helium atom scattering (HAS)

Helium atom scattering is a surface sensitive technique for probing only the top layer of surfaces whereas LEED was shown to penetrate the first few layers. The de Broglie wavelength (equation 2.9) shows that the wavelength of a particle varies inversely with particle mass and therefore, a helium beam has sub-nm wavelengths even at thermal energies. These small wavelengths are required in order to obtain atomic resolution. HAS is used to gain an insight into the degree of disorder present at a surface. This technique is non-destructive because helium atoms are very light with a larger cross section than electrons and HAS is therefore an inert probe of the surface. This is an advantage because LEED can cause electron damage to the adsorbates

sometimes resulting in reconstructions. Bonding differs between the surface and the bulk, HAS is used to gain more information about the topmost layers only. A schematic in figure 2.16 shows the difference between the use of electrons in LEED and helium in HAS.

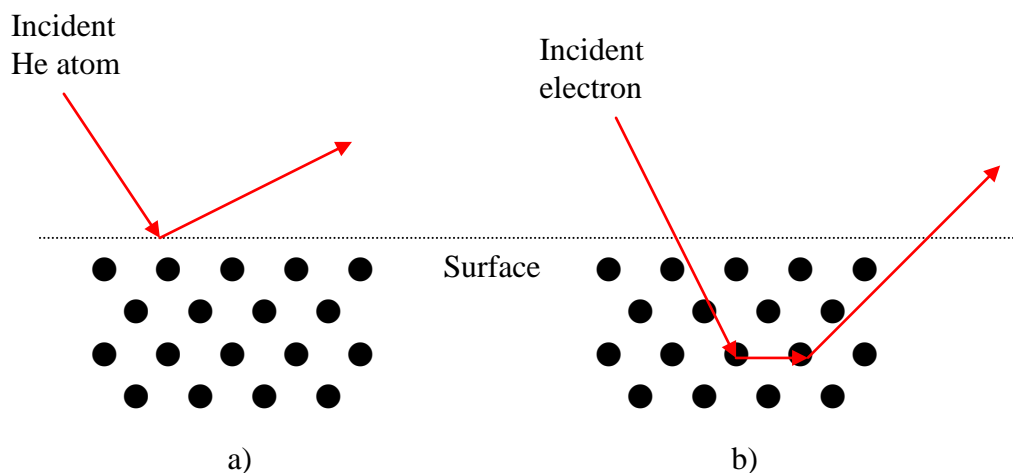


**Figure 2.16:** Diagram to show the difference in penetration depth between a) helium atom scattering and b) low energy electron diffraction.

The energy of a supersonic helium beam is determined by the nozzle temperature and calculated using equation 2.10, where  $k_b$  is the Boltzmann constant,  $m$  is the mass of helium,  $v$  is the velocity and  $T$  is the temperature of the nozzle.

$$\lambda = \frac{h}{p} \quad \text{Equation 2.9}$$

$$\frac{1}{2}mv^2 = \frac{5}{2}k_bT \quad \text{Equation 2.10}$$

$$\lambda = \frac{h}{(2Em)^{1/2}} \quad \text{Equation 2.11}$$

And therefore: 
$$\frac{\lambda}{\text{\AA}} = \frac{4.57}{(E/\text{meV})} \quad \text{Equation 2.12}$$

Typical HAS experiments are carried out with a nozzle temperature in the range 30 – 300 K resulting in a velocity of 600 – 1800 m/s and a de Broglie wavelength of 1.4 – 0.6 Å. For a nozzle temperature of 300 K (used for experiments discussed in this thesis) the energy is calculated to be 65 meV. Using the relationship given in equation 2.11 and the derived equation 2.12, the de Broglie wavelength is calculated to 0.56 Å for a nozzle temperature of 300 K (and energy of 65 meV).

HAS scattering is carried out by measuring the diffracted atoms from a monochromatic helium beam incident on the sample. The helium passes from the source, through a liquid nitrogen cold trap that freezes out any impurities and then passes through a 53 mm skimmer, which collimates the beam. The helium beam is incident on the centre of the crystal which is mounted on a  $x,y,z,\theta$  manipulator that can be tilted relative to the scattering plane. The crystal can be moved slowly through  $\theta$  using a stepper motor controlled by a computer. This allows a continuous scan to be carried out with the helium beam switched on. The incident and reflected beams remain at  $90^\circ$  to each other and the reflected beam passes from the experimental chamber, through a 3 mm aperture into a differentially pumped stage before reaching the detector (Hiden QMS). This results in an angular scan showing the intensity of helium in counts/second and can be converted to show values for parallel momentum transfer,  $\Delta K_{\parallel}$ .

Helium atom scattering experiments were used to provide an indication of the amount of order/disorder in the adsorbed water layer rather than provide specific information about the position of adsorbates on the surface. Peaks with high helium reflectivity would be observed for ordered structures whereas weaker, broader peaks would be seen for structures displaying a higher degree of disorder. The maximum specular reflectivity from the clean Pd(111) surface was recorded at  $1.1 \times 10^6$  counts/second and subsequent experiments for water adsorbed on the surface were compared to this. In addition to looking at the reflectivity from water adlayers, HAS was also used as a further indication of surface cleanliness as the presence of impurities greatly reduces the specular reflectivity.

## 2.9 Kelvin Probe Measurements

The work function of a solid is defined as the minimum energy required to remove an electron from the surface of a conducting material to a point outside of the solid, far enough away to avoid any interactions. The electron must move through the surface to be removed and therefore its energy is affected by surface characteristics, making this a surface sensitive technique. The change in work function will differ if adlayers are adsorbed or the surface reconstructs. The Kelvin probe is a vibrating metal plate used to measure the work function of a sample relative to that of the probe. When two materials with a different work function are moved together, the electrons in the material with the lower work function flow to the material with a higher work function. This produces a parallel plate capacitor where the two materials have equal and opposite charges. The voltage created over the capacitor is known as the contact potential and can be measured by applying an external backing potential until the surface charges disappear. At this point, the backing potential will equal the contact potential. The flow of charge can be measured to determine the change in work function. It should be noted that the charge created during measurements must dissipate before another experiment can be carried out, and therefore, a vibrating probe can be used to produce a varying capacitance, given by equation 2.13. As the probe oscillates above the sample, the voltage is recorded.

$$C = \frac{Q}{V} = kA/d \quad \text{Equation 2.13}$$

<i>C</i>	capacitance
<i>Q</i>	charge
<i>V</i>	voltage
<i>k</i>	dielectric constant of the medium between the parallel plates
<i>A</i>	area of the plates
<i>D</i>	spacing between the plates

The work function measurements were carried out in a collaborative project by Ahmed Omer using a Kelvin probe that consisted of a digital oscillator, tip actuator, signal amplifier and scan controller. The probe is a reference electrode and was

positioned parallel to the sample, acting as a second electrode. The flow of charge between the two electrodes can be measured to give the work function but this yields only one reading at a time as the charge must dissipate before taking a second measurement. Instead, a vibrating probe was used in order to give a varying capacitance and continual measurements. With the probe oscillating above the sample, the change in voltage was recorded. Adsorption of an electropositive substance causes an overall decrease in work function and for an electronegative substance, an increase is observed. Work function experiments were carried out and compared to density function calculations performed by Dr. George Darling.

## 2.10 References

1. D. A. King and M. G. Wells, *Surface Science*, 1972, **29**, 454-7.
2. S. S. Perry and G. A. Somorjai, *Surfaces. Encyclopedia of Inorganic Chemistry; John Wiley & Sons, Inc., New York*, 2006
3. P. A. Thiel, F. M. Hoffmann and W. H. Weinberg, *Journal of Chemical Physics*, 1981, **75**, 5556-5572.
4. P. Hollins and J. Pritchard, *Chemical Physics Letters*, 1980, **75**, 378-382.

# **Chapter 3**

## **Monolayer Water Adsorption on Pd(111)**

### 3. Monolayer water adsorption on Pd(111)

#### 3.1 Introduction

Water adsorption at metal surfaces has been a well researched topic of interest for many years and an overview of the subject is discussed in chapter 1. The wetting behaviour of a range of metals has been well documented but a limited amount of literature is available surrounding water growth on a Pd(111) substrate and it was therefore decided that it would be a good metal to investigate further. Work in the Surface Science Research Centre has previously been carried out on Pt(111) and Ru(0001) which provided a good starting point for the research carried out here. The results discussed in this thesis will be compared to previous work carried out in the group as well as that available in the literature.

The bonding energy of water to various metal surfaces gives an order of Ru>Rh>Pd>Pt>Au with calculations showing that water binds most strongly to ruthenium <sup>1</sup>. A study by Michaelides *et al.* finds similar results but there is discrepancy surrounding the position of Pd and they suggest the alternative order of Ru>Rh>Pt>Pd>Au <sup>2</sup>. Theoretical studies predict that water adsorbs intact on clean Pd(111) because it is more energetically stable than a partially dissociated layer <sup>1,3</sup>. Experiments discussed in this thesis are in agreement with these findings and results show that water adsorbs intact on Pd(111) with pseudo first order desorption kinetics and multilayer growth by sublimation of ice <sup>4,5</sup>.

Mitsui *et al.* used STM to show that at low coverages, isolated water molecules prefer to adsorb on top of a Pd atom <sup>6</sup>. As the water coverage increases, dimers and trimers form, which quickly diffuse. However, as water aggregates into large clusters, stable hexagonal rings form and remain in registry with the surface to form a long-range  $(\sqrt{3} \times \sqrt{3})R30^\circ$  structure. STM simulations and DFT calculations carried out by Cerda *et al.* predict many different structures of water clusters, all having similar binding energies <sup>7</sup>. A summary of their calculated binding energies is represented in table 3.1. They show that existing models of water adsorption are not applicable on Pd(111) substrates and present low temperature STM images and DFT calculations of

a novel submonolayer water structure and introduce a new 2-D rule for water growth. The structures observed for submonolayer D<sub>2</sub>O clusters consist of intact water molecules that remain mostly parallel to the Pd(111) surface. Aggregation of individual water molecules results in the formation of dimers, trimers and up to cyclic hexamers, the hexamer being the most stable. Interestingly, the dimer, trimer and tetramer structures have a diffusion rate faster than that of the water monomer despite their increased size.

**Table 3.1:** Calculated binding energies for various structures of water formed on Pd(111) (adapted from reference 7)

Structure	E <sub>a</sub> (eV/water molecule)
Ice <i>Ih</i> (bulk)	0.71
H-up bilayer	0.50
H-down bilayer	0.56
Dissociated bilayer	0.46
H-up lace	0.52
H-down lace	0.54
Dissociated lace	0.51
Flat & edge H-down lace	0.56
Flat & edge dissociated lace	0.53
Flat & edge H-down rosette	0.56
Flat & edge dissociated rosette	0.51

As the water coverage increases, aggregation of water molecules occurs at 40 K resulting in the formation of islands consisting of an array of hexagonal water molecules with a commensurate hexagonal honeycomb structure. Further increasing the coverage leads to an increase in the total number of hexagonal islands on the surface but the size of each island remains the same with a width of 10 – 20 Å<sup>8</sup>. Upon annealing to 80 – 100 K, the islands restructure to form regular rosette or lace type structures, which are the same size as the hexagonal islands (10 – 20 Å width). From the data described here, Mitsui *et al.* deduce that water molecules adsorb intact on

Pd(111) with all H atoms forming a H bonded network. At a point where these conditions are not possible, no more islands form. The structures grown at 40 – 100 K are metastable and are attributed to how islands grow at low temperatures by attaching flat water molecules. At higher temperatures (130 K) these flat structures disappear, forming larger islands consisting of two layers with a large unit cell in the second layer. These findings provide evidence for non-uniform wetting rather than the conventional ice bilayer.

Yamada *et al.* use electron energy loss spectroscopy (EELS) to investigate ten bilayers of water on Pd(111) <sup>9</sup>, suggesting that initial adsorption occurs by the addition of isolated water molecules in preference to cluster formation. They go on to say that that the metastable water molecules adsorbed at 85 K, form a stable bilayer structure at 128 K. Their LEED image recorded for ten bilayers of water shows quite large spots in the  $\sqrt{3}$  positions and they attribute these to large vibrational amplitudes of the surface water molecules. Later on in this section, LEED images of water on Pd(111) will be discussed in more detail. The images recorded by Yamada *et al.* shown in figure 3.1 are similar to the triangular patterns observed in the work described here for multilayer water growth.

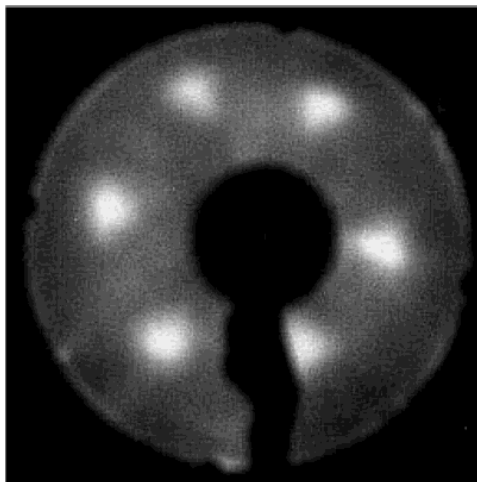


**Figure 3.1:** LEED image observed by Yamada *et al.* and reported in reference 9; analogous to the results described in this thesis. Reprinted (adapted) with permission from (T. Yamada, H. Okuyama, T. Aruga and M. Nishijima, *Journal of Physical Chemistry B*, 2003, 107, 13962-13968). Copyright (2003) American Chemical Society.

## 3.2 Temperature Programmed Desorption & Low Energy Electron Diffraction

### 3.2.1 Introduction

TPD experiments have been extensively reported for water adsorption on a range of metal surfaces. Desorption profiles provide an insight to the growth mechanism of water and the strength of the interaction between water and the substrate. For multilayer growth, two desorption peaks can be expected; one at a higher temperature due to the completion of a water monolayer and one at a lower temperature due to multilayer growth with weaker interactions between neighbouring water molecules than between water and the metal surface. This behaviour has been reported on Pt(111)<sup>10, 11</sup> and Rh(111)<sup>12, 13</sup> amongst other metal surfaces. Single desorption profiles have been observed on non-wetting surfaces with increased water coverage causing the peak to grow and not saturate. Examples of non-wetting behaviour have been observed on Au(111) and Ag(111)<sup>14</sup> (as discussed in chapter 1). Desorption profiles also provide an indication as to whether water adsorbs intact or dissociates, resulting in additional high temperature features as observed on Ru(0001)<sup>15, 16</sup>. Previous experiments on Pd(111) provide evidence for intact water adsorption<sup>8</sup>. This chapter will look at the high temperature monolayer peak observed for water adsorption on Pd(111) and chapter four will discuss the low temperature multilayer feature in more detail.

### 3.2.2 Experimental Procedures

The experiments were carried out in a UHV chamber with a background pressure of  $1 \times 10^{-10}$  mbar. The Pd(111) crystal was polished to  $\pm 0.25^\circ$  of the (111) face before being spot-welded using Ta wire to tungsten posts on the bottom of an x,y,z, $\theta$  manipulator. A dewar inside the manipulator allowed the crystal to be cooled to 100 K. A K-type thermocouple was spot-welded to the side of the crystal and a DC heating supply was used to resistively heat the sample to temperatures up to 1100 K. The Pd(111) crystal was cleaned using argon ion sputtering followed by annealing to 1100 K. This cycle was repeated and cleanliness was verified by looking at LEED images of the clean surface and by comparing TPD traces of water desorbed from the

clean surface. The background gas adsorption spectra was regularly monitored in order to detect contamination in the chamber, however these traces were not recorded and are not shown here.

Water was dosed by means of an effusive molecular beam at a constant flux (0.03 ML/s) with the crystal being held at the desired temperature. Crystalline ice is formed at a temperature of 150 K where water is mobile and able to diffuse to its preferred adsorption site. Amorphous solid water was grown by dosing water at 115 K so that it sticks without diffusing across the surface. After dosing water, the sample was cooled to 100 K and moved through  $\theta$  to a position in front of the quadrupole mass spectrometer. Whilst monitoring the relevant masses on the mass spectrometer, the temperature was ramped at a rate of 2 K/s and the resulting desorption trace was logged. The coverage of water was calculated from the desorption integral with one monolayer corresponding to the saturation of the high temperature peak ( $\theta = 1.0$ ) with the growth of the lower desorption peak at  $\sim 162$  K representing the growth of multilayer. For reference, all coverages will be quoted with respect to this. It was also possible to calculate the coverage by integrating the area under an uptake profile using the King and Wells technique.

LEED images were obtained for freshly grown water films at a filament current of 2.3 A and well-defined beam energies between 25 – 100 eV. Electron exposure was minimized in order to reduce damage to the water overlayer. Further LEED experiments were carried out using a low-current LEED system. During these experiments, the current used was 2.10 – 2.30 A, and the drain current was 50-100 nA on the original LEED system (but later reduced to 1-4 nA with the use of the low current system).

### 3.2.3 Results and Discussion

Crystalline ice was grown on a clean Pd(111) surface at 150 K and TPD measurements showed a thermal desorption peak at 175 K (figure 3.2). This peak is due to water bound to the metal surface and it saturates with increasing coverage. This

behaviour is associated with multilayer water growth and wetting of the metal surface. Increased water coverages will be discussed in greater detail in Chapter 4. The shape of the desorption profiles in figure 3.2 indicates fractional order desorption kinetics (close to first order / pseudo first order) with  $T_{\max}$  not entirely independent of coverage with a total shift of  $7^{\circ}\text{C}$  between a coverage of 0.15 and 1.0 layers of water. The maximum moves to higher temperatures with increasing water coverage. This can be attributed to the growth of islands of water. The high temperature shoulder can be attributed to desorption from step edges with desorption occurring from the outer edges inwards.

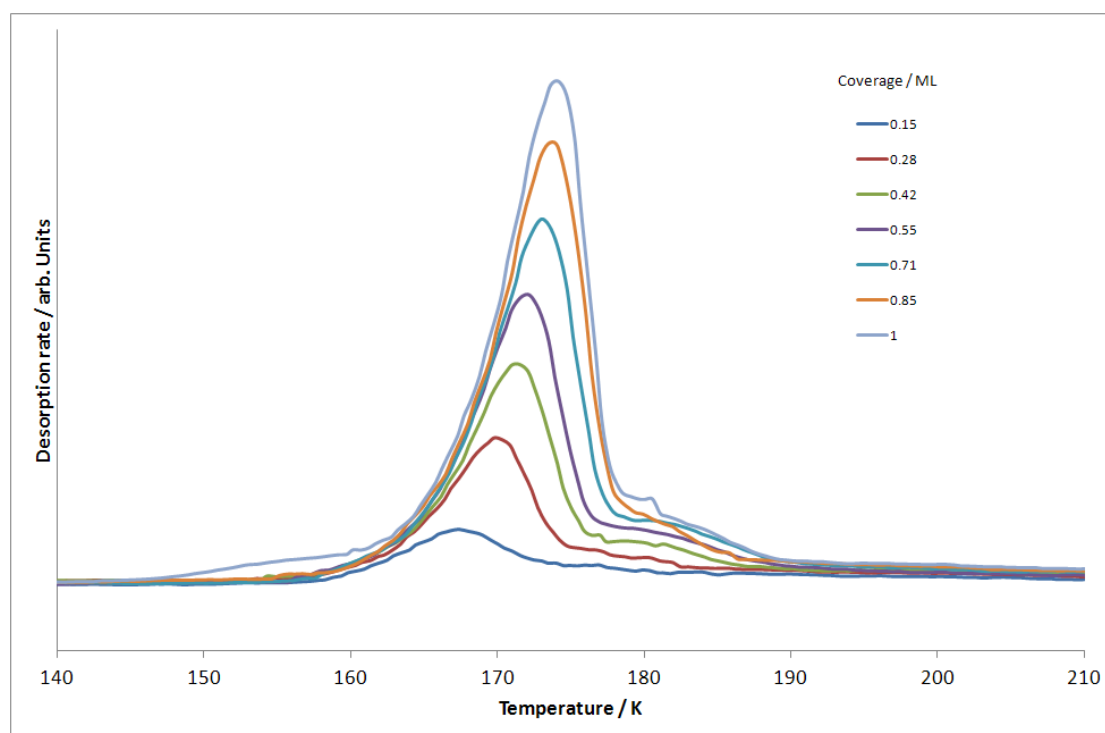


**Figure 3.2:** Temperature programmed desorption profile of water desorbing from Pd(111) after being dosed at 150 K. The peak at 170 - 175 K saturates with a coverage of one monolayer (all coverages are quoted in reference to this).

A plot of  $\ln[I(T)]$  against  $\ln[\theta_{\text{rel}}]$  provides information about the order of desorption as the gradient of this graph gives the parameter  $n$  (0,1,2). Figure 3.3 shows that for monolayer water adsorption on Pd(111), the desorption kinetics are close to first order (0.987) with an  $R^2$  value of 99.96 % showing a strong correlation.

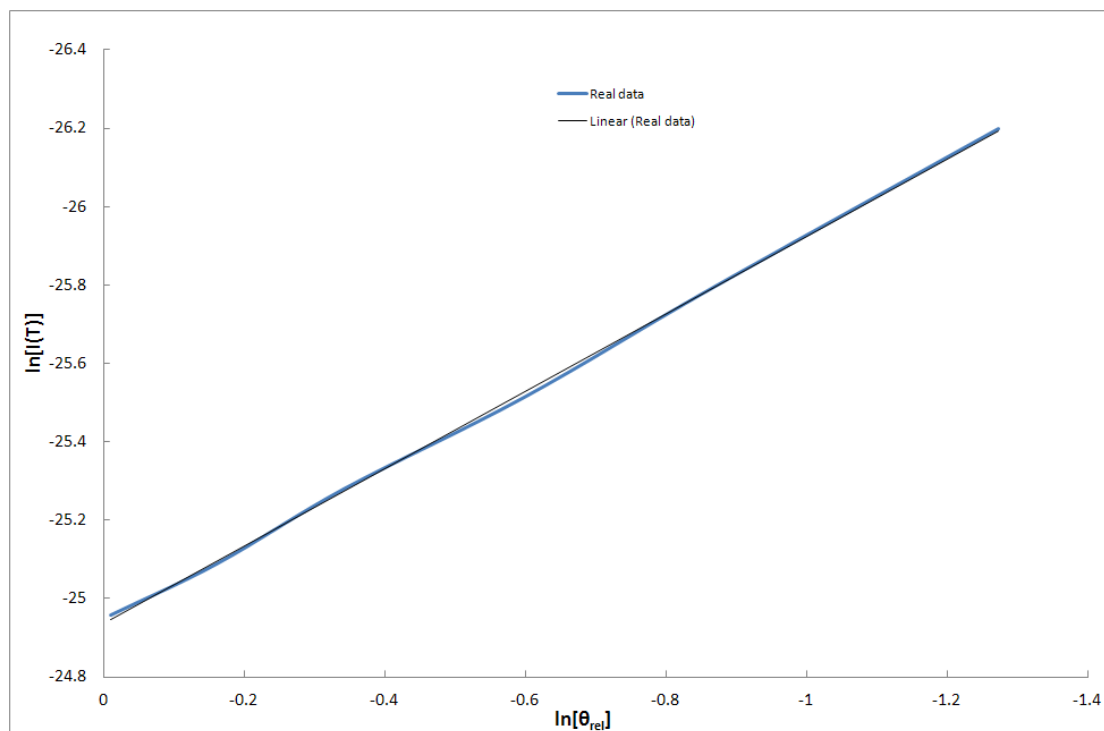


**Figure 3.3:** A plot of  $\ln[I(T)]$  against  $\ln[\theta_{rel}]$  giving a gradient and therefore value for  $n$ , of 0.987 with an  $R^2$  value of 0.996. This implies that monolayer water desorbs from Pd(111) with close to first order desorption kinetics.

Following the initial desorption experiments, a range of different coverages of ice were grown at 150 K before the surface was cooled to 100 K, at which point LEED images were recorded. A reasonably sharp  $(\sqrt{3} \times \sqrt{3})R30^\circ$  LEED pattern was observed for submonolayer coverages of water (figure 3.4). This pattern is observed only for coverages from 0.52 layers up to the point where the first layer saturates.

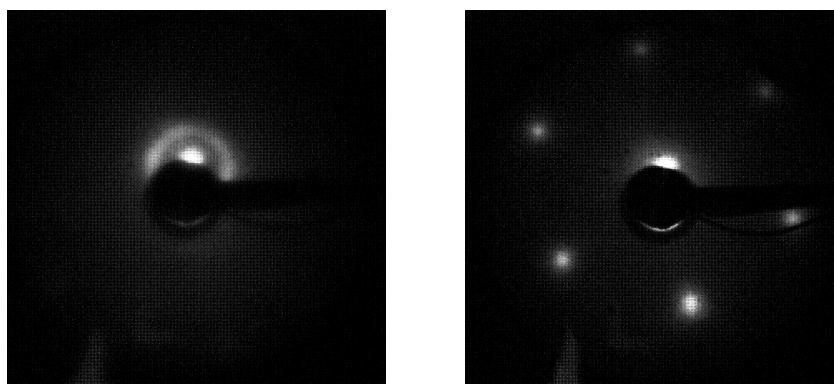


**Figure 3.4:** Low energy electron diffraction pattern for submonolayer water adsorbed on a Pd(111) surface at 150 K. a) shows a halo around the (0,0) position and b) clearly shows sharp singular spots in the  $\sqrt{3}$  positions. Beam current = 2.20 A, beam energy = 25 eV, drain current = 50 nA, water coverage = 0.71. Data from chamber 1.

The  $(\sqrt{3} \times \sqrt{3})R30^\circ$  LEED pattern indicates the formation of a commensurate wetting structure forming on the Pd(111) surface and it is therefore suggested that the first layer of water does wet the surface. A bright halo can be observed around the (0,0) position when water is adsorbed onto the surface. This halo is present for submonolayer and multilayer water coverages and in order to obtain more information, further work has been carried out by F. McBride<sup>17</sup> in conjunction with DFT calculations completed by Dr. G. Darling. The calculations provide evidence for the formation of an extended water structure / superstructure when water adsorbs on Pd(111). Additional LEED experiments found that the halo is not only observed around the (0,0) position but is also present around the integer order beams as shown in figure 3.5. The formation of a water superstructure on Pd(111) has been suggested before by Cerda *et al.* and their results are discussed throughout this thesis<sup>7</sup>.

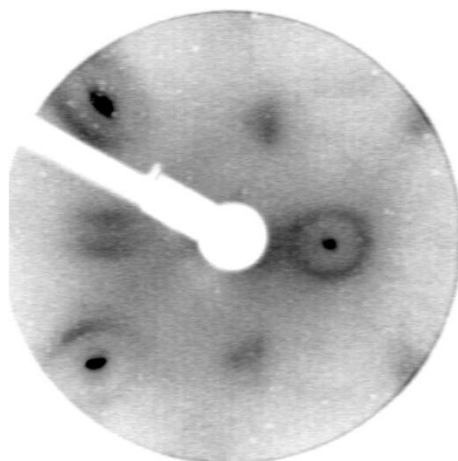


**Figure 3.5<sup>17</sup>:** Low energy electron diffraction pattern for 1.5 layers of water. The sample is rotated away from the surface normal to allow the ring around the (0,0) beam to be observed more clearly (right of the central optics). 2 metal spots are evident on the left hand side and the diffuse triangular  $\sqrt{3}$  beams are shown above and below the centre.  
Reproduced with permission from [F. McBride, A. Omer, C. M. Clay, L. Cummings, G. R. Darling, A. Hodgson *Journal of Physics: Condensed Matter*, 2012, 24, 124102]. Copyright (2012), IOP.

A similar observation has been reported for water adsorption on Rh(111) (figure 3.6)<sup>12</sup>. The group adsorbed D<sub>2</sub>O on Rh(111) at 20 K before annealing the surface to 145 K and recording LEED images using an Omicron SPA-LEED system. Due to the fragile nature of the water layers they minimised the effect of electron damage on the water structures by using an electron dose of less than 0.01 electrons per surface Rh atom. In

addition to (1 x 1) spots from the metal surface, a  $(\sqrt{3} \times \sqrt{3})R30^\circ$  structure is reported and is assigned to the formation of commensurate islands. This observation is consistent with STM carried out as part of the same study which shows islands which are approximately 2.5 nm in size which grow connected honeycomb structures with increasing coverage as shown in figure 3.5. As the coverage increases, the LEED pattern also begins to show additional structure with the observation of spots in a halo around the (0,0) position and around the  $(1/3, 1/3)$  spots starting at a coverage of 0.56. As the coverage increases towards saturation these spots become more intense and are attributed to an in-commensurate structure and the formation of a larger superstructure. This behaviour is comparable to that observed on Pd(111) and the additional features are analogous to those observed by McBride in further LEED studies<sup>17</sup>.

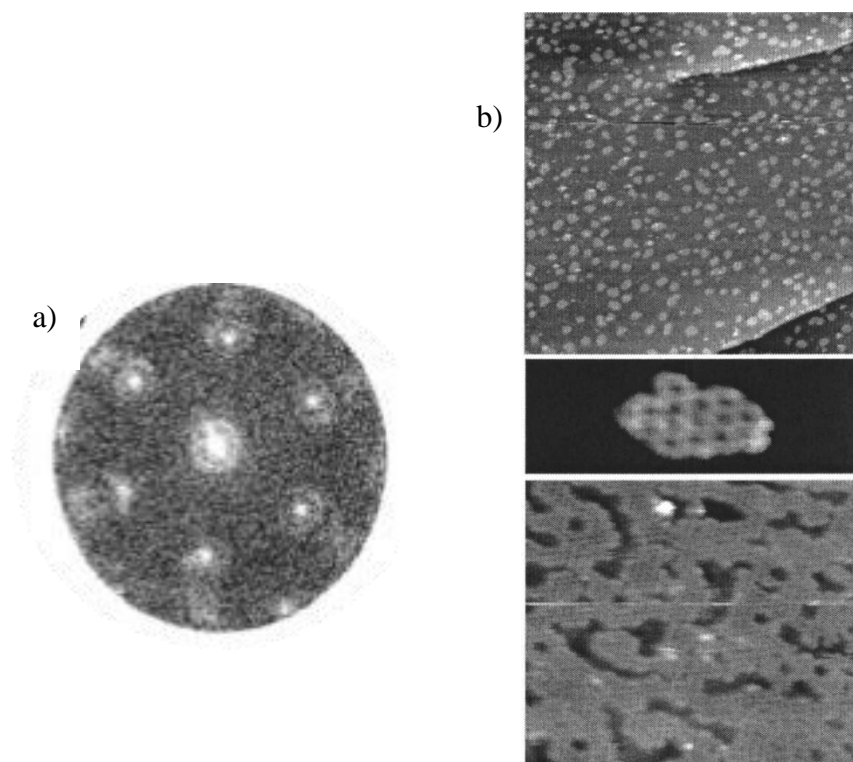


**Figure 3.6<sup>12</sup>:** **a)** Low energy electron diffraction pattern for water adsorbed on a Rh(111) surface. The images show a halo around the (0,0) spot and additional features around the spots in the  $\sqrt{3}$  position. These features are attributed to an extended superstructure. **b)** STM images showing the small islands form into a larger hexagonal network. Reprinted with permission from [A. Beniya, Y. Sakaguchi, T. Narushima, K. Mukai, Y. Yamashita, S. Yoshimoto and J. Yoshinobu, *Journal of Chemical Physics*, 2009, 130, 034706]. Copyright [2009], American Institute of Physics.

The information given here will be discussed further in Chapter 4 as the additional structure and spot splitting is connected to the growth of multilayer water on Pd(111). The change in LEED pattern has been discussed here for clarity of understanding how water grows on Pd(111). At this point it is not possible to completely separate the mono- and multilayer discussions.

### **3.3 RAIRS**

#### **3.3.1 Introduction**

RAIRS can be used to provide information about the orientation of water adsorbed on a metal surface. Flat lying water molecules cannot be detected due to surface selection rules (section 2.7). Due to the image dipole effect the dipole in a species changes upon adsorption as the free electrons in the metal substrate realign to oppose the adsorbed dipole resulting in an equal and opposite image of the dipole. Therefore, a dipole adsorbed perpendicular to the surface becomes enhanced whereas a dipole adsorbed parallel to the surface becomes a quadrupole. Here RAIRS is used to provide supporting evidence for the initial adsorption of flat lying water hexamers as reported in previous research, followed by a change in the orientation of adsorbed molecules.

#### **3.3.2 Experimental Procedures**

In order to perform RAIRS experiments, the Pd(111) crystal was cleaned by repeated Ar<sup>+</sup> ion sputter and anneal cycles before water was dosed by means of backfilling the vacuum chamber through a leak valve. The water coverage was calculated by using the TPD traces recorded after RAIRS in the same way as the coverage has been calculated throughout this work. RAIRS data was collected using a Mattson 6020 FTIR spectrometer as described in section 2.7.

### 3.3.3 Results and Discussion

The RAIRS spectra in figure 3.7 shows that for low coverages of water (submonolayer), no distinctive features can be observed but as the amount of water is increased, absorption bands begin to appear. The spectra show a librational mode of the water network ( $\sim 830 \text{ cm}^{-1}$ ), the water scissors and OH stretching modes ( $\sim 1620 \text{ cm}^{-1}$  and  $3415 \text{ cm}^{-1}$  respectively) in addition to a weak feature that appears at  $3685 \text{ cm}^{-1}$  with completion of the first layer of water. This can be attributed to non H-bonded OH groups in the upper half of the water monolayer that point towards the vacuum. Similar observations have been made for water adsorbed on Cu(001) with an intense band observed at  $3680 \text{ cm}^{-1}$  representing the H-up water structure and non H-bonded OH dangling into the vacuum<sup>18</sup>. In contrast, this feature is absent from spectra of water adsorbed on Pt(111)<sup>10</sup> and Ru(0001)<sup>16, 19</sup> which accounts for the reported H-down structure.

The IR spectra are labelled with the coverage of water and the absence of intense absorption bands below a coverage of 0.40 corresponds well with the STM work that suggests water initially adsorbs in small flat islands. These flat water molecules lie parallel to the surface and are therefore not detected by IR due to the metal surface selection rule. As the coverage increases, the band corresponding to the scissors mode ( $1615 \text{ cm}^{-1}$ ) begins to grow at a water coverage of 0.46 layers, and coincides with the appearance of a  $(\sqrt{3} \times \sqrt{3})R30^\circ$  LEED pattern. This occurs as the water adapts a more upright growth mode at which point it becomes IR active with a dipole perpendicular to the surface. As more water is packed into the structure, this band increases in intensity. The absorption band at approximately  $3362 \text{ cm}^{-1}$ , which is due to the OH stretching mode within a hydrogen bonded structure, also increases as the coverage increases above approximately 0.40. This again occurs as more water packs into the structure and forms a hydrogen bonded network. As the water coverage increases further, this band continues to increase in intensity, supporting the hypothesis for a hydrogen bonded superstructure.

The weak absorption band at  $3685\text{ cm}^{-1}$  only appears during multilayer growth and can be attributed to small amounts of free OH not participating in the large hydrogen bonded network.

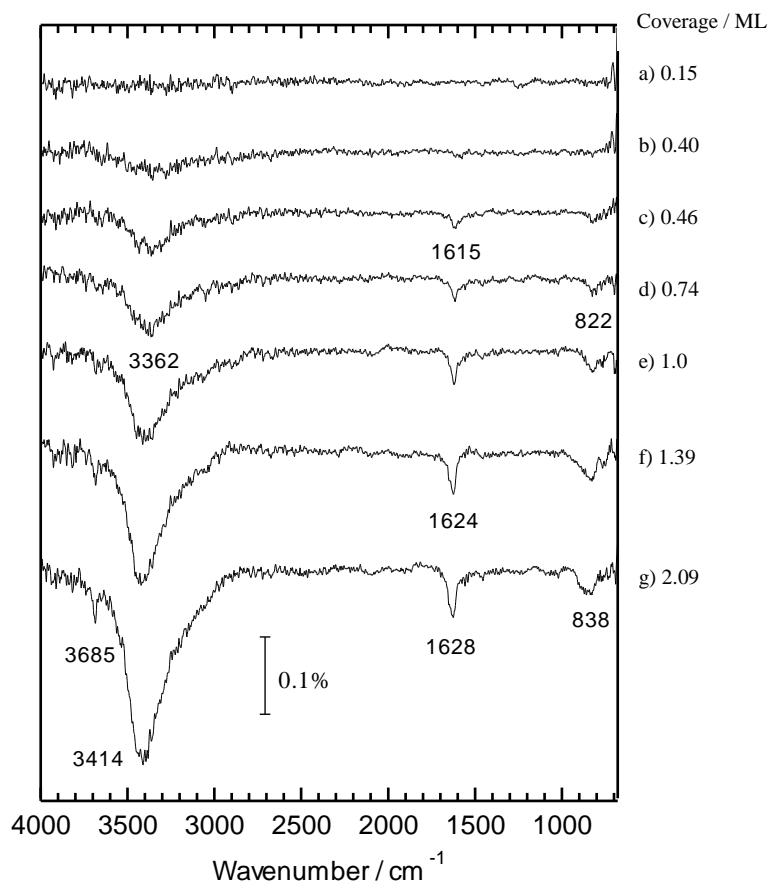


**Figure 3.7:** RAIR spectra for water adsorbed on Pd(111). The bands at  $830\text{ cm}^{-1}$ ,  $1620\text{ cm}^{-1}$  and  $3414\text{ cm}^{-1}$  are due to the librational, scissors and stretching modes of water respectively. Completion of the first layer of water gives rise to a weak band at  $3685\text{ cm}^{-1}$ , attributed to non hydrogen-bonded hydroxyl groups.

The RAIRS spectra reported here also add to the evidence that water adsorbs intact on Pd(111) with no signs of dissociation. The absorption bands detected are comparable to those observed for water adsorbed on Ru(0001), however, dissociation is detected on Ru(0001). The dissociation of water presents itself in RAIRS by a decrease in the stretching and scissors modes up to the point where they disappear completely due to the mixed layer lying parallel to the surface. As the dissociation occurs, the librational mode can be expected to increase but the position and intensity of this depends on the

nature of the structure present. This behaviour does not occur for water adsorbed on Pd(111) and the OH stretching mode continues to intensify with increasing water coverage.

In summary the RAIRS data shown here suggests that water remains flat during initial stages of growth and small flat islands begin to develop with increasing coverage with water adapting a more upright configuration. This is consistent with STM studies carried out by Cerda *et al.*<sup>7</sup> which show that initial growth occurs with water lying parallel to the surface as discussed in section 3.1. As the first water layer saturates, the growth mechanism changes and the water molecules adapt an upright / out-of-plane geometry. This growth mode would fit with DFT models discussed later which show a hexagonal chain structure or extended superstructure forming for increasing coverages of water at a point where the water molecules cannot all remain in registry with the substrate if they stay lying flat. The tilting allows more water molecules to be accommodated and a superstructure forms with extended  $(\sqrt{3} \times \sqrt{3})R30^\circ$  periodicity held in a hydrogen bonded network.

### 3.4 Collaborative Work: Work Function measurements & DFT Calculations

The surface work function is the minimum energy required to eject an electron into the vacuum at 0 K and reflects the stability of surface electrons. The larger the work function, the more stable the electrons are<sup>21</sup>. The workfunction of a metal can be described in two parts, one dependent on the metal itself and the other concerned with the electrical double layer at the surface (figure 3.8). The adsorption of water leads to the formation of a surface electric dipole layer between water and the surface, in this case, Pd(111), which in turn causes a change in work function.

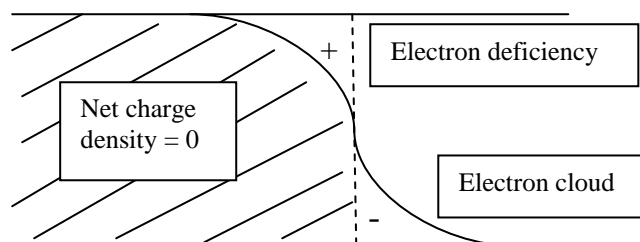


**Figure 3.8:** Schematic of the double layer at an atomically smooth metal surface.

Work function measurements were carried out both experimentally and theoretically. The literature reports the theoretical workfunction for a clean Pd(111) surface to be 5.31 eV<sup>21</sup>, compared to a reported experimental value of 5.6 eV but measurements presented here provide a change in workfunction rather than an absolute value. The independent measurements discussed here gave a very similar result for the calculated structures with flat/H-down chains ( $\Delta\Phi = -0.68$  eV) and the experimentally determined change in workfunction which shows a linear decrease in surface workfunction and a value of  $\Delta\Phi = -0.7$  eV upon completion of one layer of water (data presented in figure 3.9). As the growth mode changes and 3D ice clusters begin to form on top of the first layer of water, the workfunction continues to decrease and eventually plateaus at  $\Delta\Phi = -1.06$  eV. The reduction in workfunction is due to a decrease in surface dipole and means that the valence electrons can be more easily removed from the surface. The calculated structures with H-up bilayers gave an estimated value much further from the experimental value (refer to table 3.2). The negative change in workfunction can be associated with an electron charge transfer from the water adsorbate to the Pd(111) surface.

In addition, further DFT work carried out by Dr. Darling is reported in reference 17. This reference includes work carried out by all members of the dynamics group and shows repeats of work carried out by myself and Dr. C. Clay. Subsequent experimentation by F. McBride provides further evidence to support the DFT simulations<sup>17</sup>.

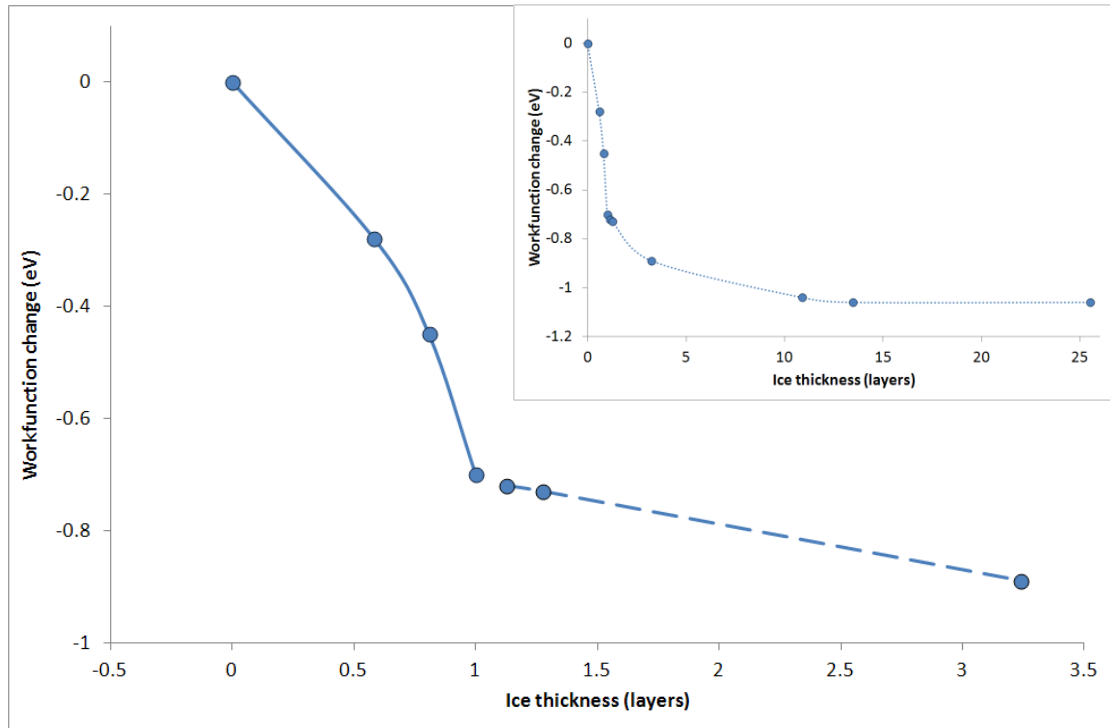


**Figure 3.9:** Data to show the change in work function for water films grown at 140 K. The change in work function for one layer of water was found to be 0.7 eV. The solid line shows the linear decrease in  $\Delta\Phi$  as the first layer completes. The inset shows the full data set as  $\Delta\Phi$  saturates. Figure reproduced with permission from Dr. Ahmed Omer.

DFT calculations (VASP) carried out by George Darling find that the simple commensurate ice bilayer does not wet the surface, instead, one mechanism suggests that water prefers to form a hydrogen bonded network made up of chains of flat and tilted water molecules embedded in a hexagonal superstructure. The proposed chain structure is shown in figure 3.8 and a view from the side (figure 3.10 a) appears to suggest a high degree of disorder but looking at an atop view of the structure (figure 3.10 b) shows chains of water molecules forming in a hexagonal superstructure.

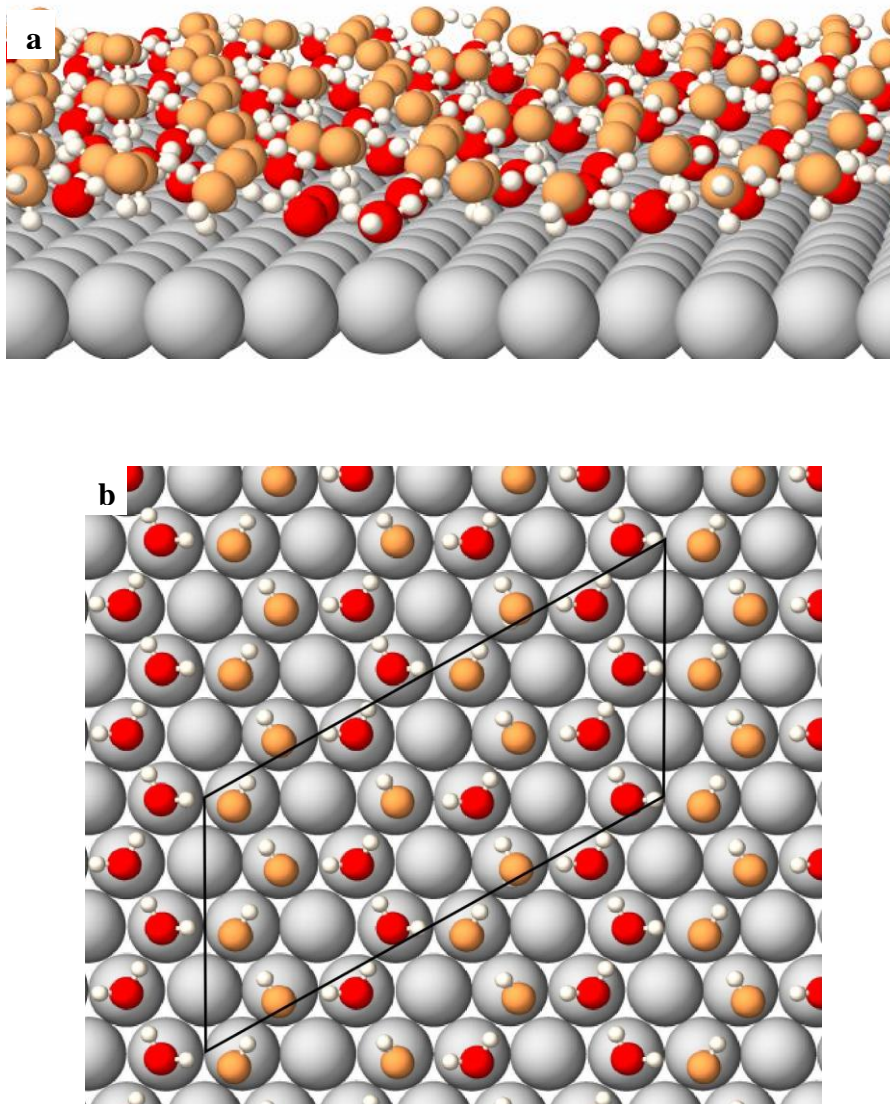


**Figure 3.10:** Schematic of the chain model for water adsorption. Red and orange spheres represent oxygen molecules along chains of water molecules. The chains form a hexagonal superstructure of water molecules. The white spheres represent hydrogen and the grey ones are atoms on the metal surface.  
 a) A side view of the chain structure suggests disorder in the water structure whereas  
 b) show the ordered chains and extended hexagonal network.

The data presented here can be discussed with reference to a study carried out by Tatarikhanov<sup>20</sup>. The group use STM simulations and DFT calculations to provide evidence for the formation of a stable hexagonal structure on Pd(111). The initial stages of growth occur with preferential adsorption of water monomers, proceeded by dimers as the coverage increases and the next most stable structure was found to be hexamers. The most stable hexamers were found to be flat or almost flat clusters as

shown in figure 3.11. Increasing the water coverage further causes an increase in density and results in a structure consisting of side-sharing hexagons which form elongated stripes as shown in figure 3.12. These stripes are only a few hexagons in width and can be compared to the chain structure found by George Darling's chain structure.

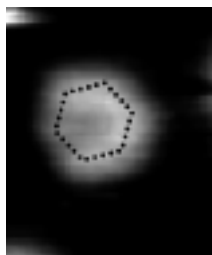


**Figure 3.11:** A single hexamer  $1.6 \times 1.6 \text{ nm}^2$ . Hexamers were found to be the most stable water clusters.  
STM conditions: 120 mV, 175 pA.  
Reprinted (adapted) with permission from (M. Tatarkhanov, D. F. Ogletree, F. Rose, T. Mitsui, E. Fomin, S. Maier, M. Rose, J. I. Cerda and M. Salmeron, *Journal of the American Chemical Society*, 2009, 131, 18425-18434). Copyright (2009) American Chemical Society.

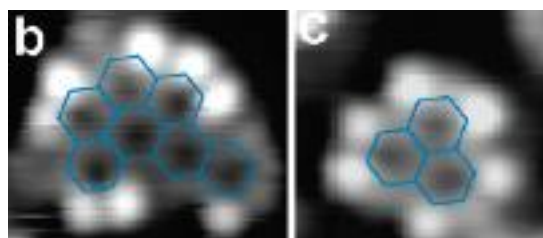
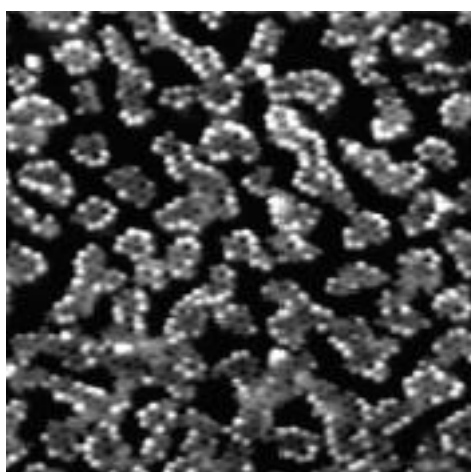


**Figure 3.12:** a) Elongated water clusters grown on Pd(111) at 45 K. The clusters are made up of side sharing hexamers up to a few cells in width as shown in more detail in b) and c).  
Reprinted (adapted) with permission from (M. Tatarkhanov, D. F. Ogletree, F. Rose, T. Mitsui, E. Fomin, S. Maier, M. Rose, J. I. Cerda and M. Salmeron, *Journal of the American Chemical Society*, 2009, 131, 18425-18434). Copyright (2009) American Chemical Society.

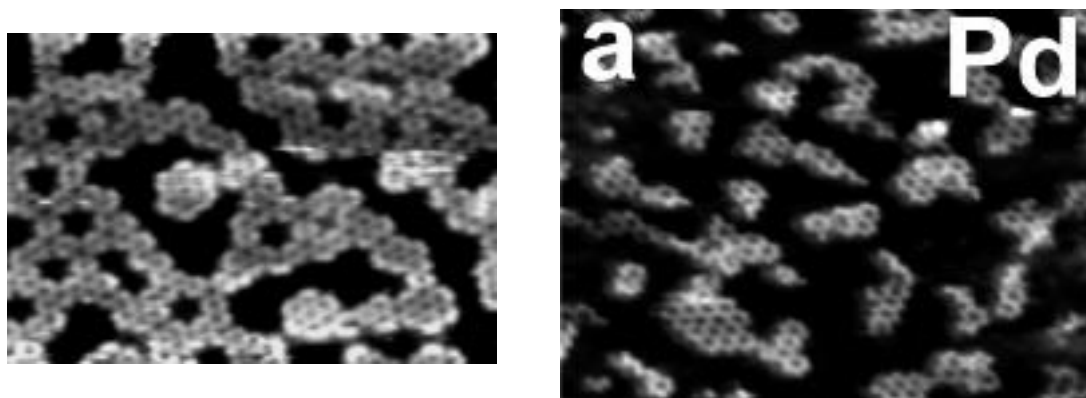


**Figure 3.13:** With increasing growth temperature, the chains of hexagons are shown to form structures with greater lateral size giving rise to an extended honeycomb structure. Reprinted (adapted) with permission from (M. Tatarkhanov, D. F. Ogletree, F. Rose, T. Mitsui, E. Fomin, S. Maier, M. Rose, J. I. Cerda and M. Salmeron, *Journal of the American Chemical Society*, 2009, 131, 18425-18434). Copyright (2009) American Chemical Society.

The group provide an explanation of a ‘peculiar’ growth mode of water forming elongated stripes of honeycomb structures 1-3 cells wide. As the water coverage is increased, an extended honeycomb network is proposed with retention of the narrow width of chains. They show that heating the striped structure formed on Pd(111) gave rise to an increase in lateral size of the water clusters and further extended the hexagonal networks which retained a  $\sqrt{3}$  periodicity relative to the substrate (figure 3.13). They observed no signs of water dissociation, consistent with the intact water desorption profiles shown in this thesis.

Cao *et al.*<sup>21</sup> carried out a DFT study of water adsorption on Pd(111) and found that water decreases the workfunction by 1.22 eV, a much larger value than measured here, which indicates that their model does not capture the structure of the water layer as well as the later DFT calculations by G. Darling. They state that the adsorption of water induces a charge build up between the water oxygen atom and the substrate atom bound to the water. They also suggest that the activation energy required to break the O-H bond for water adsorbed on clean Pd(111), is 1.09 eV. This makes the bond breaking process unfavourable at low temperatures and supports the findings that show water adsorbs intact on the surface with no indication of dissociation.

Combining LEED, DFT and workfunction data, an extended hexagonal chain structure is presented which retains its  $(\sqrt{3} \times \sqrt{3})R30^\circ$  registry even for high coverages, as will be discussed in more in chapter 4, where LEED images for multilayer water growth are described in more detail. If the chain model is applicable for the Pd(111) system, further investigation of the topmost layers of water would be required to support it. Helium atom scattering experiments were performed in order to determine whether the top layers of adsorbed water were ordered or disordered and a later discussion finds disorder in the weakly bound hydrogen network.

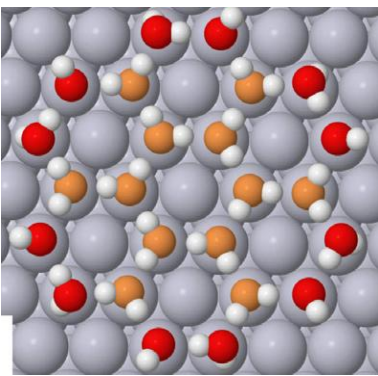
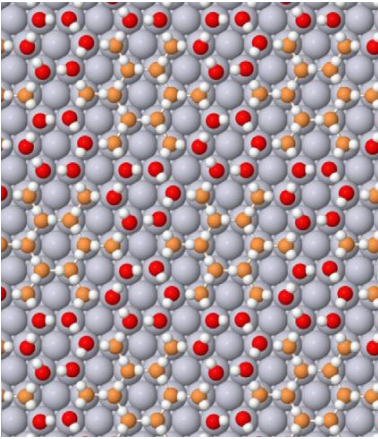
Although the initial work focused on the formation of a chain structure, more recent developments by McBride revealed additional structure in the LEED pattern, resulting in alterations being made to the DFT simulations. This progressed to the proposal of either a  $(7 \times 7)$  or  $\sqrt{52}$  superstructure which relate well to the STM work carried out by Cerda *et al.*

Further investigation by Darling *et al.* compares the rosette structure analogous to that reported by Cerda *et al.* with alternative structures. It is found that the rosette structure has a binding energy of 0.58 eV which is greater than for an extended  $\sqrt{3}$  bilayer structure but less than that of the chain structure shown in figure 3.8 (0.61 eV) and also less than the extended rosette  $(6 \times 6)$  structure. Although these structures can be shown to be fairly stable, they do not account for the splitting of the  $\sqrt{3}$  spots as shown in the LEED images. However, new insights demonstrate some possibilities for extended water structures that do accommodate the observed spot splitting. These are structures with a  $(7 \times 7)$  or  $(\sqrt{52} \times \sqrt{52})R14^\circ$  unit cell as shown in table 3.2. Although DFT cannot separate the two possible structures, it can determine that they are both as stable as the commensurate alternatives.

Table 3.2 is reproduced from reference 17 and shows the calculated binding energies and change in workfunction for a range of water structures on Pd(111) and can be compared to the earlier table reporting values calculated by Cerda *et al.*. The calculated binding energies show that compressed structures are as stable as commensurate structures and therefore it is viable to propose a more tightly bound compressed structure for the growth mode of water on the Pd(111) substrate. The

compressed structures then present reasoning behind the spot splitting observed by LEED as well as the absence of intense helium reflectivity in HAS.

**Table 3.2:** Calculated binding energies and values for the change in workfunction for various structures formed on Pd(111). Table adapted from reference 17. Figures reproduced with permission from [F. McBride, A. Omer, C. M. Clay, L. Cummings, G. R. Darling, A. Hodgson *Journal of Physics: Condensed Matter*, 2012, 24, 124102]. Copyright (2012), IOP.

Structure	Structure	$E_a$ (eV/water)	Coverage	Change in work- function (eV)
$(\sqrt{3} \times \sqrt{3})R30^\circ$ H-up bilayer		0.50	0.67	-2.9
$(\sqrt{3} \times \sqrt{3})R30^\circ$ H-down bilayer		0.55	0.67	-0.25
$(2\sqrt{3} \times 2\sqrt{3})R30^\circ$ flat/H-down chains		0.61	0.67	-0.7
$(7 \times 7)$ rosettes		0.58		
$(6 \times 6)$		0.62	0.67	-0.6

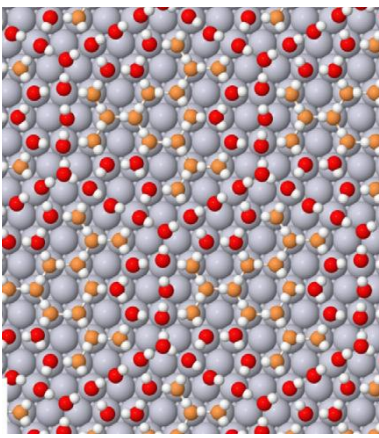
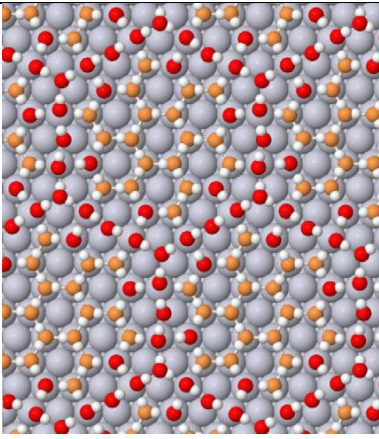
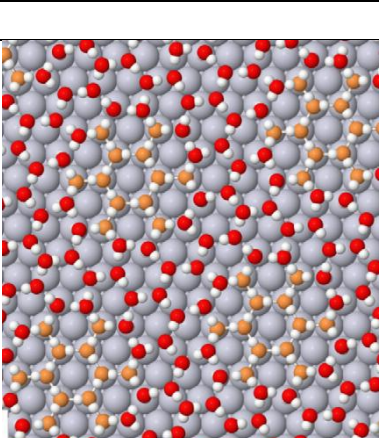
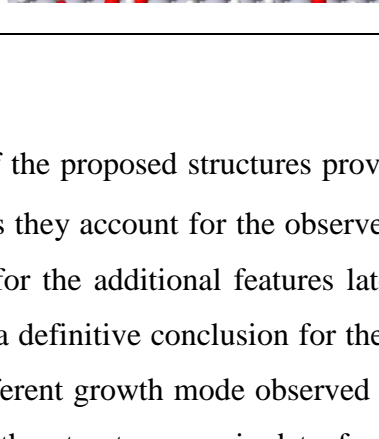
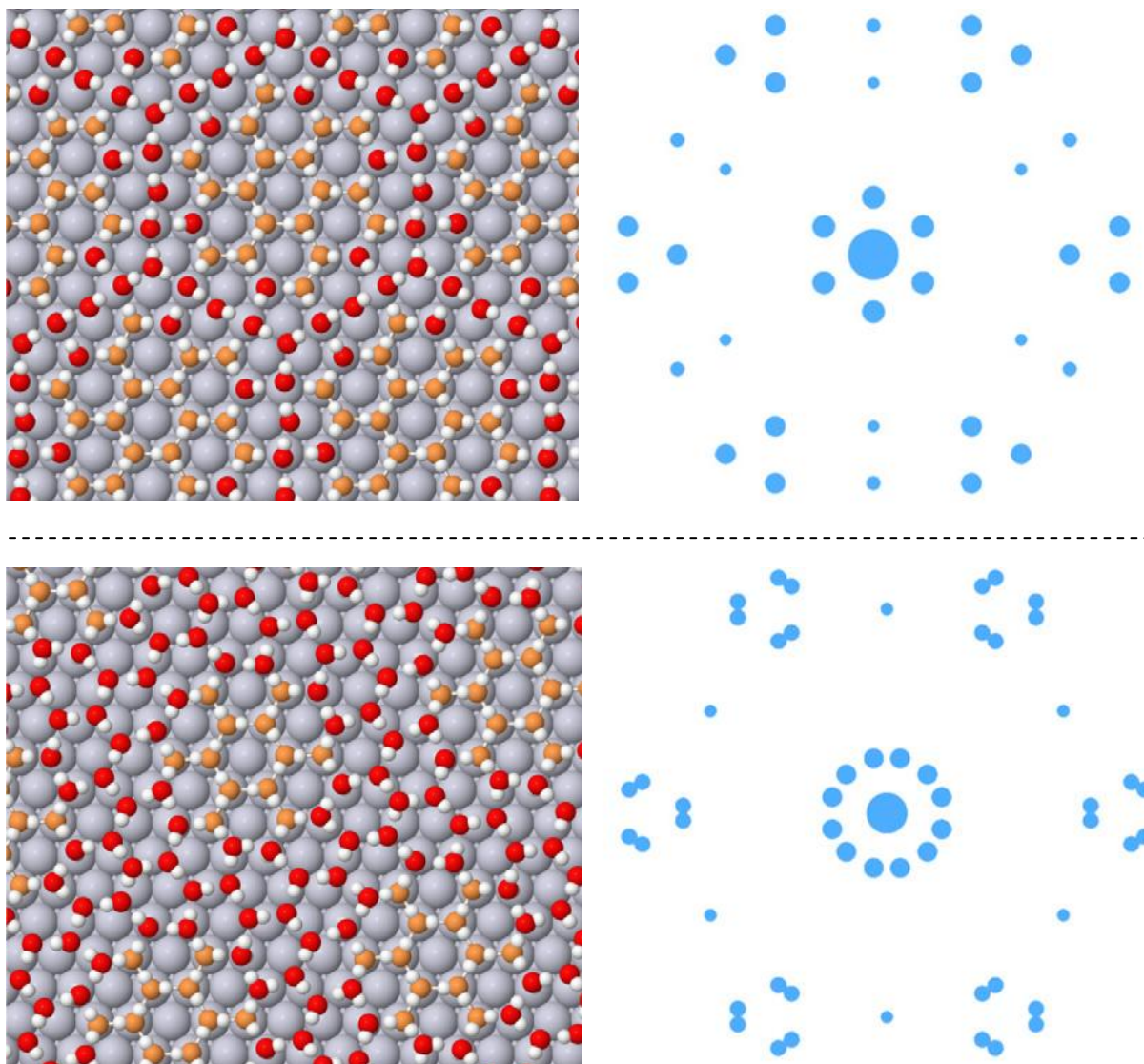
$(7 \times 7)$		0.59	0.71	-0.6
$(7 \times 7)$		0.59	0.71	-0.8
$(\sqrt{52R} \times \sqrt{52})R14^\circ$		0.61	0.81	-0.8
$(\sqrt{52R} \times \sqrt{52})R14^\circ$		0.62	0.73	-0.2

Figure 3.14 shows how two of the proposed structures provide viable options for the structure formed on Pd(111) as they account for the observed splitting of  $\sqrt{3}$  spots in the LEED images as well as for the additional features later observed by McBride. Although they do not provide a definitive conclusion for the water overlayer, they do provide an insight into the different growth mode observed for water on Pd(111) and provide a good indication of the structure required to form the additional features

observed by LEED. The relative size of the beams in the simulated images (figure 3.12) represent the relative intensity expected for single scattering of the oxygen atoms directly bonded to Pd. Weak features ( $< 5\%$  intensity of the central (0,0) beam) were omitted for clarity. In addition to accounting for the spot splitting and the ring observed around the (0,0) position, the simulations also reveal intensity near to the half order positions as observed experimentally. Of the two structures shown, the one with  $(\sqrt{52} \times \sqrt{52})R14^\circ$  periodicity is more stable and further calculations show that it has a similar binding energy to the commensurate  $(6 \times 6)$  structure but it can accommodate more water with a coverage 10 % greater. This arrangement enables the six waters surrounding the central hexagonal water network to bind closer to Pd than in the other proposed structures. This is consistent with the hypothesis of a highly packed, nearly flat growth mode for water adsorbed on Pd(111).



**Figure 3.14:** Schematics of calculated structures (left hand side) and the corresponding LEED simulations (right hand side) expected for a  $(7 \times 7)$  structure (top) and a  $(\sqrt{52} \times \sqrt{52})R14^\circ$  structure (bottom). The simulations assume that water is bound flat lying above Pd. Intensity less than 5 % of the (0,0) beam is omitted. Reproduced with permission from [F. McBride, A. Omer, C. M. Clay, L. Cummings, G. R. Darling, A. Hodgson *Journal of Physics: Condensed Matter*, 2012, 24, 124102]. Copyright (2012), IOP.

### 3.5 Helium atom scattering

#### 3.5.1 Introduction

Helium atom scattering is a non-destructive, surface sensitive technique used to probe the topmost layer of water adsorbed on the surface (section 2.8). Previous studies have been carried out using atom beam scattering to provide an insight into the structure of adsorbates on metal substrates. Due to the controversy surrounding water adsorption on Ru(0001), Gallagher *et al.* used HAS to determine the order / disorder of water adsorbed on the surface <sup>22</sup>. They find faint helium reflectivity peaks close to the second order diffraction positions and combined with DFT calculations deduce a chain structure for water adsorbed on Ru(0001). Explanations are given to account for the observation of disorder in the HAS data and long-range order present in LEED images. They propose that there is disorder in the height of oxygen atoms and positions of the protons but well defined lateral order in the location of oxygen atoms.

Kondo *et al.* also carried out HAS scattering for water adsorbed on Ru(0001) and find that as the exposure of D<sub>2</sub>O increases, the intensity of helium reflectivity decreases as a result of the reducing interaction between D<sub>2</sub>O molecules and the surface <sup>23-25</sup>. At a coverage of 1.5 L, they observe diffraction features attributed to a  $(\sqrt{3} \times \sqrt{3})R30^\circ$  superstructure. The specular reflectivity at this coverage has a maximum of 10<sup>4</sup> counts/second and the second order diffraction peaks have a parallel momentum transfer of  $\pm 3 \text{ \AA}^{-1}$ . First order diffraction peaks are not observed due to the increased corrugation of the interaction between helium and the surface. As multilayer coverages of D<sub>2</sub>O are dosed, the helium reflectivity decreases further until, at a coverage of 4 L, the (0,0) peak cannot be distinguished from the background ion counts recorded during angular scans. Kondo *et al.* propose an initial ordered layer of D<sub>2</sub>O with a  $(\sqrt{3} \times \sqrt{3})R30^\circ$  superstructure formed as the result of diffusion of D<sub>2</sub>O molecules. A morphological change occurs at a coverage of 2-3 layers and temperatures of 150 K, providing evidence for a growth mode similar to the Stranski-Krastanov model.

If a completely ordered water overlayer formed on the substrate, a sharp diffraction peak would be observed either side of the central specular reflectivity peak in the first order diffraction positions,  $(\bar{1},0)$  and  $(1,0)$ . However, for a disordered overlayer much lower helium reflectivity is expected and weaker, more diffuse bands would be observed.

### 3.5.2 Experimental Procedures

In order to obtain an initial position, a helium-neon laser was used to find the point at which the  $x,y,z$  and  $\theta$  allowed the laser to hit the crystal and reflect  $90^\circ$  to enter the chamber containing the mass spectrometer. A piece of paper was held at the end of the laser path (outside the Hiden mass spectrometer side arm on the chamber) and once the crystal was orientated in the correct position, a red laser spot was observed. This ensured that minimal optimisation was required to gain a helium signal on the QMS. Before all experiments, the helium reflectivity was optimised for the clean Pd(111) surface by adjusting the  $x,y,z$  and  $\theta$  positions to maintain the maximum helium reflectivity possible. Water was dosed onto Pd(111) at 150 K through a molecular beam to accurately control the coverage. Experiments were carried out on one monolayer of water and multilayer coverages for comparison. Once dosed, the crystal was cooled to approximately 100 K before the helium was switched on. The temperature of the helium beam was held at 300 K corresponding to a beam energy of 65 meV and de Broglie wavelength of 0.56 Å as calculated in chapter 2. Angular scan experiments were carried by scanning the crystal across a varying range of angles, while monitoring the helium reflectivity on the Hiden mass spectrometer. In addition, experiments were performed to monitor the helium reflectivity at the  $(0,0)$  position during water desorption in order to determine the point at which the specular reflectivity peak returned back to its maximum value.

### 3.5.3 Results and Discussion

The first stage of the helium atom scattering experiments involved optimising the helium reflectivity on the clean Pd(111) surface to provide the required x,y,z positions for the angular scan experiments. This was achieved by letting the helium beam into the chamber while altering the position of the crystal to optimise the helium signal on the mass spectrometer output. The helium reflectivity could be optimised to approximately  $1 \times 10^6$  counts/second at a particular temperature. The reflectivity dropped dramatically on an un-cleaned crystal and this method therefore also presents a good technique for monitoring the cleanliness of the sample. The reflectivity was optimised to the above value prior to each angular scan. The first angular scans were performed on the clean Pd(111) crystal after three or more argon ion sputter and anneal cycles. These scans spanned  $100^\circ$  from  $150^\circ$  to  $50^\circ$  and initial data was converted to provide a scale of intensity against parallel momentum transfer,  $\Delta K_{\parallel}$ . The initial scans from the clean surface show a sharp specular reflectivity peak as expected with no additional features (figure 3.15). However, a reverse scan immediately after the first one (figure 3.16) presents a different data set with the central specular reflectivity peak reduced by approximately 70 % and additional features with parallel momentum transfer of  $\pm 1.5 \text{ \AA}^{-1}$ . It is suggested that these additional features are due to hydrogen adsorbing on the metal surface from the background gases in the vacuum chamber over a period of time. This is in agreement with the hydrogen desorption observed by TPD and was confirmed by monitoring the helium reflectivity as the hydrogen desorbed from the surface. At the point where the hydrogen desorbed, the helium reflectivity increased and returned to the values obtained for a clean Pd(111) surface. The background pressure of the chamber was maintained at approximately  $1 \times 10^{-10}$  mbar before the dosing of gases and a typical scan took between 30 and 160 minutes with a scan rate of 0.01 degree per second. For the experiments involving a backward scan, the time delay is a lot longer than the chamber would normally be left for without re-cleaning the crystal. The forward scan in figure 3.15 shows a sharp specular peak but it should be noted that this is greatly reduced from the signal given when optimising the beam (17 % of the maximum) highlighting the need to maintain a clean crystal. This makes HAS difficult to interpret and in order to provide the best possible data, it is recommended that forward scans are carried out immediately and data from backward scans are treated with

caution due to the high possibility of contamination / readsorption onto the crystal surface.

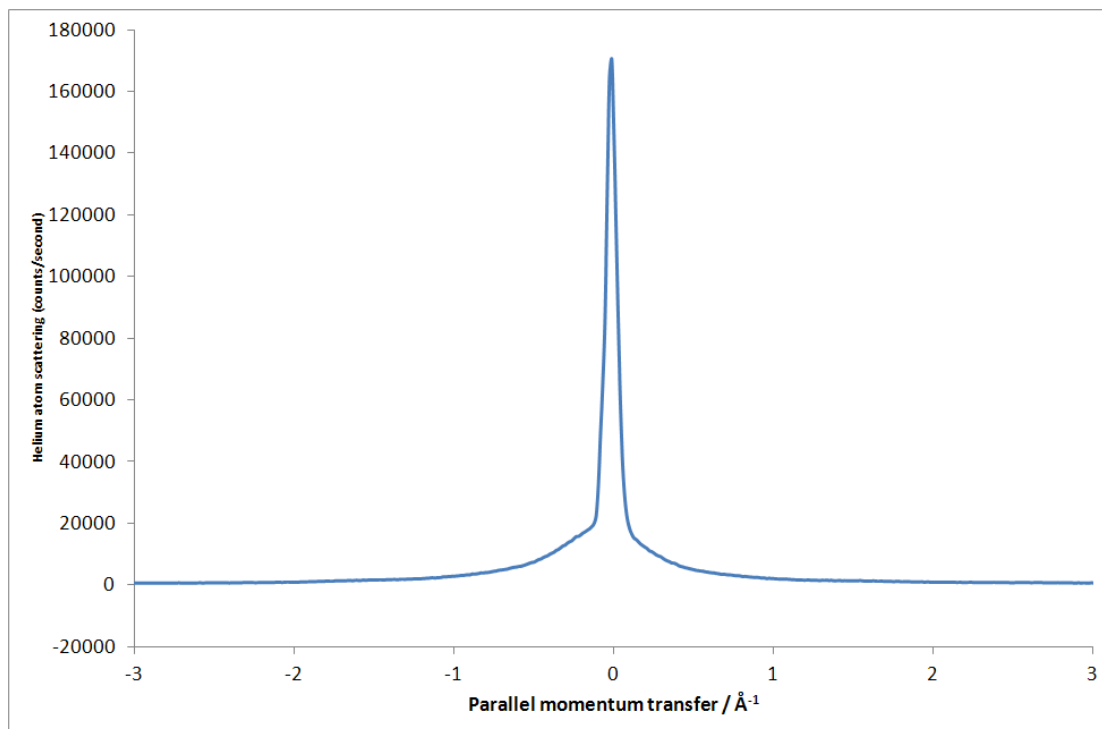


**Figure 3.15:** Helium atom scattering from clean Pd(111). Angular scans were performed immediately after cleaning and cooling the sample.

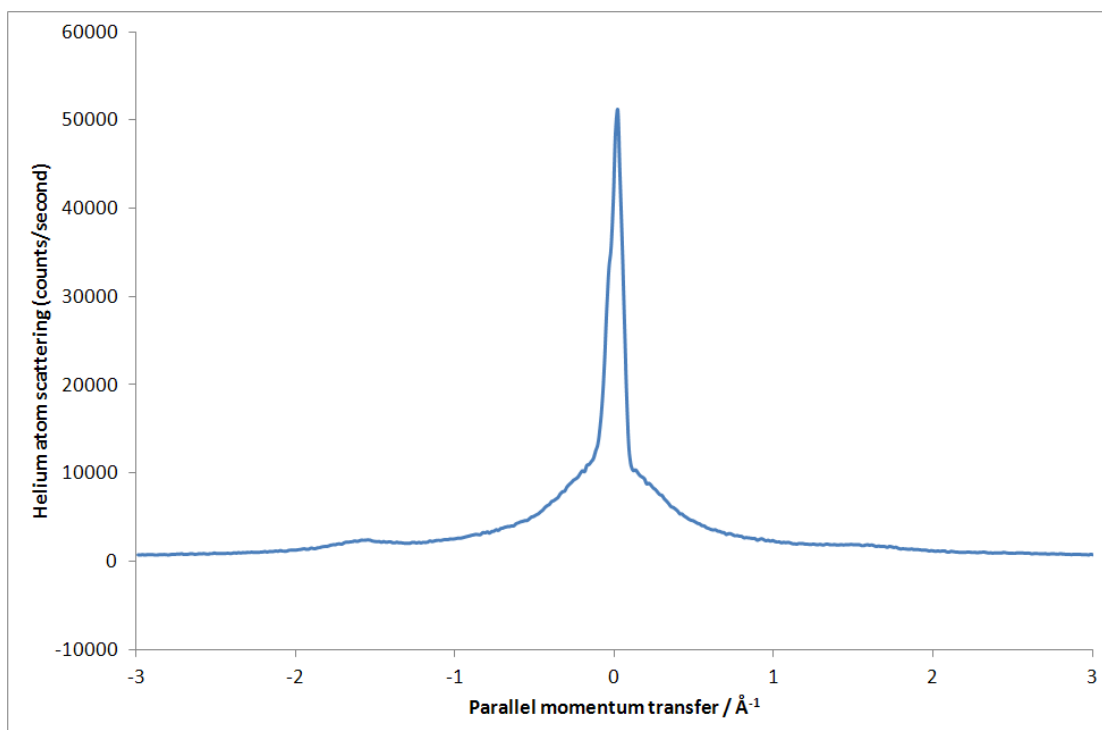


**Figure 3.16:** Reverse scan of figure 3.11. Helium atom scattering was carried out on clean Pd(111) immediately after the previous scan. A drop in the specular reflectivity is observed along with additional features with a parallel momentum transfer of  $\pm 1.5 \text{ \AA}^{-1}$  close to the  $(1/3, 1/3)$  diffraction positions due to contamination with gases from the background. This specular peak for this scan is 70 % lower than the forward scan in figure 3.15 and is only 5 % of the optimised beam value.

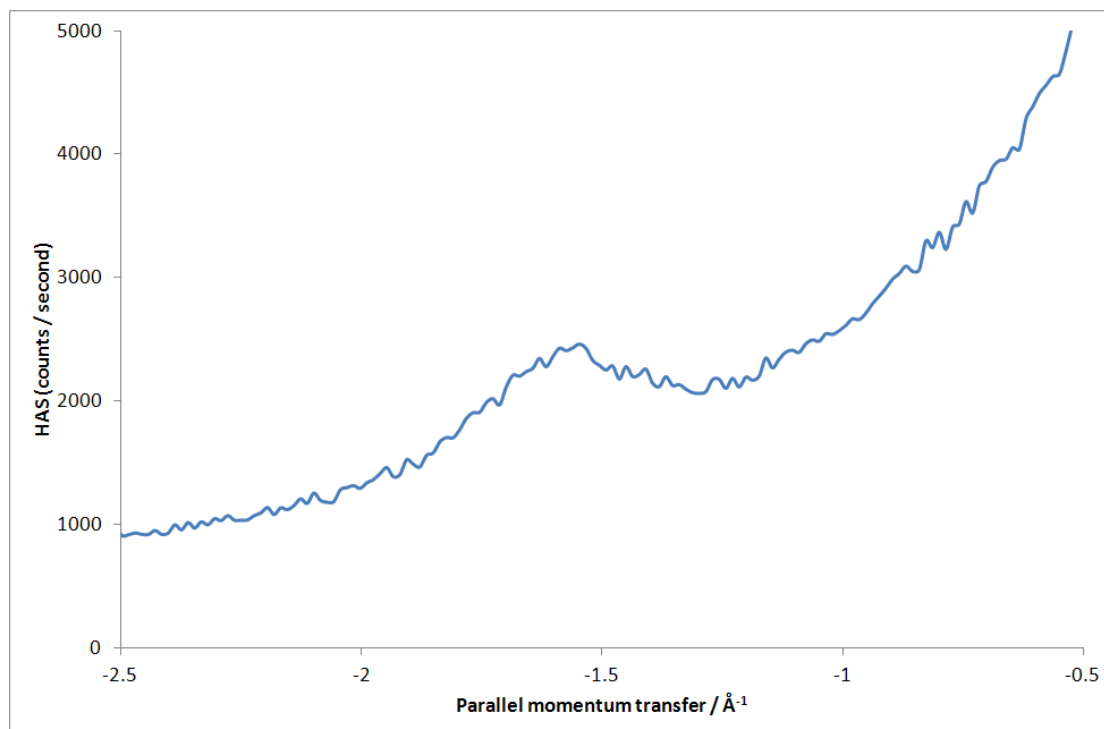


**Figure 3.17:** Close up of the broad maxima at approximately  $\pm 1.5 \text{ \AA}^{-1}$  observed in figure 3.16. Although small in relation to the specular, the adsorption of background hydrogen is responsible for this peak due to the long scan time used for these experiments.

A coverage of just less than one monolayer of water was prepared at 150 K on Pd(111) and angular helium atom scattering scans were recorded from this film. As seen with scattering from the clean surface, a central specular reflectivity peak is observed with an intensity of 15,000 counts/second. Prominent features can also be observed at  $\Delta K_{\parallel} \pm 1.5 \text{ \AA}^{-1}$  (figure 3.20). These bands are weaker and broader than the specular reflectivity peak (figure 3.19) suggesting disorder in the overlayer structure as sharp features would be observed for a highly ordered overlayer structure as seen on Rh(111). Figure 3.18<sup>26</sup> shows a HAS spectrum for scattering from 1 BL water adsorbed on Rh(111) taken from Gibson *et al.* The spectrum shows the sharp narrow features expected for scattering from an ordered  $(\sqrt{3} \times \sqrt{3})R30^\circ$  overlayer. The broad maxima appear close to the  $(1/3, 1/3)$  diffraction positions and are consistent with the LEED pattern recorded although sharp features do not exist.

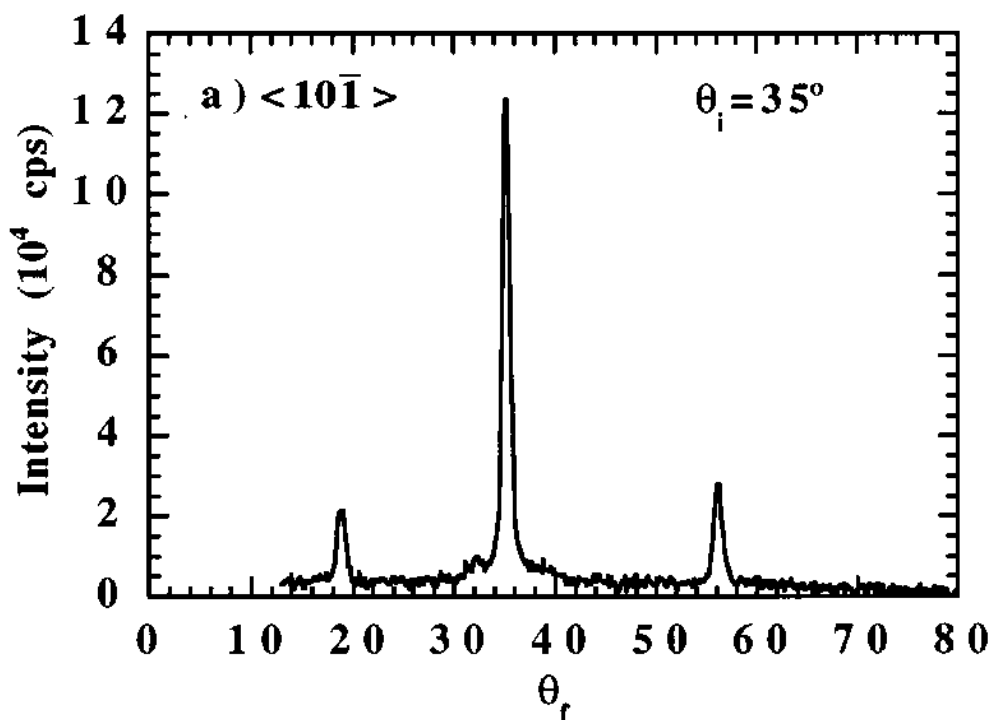


**Figure 3.18:** HAS of 1 BL of water adsorbed on Rh(111) at 140 K <sup>26</sup>. The 2 sharp peaks either side of the specular are due to the  $\sqrt{3}$  structure. Additional features close to the specular are attributed to an extended superstructure. Reprinted with permission from [K. D. Gibson, M. Viste and S. J. Sibener, *Journal of Chemical Physics*, 2000, 112, 9582-9589]. Copyright [2000], American Institute of Physics.

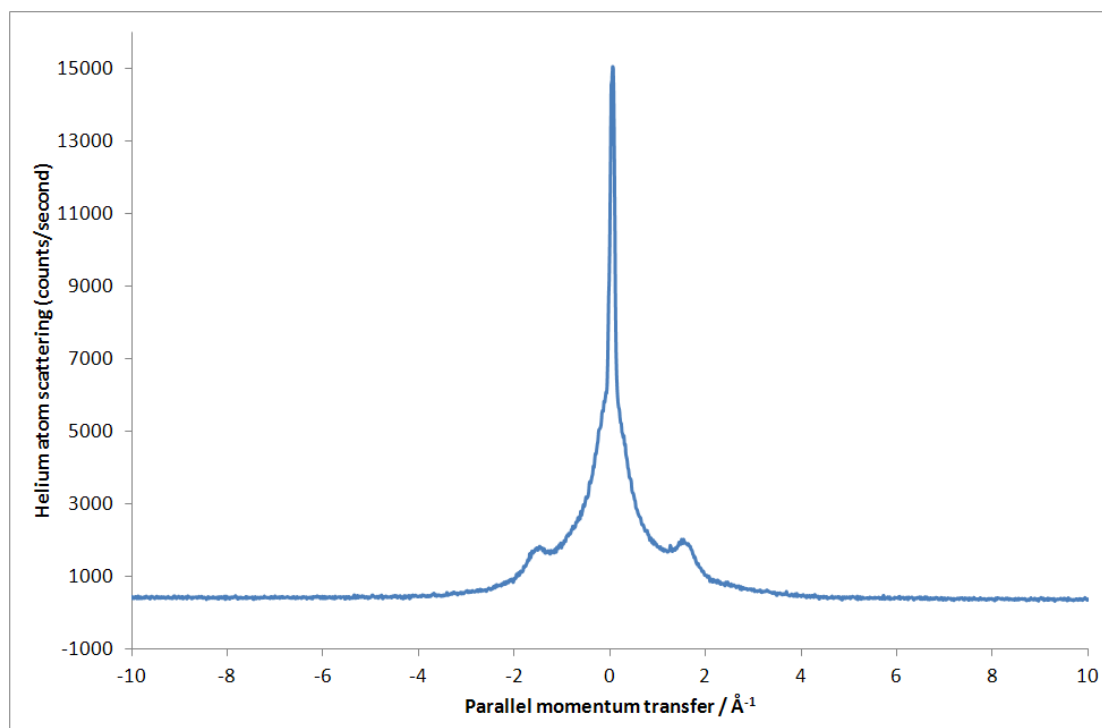


**Figure 3.19:** Helium atom scattering from approximately 0.86 ML water grown at 140 K. The specular reflectivity peak has an intensity of 15,000 counts/second and additional features are observed at  $\Delta K_{\parallel} \pm 1.5 \text{ \AA}^{-1}$  which are shown in more detail in figure 3.20.

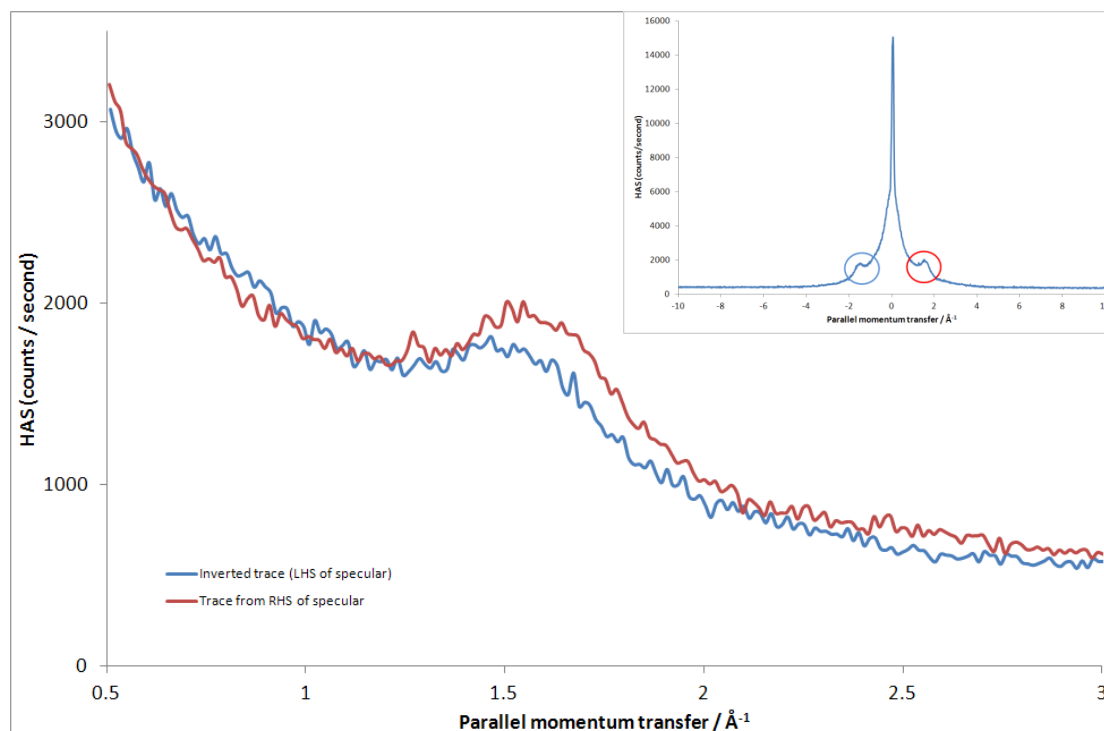


**Figure 3.20:** Close up of the features with parallel momentum transfer of  $\pm 1.5 \text{ \AA}^{-1}$ . Taken from data shown in figure 3.19. Inset shows figure 3.19 for reference.

In addition to the sharp  $\sqrt{3}$  features observed on Rh(111), additional features are observed close to the specular peak which have not been observed for Pd(111). Gibson *et al.* attribute the additional features to the presence of larger superstructure periodicity and also co-adsorbed species and suggest that oxygen could be adsorbing on the surface during the cooling process after cleaning the crystal<sup>26</sup>. Although these features are not observed on Pd(111), evidence for an extended superstructure is supported by DFT and LEED. It is possible that the broad base to the specular He intensity masks any small features that may have been associated with an extended superstructure. The changes in the HAS pattern for multilayer water combines with this evidence but will be discussed in more detail in Chapter 4.

The intensity of the specular peak on the clean Pd(111) was found to decrease with time, suggesting that the surface becomes contaminated, highlighting the need to complete experiments as quickly as possible once the crystal has been cleaned. TPD experiments after HAS confirmed that background hydrogen in the chamber adsorbs onto the Pd(111) surface and reduces the intensity of the helium reflectivity from the

clean surface. As the hydrogen desorbs, the specular reflectivity recovers and returns to the value expected from the clean surface.

Therefore, in conjunction with helium atom scattering, temperature programmed desorption experiments were carried out to monitor the desorption of water and hydrogen alongside the reflectivity of helium. This was completed by preparing water layers of varying coverages on Pd(111) at 140 K. Once prepared, the crystal was moved to the position required to obtain the maximum helium reflectivity from the clean surface. Once in position, the cooled helium beam was let into the main chamber and monitored using the Hiden mass spectrometer. Temperature programmed desorption profiles for hydrogen and water were recorded as explained in section 3.2.2 and the data can be seen in figures 3.21 and 3.22. The helium remains at a steady intensity as the temperature is ramped and does not change as the water multilayer desorbs. As the water monolayer begins to desorb the helium reflectivity begins to increase, peaking at the point where all of the water has desorbed from the surface. Due to the suggestion that hydrogen has an effect on both water TPD and helium scattering experiments, further monitoring was carried out to see what occurred at the point where hydrogen desorbs. As the temperature increased after desorption of the water monolayer, the helium reflectivity slowly decreased but a rise was observed at the point where hydrogen desorbed, this time peaking at the point where all of the hydrogen had desorbed. The reflectivity at this point was higher than it was once the water had desorbed (figure 3.22), providing further evidence for a degree of interference from hydrogen during adsorption experiments on Pd(111). Previous studies of hydrogen desorption on Pd(111) shows that hydrogen adsorbs at 3-fold face-centred cubic (fcc) sites, forming an ordered structure with  $(\sqrt{3} \times \sqrt{3})R30^\circ$  periodicity as the coverage reaches  $\frac{1}{3}$  and  $\frac{2}{3}$  monolayers (these coverages containing one and two sites occupied by hydrogen respectively). Above 50 K hydrogen dissociates allowing further adsorption to a coverage of one monolayer at which point almost all fcc sites become occupied by hydrogen.

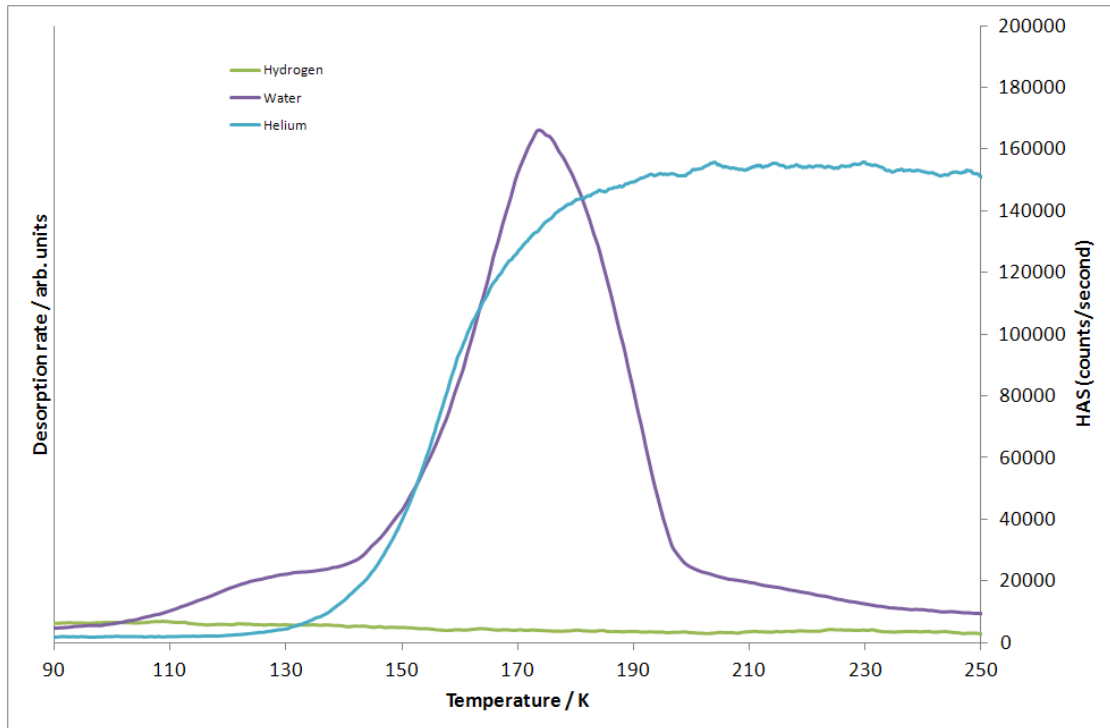


**Figure 3.21:** The helium atom reflectivity remains close to zero during multilayer water desorption and begins to increase as the monolayer desorbs reaching a maximum once all of the water has desorbed from the surface.

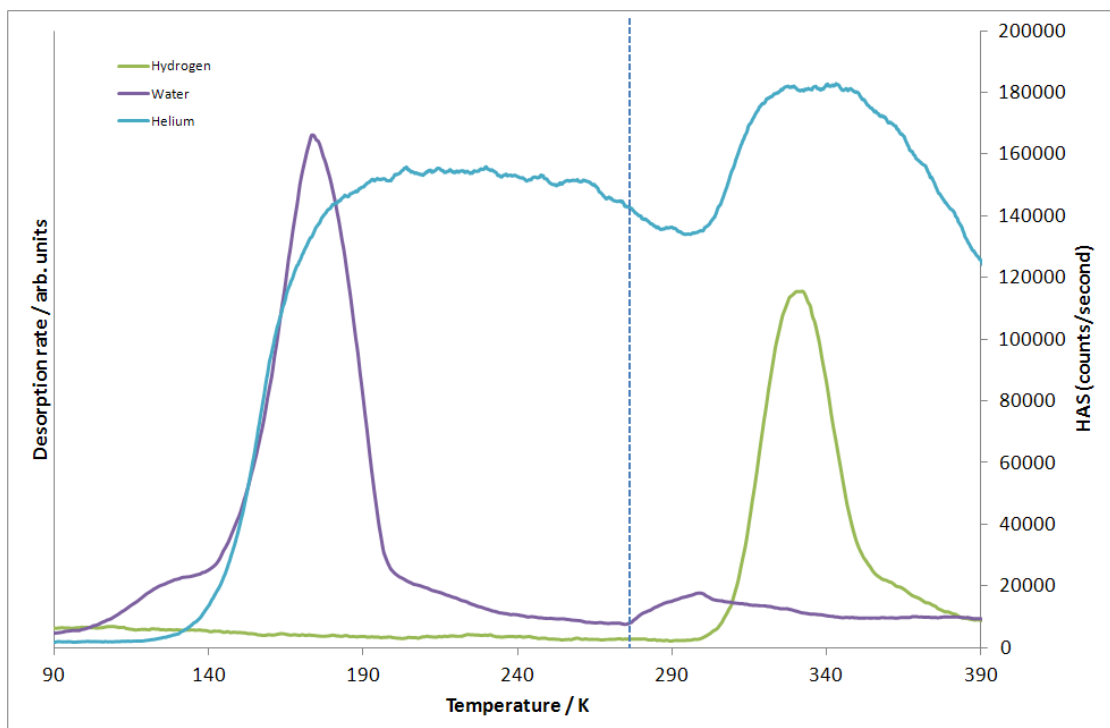


**Figure 3.22:** The helium reflectivity is shown as a function of water and hydrogen desorption. As the water monolayer begins to desorb from the surface, the helium reflectivity increases but does not return to a maximum reflectivity value until hydrogen desorbs. The left hand side of the line shows water desorbing followed by thermal desorption of hydrogen on the right hand side of the line.

It is well documented that palladium has a high affinity for hydrogen and it has been shown that at low coverages, saturation of the chemisorbed surface layer occurs with no penetration into the bulk and a  $(1 \times 1)$  structure is observed. Salmeron *et al.* report that hydrogen occupies subsurface sites in preference to the bulk and that these sites are comparable in stability to surface bound hydrogen<sup>27, 28</sup>. They state that it is the subsurface hydrogen that influences the order and structure of adsorbates. For example,  $(2 \times 2) - O$  islands formed on Pd(111) compress to  $(\sqrt{3} \times \sqrt{3})R30^\circ - O$  structures upon adsorption of hydrogen at 150 K.

Gdowski *et al.*<sup>29, 30</sup> report that hydrogen adsorbs in the near surface region and can easily move into the bulk at temperatures between 90-200 K. They show that for coverages less than  $\frac{2}{3}$  monolayer, a  $(\sqrt{3} \times \sqrt{3})R30^\circ$  structure is observed, and for higher coverages, the  $(1 \times 1)$  structure mentioned above, is recorded. Further investigation by Charles *et al.*<sup>31</sup> provides a link between hydrogen occupying subsurface sites on Pd(111) and the stability of hydrogen bound to the surface. The atoms adsorbed on the surface preferentially occupy sites away from areas populated with subsurface hydrogen. Changes in the electronic structure of the top palladium layer decreases the stability of adsorbed hydrogen, thus hydrogen overlayer vacancies form in this area with a  $(\sqrt{3} \times \sqrt{3})R30^\circ$  structure.

During the experiments described here, hydrogen adsorbs on the palladium surface during periods of inactivity and it is found that they appear in the helium atom scattering scans carried out on the 'clean' surface in the same position as the water adlayer. It is therefore evident that the adsorption of hydrogen can affect the adsorption of any overlayers on the surface. The problems associated with hydrogen were first noticed during the helium atom scattering experiments in the second UHV chamber and hadn't been observed during initial LEED / TPD experiments in the first UHV chamber. For future work on Pd(111), it is essential that every step is taken to ensure a clean Pd(111) surface is maintained without adsorption of any contaminants, especially hydrogen. It is believed that the structure due to the  $(\sqrt{3} \times \sqrt{3})R30^\circ$  pattern is real and can be observed, however it is suggested that results are treated with caution to ensure that adsorption of background gases does not interfere with HAS experiments or any other form of analysis for water adsorbed on Pd(111).

The HAS work that I carried out is reported here and was later repeated by McBride. The unusual behaviour found for the scattering from water grown on Pd(111) was confirmed. We both found that the specular peak was only observed below the point at which the first layer saturates and the faint (1/3, 1/3) diffraction peaks are again weakly observed at approximately  $\pm 1.5 - 1.7 \text{ \AA}^{-1}$ . McBride also observes a specular peak with reduced intensity from the optimised beam (0.6 %) and the data presented follows the same trend (figure 3.23). However, the data shown here shows a reduction to 1.5 % of the specular reflectivity (figure 3.24) which highlights the sensitivity of the water layer to HAS at coverages of water just below one monolayer. All adsorption sites become quickly occupied as the monolayer approaches saturation until a complete monolayer forms and the reflectivity drops to 0 % of the specular. Additional work carried out by McBride<sup>17</sup> took into account the need for a clean surface and their results confirmed that the broad maxima at  $\pm 1.5 - 1.7 \text{ \AA}^{-1}$  were due to the water layer.

Comparative data sets are shown in figures 3.23 (McBride *et al.*) and 3.24 (data I obtained) and highlight the sensitivity of HAS to water coverages close to one monolayer.

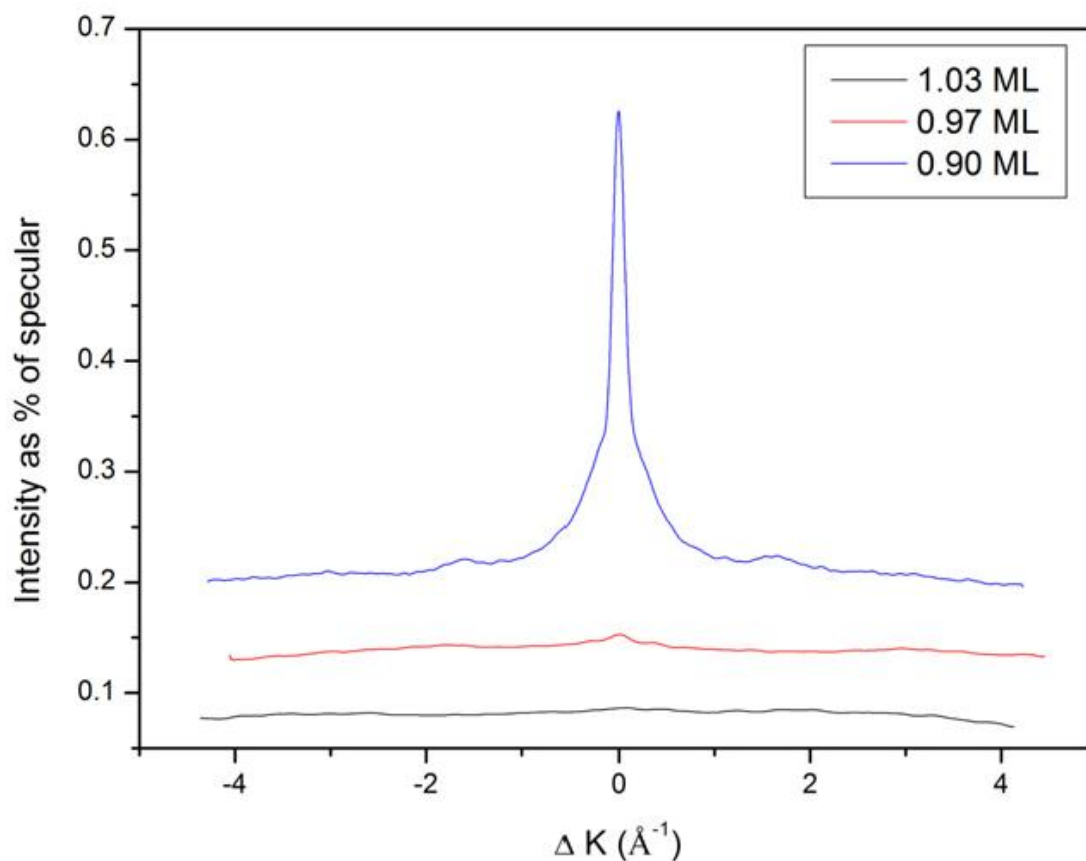


**Figure 3.23:** Helium atom scattering traces for coverages just below and just over 1ML. It can be seen that the main specular peak is almost completely masked at 0.97 ML and as the water layer saturates, the peak disappears completely. This is in agreement with my results shown in figure 3.24. Reproduced with permission from [F. McBride, A. Omer, C. M. Clay, L. Cummings, G. R. Darling, A. Hodgson *Journal of Physics: Condensed Matter*, 2012, 24, 124102]. Copyright (2012), IOP.

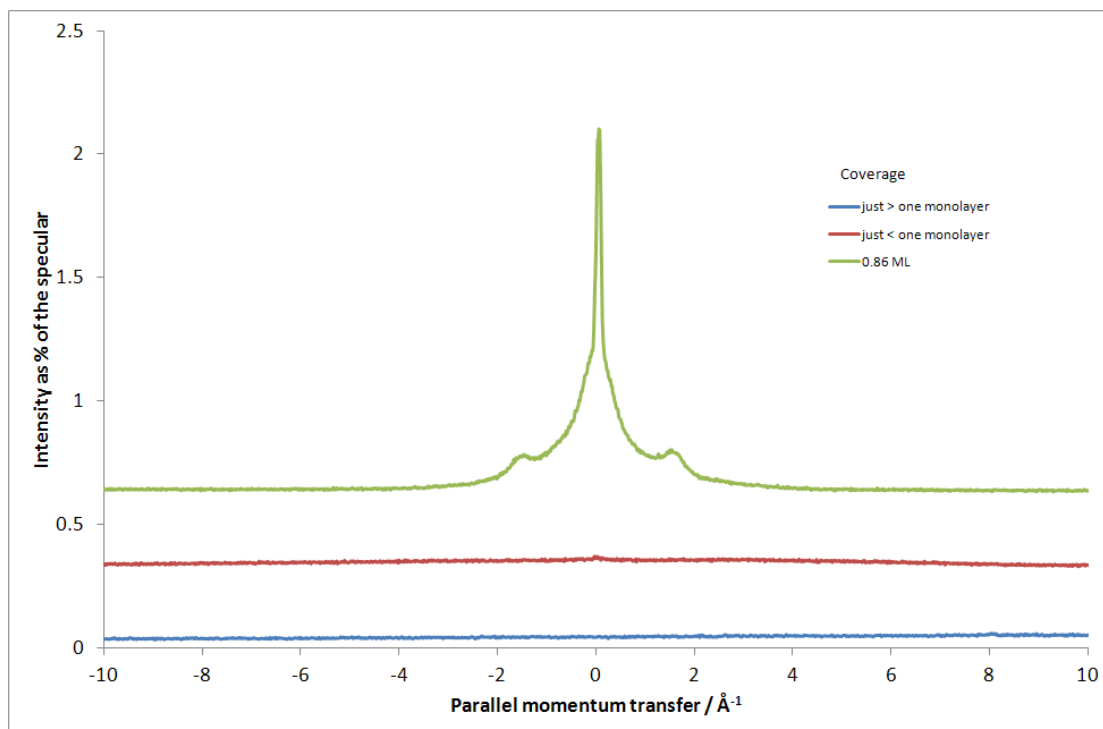


**Figure 3.24:** Helium atom scattering traces for coverages just below and just over 1ML. For a water coverage of 0.86 ML, the intensity of the specular is reduced to only 1.5 % of that for the optimised beam on a clean surface. The intensity rapidly reduces with increasing coverage until it is masked completely as the multilayer begins to grow.

The trace shown for the onset of multilayer growth will be discussed in Chapter 4 along with findings by the group for HAS from the mixed OH/water layer grown on Pd(111).

### 3.6 Conclusions: Monolayer water adsorption on Pd(111)

Initial temperature programmed desorption experiments show behaviour that has been observed for water adsorbed on many other surfaces with saturation of the monolayer peak at 175 K. It has been shown that there is a shift of 7°C of the maximum desorption temperature between a water coverage of 0.15 and 1.0 layers which indicates close to first order desorption kinetics as confirmed by the plot shown in figure 3.2. The TPD traces shown in this chapter confirm that water adsorbs and desorbs intact from Pd(111) with no signs of dissociation. LEED experiments revealed a  $(\sqrt{3} \times \sqrt{3})R30^\circ$  pattern for submonolayer water adsorption, in-line with experiments carried out on other surfaces and indicated an initial wetting layer on Pd(111). However, a halo around the (0,0) spot provided evidence for a more complicated growth mechanism and the formation of an extended superstructure. Submonolayer water adsorption occurs by means of small flat domains with commensurate  $(\sqrt{3} \times \sqrt{3})R30^\circ$  periodicity. These flat domains are separated by disordered domain boundaries with further water adsorbing in a H-down configuration. In-line with STM work carried out by Cerda *et al.*, it is suggested that the smaller clusters of water aggregate to form islands and after completion of the first layer, form an extended superstructure (see chapter 4) which leaves the first layer of water exposed and therefore detectable by LEED.

During helium atom scattering experiments it became clear that the presence of hydrogen affects the adsorption of water and needs to be eliminated as much as possible to ensure that water adsorbs on a clean Pd(111) substrate. Throughout these experiments it was shown that the hydrogen adsorbed on the surface is observed in the HAS spectra due to the fact that hydrogen begins to form ordered  $(\sqrt{3} \times \sqrt{3})R30^\circ$  structures on Pd(111) with increasing coverage. The hydrogen presence could also add to the presence of a shoulder observed in the TPD spectra although this is primarily attributed to the desorption from step edges during aggregation of water

clusters. These findings are in agreement with previous studies of hydrogen adsorption on Pd(111) which show that hydrogen adsorption and dissolution into the bulk and subsurface sites has an effect on how any further adsorbates bind to the surface<sup>6, 29, 32</sup>. The HAS goes on to show that the broad scattering maxima close to the  $(1/3, 1/3)$  diffraction positions is due to the weakly ordered water structure, more specifically, a weakly ordered hydrogen network adsorbing flat on the surface or in a H-down motif, displaying minimal order from the positioning of H-atoms. This enables us to provide an explanation for the apparent order displayed in the LEED images with LEED being sensitive to the O and Pd atom positioning rather than the hydrogen atoms.

RAIRS, DFT calculations and workfunction data add evidence for a different growth mechanism and provide evidence for a chain structure on Pd(111). Various possibilities for stable water structures have been discussed with experimental evidence favouring the approximately  $(7 \times 7)$  or  $\sqrt{52}$  superstructures which account for the interesting LEED patterns observed for multilayer water growth discussed in chapter 4. RAIR data shows that water initially adsorbs with flat lying water molecules but compresses, adsorbing upright water molecules. In agreement with this, DFT calculations lead to the suggestion of a chain structure consisting of flat and tilted water molecules, which form a hexagonal superstructure with a H-down network. The experimentally determined value for the change in workfunction complements the calculated values for water taking on a flat/H-down network. This data strengthens the hypothesis for water initially adsorbing flat. This different mode for water adsorption provides a reason for the absence of strong first order diffraction peaks in helium atom scattering spectra. The absence of the strong diffraction peaks is due to the disorder found in the hydrogen positions in contrast to the order of the oxygen positions as found by LEED. The evidence for a different mode of water growth continues in chapter 4 where multilayer water growth is investigated.

### 3.7 References

1. S. Meng, E. G. Wang and S. W. Gao, *Physical Review B*, 2004, **69**, 195404.
2. A. Michaelides, V. A. Ranea, P. L. de Andres and D. A. King, *Physical Review Letters*, 2003, **90**, 216102.
3. G. S. Karlberg, G. Wahnstrom, C. Clay, G. Zimbitas and A. Hodgson, *Journal of Chemical Physics*, 2006, **124**, 204712.
4. M. Wolf, S. Nettesheim, J. M. White, E. Hasselbrink and G. Ertl, *Journal of Chemical Physics*, 1991, **94**, 4609-4619.
5. X. Y. Zhu, J. M. White, M. Wolf, E. Hasselbrink and G. Ertl, *Journal of Physical Chemistry*, 1991, **95**, 8393-8402.
6. T. Mitsui, M. K. Rose, E. Fomin, D. F. Ogletree and M. Salmeron, *Science*, 2002, **297**, 1850-1852.
7. J. Cerda, A. Michaelides, M. L. Bocquet, P. J. Feibelman, T. Mitsui, M. Rose, E. Fomin and M. Salmeron, *Physical Review Letters*, 2004, **93**, 116101.
8. E. Fomin, M. Tatarkhanov, T. Mitsui, M. Rose, D. F. Ogletree and M. Salmeron, *Surface Science*, 2006, **600**, 542-546.
9. T. Yamada, H. Okuyama, T. Aruga and M. Nishijima, *Journal of Physical Chemistry B*, 2003, **107**, 13962-13968.
10. S. Haq, J. Harnett and A. Hodgson, *Surface Science*, 2002, **505**, PII S0039-6028(0002)01152-01154.
11. G. Zimbitas, S. Haq and A. Hodgson, *Journal of Chemical Physics*, 2005, **123**, 174701.
12. A. Beniya, Y. Sakaguchi, T. Narushima, K. Mukai, Y. Yamashita, S. Yoshimoto and J. Yoshinobu, *Journal of Chemical Physics*, 2009, **130**, 034706.
13. A. Beniya, S. Yamamoto, K. Mukai, Y. Yamashita and J. Yoshinobu, *Journal of Chemical Physics*, 2006, **125**, 054717.
14. A. Michaelides and K. Morgenstern, *Nature Materials*, 2007, **6**, 597-601.
15. K. Andersson, A. Nikitin, L. G. M. Pettersson, A. Nilsson and H. Ogasawara, *Physical Review Letters*, 2004, **93**, 196101.
16. C. Clay, S. Haq and A. Hodgson, *Chemical Physics Letters*, 2004, **388**, 89-93.
17. F. McBride, A. Omer, C. M. Clay, L. Cummings, G. R. Darling, A. Hodgson *Journal of Physics: Condensed Matter*, 2012, **24**, 124102

18. T. Schiros, S. Haq, H. Ogasawara, O. Takahashi, H. Ostrom, K. Andersson, L. G. M. Pettersson, A. Hodgson and A. Nilsson, *Chemical Physics Letters*, 2006, **429**, 415-419.
19. D. N. Denzler, C. Hess, R. Dudek, S. Wagner, C. Frischkorn, M. Wolf and G. Ertl, *Chemical Physics Letters*, 2003, **376**, 618-624.
20. M. Tatarkhanov, D. F. Ogletree, F. Rose, T. Mitsui, E. Fomin, S. Maier, M. Rose, J. I. Cerda and M. Salmeron, *Journal of the American Chemical Society*, 2009, **131**, 18425-18434.
21. Y. L. Cao and Z. X. Chen, *Physical Chemistry Chemical Physics*, 2007, **9**, 739-746.
22. M. Gallagher, A. Omer, G. R. Darling and A. Hodgson, *Faraday Discuss*, 2009, **141**, 231-249; discussion 309-246.
23. T. Kondo, H. S. Kato, M. Bonn and M. Kawai, *J Chem Phys*, 2007, **127**, 094703.
24. T. Kondo, H. S. Kato, M. Bonn and M. Kawai, *J Chem Phys*, 2007, **126**, 181103.
25. T. Kondo, S. Mae, H. S. Kato and M. Kawai, *Surface Science*, 2006, **600**, 3570-3574.
26. K. D. Gibson, M. Viste and S. J. Sibener, *Journal of Chemical Physics*, 2000, **112**, 9582-9589.
27. T. Mitsui, E. Fomin, D. F. Ogletree, M. Salmeron, A. U. Nilekar and M. Mavrikakis, *Angewandte Chemie-International Edition*, 2007, **46**, 5757-5761.
28. M. Salmeron, *Topics in Catalysis*, 2005, **36**, 55-63.
29. G. Gdowski and T. E. Felter, *Abstracts of Papers of the American Chemical Society*, 1986, **192**, 154
30. G. E. Gdowski, T. E. Felter and R. H. Stulen, *Surface Science*, 1987, **181**, L147-L155.
31. E Charles H Sykes, Luis C Fernández-Torres, Sanjini U Nanayakkara, Brent A Mantooth, Ryan M Nevin and Paul S Weiss, *Proceedings of the National Academy of Sciences*, 2005, **102**, 17907-17911.
32. W. Eberhardt, S. G. Louie and E. W. Plummer, *Physical Review B*, 1983, **28**, 465-477.

## **Chapter 4**

# **Multilayer Water Growth on Pd(111)**

## **4. Multilayer water growth on Pd(111)**

### **4.1 Introduction**

A background to water adsorption on metal surfaces was presented in chapter 1 alongside a discussion of the available literature for water adsorption studies on Pd(111). It is clear that the adsorption – desorption process differs for multilayer growth to that of the monolayer. In this chapter, the growth of water multilayers on Pd(111) is investigated by use of TPD, LEED and HAS. The data will be compared to monolayer growth presented in chapter 3 as well as examples on other metal substrates. The data presented in this section was recorded in two separate UHV chambers and for clarity each image is labelled as either chamber one (initial chamber) or chamber two (with low current LEED system).

### **4.2 Temperature programmed desorption and low energy electron diffraction**

The data discussed here follows on from the discussion about monolayer water adsorption given in chapter 3. All experimental techniques were described in chapter 3 and have therefore been omitted from this section. As shown previously, the water monolayer desorbs at ~175 K. Increasing the coverage further leads to a second desorption peak at a temperature of 160 K, which is due to water bound to the first monolayer and desorbs at a lower temperature due to the weaker nature of water – water hydrogen bonds between adjoining water molecules in comparison to the covalent bonding between the water molecules and the metal surface. Saturation of the lower temperature feature does not occur and the desorption behaviour initially indicates multilayer growth and wetting of the Pd(111) surface. Figure 4.1 shows the onset of multilayer growth and figure 4.2 shows the continued growth of the multilayer feature which continues with increasing water coverage. Figure 4.2 shows that the monolayer peak saturates and the coverage of this peak remains constant during the growth of the lower temperature peak. However, figure 4.2 shows that under some circumstances the

monolayer peak continues to grow with increasing coverage which could be due to contamination in the chamber. The growth temperature of the water was 150 K for these experiments which is close to the desorption temperature. A small difference in temperature could cause desorption / re-adsorption while water is still being dosed and this may have caused the different growth mode for the data set shown in figure 4.2. However, in the follow on work carried out by F. McBride, an adsorption temperature of 140 K was used and gave results comparable to those presented in this thesis for TPD, LEED and HAS.

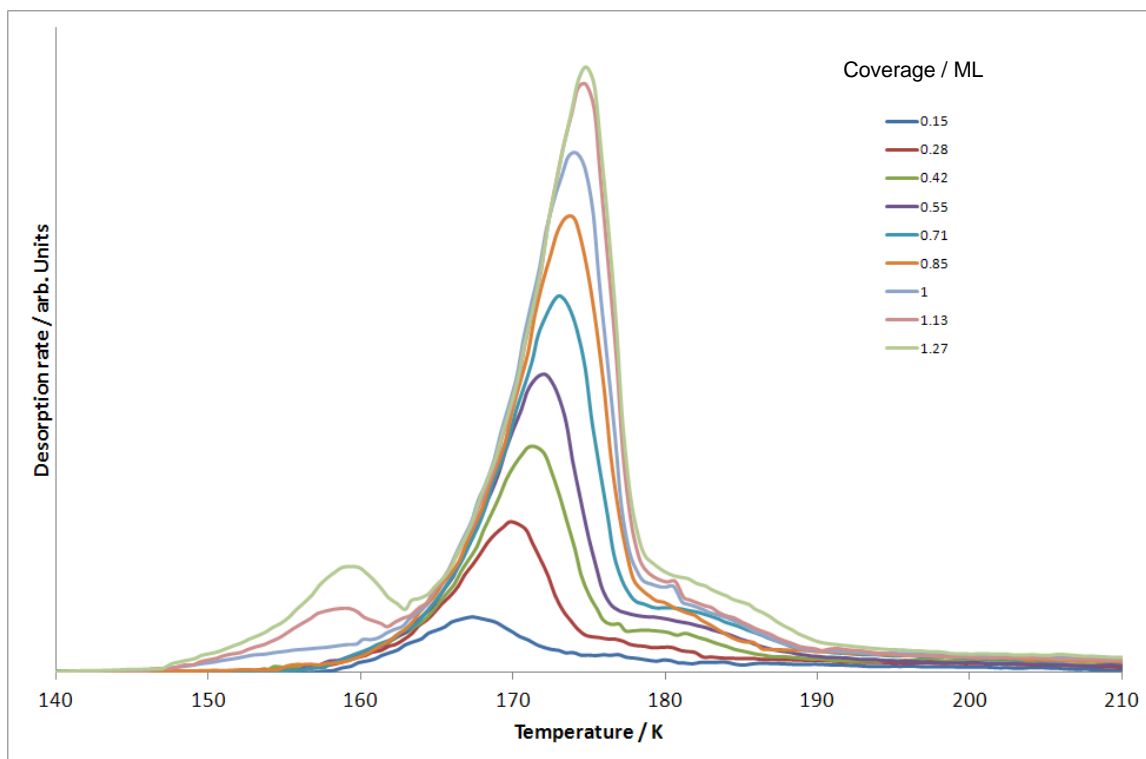


**Figure 4.1:** Temperature programmed desorption profile of water desorbing from Pd(111) after being dosed at 150 K. The peak at approximately 175 K saturates with a coverage of one monolayer (all coverages are quoted in reference to this). Onset of multilayer growth is shown with desorption at ~ 155-165 K. Data recorded using chamber 1.

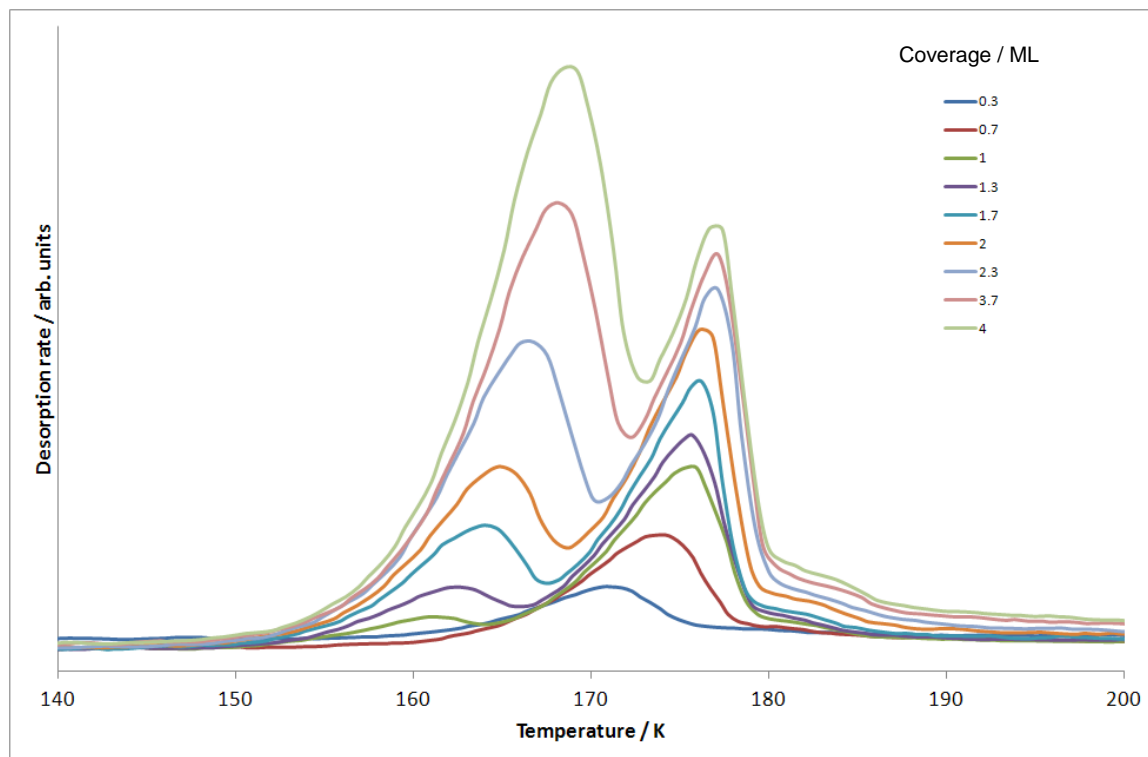


**Figure 4.2:** Temperature programmed desorption profile showing multilayer water desorption from Pd(111). The peak at  $\sim 165$  K is indicative of multilayer growth and continues to grow with increasing water coverage. Data recorded using chamber 1.

As discussed in chapter 3, the simple multilayer water hypothesis is too simple to assign to the growth mode of water on Pd(111). LEED experiments were carried out at water coverages ranging from one layer of water to 85 layers and at the point of saturation, the  $\sqrt{3}$  spots split to form a pattern consisting of three spots in the form of an inward pointing triangle (figure 4.3). This LEED pattern persists as the water coverage increases beyond one layer, although it gradually becomes more diffuse. Initial LEED images were recorded in the first vacuum chamber and later the experiments were repeated in the chamber equipped with a low current LEED system. The data presented here is separated by chamber and the reader is referred to section 4.2.2 where the results from each chamber are compared in summary.

### 4.2.1 LEED : Chamber 1

Figure 4.3 shows the low energy electron diffraction pattern for water adsorbed on Pd(111) at 150 K. It shows the single spots from sub-monolayer water coverage splitting into three separate spots which form a triangle pointing inwards towards the 0,0 position. The splitting of spots occurred at the point of monolayer saturation and remained for higher coverages. The observed change in LEED pattern for water adsorbed on Pd(111) could be attributed to structural changes of the first layer of water as the multilayer begins to form in connection with the onset of cluster growth.

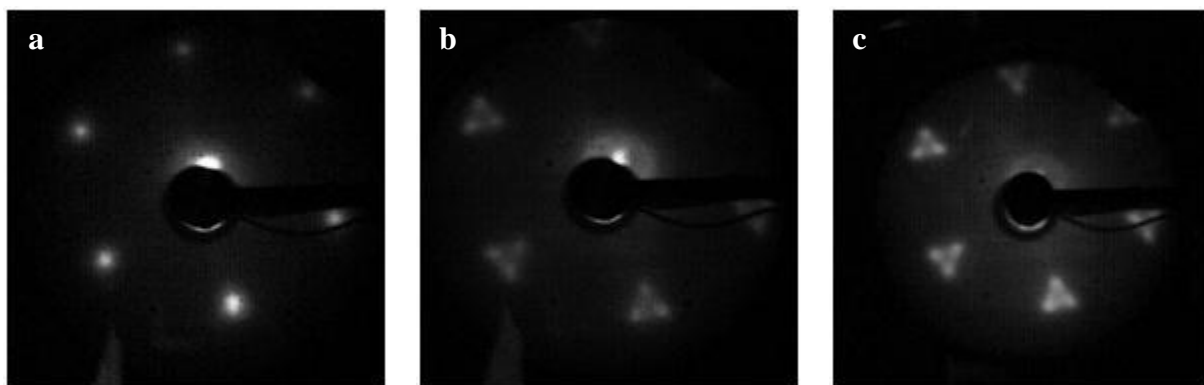


**Figure 4.3:** Low energy electron diffraction pattern for water adsorbed on Pd(111) at 150 K. The drain current for the images shown here was in the region 50 – 100 nA. Images a-c show 0.8, 1.2 and 4 layers of water respectively. All images recorded in chamber 1.

The observed change in LEED pattern for water adsorbed on Pd(111) could be attributed to structural changes of the first layer of water as the multilayer begins to form in connection with the onset of cluster growth. As saturation of the first layer occurs and the spots split, a more dense structure forms consistent with the formation of domain boundaries and cluster growth. LEED spots related to the Pd surface can be seen even for water coverages up to ~ 80 layers of crystalline ice (figure 4.4), indicating a non-wetting surface and the formation of ice clusters in preference to uniform layers. Although water

TPD experiments initially suggested wetting of the first monolayer of water on Pd(111), further evidence of cluster formation will be discussed in the following sections.

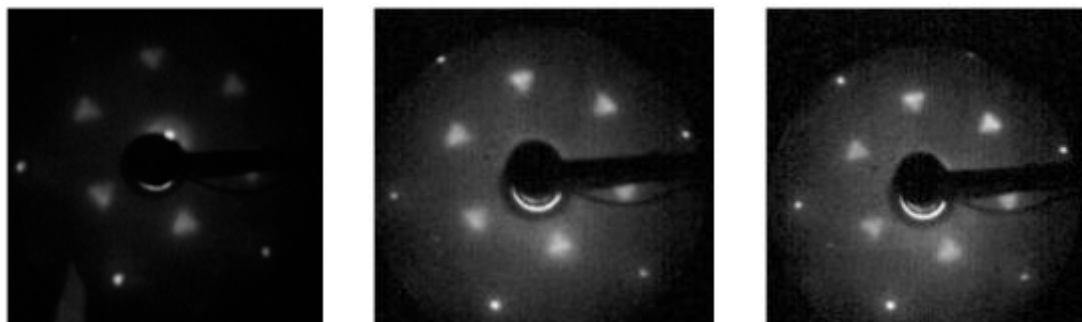


**Figure 4.4:** Low energy electron diffraction pattern for water adsorbed on Pd(111) at 150 K. These images show the triangle pattern of spots in the  $\sqrt{3}$  position due to multilayer water adsorption and also show the (1 x 1) spots of the Pd(111) surface. This image was recorded reproducibly for coverages ranging between 1 – 80 layers of water suggesting that water does not undergo layer-by-layer growth on the Pd(111) surface. Images recorded in chamber 1.

- a) 2 layers of water, 54 eV, 50 nA
- b) 10 layers of water, 55 eV, 50 nA
- c) 20 layers of water, 50 eV, 45 nA

Interestingly, although the triangular pattern of three spots appears during multilayer growth, the pattern was also found to appear after prolonged exposure of the water layer to the electron beam. Figure 4.5 shows how the LEED image changes over time as the electron beam remains incident on the sample. Initially a single circular spot can be observed in the  $\sqrt{3}$  position which is surrounded by a faint triangle. Over time the large spot appears to split into three distinct spots that fill the triangular shape. This suggests that electron damage can cause the water layer to restructure and at this point it was unknown whether the splitting of spots was due to the growth mode or completely due to electron damage. The LEED images were therefore recorded in a second chamber using a low current LEED system and the results from these experiments are discussed in section 4.3.2.

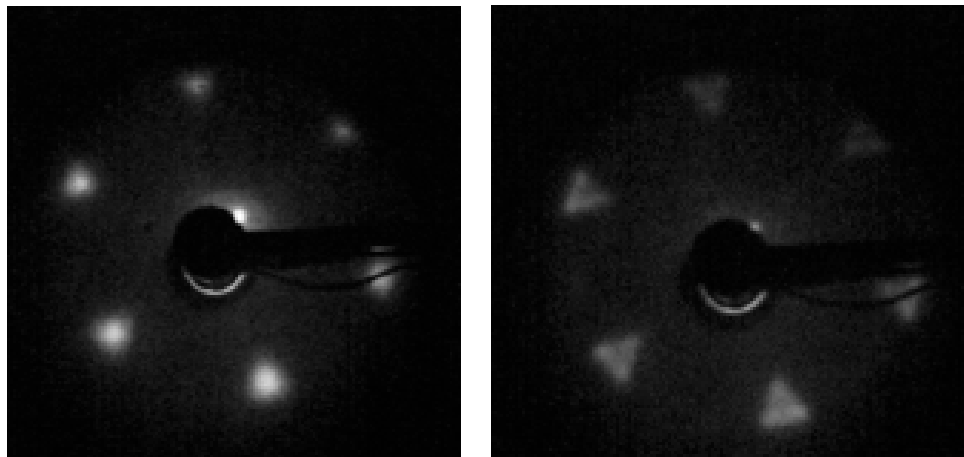


**Figure 4.5:** Low energy electron diffraction pattern for water adsorbed on Pd(111) at 150 K. Images were recorded at 26 eV with a drain current of 50 nA in chamber 1. Images here show how electron damage causes restructuring over time.

- LEED image recorded as soon as the electron beam was switched on. A bright spot in the  $\sqrt{3}$  position is surrounded by a faint triangle
- LEED image recorded during the same experiment after increased exposure to the electron beam. The  $\sqrt{3}$  spots have split into three spots and form a triangle pointing inwards towards the (0,0) position.

Electron damage of adsorbed overlays has been reported previously. Schiros *et al.* demonstrated that the water layer formed on Cu(110) occupied a (7 x 8) superstructure but this is quickly damaged by electron exposure, at which point a sharp  $c(2 \times 2)$  LEED pattern is observed<sup>1</sup>. This LEED pattern is shown in figure 4.6. The delicate nature of water overlayers highlights the importance of minimising the time that the adsorbed structure is exposed to the electron beam in order to prevent reconstructions. LEED images recorded in the first chamber highlight the importance of minimising electron damage as the pattern observed after inducing electron damage rendered the previous results inconclusive and further work was required to determine what the LEED patterns looked like under conditions where very little damage could be done to the water layers.

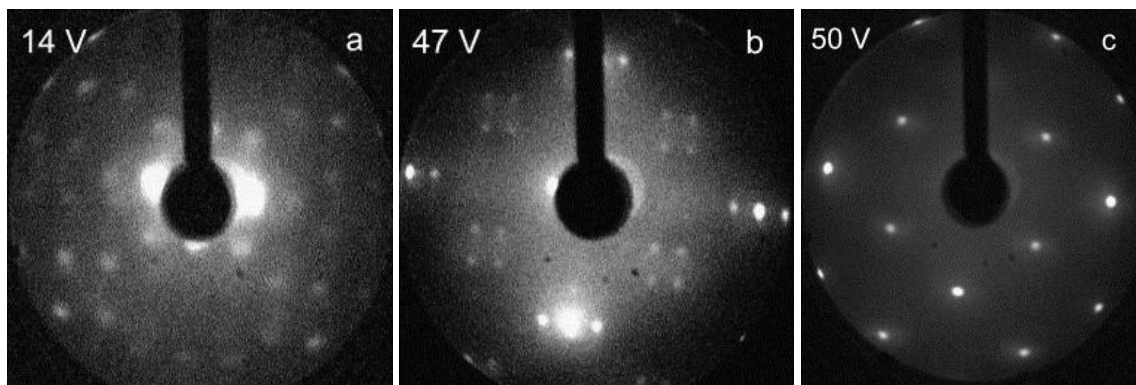


**Figure 4.6:** Low energy electron diffraction pattern for water adsorbed on Cu(110) at 140 K  
**a)** (7 x 8) superstructure taken at 14 eV  
**b)** (7 x 8) superstructure taken at 47 eV  
**c)** (2 x 2) structure formed after electron damage occurs to the (7 x 8) structure  
 Images from Schiros *et al.*<sup>1</sup>  
 Reprinted from T. Schiros, S. Haq, H. Ogasawara, O. Takahashi, H. Ostrom, K. Andersson, L. G. M. Pettersson, A. Hodgson and A. Nilsson, *Chemical Physics Letters*, 2006, 429, 415-419., Copyright (2006), with permission from Elsevier.

Many more reports can be found in the literature investigating electron induced dissociation including the work carried out by Zhou *et al.* They studied how electrons at 50 eV induce the dissociation of mono- and multilayer  $\text{CHCl}_3$  adsorbed on Ag(111) at 100 K<sup>2</sup>. The same group also show that under the same experimental conditions,  $\text{NH}_2$ ,  $\text{NH}$  and  $\text{H}$  are produced on a Pt(111) surface from the irradiation of  $\text{NH}_3$  adsorbed on the surface. Further research provides evidence for the cleavage of C – H bonds to form  $\text{CH}_3$  and  $\text{H}$  along with the loss of carbon containing species following electron damage to methane adsorbed on Pt(111) at 55 K. Prior to causing electron damage, methane desorbs from the surface intact at 65 K evident from a single desorption peak. Selective dissociation presents additional features in the TPD due to the selective dissociation of the adsorbed species.

Another group investigating damage to overlayers induced by low energy electrons are Sanche *et al.* A lot of their work focuses on biological samples and shows that electrons in the range 3 – 20 eV can cause irreversible damage to single and double strands of DNA, causing them to break<sup>3,4</sup>. However, in addition to their extensive studies for DNA, they present a study relating to low energy electron induced fragmentation of water<sup>5,6</sup>. They use charge trapping measurements and find that the greatest amount of charge

stabilisation occurs in a water film with electron energies near to zero and between 6 and 10 eV. They conclude that measurements with low energy electron beams can be carried out as long as electron exposure is minimised as much as possible along with the time spent at the high cross section energies.

It is clear from the evidence found in the literature that overlayers adsorbed on metal surfaces can be fragile and therefore readily damaged by impinging electron beams. It is therefore suggested that electron damage is caused to the extended  $(\sqrt{3} \times \sqrt{3})R30^\circ$  structure causing the elongated spots in the  $\sqrt{3}$  position to split into three spots, forming an inward pointing triangle. This conclusion is further supported by TPD experiments. TPD traces were recorded following LEED experiments of the water shoulder as shown in figure 4.7. In future work, great care should be taken to minimize the amount of damage caused by electrons in order to provide a clearer picture of the structure formed when water adsorbs on the Pd(111) surface.

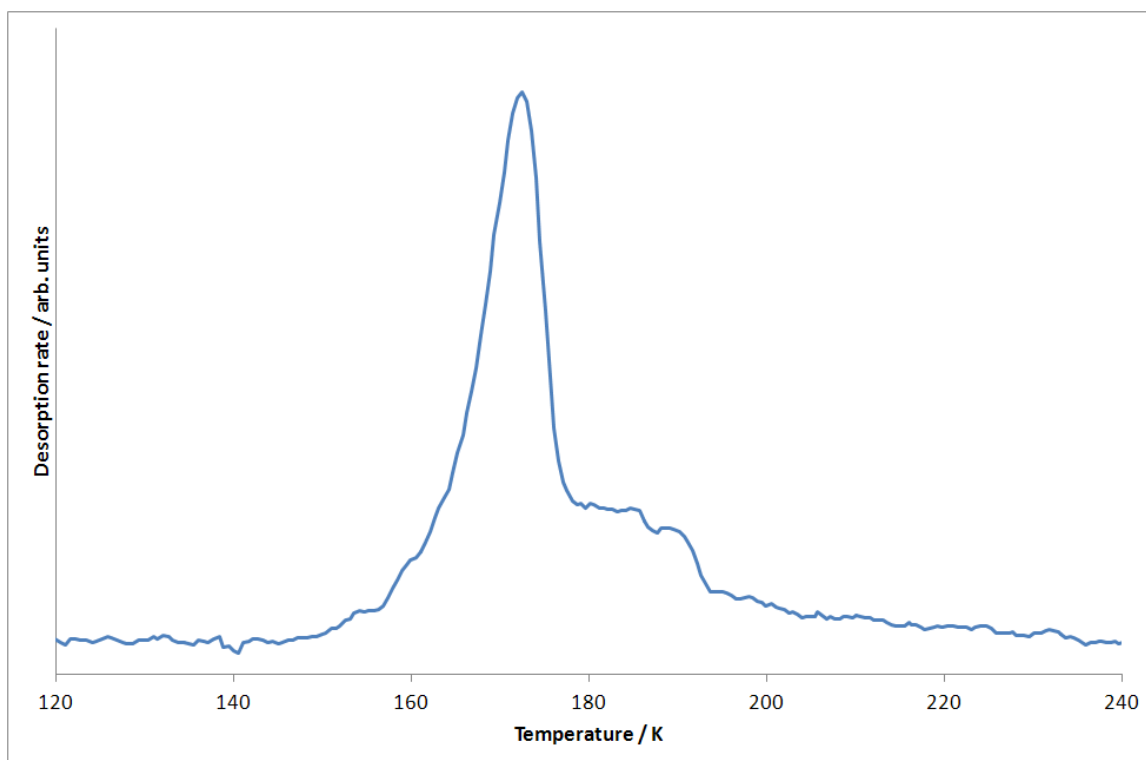


**Figure 4.7:** Water desorption from Pd(111). The high temperature shoulder is much more prominent after irradiation with the electron beam during LEED experiments. Data from chamber 1. Water coverage here was less than one monolayer but this behaviour is observed at all coverages. The LEED was recorded at 26 eV with a drain current of 50 nA in chamber 1.

There are some theoretical models available that show total ionization energy cross section as a function of electron energy including the paper by Vinodkumar *et al.* Figure 4.8 shows their findings for free water, ice and amorphous water <sup>7</sup>. This data is comparable to experimental results obtained by other researchers. From the graph, it can be seen that the electron energies used for all experiments described here, are close to the peak resulting in a high possibility that exposure will cause damage to the adsorbed water. Using an electron beam in the range 10 – 100 eV cannot be avoided during LEED experiments but the recorded images should be treated with caution to try and distinguish the structure formed as water adsorbs on Pd(111) from that formed due to electron damage.

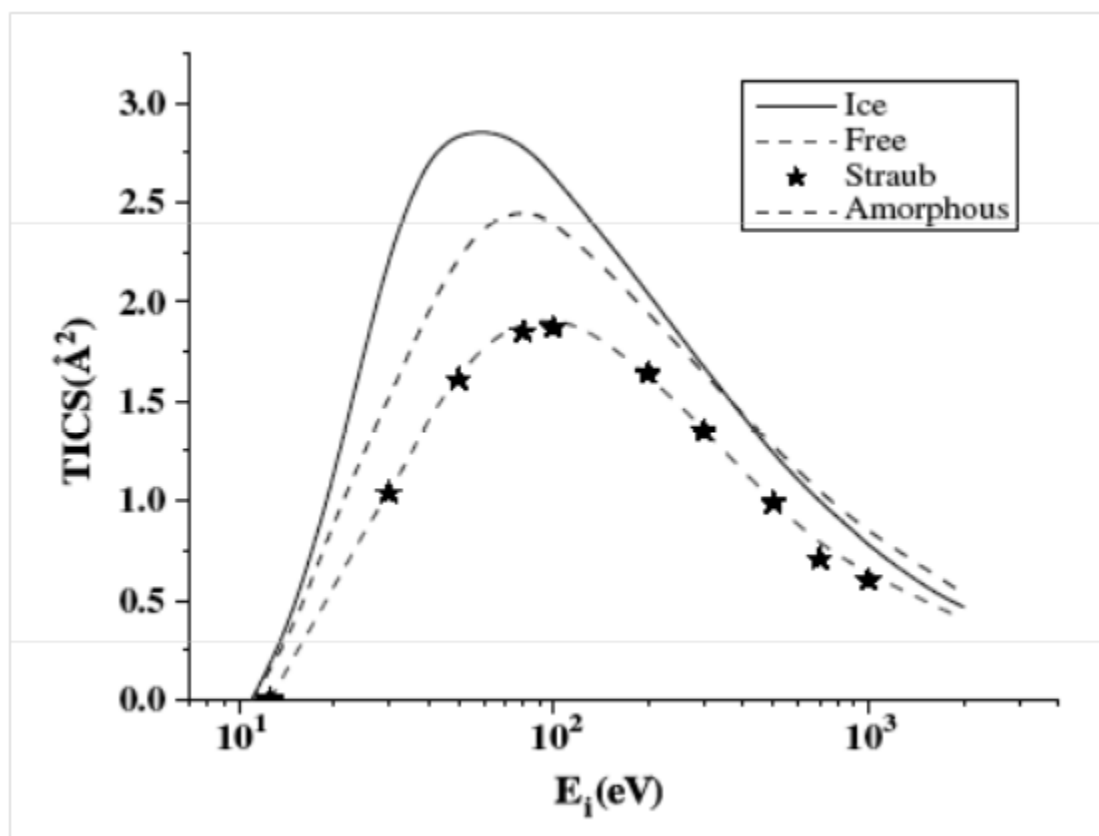


**Figure 4.8<sup>7</sup>:** Total ionization cross sections for e-H<sub>2</sub>O scattering in various phases. Reprinted from M. Vinodkumar, K. N. Joshipura, C. G. Limbachiya and B. K. Antony, *Nuclear Instruments and Methods in Physics Research Section B: Beam Interactions with Materials and Atoms*, 2003, 212, 63-66., Copyright (2003), with permission from Elsevier.

#### 4.2.2 LEED : Chamber 2

The desorption and LEED experiments were all repeated in a second chamber which was initially prepared for a helium atom scattering investigation. As before, all experiments were carried out with a base pressure of  $1 \times 10^{-10}$  mbar and the crystal was mounted and cleaned in the same way. This chamber was equipped with a VG mass spectrometer and low current LEED system. Initial findings were similar to before with multilayer desorption being observed for increasing coverages of water dosed at 150 K (Fig. 4.9). However, the more sensitive nature of the mass spectrometer showed additional features in the desorption traces; following the desorption of water at 162 – 175 K, a hydrogen desorption profile was detected at 350 K (figure 4.9). During the experiments in the previous chamber a shoulder was present on all desorption profiles and it was initially thought that this could be due to desorption at step edges or that it was related to the formation of clusters. One possibility is that adsorption of hydrogen to the clean Pd(111) affects the way in which water then adsorbs to the surface and this presents itself in the desorption profile in the form of a shoulder.

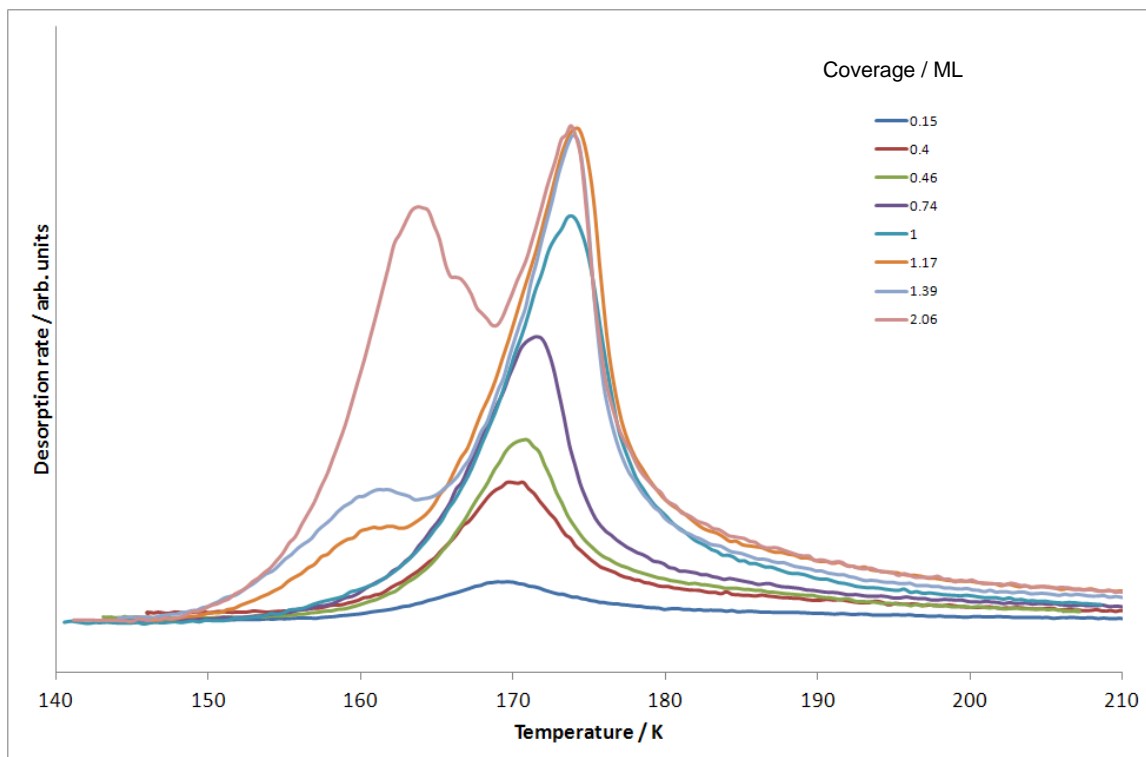


**Figure 4.9:** Water desorption from Pd(111) after adsorption at 150 K in a second UHV chamber. There is a long trailing edge on each desorption profile but no evidence of a distinct shoulder as seen previously. As the multilayer grows, the monolayer peak remains saturated.

Figure 4.10 shows hydrogen desorption profiles and figure 4.10 below, the corresponding water desorption profiles, recorded during the same heating cycle by ramping the temperature to greater than 400 K to record the desorption of both gases. This shows that the amount of water adsorbed is not directly related to the amount of hydrogen adsorbed. Instead, it was found that the amount of hydrogen adsorbed on the surface increased with time ie, the longer the crystal was left between cooling and dosing, the greater the amount of hydrogen adsorbed on the surface. The amount of background hydrogen present in the chamber was reduced as much as possible with the use of a titanium sublimation pump and by cooling the TSP cold trap with liquid nitrogen. However, traces of hydrogen were still detected in most experiments. At this stage it was unclear as to how the hydrogen may affect the adsorption behaviour of water but further results are reported later providing evidence for hydrogen adsorption clearly affecting helium scattering experiments on Pd(111).

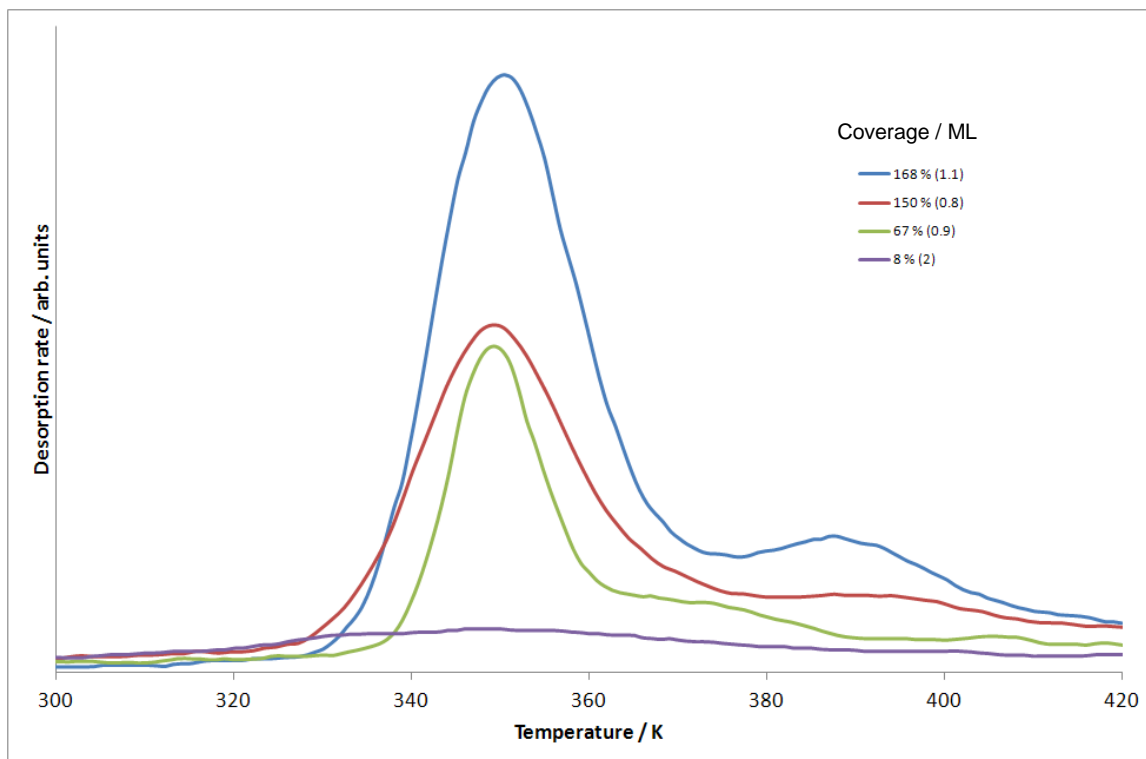


**Figure 4.10:** Hydrogen desorption from Pd(111) after the desorption of water. The size of the profiles indicates that the amount of hydrogen desorbed is not directly related to the amount of water adsorbed on the surface.

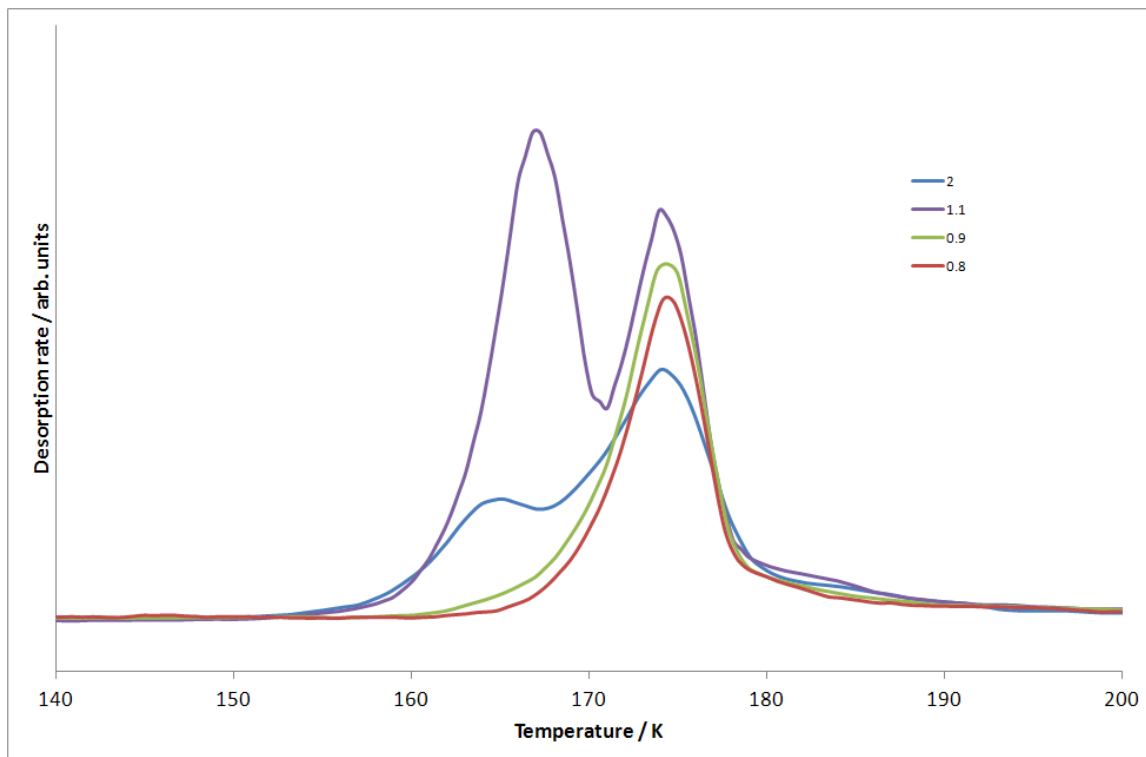


**Figure 4.11:** Water desorption from Pd(111) after adsorption at 150 K in a second UHV chamber. There is a long trailing edge on each desorption profile but no evidence of a distinct shoulder as seen previously.

In figure 4.11 it can be seen that the monolayer peak does not saturate and continues to grow with increasing water coverage as was sometimes observed in the first vacuum chamber. The recorded hydrogen desorption profiles provide evidence to suggest that background desorption does affect subsequent water adsorption. The amount of desorbing hydrogen does not increase with increased water coverage, instead it differs depending on the cleanliness of the underlying palladium surface.

In addition to repeating desorption experiments, LEED experiments were repeated using a low current LEED system in order to gain further insight into the unusual pattern and spot splitting observed previously. As expected, a sharp  $(1 \times 1)$  LEED pattern was observed for the clean Pd(111) surface and sharp  $\sqrt{3}$  spots were observed for submonolayer coverages of water. At the point of saturation of the first water layer, a change in pattern was observed but was slightly different to that seen before. An inward pointing triangle was observed but it did not appear to be split into three distinct spots, instead a diffuse triangular shaped diffraction pattern was observed (figure 4.12) although under closer inspection it is possible to resolve the spots and view the three spots that make up the triangle. The change in pattern remains consistent with initial suggestions that antiphase domain boundaries form and that the amount of order in the oxygen positions increases as the monolayer saturates. As discussed in section 4.2.1, it has been suggested that the splitting of spots was due to electron damage of the water film, and is therefore avoided in additional experiments carried out using a low current LEED system. As damage was not caused in the second chamber, the data shown here confirms that the triangular pattern is caused by the water structure grown on Pd(111) despite electron damage contributing to changes in the first vacuum chamber. Although the resolution of the images is poor in comparison to those recorded in the first chamber, close inspection allows the three spots to be resolved.

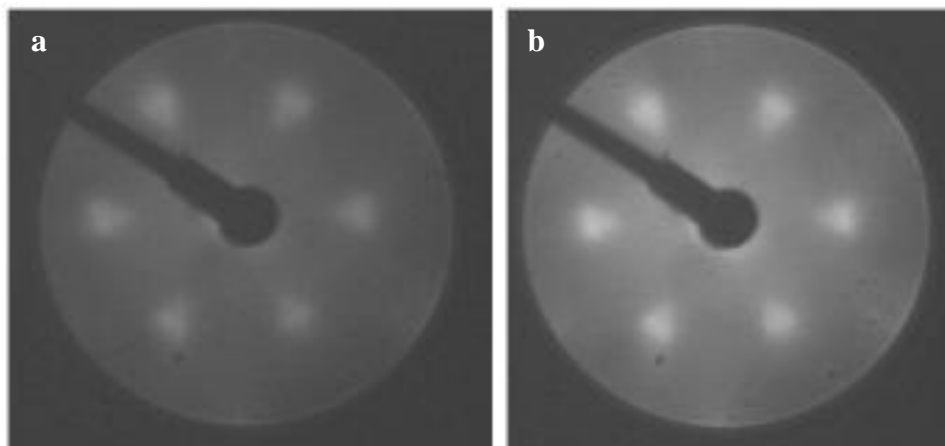


**Figure 4.12:** Low energy electron diffraction pattern for water adsorbed on Pd(111) at 150 K in the second vacuum chamber with the low current LEED system. A diffuse triangular diffraction pattern was observed and upon closer inspection, the three split spots can be observed although they are not as distinct as the ones observed in the first chamber (figure 4.4). These images were recorded at 30 eV with a drain current of 1-4 nA with a water coverage of 1.5 (a) and 3.0 (b).

Further investigation was carried out into the splitting of the spots and it became clear that the triangular pattern can be attributed to the multilayer water structure grown on Pd(111). The results from the first vacuum chamber show that electron damage can cause restructuring and the water layer is sensitive to damage, however, experiments in the second chamber illustrate the reproducibility of growing a multilayer structure that gives rise to a LEED pattern with three spots in the form of an inward pointing triangle. The LEED images shown in figure 4.12 show that the triangle was observed as soon as the electron beam hit the sample and remained visible during expose. Electron damage could not be responsible for this pattern because it would take ten times the electron dose to cause damage and therefore an exposure time in excess of six minutes. Figure 4.13 shows the triangular pattern observed as soon as the electron beam hit the sample.

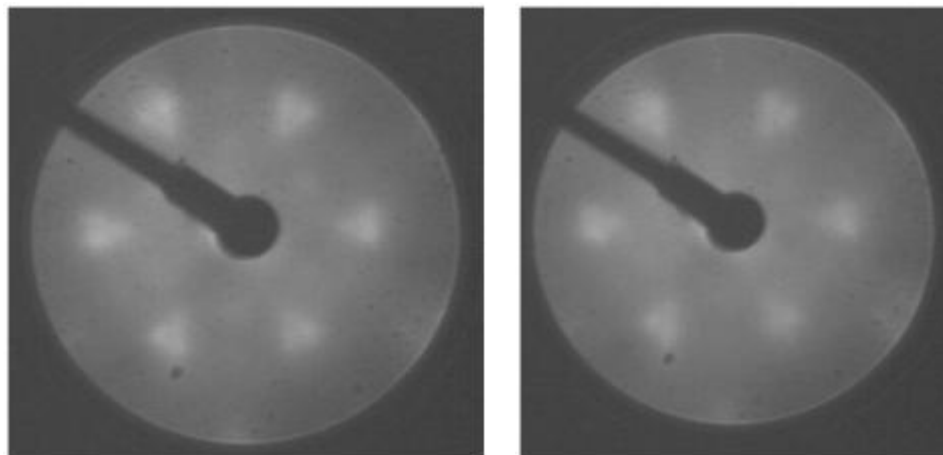


**Figure 4.13:** Low energy electron diffraction pattern for water adsorbed on Pd(111) at 150 K in the second vacuum chamber. Images were recorded at 28 eV with a drain current of 3 nA. These images were recorded after exposing the water layer to the electron beam for approximately 30 seconds. The spot slitting can be observed although the resolution is not as clear as for the first chamber. These images show that electron damage is not responsible for the spot splitting and that the unusual pattern is reproducibly observed on a freshly grown water layer. The coverage of water was approximately 1.5 layers.

The elongated feature in the  $\sqrt{3}$  position can be attributed to an extended superstructure with long range order. Although initial experimentation had led to the belief that electron damage could be the defining factor for the splitting of the LEED spots, further work was carried out by the dynamics group as a continuation of the project discussed in this thesis. This work provides evidence for the formation of an extended superstructure which despite being sensitive to electron damage, does form the structure which displays the spot splitting behaviour. The group do acknowledge that the electron exposure needs to be kept to a minimum in order to reduce the chances of damaging the delicate structure. The observed LEED pattern can be attributed to anti-phase ordering of the commensurate  $(\sqrt{3} \times \sqrt{3})R30^\circ$  water domains and the formation of a large superstructure on Pd(111) as seen previously on other metal substrates, for example Rh(111)<sup>8,9</sup>.

### 4.2.3 Summary of LEED from two chambers

As discussed in Chapter 3, McBride *et al.*<sup>10</sup> compared experimental LEED images to simulations calculated by Dr. George Darling. This data forms an extension to the work I carried out and it is therefore important to be presented here as part of the discussion of the data. In Chapter 3, it was shown the structure formed when water adsorbs on Pd(111) begins to grow at sub-monolayer coverages but it begins to order and sharpen up following saturation of the first layer. As the structure orders, the triangular  $(1/3, 1/3)$  spots split into three individual spots with no intensity remaining in the central position. An additional ring is also observed around the integer order beams and remains visible up to approximately 80 layers. This is in agreement with my original experimentation that showed the triangle of three spots persisted, even for coverages up to 80 layers. This still fits with the model of 3D cluster growth exposing an underlying water layer, as reported previously by Kimmel *et al.*<sup>11</sup> McBride *et al.*<sup>10</sup> carried out further analysis and found that the size of the LEED spots and the ring around the integer order beams leads to the estimation of a coherent oxygen domain size of roughly 80 Å and greater for larger water coverages. Figure 4.14 shows the LEED image including the  $(1/3, 1/3)$  beams and additional features.

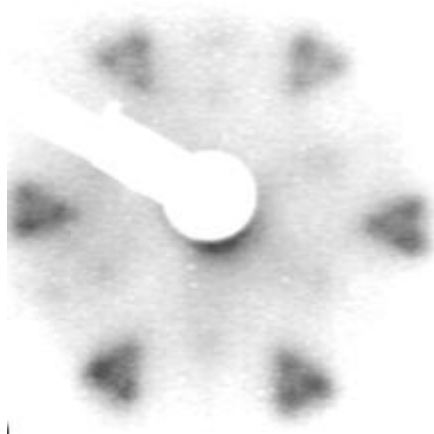


**Figure 4.14<sup>10</sup>:** Low energy electron diffraction pattern for 1.5 layers of water adsorbed on Pd(111) at 140 K. Taken at 53 eV. Reproduced with permission from [F. McBride, A. Omer, C. M. Clay, L. Cummings, G. R. Darling, A. Hodgson *Journal of Physics: Condensed Matter*, 2012, 24, 124102]. Copyright (2012), IOP.

LEED simulations were also shown in Chapter 3 as it becomes difficult to separate the discussion about LEED into clear cut mono- and multi- layer information. It has been shown that the structure begins to form at submonolayer coverages but becomes more ordered once the first layer completes. As the coverage increases, the LEED images remain relatively sharp and detectable for high coverages of water. This is due to the compressed, tightly bound network of oxygen binding to Pd. The LEED pattern remains prominent despite the lack of order in the hydrogen network as determined by HAS and DFT. The values quoted for the change in workfunction upon completion of the first layer of water were discussed in Chapter 3 and a coherent result of  $\Delta\Phi = -0.68 \text{ eV}$  (calculated) and  $\Delta\Phi = -0.70 \text{ eV}$  (experimental) provided evidence for a flat/H-down structure. As the growth mode changes and 3D ice clusters begin to form, the change in workfunction decreases at a slower rate until it saturates and becomes constant at  $\Delta\Phi = -1.06 \text{ eV}$ . For completion, figure 4.15 shows the change in workfunction for completion of the monolayer and continues to show the plateau for multilayer water.

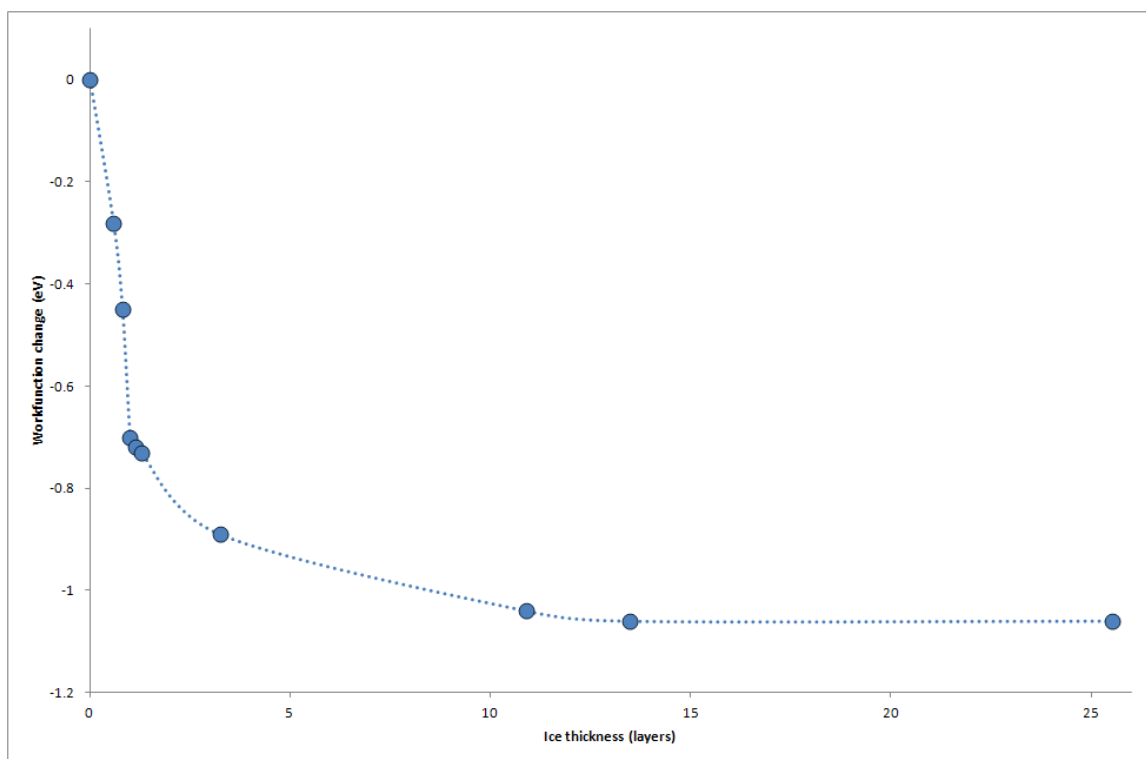


**Figure 4.15:** Change on workfunction ( $\Delta\Phi$ ) as water adsorbs on Pd(111). The saturation of the first layer occurs at  $\Delta\Phi = -0.7 \text{ eV}$  and is discussed in chapter 3.  $\Delta\Phi$  saturates at  $-1.06 \text{ eV}$  between 10 and 13 layers of water.

### 4.3 Chloroform Adsorption and Isothermal Desorption

#### 4.3.1 Introduction

The adsorption of various hydrophobic molecules has been used to probe water overlayers and provide further information about the underlying structure. Such molecules include chlorodifluoromethane ( $\text{CHF}_2\text{Cl}$ )<sup>12</sup>, carbon tetrachloride ( $\text{CCl}_4$ )<sup>13</sup> and chloroform ( $\text{CHCl}_3$ )<sup>14, 15, 12</sup>. Temperature programmed desorption has been used to study the interactions between chloroform and water and initial findings show that  $\text{CHCl}_3$  adsorbs on catalytic metal surfaces at 100 K with no evidence of dissociation<sup>16</sup>. Experiments on Pt(111) show that  $\text{CHCl}_3$  weakly adsorbs to water films by physisorption due to it being a hydrophobic molecule<sup>17</sup>. As the chloroform desorbs it does not dissociate or become incorporated into the bulk. These findings suggest that chloroform is a good molecule for probing the growth of water films on the Pd(111) surface, in contrast to hydrophilic molecules such as  $\text{NH}_3$  which hydrogen bond to water films before dissolving into the bulk as the temperature is increased<sup>18</sup>. In this section, the adsorption of  $\text{CHCl}_3$  on top of amorphous solid water (ASW) and crystalline ice (CI) water films will be investigated on Pd(111).

Previous studies involving multilayer growth of water on Pt (111)<sup>17</sup> have shown that chloroform adsorption/desorption provides a useful means of probing the ice structure and gives an insight into the growth mechanism of ASW and CI. The binding energy of  $\text{CHCl}_3$  adsorbed onto ice depends upon the structure and thickness of the underlying ice. Above a particular thickness, the desorption behaviour of  $\text{CHCl}_3$ , shown by TPD, becomes independent of the ice thickness or structure and a single desorption peak occurs at ~145 K. A single  $\text{CHCl}_3$  peak has previously been observed by Schaff *et al.* for desorption from thick crystalline and amorphous ice structures (~80 layers)<sup>19</sup>. These findings are in agreement with data obtained here for thick layers of ice (>80 layers CI and >2 layers ASW). However, for thinner water films on Pd(111) additional features are observed in the TPD spectra due to the adsorption of  $\text{CHCl}_3$  on the first layer of water and adsorption on the Pd surface as the water multilayer desorbs.

### 4.3.2 Experimental

All of the experiments described in this section were carried out in the same UHV chamber (first chamber) and were not repeated in a second chamber. Chloroform was adsorbed onto the Pd(111) surface by means of an effusive molecular beam after cleaning of the crystal was carried out using argon ion sputter and anneal cycles. Experiments on the clean Pd(111) surface were carried out by cooling the crystal to 100 K before letting the beam into the main chamber and dosing the crystal for a given amount of time. Following adsorption, TPD measurements were carried out as described in section 3.2.2. As described for water adsorption, the coverage of  $\text{CHCl}_3$  on the surface was determined by integrating the area underneath the desorption profile and assigning one monolayer of  $\text{CHCl}_3$  to the onset of multilayer growth. For chloroform adsorption experiments on top of water films grown at 115 K and 140 K, water was dosed as described in section 3.2.2 before the crystal was cooled to 100 K and chloroform was dosed on top of the water film. The coverage of  $\text{CHCl}_3$  used for dosing on top of the water films was just below one monolayer. TPD traces were recorded at a constant ramp rate with the masses for water and chloroform being monitored on the mass spectrometer.

### 4.3.3 Results and Discussion : Chloroform Adsorption

Chloroform was dosed onto clean Pd(111) at 110 K and TPD spectra were recorded for a range of coverages . A low coverage  $\text{CHCl}_3$  peak at  $\sim 185$  K can be attributed to interaction between  $\text{CHCl}_3$  and the surface. This peak saturates and gives a coverage defined arbitrarily as one monolayer. Above saturation, a  $\text{CHCl}_3$  multilayer peak appears at  $\sim 140$  K and continues to grow with increasing coverage (figure 4.16). The structure of ice films was probed by dosing just less than one monolayer of  $\text{CHCl}_3$  (figure 4.17) in order to ensure that multilayer interactions between chloroform molecules do not complicate the system.

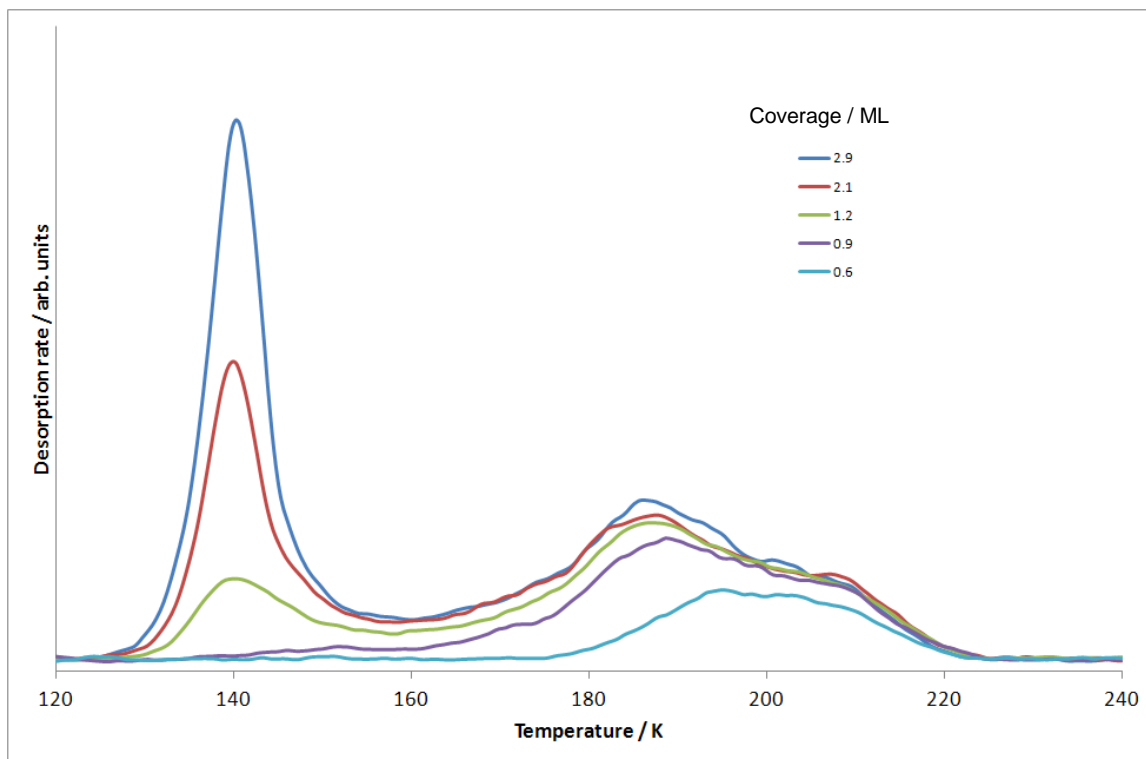


**Figure 4.16:** Chloroform desorption from Pd(111). Submonolayer coverages of  $\text{CHCl}_3$  desorb at 185 K and a multilayer peak grows at 140 K following saturation of the high temperature feature.

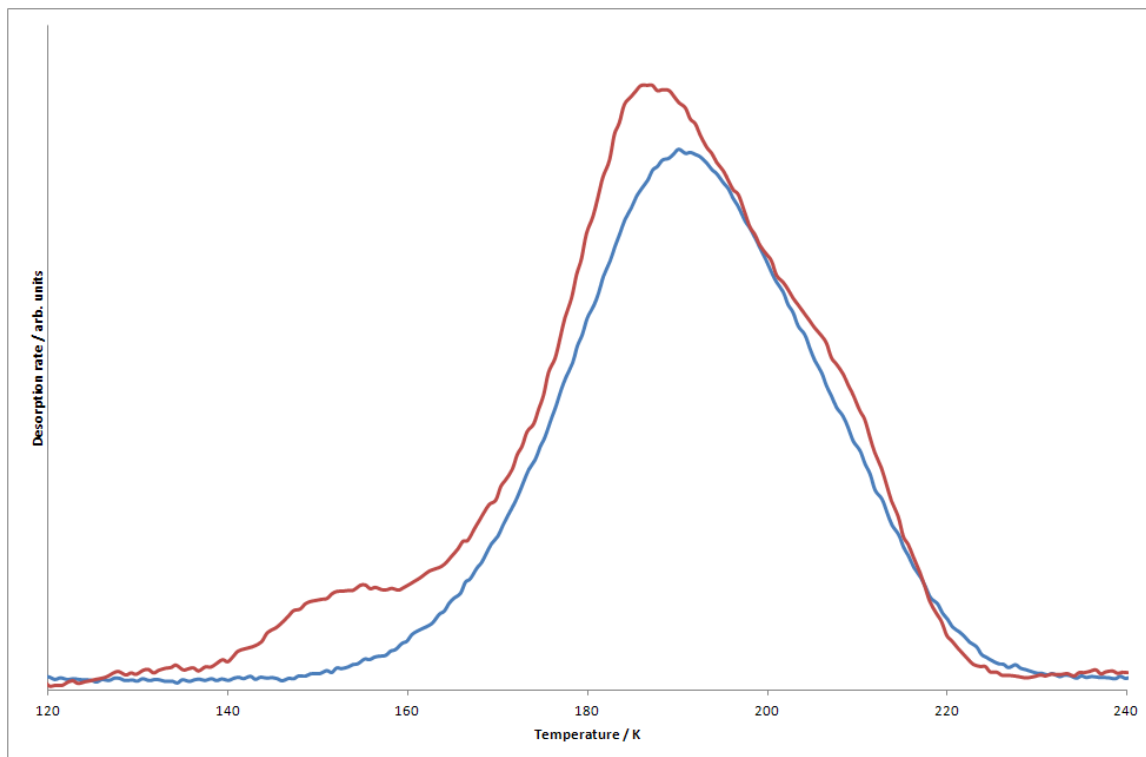


**Figure 4.17:** The blue trace indicates the chloroform dose used for dosing on top of water films. A coverage of just less than one monolayer was used and care was taken to ensure multilayer coverages were not dosed.

ASW was grown on clean Pd(111) at 115 K, where water is not mobile, before cooling the sample to 110 K and dosing it with  $< 1$  ML  $\text{CHCl}_3$ . The  $\text{CHCl}_3$  TPD spectra show three distinguishable peaks at  $\sim 172 - 220$  K, 150 K and 145 K (figure 4.18). The three peaks can be attributed to chloroform desorbing from the Pd(111) surface (170 – 220 K), the first layer of adsorbed water (150 K) and multilayer coverages of water (145 K). Desorption from the water layers occurs at a lower temperature due to the weaker interaction between  $\text{CHCl}_3$  and water molecules in comparison to those between  $\text{CHCl}_3$  and the metal surface. At coverages above approximately 2 layers, the water completely blocks all adsorption sites on the surface and a single peak is observed at 145 K due to desorption from multilayer water. The rapid coverage of the surface suggests more water contact with the metal surface when compared to CI, on which, water forms clusters in preference to complete layers. The desorption behaviour of chloroform described here shows that ASW adsorbs by layer-by-layer growth on Pd(111)

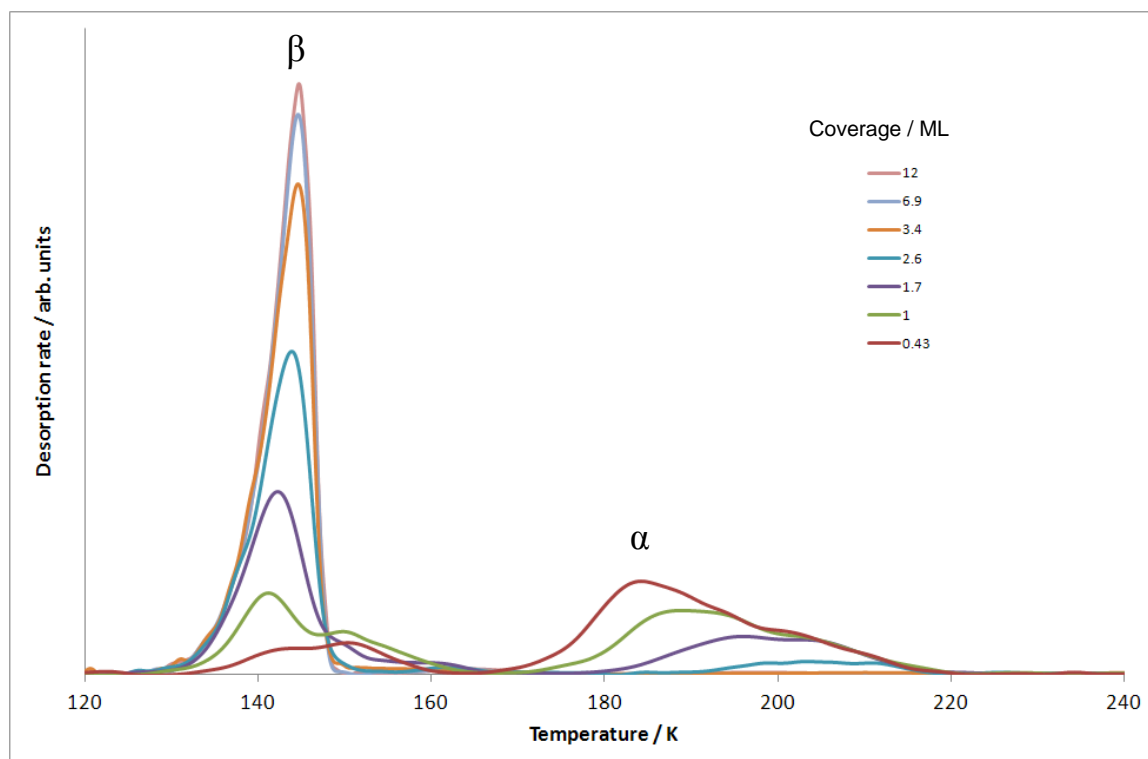


**Figure 4.18:** Chloroform desorption from amorphous solid water films of varying coverage, grown at 115 K. The  $\alpha$  peak is due to water desorbing from the metal surface and diminishes between 2-3 layers of water. The  $\beta$  peak is due to water desorbing from underlying water layers. A small shoulder can be seen on the  $\beta$  peak which is attributed to water desorbing from the first layer of water and also disappears with a coverage of 2 layers of water.

Using the same method as above, layers of crystalline ice were grown at 150 K before being probed with  $\text{CHCl}_3$  at 110 K. TPD spectra again show three peaks at 170 – 220 K, 150 K and 145 K due to chloroform desorption from the Pd(111) surface, the first layer of water and multilayer water respectively (figure 4.19). For coverages up to 10 layers of CI, a broad surface peak can be identified in the same position as  $\text{CHCl}_3$  desorbing from the clean Pd(111) substrate (170 – 220 K). As the adsorption sites become blocked, this peak diminishes and two lower temperature peaks appear due to  $\text{CHCl}_3$  adsorbed on multilayer ice (145 K) and  $\text{CHCl}_3$  adsorbed on the first layer of water (150 K). As the water coverage increases, the relative proportion of these two peaks changes and at water coverages above ~80 layers the smaller peak disappears, leaving a single peak at 145 K. The desorption behaviour discussed here shows a difference in growth mode between ASW and CI with ASW following a layer-by-layer growth mode whereas CI displays Stranski-Krastonov growth characteristics. These results provide additional support for the conclusions of the LEED experiments and suggest that cluster formation occurs, as the metal surface remains exposed for high coverages enabling  $\text{CHCl}_3$  to interact with the first layer.

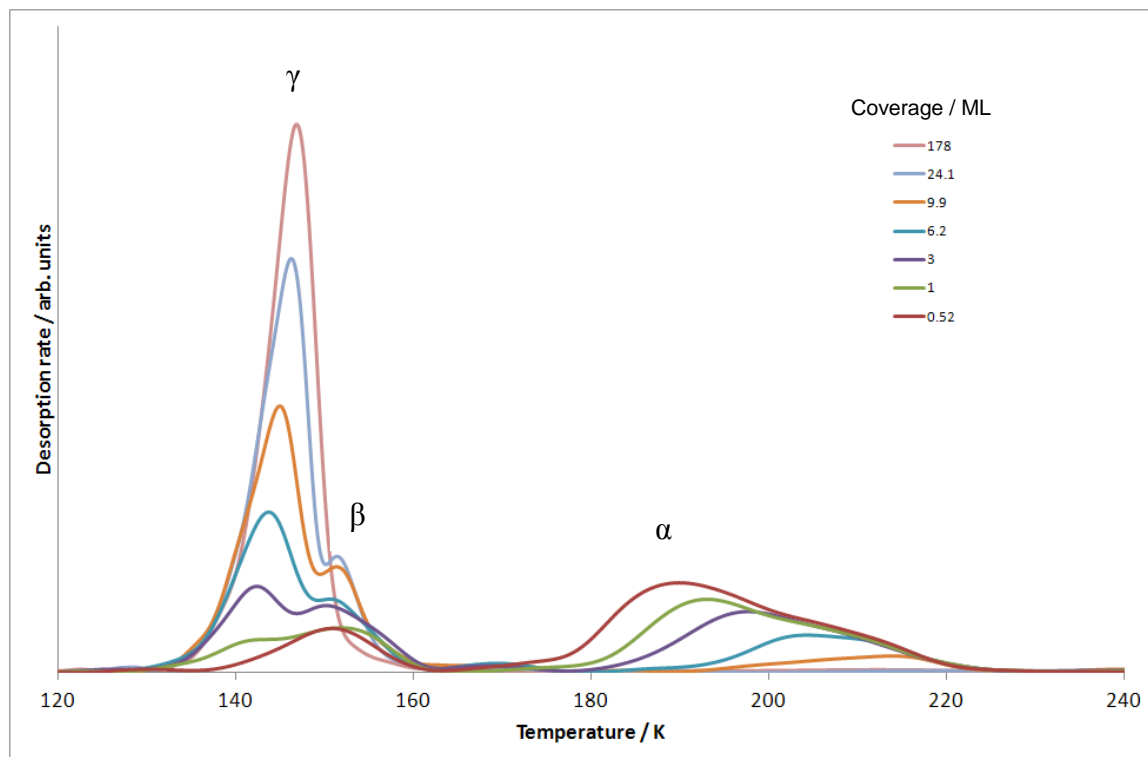


**Figure 4.19:** Chloroform desorption from crystalline ice layers of varying coverage, grown at 140 K. The  $\alpha$  peak is due to water desorbing from the metal surface and is observed for up to 10 layers of water. The  $\beta$  peak is due to water desorbing from the first monolayer of ice and exists for up to 80 layers of water. The  $\gamma$  peak grows with increasing coverage and is due to water adsorbed on multilayer ice. As the surface desorption sites become blocked, this peak becomes the only feature in the desorption profiles for coverages of ice exceeding 80 layers.

The water TPD characteristics change when  $\text{CHCl}_3$  is dosed on top of water films grown either at 115 K or 150 K.  $\text{CHCl}_3$  desorbs from the bare monolayer and water multilayer at 145 – 150 K. At low water coverages, a desorption peak appears at 160 K, as opposed to 175 K seen for the monolayer desorbing from clean Pd(111) without  $\text{CHCl}_3$  adsorbed on top. This peak is saturated and is followed by the appearance of a second peak at 165 – 170 K that continues to grow and shift to higher temperature with increased coverage, eventually masking the lower temperature peak. These features indicate significant differences in the desorption kinetics as compared to, for example Pt(111) where the water TPD remained unchanged with  $\text{CHCl}_3$  exposure<sup>17</sup>. The changes seen in the water TPD suggest that there is no bare metal visible to the chloroform, however,  $\text{CHCl}_3$

reaches the surface as the water desorbs, causing the water films to reconstruct and form large clusters reducing the desorption rate. This could be due to the fact that  $\text{CHCl}_3$  permeates through to the metal surface and preferentially occupies metal adsorption sites, resulting in the formation of large water clusters on the surface. As the size of water clusters increase, the surface area is reduced and the water desorption rate drops. The increase in the maximum desorption temperature for the water multilayer is most likely due to the restructuring that occurs during the simultaneous desorption of water and chloroform. The traces shown in figures 4.20 and 4.21 were recorded simultaneously with chloroform desorption.

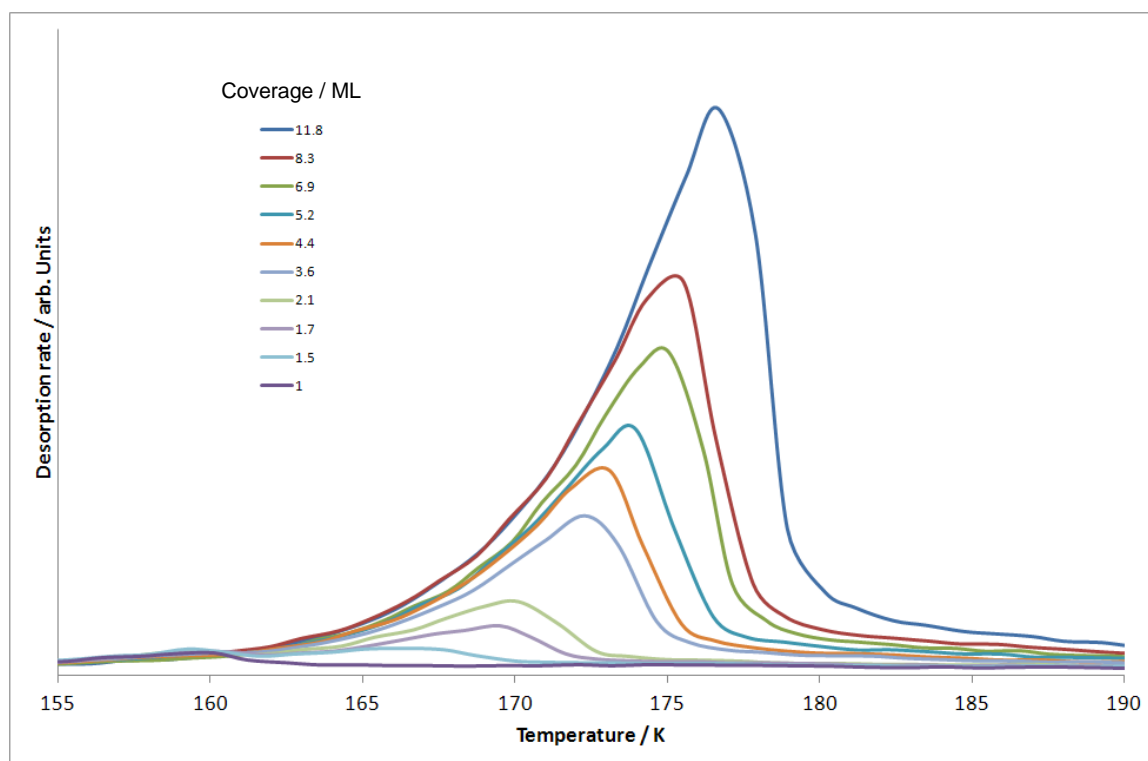


**Figure 4.20:** Water desorption from Pd(111) after chloroform desorption experiments. The water monolayer desorbs at 160 K; 15 K lower than water desorption from the sample without probing with chloroform. At the point of saturating this peak, the multilayer grows at a similar temperature as seen previously (165 K) and continues to grow with increasing water coverage. Desorption recorded simultaneously with chloroform desorption.

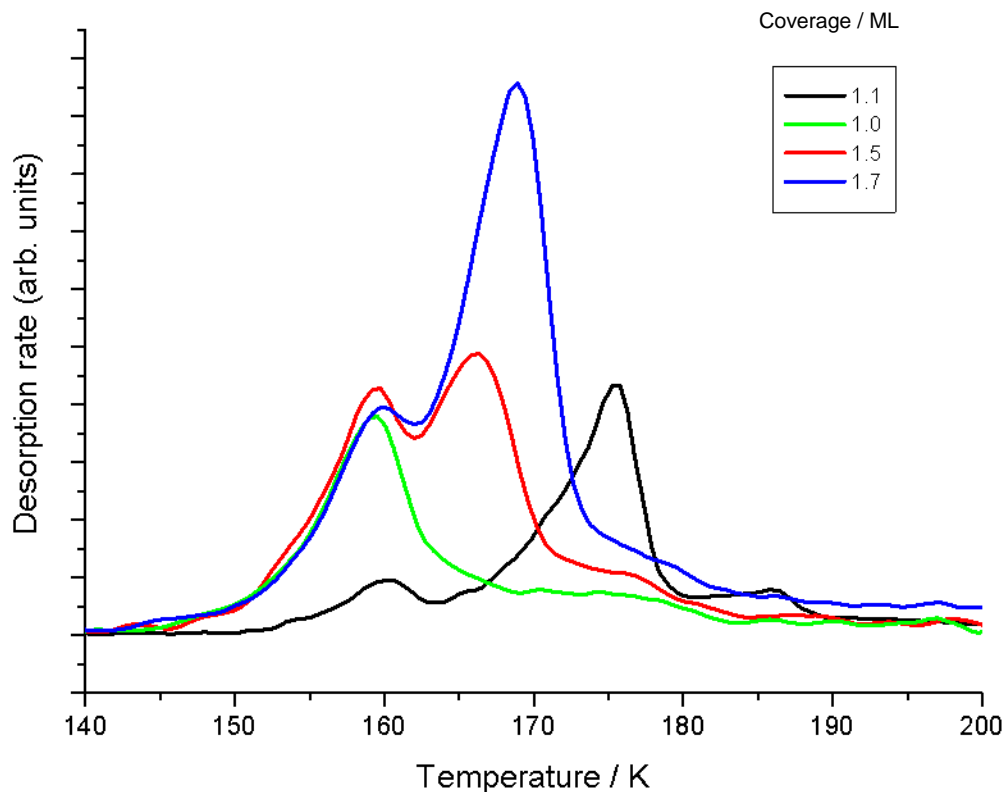


**Figure 4.21:** Water desorption from Pd(111) after chloroform desorption experiments. The water monolayer desorbs at 160 K; 15 K lower than water desorption from the sample without probing with chloroform (black trace). At the point of saturating this peak, the multilayer grows at a similar temperature as seen previously (165 K) and continues to grow with increasing water coverage. These traces are taken from figure 4.20 to show the desorption peaks more clearly.

If the water multilayer formed on Pd(111) as a wetting layer followed by 3-D cluster growth then this would be apparent in the desorption kinetics. To probe this, isothermal desorption experiments were performed to determine how the desorption rate changed with film thickness. Zero-order desorption kinetics would be expected for water grown in layers with a constant surface area but previous studies have found that water shows non-zero desorption kinetics. A study by Smith *et al.* reports the differences in isothermal desorption of 56 layers of ASW from Ru(001) and Au(111)<sup>20, 21</sup>. Initially, the desorption rate rapidly increases followed by a decrease to approximately half the rate and at this

point the desorption kinetics differ depending on the hydrophilicity of the metal substrate. Au(111) wavers further from zero-order kinetics than Ru(001) due to its hydrophobic nature causing non-wetting behaviour.

On Pd(111) ASW of 30 – 120 layers was grown at 115 K before the surface was heated to 165 K and held at this temperature. An initial rapid increase in desorption rate was observed due to the sharp increase in temperature. This was followed by an immediate decrease in desorption rate as crystallisation of the ASW occurred. Following this phase transition the desorption rate then began to plateau as the multilayer desorbed, before slowly reducing back to the base level due to sublimation of the water film. This behaviour can be associated with a non-wetting mechanism and the formation of ice clusters. The three stages observed in the isothermal desorption spectra have previously been reported and categorised as the phase transition, plateau and droplet regions respectively<sup>22</sup>. Zero-order desorption kinetics would show a constant desorption rate in the plateau region of the isothermal desorption spectra and for situations involving submonolayer growth, the plateau region would not exist, with the trace going from transition phase directly to the droplet region.

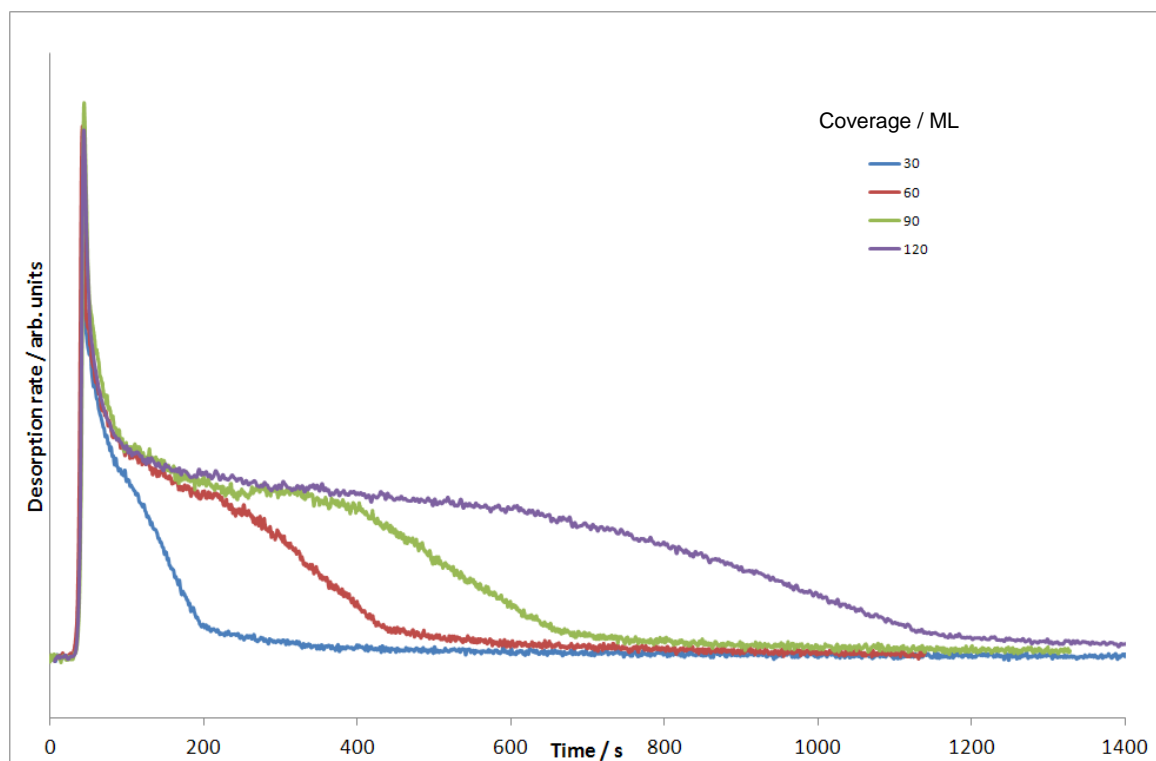


**Figure 4.22:** Isothermal desorption profiles for 30 – 120 layers of water grown at 115 K. Crystallisation of the water occurs before the multilayer desorbs followed by sublimation of the water film. This behaviour suggests that water does not wet by layer-by-layer growth, instead islands of ice clusters form.

#### 4.4 Helium atom scattering

HAS was also carried out on multilayer water and at the point where the first layer saturates the specular peak disappears completely. Figure 4.23 shows two traces for helium atom scattering from water dosed at just less than saturation point (0.98 ML) and just above saturation point (1.2 ML). As the water layer comes close to saturation the specular reflectivity is of weak intensity with a maximum value of approximately 700 counts/second (the data for this peak is shown on the same axis as the second data set and therefore all values have been increased by 1000 cps).

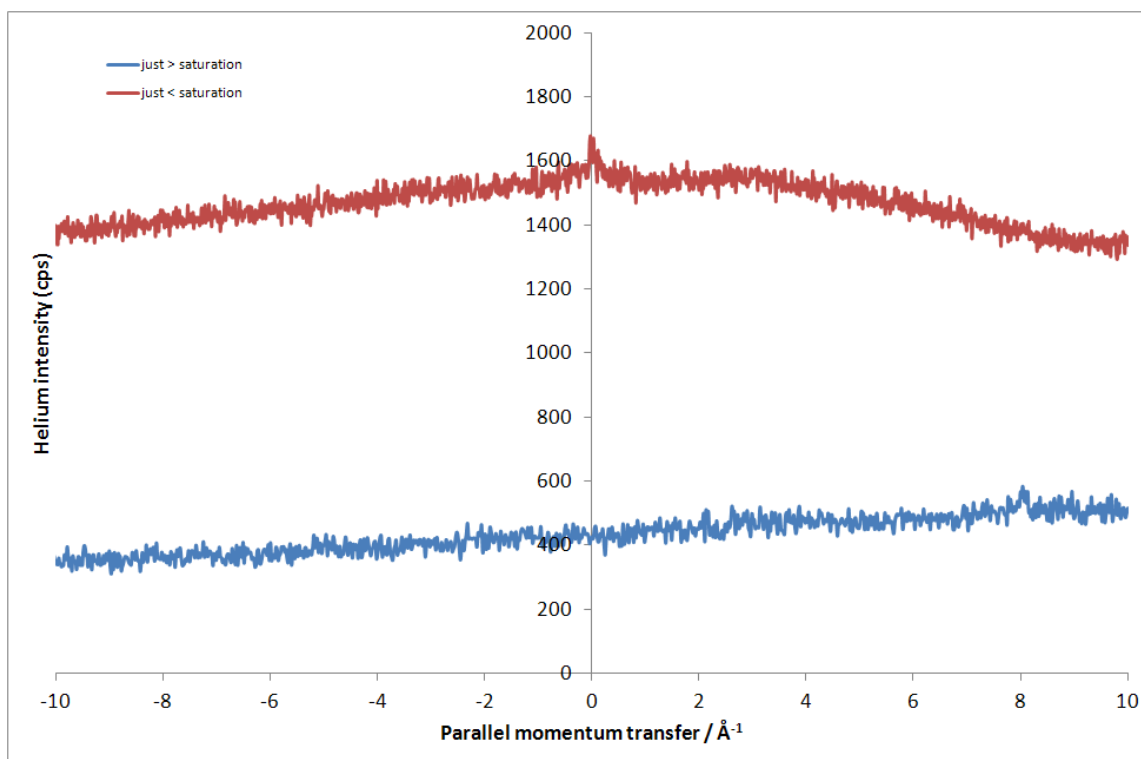


**Figure 4.23:** Helium atom scattering from multilayer water grown at 140 K. The intensity of the specular reflectivity peak is weak with a maximum of 700 counts/second. Two weak side bands appear at  $\pm 3 \text{ \AA}^{-1}$  with a maximum reflectivity just above the noise level. This image was taken just as the multilayer began to grow but the specular peak completely disappeared as the coverage was increased further.

As discussed in chapter 3, sharp, narrow features can be expected in helium atom scattering spectra for ordered structures. However, at the point where the first layer of water saturates on Pd(111) and the multilayer begins to grow, the specular peak disappears completely and there are no distinguishable features as shown by the blue trace in figure 4.23. This data shows the sensitivity of HAS and clearly highlights a change in growth mode at the point of monolayer saturation.

This suggests disorder in the overlayer and full coverage of the surface layer. However, this unusual result was unexpected and was repeated by McBride who recorded the same results as discussed here<sup>10</sup>. It has been shown that LEED is sensitive to the positions of O and Pd and it has been predicted that an O-ordered superstructure exists with a size of up to and in excess of 80 Å. HAS on the other-hand, is sensitive to the corrugation of the

surface layer including the positioning of hydrogen atoms. As water adsorbs onto the Pd(111) surface, the intense specular peak reduces in intensity until it completely disappears – this behaviour can be attributed to local disorder in the orientation of hydrogen. This indicates that the first layer of water adsorbs flat and is tightly bound to the metal substrate giving rise to the  $(\sqrt{3} \times \sqrt{3})R30^\circ$  LEED image. However, disorder in the hydrogen network leads to a diminished helium reflectivity which is completely masked during multilayer water growth. Heating and desorbing the multilayer water reveals the He specular peak confirming that the initial single layer of water does adsorb intact on Pd(111). This provides evidence to show that the underlying structure does not change as the multilayer grows, instead it stabilises growth.

Gibson *et al.* carried out HAS experiments for water layers on Rh(111) and find that as water multilayers are grown, the peaks associated with the  $(\sqrt{3} \times \sqrt{3})R30^\circ$  structure begin to diminish<sup>23</sup>. This occurs gradually, unlike the trend seen here for Pd(111) which shows no distinguishable peaks for multilayer water growth.

In addition to repeating the HAS carried out on submonolayer and multilayer water, McBride also carried out HAS experiments on the mixed OH/water layer for comparison. In contrast to the behaviour observed on multilayer water, the HAS shows intense high order diffraction peaks indicative of a highly corrugated and well ordered commensurate structure. This data supports the work presented in Chapter 5 which shows that the mixed OH/water phase adopts a coplanar hexagonal  $(\sqrt{3} \times \sqrt{3})R30^\circ$  structure. A hydrogen bonded network forms with one hydrogen between each oxygen atom giving rise to a sharp LEED pattern with no evidence for the formation of an extended superstructure. Formation of this phase will be discussed in greater detail in Chapter 5. The HAS spectrum recorded by McBride is shown in figure 4.24.

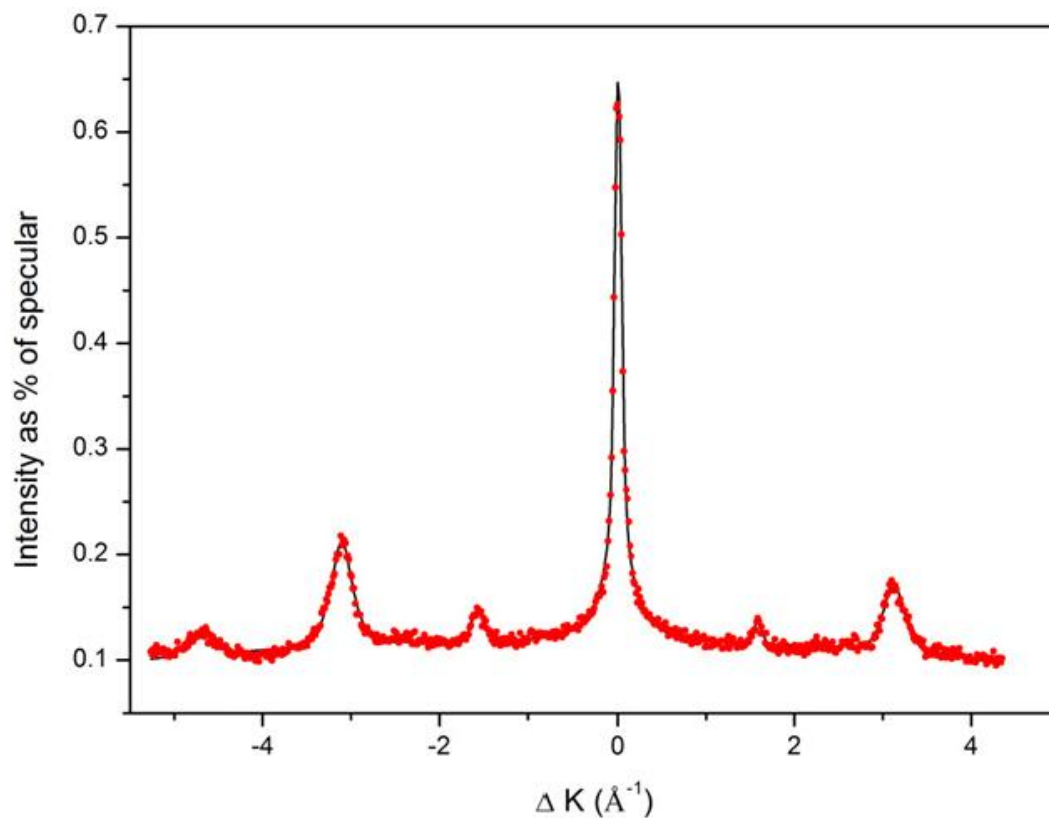


**Figure 4.24<sup>10</sup>:** Helium atom scattering from a complete  $(\sqrt{3} \times \sqrt{3})R30^\circ$  mixed OH/water layer. Reproduced with permission from [F. McBride, A. Omer, C. M. Clay, L. Cummings, G. R. Darling, A. Hodgson *Journal of Physics: Condensed Matter*, 2012, 24, 124102]. Copyright (2012), IOP.

#### 4.4 Concluding remarks

Various surface analytical techniques have been used to determine how multilayer water adsorbs on Pd(111). TPD experiments initially indicated multilayer growth due to the saturation of a high temperature desorption peak at 175 K followed by the growth of a lower temperature feature at 165 K which did not saturate with increasing coverage. Early LEED images in the first vacuum chamber showed a commensurate  $(\sqrt{3} \times \sqrt{3})R30^\circ$  structure as predicted for wetting via layer-by-layer growth. Further investigation found that compression of the water structure caused a change in LEED pattern resulting in inward pointing triangles forming in the  $\sqrt{3}$  positions. This has been attributed to the formation of domain boundaries as the water structure compresses to accommodate more water molecules at the onset of multilayer growth. In order for a  $(\sqrt{3} \times \sqrt{3})R30^\circ$  structure to form on Pd(111), 5.4% compression of the lateral spacing on the close packed face would be required to match the spacing of hexagonal ice and therefore it was not a surprising result not to see layer-by-layer growth. The LEED pattern also presented additional features in the form of a diffuse ring around the (0,0) beam and a ring around the half-order positions. LEED simulations were produced to account for these additional features and predicted many models. The most favourable were a  $(7 \times 7)$  structure and a structure with  $(\sqrt{52} \times \sqrt{52})R14^\circ$  periodicity, the latter being the most stable. The predicted structures have a change in workfunction close to the experimental value of  $\Delta\Phi = -0.7$  eV and therefore lead to the hypothesis of a flat/H-down water network. The first layer is compressed and stabilise the growth of 3D ice clusters in the multilayer.

HAS and TPD experiments show that hydrogen affects the growth mechanism and may be responsible for the additional shoulder present in TPD traces. In addition, electron damage comes into play when studying the delicate overlayer with electron induced restructuring of adsorbed water. This was evident in the LEED images with spot splitting occurring in the  $\sqrt{3}$  position during electron exposure. This splitting occurred over time with electron energy incident on the sample during experiments carried out in the first

vacuum chamber. Further confirmation was provided in TPD spectra recorded after LEED experiments, showing a significant high temperature peak which could be attributed to a change in structure or electron induced dissociation. However, minimising electron damage by using a low current LEED system in a second vacuum chamber still shows us the spot splitting in the LEED images and these images are reproducible. This implies that the LEED pattern recorded is due to the extended superstructure growing following completion of the first layer of water rather than electron damage. The oxygen forms a tightly bound network with Pd, enabling the structure to accommodate more water. The first layer remains intact and can be detected even for 80 layers of water.

The data presented in chapters 3 and 4 tells us that water adsorption on Pd(111) does not proceed via simple layer-by-layer growth and formation of a simple commensurate structure. Instead, qualities of SK growth are apparent with evidence pointing towards 3D ice cluster growth. This correlates well with previous studies carried out by STM and DFT as discussed in detail in the text. Water adsorbs atop Pd with areas of flat water which have  $(\sqrt{3} \times \sqrt{3})R30^\circ$  periodicity. These commensurate flat water sections are separated by anti-phase domain boundaries which act to relieve strain between the clusters. Rings of water attach for multilayer growth and consist of a weakly bound hydrogen network in a mostly H-down configuration. The oxygen atoms are found to bind more strongly to Pd and present order in the LEED images. However, HAS reveals a high level of disorder on a local scale which results in a lack of any features other in the HAS spectra other than the background reflectivity.

#### 4.6 References

1. T. Schiros, S. Haq, H. Ogasawara, O. Takahashi, H. Ostrom, K. Andersson, L. G. M. Pettersson, A. Hodgson and A. Nilsson, *Chemical Physics Letters*, 2006, **429**, 415-419.
2. X. L. Zhou, P. M. Blass, B. E. Koel and J. M. White, *Surface Science*, 1992, **271**, 427-451.
3. Z. J. Li, P. Cloutier, L. Sanche and J. R. Wagner, *Journal of the American Chemical Society*, 2010, **132**, 5422-5427.
4. Y. Zheng and L. Sanche, *Journal of Chemical Physics*, 2010, **133**, 155104.
5. M. Michaud, A. Wen and L. Sanche, *Radiation Research*, 2003, **159**, 3-22.
6. W. C. Simpson, T. M. Orlando, L. Parenteau, K. Nagesha and L. Sanche, *Journal of Chemical Physics*, 1998, **108**, 5027-5034.
7. M. Vinodkumar, K. N. Joshipura, C. G. Limbachiya and B. K. Antony, *Nuclear Instruments and Methods in Physics Research Section B: Beam Interactions with Materials and Atoms*, 2003, **212**, 63-66.
8. A. Beniya, Y. Sakaguchi, T. Narushima, K. Mukai, Y. Yamashita, S. Yoshimoto and J. Yoshinobu, *Journal of Chemical Physics*, 2009, **130**, 034706.
9. A. Beniya, S. Yamamoto, K. Mukai, Y. Yamashita and J. Yoshinobu, *Journal of Chemical Physics*, 2006, **125**, 054717.
10. F. McBride, A. Omer, C. M. Clay, L. Cummings, G. R. Darling, A. Hodgson, *Journal of Physics: Condensed Matter*, 2012, **24**, 124102.
11. G. A. Kimmel, N. G. Petrik, Z Dohnalek, B. D. Kay , *Journal of Chemical Physics*, 2007, **126**, 114702.
12. D. J. Safarik, R. J. Meyer and C. B. Mullins, *Journal of Chemical Physics*, 2003, **118**, 4660-4671.
13. C. Clay and A. Hodgson, *Current Opinion in Solid State & Materials Science*, 2005, **9**, 11-18.
14. G. Held and D. Menzel, *Surface Science*, 1995, **327**, 301-320.
15. V. Sadtchenko, K. Knutsen, C. F. Giese and W. R. Gentry, *Journal of Physical Chemistry B*, 2000, **104**, 2511-2521.

16. F. Fournier, H. Dubost, S. Carrez, W. Q. Zheng and B. Bourguignon, *Journal of Chemical Physics*, 2005, **123**, 184705.
17. G. Zimbitas and A. Hodgson, *Chemical Physics Letters*, 2006, **417**, 1-5.
18. H. Ogasawara, N. Horimoto and M. Kawai, *Journal of Chemical Physics*, 2000, **112**, 8229-8232.
19. J. E. Schaff and J. T. Roberts, *Surface Science*, 1999, **426**, 384-394.
20. J. A. Smith, F. E. Livingston and S. M. George, *Journal of Physical Chemistry B*, 2003, **107**, 3871-3877.
21. R. S. Smith, C. Huang, E. K. L. Wong and B. D. Kay, *Surface Science*, 1996, **367**, L13-L18.
22. P. Lofgren, P. Ahlstrom, J. Lausma, B. Kasemo and D. Chakarov, *Langmuir*, 2003, **19**, 265-274.
23. K. D. Gibson, D. R. Killelea and S. J. Sibener, *Journal of Physical Chemistry C*, 2009, **113**, 13325-13330.

## **Chapter 5**

### **Mixed OH/water structures on Pd(111)**

## 5. Mixed OH/water structures on Pd(111) <sup>1</sup>

### 5.1 Introduction to the paper

This chapter includes a paper published in the journal *Surface Science*, on which I am the second author. I was present in the lab during all data capture and actively involved in analysis and discussions about the data. The experimental data were obtained by myself and Chris Clay. Some of the experiments were carried out individually by me along with the data analysis and construction of figures for the paper:

- Water adsorption experiments carried out individually and with Chris Clay
- Mixed OH/water and LEED experiments were combined with those carried out by Chris Clay and many were carried out together
- CO titrations were carried out individually and data was combined with those carried out by Chris Clay
- Hydrogen experiments were carried out individually by me and I analysed the data to construct figure 5.5 and provide the explanation surrounding the figure given in the paper
- As the work presented here was carried out during the beginning of the project, there is no available data for multilayers but this would be recommended for the group in the future

The details from the paper are inserted exactly as found in the publication, however the headings and figures are labelled in-line with the numbering system used throughout this thesis.

Reprinted from C. Clay, L. Cummings and A. Hodgson, *Surface Science*, 2007, 601, 562-568, Copyright (2007), with permission from Elsevier.

## 5.2 Mixed water/OH structures on Pd(111)

### 5.2.1 Abstract

Chemisorbed O and water react on Pd(111) at low temperatures to form a mixed OH/H<sub>2</sub>O layer with a  $(\sqrt{3} \times \sqrt{3})R30^\circ$  registry. Reaction requires at least two water molecules to each O before the  $(2 \times 2)O$  islands are consumed, the most stable OH/water structure being a  $(OH + H_2O)$  layer containing 0.67 ML of oxygen, formed by the reaction  $3H_2O + O \rightarrow 2(H_2O + OH)$ . This structure is stabilised compared to pure water structures, decomposing at 190 K as OH recombines and water desorbs. The  $(\sqrt{3} \times \sqrt{3})R30^\circ - (OH + H_2O)$  phase cannot be formed by O/H reaction and is distinct from the  $(\sqrt{3} \times \sqrt{3})R30^\circ$  structure formed by O/H coadsorption below 200 K. Mixed OH/water structures do not react with coadsorbed H below 190 K on Pd(111), preventing this phase catalyzing the low temperature  $H_2/O_2$  reaction which only occurs at higher temperatures.

### 5.2.2 Introduction

Understanding the inter-conversion of oxygen, hydrogen, water and hydroxyl overlayers at metal surfaces is integral to unravelling the processes underpinning the  $H_2/O_2$  fuel cell reaction and related heterogeneous catalytic redox reactions. Despite substantial theoretical and experimental efforts, the fragile nature of the hydrogen bond and the comparative strength of the water–water and water–metal interaction <sup>2</sup> have led to considerable difficulties in understanding water adsorption <sup>3</sup>, or in distinguishing OH from water in thin film studies <sup>4</sup>. Hydrogen bonding complicates the use of vibrational spectroscopy, and although electron and X-ray based spectroscopies can distinguish OH from H<sub>2</sub>O, care is needed to avoid electron damage <sup>5</sup>. Depending on the growth conditions and reactivity of the metal, water may either wet metal surfaces, forming two dimensional ices with a complete hydrogen bond network, form non-wetting clusters, or

dissociate to form hydroxyl, hydrogen and possibly oxygen on the surface<sup>2-4, 6</sup>. As a result of this complexity, the characterisation of OH and OH/water structures lags behind our understanding of many other reaction systems. Recently theoretical calculations have suggested that the intermediate in the water–oxygen reaction on Pt(111) is a mixed OH/H<sub>2</sub>O structure, stabilised by formation of a hydrogen bonding network between OH and water<sup>7-9</sup>. This structure was initially attributed to a pure hydroxyl overlayer<sup>10</sup>, but recent experiments confirm that a stable mixed (OH + H<sub>2</sub>O) phase is formed<sup>11</sup> and that this structure is consistent with the intermediates identified in the H<sub>2</sub>/O<sub>2</sub> and O/water reactions on Pt(111)<sup>12, 13</sup>. This phase has a hexagonal ( $\sqrt{3} \times \sqrt{3}$ )R30° – O backbone<sup>12</sup>, each (OH + H<sub>2</sub>O) species having three hydrogen bonds, and is stable up to ~210 K<sup>11</sup>. A partially dissociated (OH/H<sub>2</sub>O/H) phase is believed to form on Ru(0001)<sup>5, 14, 15</sup> and mixed OH/water structures have also been reported on f.c.c. (110) metal surfaces<sup>6</sup>.

The water formation reaction occurs above 220 K on Pd(111)<sup>16</sup> following the reaction of a (2 × 2) oxygen overlayer with hydrogen. Reaction to form water is a two step process<sup>17</sup>,



with water desorbing from the surface at these temperatures. Molecular beam experiments concluded that the rate limiting step is the addition of hydrogen to oxygen to form hydroxyl<sup>17</sup>, Eq. (5.1). STM images show a (2 × 2) oxygen overlayer rearranging into a compressed ( $\sqrt{3} \times \sqrt{3}$ )R30° structure when hydrogen is adsorbed at temperatures below 200 K<sup>18</sup>. As the crystal is heated above 200 K hydrogen desorbs, or goes sub-surface, and the (2 × 2)O overlayer reappears. As no change is observed in the total coverage of oxygen, the  $\sqrt{3}$  phase is believed to be a coadsorbed O/H structure, rather than OH, since addition of hydrogen to hydroxyl was thought to be fast and immediately leads to water desorption<sup>17</sup>. Only if the surface is heated above 220 K in the presence of a hydrogen atmosphere do oxygen and hydrogen react at the surface, water immediately

desorbing from the Pd(111) <sup>16</sup>. In contrast when oxygen and water are coadsorbed on Pd(111) a new high temperature peak appears in the thermal desorption spectrum <sup>19, 20</sup> and this was attributed to a hydroxyl overlayer by analogy with Pt(111) <sup>10</sup>, although this phase was not fully characterised.

In this paper, we investigate the reaction between O and water and the stability of OH/H<sub>2</sub>O structures formed on Pd(111). A( $\sqrt{3} \times \sqrt{3}$ )R30° – (OH + H<sub>2</sub>O) structure is formed which decomposes 20 K above the temperature at which water desorbs. We explore how the stability of this phase depends on its composition and show that reaction is consistent with formation of a mixed (OH + H<sub>2</sub>O) structure containing  $\frac{2}{3}$  ML of oxygen. Finally we show that the OH/H<sub>2</sub>O phase is un-reactive towards hydrogen, with the result that this structure cannot catalyse low temperature reaction of H<sub>2</sub> and O<sub>2</sub> to form water. This behaviour is consistent with low temperature H<sub>2</sub>/O<sub>2</sub> reaction occurring on Pt(111) but not on Pd(111) <sup>16</sup>.

### 5.2.3. Experimental

Experiments were performed in an ultra high vacuum (UHV) chamber with a total background pressure of less than  $1 \times 10^{-10}$  mbar, equipped with a quadrupole mass spectrometer (QMS), low energy electron diffraction (LEED) optics and a two stage differentially pump molecular beam, the details of which are described elsewhere. A Pd(111) crystal was spot welded to two wires and mounted on Ta posts which fed directly in to a liquid nitrogen cooled manipulator. The crystal could be rapidly heated and cooled between 100 and 1100 K by resistively heating the support wires, allowing the desorption of products to be monitored accurately during temperature programmed desorption (TPD). The surface was cleaned by repeated sputter and annealing cycles at 1100 K. Gases were dosed using a thermal, effusive molecular beam to provide accurate control of the surface coverage. Above 210 K molecular oxygen dissociates on Pd(111) forming atomic oxygen with a saturation coverage of 0.25 ML at 323 K <sup>21</sup> and a sharp (2 x 2) LEED pattern. The coverage of atomic oxygen was determined by CO titration at

273 K, using the beam to deposit CO and detecting the CO<sub>2</sub> product. This signal was calibrated against saturation coverage of the (2 x 2)O layer and was repeatable to  $\pm 2\%$ . Disordered atomic oxygen overlayers were formed by limiting the annealing temperature to 210 K. Saturating the Pd(111) surface with molecular oxygen at 110 K and heating above 210 K gave rise to a surface with the same O coverage as formed by O<sub>2</sub> dissociation at 323 K. Water was adsorbed at temperatures above 143 K on the clean Pd(111) surface, just below the desorption peak of a water multilayer, Fig. 5.1, to form an ordered ice monolayer. On the oxygen covered surface the adsorption temperature was increased to 170 K, allowing the OH/H<sub>2</sub>O phase to form but preventing water adsorption on the bare metal. TPD was used to follow the development of water and mixed OH/water films. The water coverage was calculated from the desorption integral of the saturated monolayer peak and calibrated against completion of the  $(\sqrt{3} \times \sqrt{3})R30^\circ - 2H_2O$  LEED pattern at 0.67 ML. The stoichiometry of the O/H<sub>2</sub>O reaction was also investigated by following the reaction between chemisorbed <sup>16</sup>O and H<sub>2</sub> <sup>18</sup>O (Isotek 95% (18)O). Oxygen 16/18 exchange could be seen in the water decomposition products, while the isotope ratio of the chemisorbed O left on the surface was determined from CO titration using the mass 44 and 46 peaks. The latter provides an unambiguous measure of O exchange between chemisorbed O and water. Throughout the paper the term OH<sub>x</sub> is used to specify the total oxygen, OH and water coverage adsorbed at the metal.

#### 5.2.4. Results

When water is adsorbed on clean Pd(111) at 143 K the temperature programmed desorption profile shows a stabilised monolayer which desorbs near 175 K, Fig. 5.1a, with a multilayer peak forming at lower temperature as the coverage is increased, Fig. 5.1b. Multilayer water desorbs at a lower temperature than the monolayer since the increased hydrogen bonding in water multilayers is insufficient to compensate the favourable water-metal interaction. This behaviour is consistent with that reported earlier and similar to that seen on other metal surfaces which form a stable wetting layer<sup>22</sup>. A shoulder appears on the trailing edge of the monolayer peak near 180 K and becomes

more prominent as the coverage exceeds 1 ML, eventually developing into a tail to the desorption profile for thicker films (Fig. 5.1b). Multilayer water does not wet the first ice layer on Pd(111), forming 3D clusters and regions of bare monolayer<sup>23</sup>, and we attribute this shoulder to formation of clusters. The TPD shoulder could be suppressed for coverages below 0.67 ML water by carefully optimising the adsorption conditions, consistent with kinetic effects influencing the growth of small 3D ice clusters. The structure and growth morphology of the pure water multilayer will be discussed further in a future publication<sup>24</sup>. The TPD profile shows no indication of a high temperature water desorption peak, such as seen near 210 K on Ru(000 1) and other reactive surfaces, associated with partial dissociation to form a mixed H/OH/H<sub>2</sub>O phase<sup>25</sup>. Adsorption of the first monolayer of water gives an intense  $(\sqrt{3} \times \sqrt{3})R30^\circ$  pattern as the coverage reaches 0.67 ML, again in agreement with previous studies<sup>20</sup>, and with STM images which show ordered hexagonal water networks forming at low temperature<sup>26</sup>.

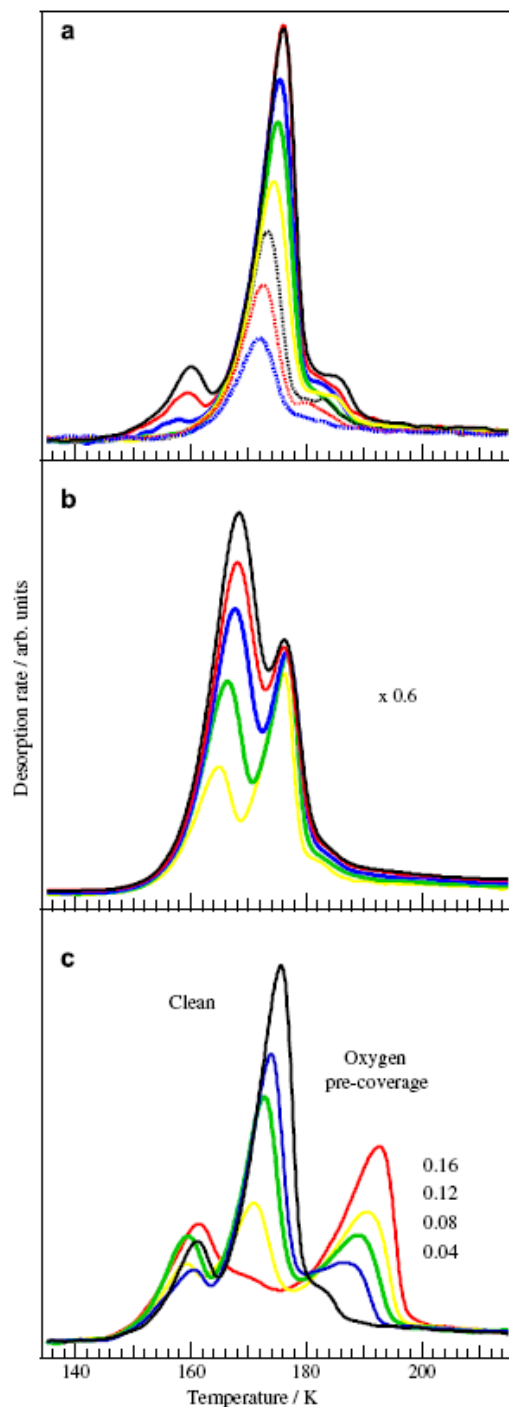


**Figure 5.1** a) Desorption of water from Pd(111) after growth of an ordered ice film at 150 K showing the monolayer peak near 175 K and initial stages of growth of the multilayer peak, ~158 K, for a coverage of 0.17, 0.26, 0.35, 0.44, 0.52, 0.61, 0.70, 0.79 ML.  
 b) Multilayer TPD of 1.0, 1.3, 1.5, 1.7 and 1.9 ML water.  
 c) TPD spectrum of H<sub>2</sub>O following the adsorption of water (0.70-0.80 ML) onto clean and O pre-covered Pd(111) at 143 K. As the total oxygen coverage is increased towards 0.16 ML the intact water monolayer peak near 176 K disappears and water desorbs from a multilayer peak or from the mixed OH/H<sub>2</sub>O phase near 193 K. Heating rate 2 K s<sup>-1</sup>.

Water adsorption can be stabilised by as much as 20 K compared to the monolayer peak by pre-dosing the Pd(111) surface with atomic oxygen, Fig. 5.1c. As the oxygen coverage is increased the monolayer desorption peak drops in intensity and a new peak grows at higher temperature. The monolayer peak disappears completely as the high temperature peak saturates and the new phase completely covers the Pd(111) surface. In all further discussions the TPD peak arising from the reaction of oxygen and water near 190 K will be termed the mixed OH/H<sub>2</sub>O peak for clarity, justification for this is given below. Molecular beam uptake and CO titration experiments indicate that the total atomic oxygen coverage required to completely remove the monolayer water peak is 0.17 ML, the peak saturating with a total OH<sub>x</sub> coverage of  $(0.67 \pm 0.04)$  ML. Altering the composition of the first layer changes the stability and growth of subsequent water multilayers, as seen by the variation in the position of the multilayer peak at 155 K, Fig. 5.1c.

Whether or not the structure formed by reaction of water and oxygen is due to water coadsorbed with O, pure hydroxyl or a mixed OH/H<sub>2</sub>O structure can be established by measuring the amount of water taken up by O and the exchange of O labelled isotopes between chemisorbed O and water during reaction. Water uptake was measured as a function of the oxygen pre-coverage at 170 K, Fig. 5.2. At this temperature water adsorbed at clean Pd(111) will desorb (Fig. 5.3) and any remaining on the surface must be incorporated into the stabilised structure. As water is adsorbed on a (2 x 2)O overlayer extra LEED spots start to appear in the  $\sqrt{3}$  positions and become intense as the water coverage increases, (shaded area, Fig. 5.2). Above a composition of 1.5 waters to one oxygen the (2 x 2) spots start to dim and completely disappear above a ratio of approximately 2H<sub>2</sub>O:1O, leaving a sharp  $(\sqrt{3} \times \sqrt{3})R30^\circ$  pattern. This LEED pattern persists until water adsorption saturates. Heating this surface to drive water off allows the (2 x 2)O layer to reform with the same O coverage as originally dosed (as determined by CO titration). The stabilised  $(\sqrt{3} \times \sqrt{3})R30^\circ$  structure formed on Pd(111) is able to accommodate a range of different water/oxygen compositions, Fig. 5.2. At low coverage, less than 0.1 ML, the overlayer incorporates ~4 waters for every oxygen on the surface. As the total OH<sub>x</sub> coverage increases the relative amount of hydrogen tied up in the

overlayer drops, the complete (2 x 2)O layer adsorbing ca. 0.53 ML water. This behaviour is very similar to the reaction between water and O on Pt(111) where a mixed OH/H<sub>2</sub>O phase is formed, the exact amount of water stabilised by OH being sensitive to the precise adsorption temperature used.

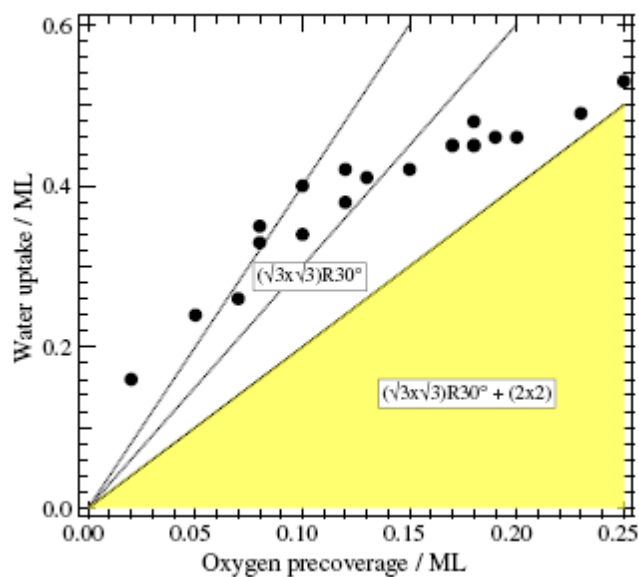
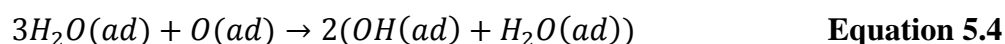


**Figure 5.2** Saturation uptake of H<sub>2</sub>O on to oxygen pre-covered Pd(111) at 170 K as a function of oxygen coverage (solid points). The dotted lines indicate H<sub>2</sub>O/O ratio of 4, 3 and 2. Above an H<sub>2</sub>O/O ratio of ~2 the LEED pattern shows only  $\sqrt{3}$  spots. For an H<sub>2</sub>O/O ratio of <2 extra LEED spots are observed in the (2 x 2) positions along with the  $\sqrt{3}$  spots (shaded regime).

The 2H<sub>2</sub>O:1O reaction stoichiometry required to remove the (2 x 2)O LEED pattern implies that excess hydrogen is present in the stabilised OH<sub>x</sub> structure, over and above that needed to form a pure OH phase by the reaction



The excess water may either be incorporated into the structure, stabilising OH by forming a hydrogen bonded OH/ H<sub>2</sub>O network, or might disproportionate to form coadsorbed OH and H. The latter can be ruled out for a number of reasons. First there was no evidence from TPD studies for H<sub>2</sub> being formed on the surface after water/O reaction. On Ru(0001), where H<sub>2</sub>O dissociates at higher temperatures <sup>27</sup>, thermal desorption experiments report hydrogen desorbing above the water desorption threshold, leaving oxygen at the surface. No hydrogen was seen desorbing after water adsorption on either the clean or oxygen pre-covered Pd(111), while the O coverage determined from CO titration was the same as that originally dosed. Secondly the stability of the OH<sub>x</sub> structure depends on its hydrogen content, decreasing when less water was adsorbed. This can be seen by altering the water/oxygen ratio and following the TPD profiles as a function of hydrogen content, while maintaining a fixed total OH<sub>x</sub> coverage, Fig. 5.3b. The most stable overlayer is formed by reaction with a composition of ~3 waters to one oxygen and desorbs almost 20 K higher in temperature than the monolayer peak. Reducing the hydrogen content but keeping a constant OH<sub>x</sub> coverage, Fig. 5.3b, causes the overlayer to become destabilised, the desorption rate increasing and the peak shifting 3 K to lower temperature as the water oxygen ratio drops to <2. Fig. 5.3c shows the change in the decomposition peak for water/O ratios between 2 and 4.5, taken by varying the O coverage and saturating with water at 170 K. Again, the structure formed with a composition of 3 water/O has the highest desorption temperature, the peak shifting down in temperature again as the structure becomes water rich. This same effect is observed as the total H<sub>2</sub>O coverage is held constant and the oxygen coverage altered, indicating that this effect is not associated simply with island size and coverage. Evidently the presence of water stabilises the overlayer by forming a hydrogen bonding network, rather than destabilising it by forming adsorbed H which competes for space on the surface. The OH/H<sub>2</sub>O structures have the greatest stability for the reaction stoichiometry



This behaviour is consistent with formation of a mixed  $(\sqrt{3} \times \sqrt{3})R30^\circ - 2(OH + H_2O)$  structure on Pd(111), stabilised by completion of the hydrogen bonding network between OH and water.

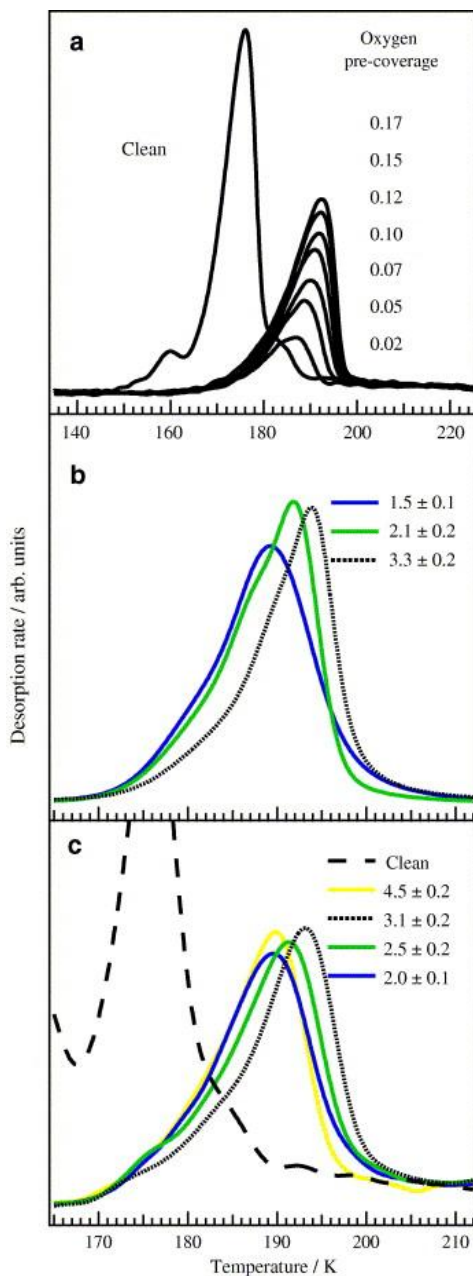


**Figure 5.3** a) Thermal desorption spectra of H<sub>2</sub>O from Pd(111) following adsorption of H<sub>2</sub>O on clean Pd (at 150 K) and O pre-covered surfaces at 170 K.  
 b) TPD curves showing the thermal desorption spectra of H<sub>2</sub>O from the same total OH<sub>x</sub> coverage, 0.64 ML, but with varying total amounts of hydrogen – shown in the legend by the water/oxygen ratio.  
 c) Detail showing the shift in TPD peak for OH/H<sub>2</sub>O structures formed at 170 K by saturating different O coverage with water as a function of the water/oxygen ratio. Heating rate 2 K s<sup>-1</sup>.

The formation of a mixed OH/H<sub>2</sub>O structure can be confirmed using isotope exchange experiments. When chemisorbed <sup>16</sup>O and H<sub>2</sub> <sup>18</sup>O is reacted to form the OH/H<sub>2</sub>O structure and then heated, the water which desorbs as it decomposes contains both <sup>16</sup>O and <sup>18</sup>O isotopes, showing that chemisorbed <sup>16</sup>O has reacted with the H<sub>2</sub> <sup>18</sup>O. The reaction stoichiometry can be obtained by comparing the coverage of <sup>16</sup>O and <sup>18</sup>O isotopes left on the surface using the CO titration. Fig. 5.4 shows the <sup>16</sup>O/<sup>18</sup>O coverage following reaction of a saturated (2 x 2) <sup>16</sup>O layer with different doses of H<sub>2</sub> <sup>18</sup>O. Complete reaction of the 0.25 ML (2 x 2)O phase leaves 0.18 ML of <sup>18</sup>O on the surface. Assuming that OH and H<sub>2</sub>O in the mixed phase exchange protons fast, scrambling the identity of OH and H<sub>2</sub>O, indicates a reaction stoichiometry <sup>16</sup>O + (2.6 ± 0.5)H<sub>2</sub> <sup>18</sup>O for the 0.25 ML (2 x 2)O structure. For lower O coverage an average reaction stoichiometry <sup>16</sup>O + (3.1 ± 0.5)H<sub>2</sub> <sup>18</sup>O is obtained, consistent with the formation of the mixed  $(\sqrt{3} \times \sqrt{3})R30^\circ - 2(OH + H_2O)$  structure by Eq. (5.4). For lower water doses (Fig. 5.4) the <sup>16</sup>O/<sup>18</sup>O exchange implies a much lower H<sub>2</sub>O/O ratio. This indicates that reaction and exchange occurs between the OH/H<sub>2</sub>O structure and excess unreacted O adsorbed on the surface. The isotope experiments rule out the  $(\sqrt{3} \times \sqrt{3})R30^\circ$  structure being associated with an O/H<sub>2</sub>O coadsorption structure analogous to the compressed  $\sqrt{3}$  layer seen when O is coadsorbed with H<sup>18</sup>.

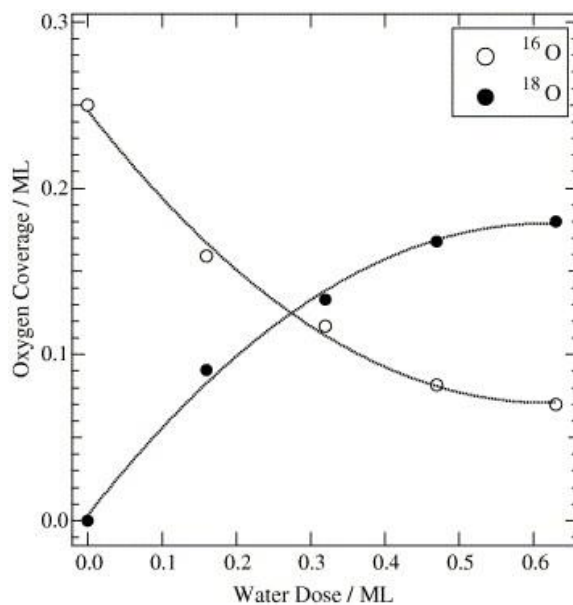


**Figure 5.4** Plot of the  $^{18}\text{O}$  and  $^{16}\text{O}$  coverage left on the surface after adsorption of different doses of  $\text{H}_2^{(18)}\text{O}$  onto a saturated  $(2 \times 2)^{(16)}\text{O}$ -Pd surface at 165 K, followed by thermal decomposition of the product. The oxygen coverage is calculated from CO titration at 273 K by integrating the  $\text{CO}_2$  signal at masses 44 and 46.

Since the OH/ $\text{H}_2\text{O}$  structure on Pt(111) acts as an intermediate in the low temperature reaction to form water, we investigated the reactivity of  $\text{H}_2$  with the mixed OH +  $\text{H}_2\text{O}$  structure on Pd(111) to see if a similar low temperature reaction occurs. Two series of experiments were carried out. Firstly mixed OH/ $\text{H}_2\text{O}$  structures of different coverage (0.35–0.65 ML) were grown on the surface and exposed to background hydrogen (3 L) at 170 K, where any water formed would desorb (Fig. 5.1). The hydrogen was pumped away and then the water TPD recorded. The TPD from the adlayer showed the OH/ $\text{H}_2\text{O}$  structure remained on the surface and had not reacted to form  $\text{H}_2\text{O}$ . In a second series of experiments the  $(2 \times 2)\text{O}$  structure and islands of OH/ $\text{H}_2\text{O}$  were separately exposed to  $\text{H}_2$  from the molecular beam while the scattered gas was analysed for any reaction products. The sample was then heated to desorb any remaining adsorbate, the H recombining and desorbing above 300 K. An example is shown in Fig. 5.5, where adsorption and desorption of water and  $\text{H}_2$  from the  $(2 \times 2)\text{O}$  structure and sub-saturation islands of the OH/ $\text{H}_2\text{O}$  structure are compared. The  $(2 \times 2)\text{O}$  surface was held at 110 K while  $\text{H}_2$  was adsorbed (Fig. 5.5a) to give a surface which shows a  $(\sqrt{3} \times \sqrt{3})R30^\circ$  LEED pattern. No

H<sub>2</sub>O was produced either during exposure of the (2 × 2)O to H<sub>2</sub> at 110 K, or as the surface was heated to desorb H<sub>2</sub>. Since H<sub>2</sub>O is found to be desorbed reversibly from OH/H<sub>2</sub>O structures, this indicates there is no reaction between chemisorbed O and H. Mixed OH/H<sub>2</sub>O structures (0.60, 0.47 and 0.40 ML OH<sub>x</sub>) were prepared and dosed with H<sub>2</sub> at a temperature of 170 K, where any water formed by reaction will desorb promptly. No water signal was observed as the surface is exposed to H<sub>2</sub>, Fig. 5.5b. When the sample was then heated the water TPD traces show a peak near 190 K consistent with the original coverage of the OH/H<sub>2</sub>O phase. Once H desorption is complete, and the surface cooled, the (2 × 2)O LEED pattern reappeared on the surface. We conclude that the mixed OH/H<sub>2</sub>O structure does not react with adsorbed H at low temperatures ( $T \leq 190$  K) on Pd(111).

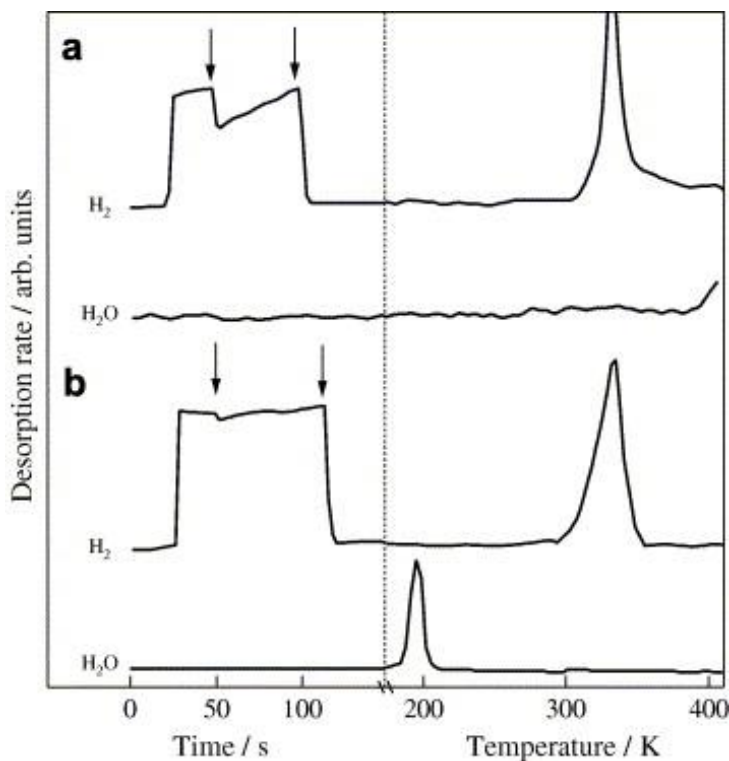


**Figure 5.5** Plot showing the partial pressure of H<sub>2</sub> and H<sub>2</sub>O during the exposure of a) (2 × 2)O layer and b) 0.60 ML (OH + H<sub>2</sub>O) to a H<sub>2</sub> beam (left hand frame) and then the desorption of the products (right hand frame). The increase in partial pressure of H<sub>2</sub> (left hand frame) shows where the beam is admitted to the chamber, while the arrows indicate where a flag in the chamber is moved to expose the sample. The corresponding H<sub>2</sub>O partial pressure is shown below and does not change as the surface is exposed to H<sub>2</sub>, the surface is then heated (right hand frame) to desorb water and H<sub>2</sub> from the surface.

### 5.2.5. Discussion

The reaction between water and O on Pd(111) shows an almost identical behaviour as found on Pt(111) <sup>10, 11</sup>. On that surface density functional calculations <sup>8, 9, 28</sup> and experiment <sup>11, 29</sup> find a flat overlayer containing alternating water and hydroxyls arranged in hexagonal rings with a total OH<sub>x</sub> coverage of 0.67 ML. The OH<sub>x</sub> is adsorbed in the atop site, stabilised by completing the hydrogen bonding network. As this structure is completed extra faint (3 x 3) spots are observed in LEED, associated with formation of a proton ordered (3 x 3) superstructure which is also seen in STM <sup>12</sup>. The (3 x 3) arrangement on Pt(111) is thought to arise from a cyclic arrangement of water within the overall hexagonal network <sup>11</sup>, three adjacent waters having their protons pointing in a ring linked by OH groups whose H points out from the ring <sup>11, 29</sup>. No (3 x 3) LEED spots were seen for the mixed OH/H<sub>2</sub>O structures on Pd(111), implying that the hydrogen bonding network of OH/H<sub>2</sub>O on Pd(111) prefers to form domains of a  $\sqrt{3}$  structure rather than ordering the protons into a cyclic arrangement. Decomposition of the OH/water phase to desorb water from Pt(111)-(OH + H<sub>2</sub>O) is associated with a number of different elementary steps, including proton transfer and OH disproportionation, leading to kinetics which depend on both the composition and density of defects in the structure <sup>30</sup>. Decomposition of the OH/H<sub>2</sub>O structures occurs at a slightly lower temperature on Pd(111) than on Pt(111), 190 K rather than 210 K, but otherwise the kinetic behaviour appears very similar.

The OH/H<sub>2</sub>O structure on Pt(111) is formed as the key intermediate in the low temperature water formation reaction, the  $(\sqrt{3} \times \sqrt{3})R30^\circ$  mixed OH/H<sub>2</sub>O structure being formed either by O/water reaction or by reaction of H<sub>2</sub> and O<sub>2</sub> <sup>12, 13, 31</sup>. The H<sub>2</sub>/O<sub>2</sub> reaction on Pt(111) is autocatalytic <sup>31, 32</sup>, water formed by OH + H reaction reacts with O to form more OH, avoiding the slow H + O recombination step. On Pd(111) no low temperature reaction has been reported and the rate determining step is again believed to be the addition of hydrogen to oxygen to form hydroxyl <sup>17</sup>. STM images suggest that reaction starts to occur only above 220 K at step edges <sup>16</sup>. The results presented here indicate that reaction of O and water will form OH at low temperature, just as on Pt(111).

However, the OH/H<sub>2</sub>O structure formed does not react with H, Eq. (5.2), but decomposes when heated above 190 K to desorb water and leave O and H coadsorbed on the surface. This implies that the H + OH reaction, which other studies have suggested is fast above 220 K<sup>17</sup>, certainly does not occur at temperatures below 190 K. Whereas on Pt(111) the barrier for hydrogen to add to a mixed OH/H<sub>2</sub>O phase is sufficiently low that reaction occurs below 150 K, this reaction is too slow on Pd(111) for the mixed OH/H<sub>2</sub>O structure to act as an intermediate in the water formation reaction at low temperatures.

When O and H are coadsorbed on Pd(111) below 200 K a  $(\sqrt{3} \times \sqrt{3})R30^\circ$  structure has been reported which was attributed to a compression of the (2 x 2)O islands<sup>18</sup>. Our results confirm that this is not the same structure as the  $(\sqrt{3} \times \sqrt{3})R30^\circ$  mixed OH/H<sub>2</sub>O formed by O/water reaction. A  $(\sqrt{3} \times \sqrt{3})R30^\circ$  LEED pattern appears as H is coadsorbed with O and disappears as the surface is heated to 210 K. No water was formed, the O islands reforming on the surface, consistent with a compression of the O structure as proposed by Mitsui *et al.*<sup>16, 18</sup> The alternative explanation, that H and O react to form OH but the OH + OH reaction does not lead to water formation, is inconsistent with the decomposition of OH/water structures at 190 K.

### 5.2.6. Conclusion

Oxygen reacts with water at low temperature on Pd(111) to form a mixed OH/H<sub>2</sub>O overlayer with a  $(\sqrt{3} \times \sqrt{3})R30^\circ$  periodicity. This phase is stabilised by hydrogen bonding between hydroxyl and water. As the water/oxygen ratio reaches 3–1 the (OH + H<sub>2</sub>O) hydrogen bond network completes and the overlayer becomes kinetically stable to decomposition compared to structures with different OH/H<sub>2</sub>O ratios. The OH/H<sub>2</sub>O phase does not react with H to form water, indicating that the reaction between hydroxyl and H is slow at temperatures below 190 K. This is in contrast to Pt(111) where hydrogenation of OH/H<sub>2</sub>O structures is fast, allowing low temperature reaction of H<sub>2</sub> and O<sub>2</sub> to form water.

### 5.2.7. References

1. C. Clay, L. Cummings and A. Hodgson, *Surface Science*, 2007, **601**, 562-568.
2. P. A. Thiel and T. E. Madey, *Surface Science Reports*, 1987, **7**, 211-385.
3. A. Verdager, G. M. Sacha, H. Bluhm and M. Salmeron, *Chemical Reviews*, 2006, **106**, 1478-1510.
4. C. Clay and A. Hodgson, *Current Opinion in Solid State & Materials Science*, 2005, **9**, 11-18.
5. K. Andersson, A. Nikitin, L. G. M. Pettersson, A. Nilsson and H. Ogasawara, *Physical Review Letters*, 2004, **93**, 196101.
6. M. A. Henderson, *Surface Science Reports*, 2002, **46**, 5
7. G. S. Karlberg, F. E. Olsson, M. Persson and G. Wahnstrom, *Journal of Chemical Physics*, 2003, **119**, 4865-4872.
8. A. Michaelides and P. Hu, *Journal of Chemical Physics*, 2001, **114**, 513-519.
9. A. Michaelides and P. Hu, *Journal of the American Chemical Society*, 2001, **123**, 4235-4242.
10. G. B. Fisher and B. A. Sexton, *Physical Review Letters*, 1980, **44**, 683-686.
11. C. Clay, S. Haq and A. Hodgson, *Physical Review Letters*, 2004, **92**, 046102.
12. K. Bedurftig, S. Volkening, Y. Wang, J. Wintterlin, K. Jacobi and G. Ertl, *Journal of Chemical Physics*, 1999, **111**, 11147-11154.
13. C. Sachs, M. Hildebrand, S. Volkening, J. Wintterlin and G. Ertl, *Science*, 2001, **293**, 1635-1638.
14. C. Clay, S. Haq and A. Hodgson, *Chem. Phys. Lett.*, 2004, **288**, 80.
15. P. J. Feibelman, *Science*, 2002, **295**, 99-102.
16. T. Mitsui, M. K. Rose, E. Fomin, D. F. Ogletree and M. Salmeron, *Journal of Chemical Physics*, 2002, **117**, 5855-5858.
17. T. Engel and H. Kuipers, *Surface Science*, 1979, **90**, 181-196.
18. T. Mitsui, M. K. Rose, E. Fomin, D. F. Ogletree and M. Salmeron, *Surface Science*, 2002, **511**, 259-266.
19. M. Wolf, S. Nettesheim, J. M. White, E. Hasselbrink and G. Ertl, *Journal of Chemical Physics*, 1990, **92**, 1509-1510.

20. M. Wolf, S. Nettesheim, J. M. White, E. Hasselbrink and G. Ertl, *Journal of Chemical Physics*, 1991, **94**, 4609-4619.
21. H. Conrad, G. Ertl, J. Kuppers and E. E. Latta, *Surface Science*, 1977, **65**, 245-260.
22. S. Haq, J. Harnett and A. Hodgson, *Surface Science*, 2002, **505**, 171
23. G. A. Kimmel, N. G. Petrik, Dohn, Z. lek and B. D. Kay, *Physical Review Letters*, 2005, **95**, 166102.
24. C. Clay, L. Cummings, A. Hodgson, in preparation.
25. C. Clay, S. Haq and A. Hodgson, *Chemical Physics Letters*, 2004, **388**, 89-93.
26. T. Mitsui, M. K. Rose, E. Fomin, D. F. Ogletree and M. Salmeron, *Science*, 2002, **297**, 1850-1852.
27. D. N. Denzler, S. Wagner, M. Wolf and G. Ertl, *Surface Science*, 2003, **532**, 113-119.
28. G. S. Karlberg, Wahnström, *Physical Review Letters*, 2004, **92**, 136103.
29. G. Held, C. Clay, S. D. Barrett, S. Haq and A. Hodgson, *Journal of Chemical Physics*, 2005, **123**, 064711.
30. G. S. Karlberg, G. Wahnstrom, C. Clay, G. Zimbitas and A. Hodgson, *Journal of Chemical Physics*, 2006, **124**, 204712.
31. S. Volkening, K. Bedurftig, K. Jacobi, J. Wintterlin and G. Ertl, *Physical Review Letters*, 1999, **83**, 2672-2675.
32. K. M. Ogle and J. M. White, *Surface Science*, 1984, **139**, 43-62.

# **Chapter 6**

## **Ultrafast surface dynamics**

## 6.1 Introduction

### 6.1.1 Femtochemistry

In 1999, Ahmed Zewail won a Nobel Prize for showing that it is possible to use fast laser dynamics to determine how atoms move in molecules during a chemical reaction<sup>1</sup>. Zewail was the first person to use femtosecond laser pulses to initiate chemical reactions and observe the outcome of the reaction a short time later. He initiated the ring opening of cyclobutane molecules to form two ethylene molecules and using a fs laser pulse and detected a transition state which had a lifetime of only a few hundred fs<sup>2</sup>. The use of femtochemistry now allows scientists to determine whether chemical reactions proceed via a transition state or whether they proceed in one step.

A group at IBM adapted the technique used by Zewail in order to investigate reaction mechanisms for processes which take place on a solid surface<sup>3</sup>. During their experiments, a femtosecond laser pulse was used induce the NO desorption reaction from Pd(111). They found that NO desorbs intact from Pd(111) when induced with 200 femtosecond laser pulses. They determined the yield and energy distribution of the desorbed molecules and showed that desorption induced by femtosecond laser pulses follows a different mechanism to thermal and photochemical processes.

During chemical reactions, bonds form and break on a femtosecond time scale ( $10^{-15}$  s) and femtochemistry can be employed to investigate the dynamics of chemical processes. Reactions can be initiated thermally and during these reactions, the phonons and electrons are in thermal equilibrium meaning that the two cannot be distinguished from each other. However, ultrashort laser pulses can be used to overcome this problem and determine reaction dynamics. A metal substrate can be described as having two energy baths, a thermal energy part contained in the electrons and lattice vibrations contained in the phonons<sup>4</sup>. An equilibrium exists between the two baths until a femtosecond laser pulse excites electrons, increasing their energy in comparison to the phonons. The excited electrons can be considered to be hot electrons and they may remain in a high energy state for a few picoseconds before equilibrating with the lattice vibrations. This mechanism provides a means of investigated the difference between electron and phonon mediated processes by

allowing a laser to induce a higher energy excited state while the thermal relaxation back to equilibrium is monitored. Figure 6.1 illustrates the mechanism of energy flow at metal surfaces proceeding excitation by a femtosecond laser.

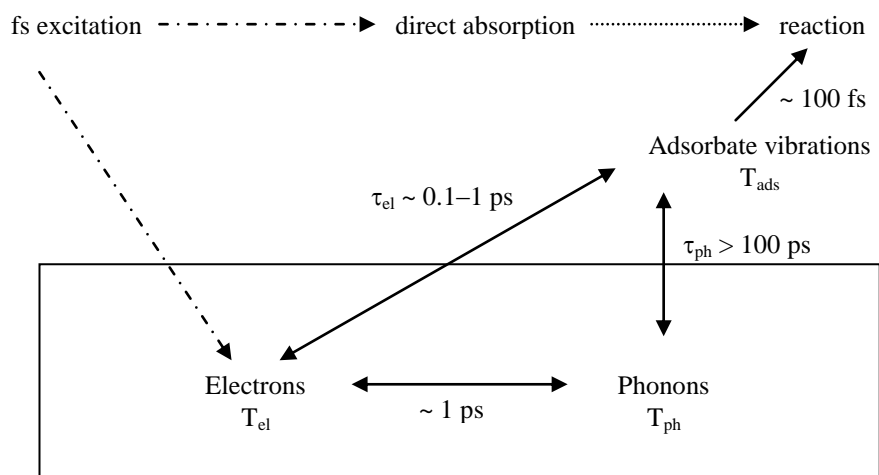


**Figure 6.1:** Schematic to show femtosecond laser pulse induced energy flow at a metal surface. The fs laser pulse excites electrons to a higher energy state before they equilibrate back to their original state as a function of electron – phonon coupling time. Figure adapted from reference 4

Figure 6.2 clearly illustrates the difference in time scale of the temperature transition for electron and phonon heat baths with temperatures  $T_{el}$  and  $T_{ph}$  respectively. The example shown is often shown in the literature but this particular example is cited from reference 4.

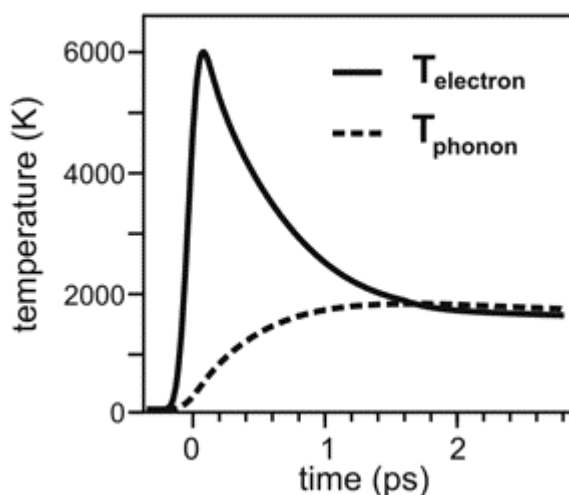


**Figure 6.2<sup>4</sup>:** Schematic to illustrate the two temperature model with typical temperature transients for electron and phonon heat baths with temperatures  $T_{el}$  and  $T_{ph}$  respectively. For the example shown, the substrate metal is Ru and a 120 fs laser pulse was used with  $50 \text{ mJ/cm}^2$  at 800 nm centre wavelength. Reprinted (adapted) with permission from (C. Frischkorn and M. Wolf, *Chemical Reviews*, 2006, 106, 4207-4233). Copyright (2006) American Chemical Society.

Reactions initiated by thermal activation proceed via the electronic ground state, equally dispersing energy between translational, rotational and vibrational degrees of freedom. The energy provided to the electrons and phonons by conventional heating methods, has sufficient time to equilibrate. However, reactions initiated by femtosecond laser pulses result in the formation of electron-hole pairs due to electronic excitation. The resultant products from an activated process often have a varied energy distribution over all possible degrees of freedom and a change of the equilibrium bond length occurs during the electronic transitions. The activation process results in a different reaction mechanism for a reaction initiated by a femtosecond laser pulse to that of a thermally initiated process, and in some cases, different reaction products can be formed.

For example Bonn *et al.*<sup>5</sup> investigated the reaction between CO and O adsorbates on ruthenium. Heating the surface containing the two adsorbates leads to the desorption of CO but no reaction to form  $\text{CO}_2$ . However, when femtosecond laser pulses are introduced to initiate the reaction,  $\text{CO}_2$  desorption is observed in addition to CO. This tells us that CO desorption is a thermally activated process initiated by phonons whereas the oxidation of CO is initiated by hot electrons when fs laser pulses provide sufficient energy to overcome the reaction barrier. During thermal initiation, the

phonons to not provide enough energy to produce  $\text{CO}_2$ , hence only CO desorption is detected. Figure 6.3 illustrates the two reaction pathways (thermal and femtosecond laser excitation) for the co-adsorption of CO and O on Ru(0001).

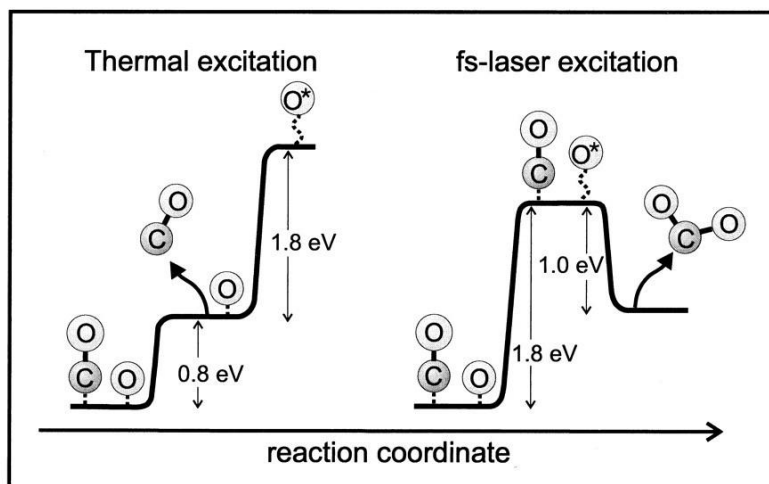


**Figure 6.3<sup>5</sup>:** Schematic to illustrate the thermal and fs-laser excitation of carbon monoxide and oxygen co-adsorbed on ruthenium.

- Thermal excitation leads to the desorption of CO only due to the lower energy required for the desorption in comparison to O activation.
- Femtosecond laser excitation also leads to the desorption of  $\text{CO}_2$  due to coupling of the adsorbate to the phonon bath of the ruthenium substrate. The oxidation reaction is initiated by hot substrate electrons, occurring on a sub-picosecond time scale.

From [M. Bonn, S. Funk, C. Hess, D. N. Denzler, C. Stampfl, M. Scheffler, M. Wolf and G. Ertl, *Science*, 1999, 285, 1042-1045]. Reprinted with permission from AAAS.

### 6.1.2 Surface Reactions Initiated by Femtosecond Laser Pulses

There are two models for initiating reactions at surfaces by using femtosecond laser pulses. The first of these is by means of energy transfer by electronic friction between the adsorbate and the surface (figure 6.4). The energy flow in the system is determined by phonon and electron coefficients. As the excited electrons move between the adsorbate and the surface, they provide sufficient energy to the adsorbate to initiate the desorption process.

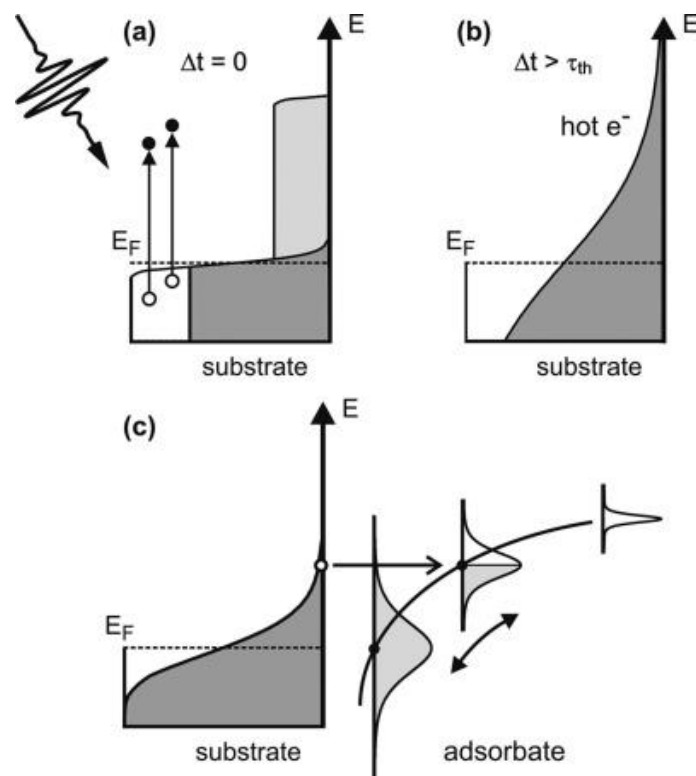


**Figure 6.4<sup>4</sup>:** a) A femtosecond laser pulse excites electrons in the metal resulting in a unequal population distribution.  
 b) Thermalisation occurs on a time scale of 10-100 fs, resulting in a hot electron distribution that has a high energy tail.  
 c) Electron flow enables an adsorbate-derived affinity level to be populated by electrons from the substrate. A changed charge distribution initiates adsorbate motion. Electron flow between the metal and substrate is subject to friction /damping.  
 Reprinted (adapted) with permission from (C. Frischkorn and M. Wolf, *Chemical Reviews*, 2006, 106, 4207-4233). Copyright (2006) American Chemical Society.

The second model involves desorption induced by multiple electronic transitions (DIMET) by which, a laser incident on the sample causes the formation of hot electrons through electronic excitation (figure 6.5). These hot electrons populate previously unoccupied energy levels, creating an electronically excited potential energy state (PES). When the electrons relax back to the ground state, the excess energy is converted into kinetic/vibrational energy. Continuous excitation and relaxation provides enough energy to initiate desorption from the surface. The reader is referred to reference 1 for a more in-depth explanation of the processes discussed here.

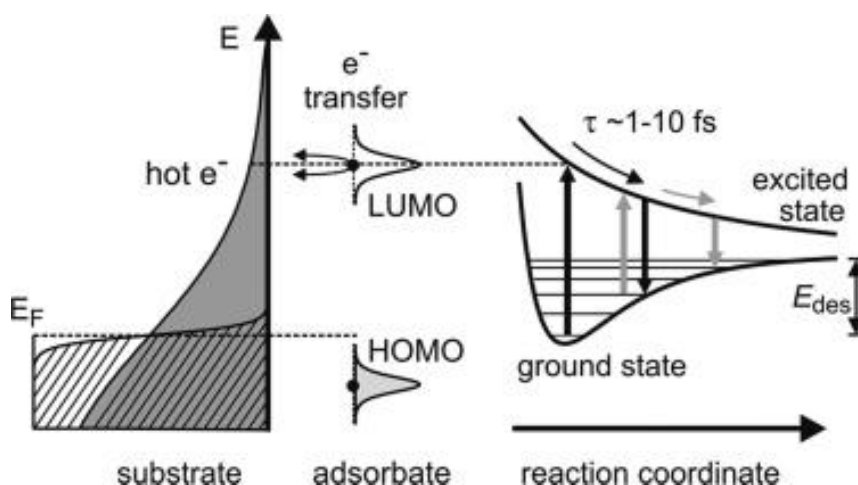


**Figure 6.5<sup>4</sup>:** Non adiabatic energy coupling between electronic and nuclear degrees of freedom. Electrons are repeatedly transferred from the high energy tail of the electronically excited occupied state of the substrate to an unoccupied molecular orbital of the adsorbate-substrate complex. The hashed region depicts a population of cold electrons that do not have enough energy to reach the unoccupied levels. Reprinted (adapted) with permission from (C. Frischkorn and M. Wolf, *Chemical Reviews*, 2006, 106, 4207-4233). Copyright (2006) American Chemical Society.

### 6.1.3 Hydrogen Recombination

Hydrogen recombination involves the formation of hydrogen gas from the combination of hydrogen atoms separately adsorbed on a metal surface (equation 6.1). Hydrogen recombination on Cu(111) has been well documented and the thermal reaction dynamics have been extensively studied. However, no studies exist to determine whether the reaction is driven by phonons or hot electrons and whether the reaction proceeds via a different mechanism during electronic excitation. The H<sub>2</sub>/Cu(111) system attracted attention as a model system due to the fact that copper has a filled d-band which simplifies electronic structure calculations and because hydrogen is light, it has a relatively small number of quantum states.



The first molecular beam study of hydrogen on copper was reported by Balooch *et al.*<sup>6</sup> They show that the adsorption of hydrogen is an activated process and that the probability for adsorption occurring at a given translational energy decreases with an increase in angle of incidence to the sample. The kinetic energy distributions for D<sub>2</sub> and H<sub>2</sub> have been determined by Rettner *et al.* who show that dissociative adsorption of D<sub>2</sub> on Cu(111) is an activated process, with both translational and vibrational energy able to overcome the activation barrier<sup>7, 8</sup>. They report the first quantum state specific measurements of the velocity distributions for recombinative desorption on an activated system.

#### 6.1.4 Resonance Enhanced Multiphoton Ionisation (REMPI)

Tunable UV laser light can be used for REMPI to detect specific quantum states of small molecules (hydrogen and deuterium were used for experiments described in this thesis). H<sub>2</sub> and D<sub>2</sub> undergo a (2+1) REMPI process, which involves multiphoton absorption (two photons) to excite the molecule from the ground state to an electronically excited state. Following this excitation, ionisation occurs and in the case of a (2+1) REMPI scheme, one photon is required for this step. The difference in energy between the ground and excited states depends on the initial v,J state of the molecule and therefore, specific v,J states can be ionised by using the required wavelength of light. A tuneable dye laser can be used in order to produce light of a particular wavelength. Figure 6.6 shows a schematic representation of the (2+1) REMPI process. This scheme was first published by Marinero *et al.* in 1982<sup>9</sup>.

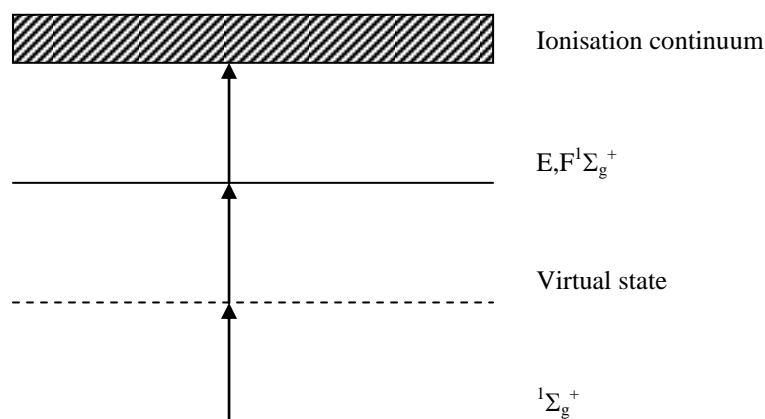


**Figure 6.6** Schematic of a (2+1) REMPI scheme for hydrogen and deuterium.

## 6.2. Experimental Techniques

All experiments discussed in this section were carried out with the UHV chamber described in section 2.1. The Cu(111) crystal was mounted by threading Ta wire through pre-drilled holes in the sample which were then spot-welded to Ta posts on the x,z,z manipulator. As discussed previously, the sample could be cooled by means of a liquid nitrogen dewar and resistively heated using an AC power supply (section 2.1). The Cu(111) sample was cleaned by argon ion sputtering followed by annealing to a temperature of 1000 K.

### 6.2.1 Atom Beam Source

A directional beam of hydrogen atoms can be generated using a microwave discharge powered source. The atom beam source used for experiments discussed in this thesis was adapted from equipment reported by Evenson<sup>10</sup> and a schematic is shown in figure 6.7. The original apparatus was used by the Dynamics Group in Liverpool's Surface Science Centre for past experiments (circa 2003) but had since been broken. Using the available literature, I redesigned the beam with a view to using compressed air for the cooling medium in preference to carbon tetrachloride. The dimensions used were obtained by measuring the relevant distances on the chamber to ensure that the

beam could make a sufficient seal and fit into the existing space. It was essential to make sure the lengths were correct as a wider bore was necessary at one end of the beam to allow it to fit in the supporting flanges. At the other end, the glass beam had to fit into the microwave cavity and taper to a small nozzle to allow a directional flow through the aperture leading into the main chamber (skimmer). Further considerations need to be made to ensure that the outer cooling jacket extended as close to the tip of the nozzle as possible in order to maximize the area of the beam that could be cooled. The source was situated in the first stage of the UHV chamber, replacing the molecular beam source shown in figure 2.1. It consisted of a 6 mm gas delivery tube encased by a cooling jacket through which compressed air was circulated. The cooling jacket was essential to prevent the delivery tube from melting due to the large amount of heat generated by the microwave discharge source. Pyrex was used to make the body of the atom beam because it is transparent to microwaves. An x,y,z manipulator allowed a small amount of movement once the beam had been attached to the chamber. This allowed the 0.5 mm nozzle of the gas delivery tube to be aligned to a conical skimmer, through which the beam of atoms entered into the main chamber following a highly directional path towards the crystal. The gas (in this case hydrogen) enters the gas delivery tube where is subjected to a microwave discharge source, lit with a Tesla spark coil (~150 W power), causing the production of atoms (H atoms for work discussed here). The magnetron power supply for the microwave cavity was operated from 40 – 200 W at a frequency of 2450 MHz. The microwave discharge produced is shown in figure x and has a characteristic red glow due to Balmer emission. The discharge remains stable over a range of pressures but for experiments discussed in this thesis, a pressure of 2.0 Torr was used.

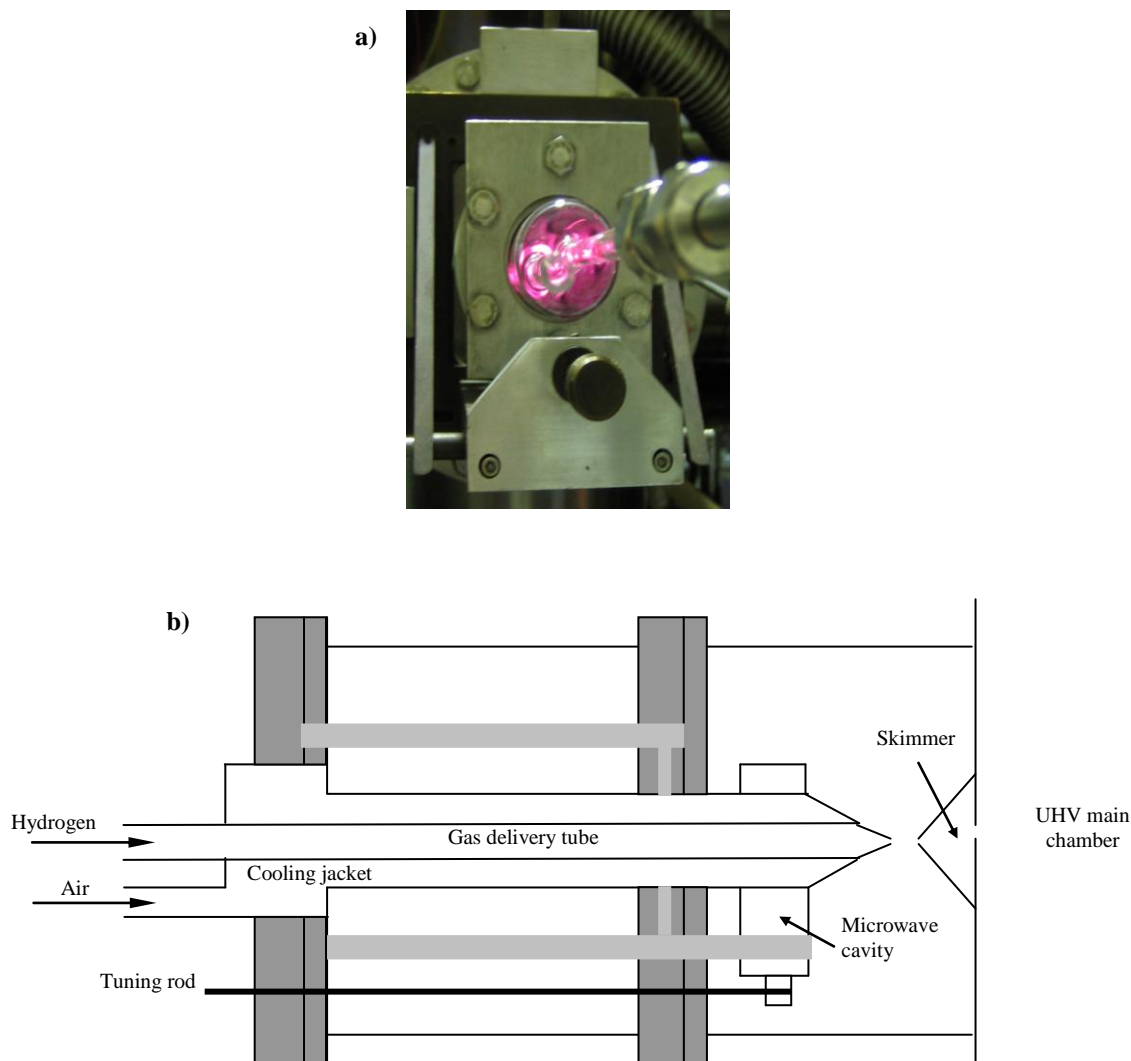


**Figure 6.7:** a) A photograph of the lit microwave discharge of hydrogen. Image shows a view of the atom beam source looking towards the air and hydrogen inlets.  
 b) Schematic of the atom beam source fitted in place of the molecular beam shown in figure 2.1. The tuning rod enabled tuning of the microwave cavity in order to light the discharge. The nozzle at the end of the gas delivery tube was aligned to the skimmer allowing a directional beam of H/D atoms to enter the main vacuum chamber. Air was circulated through the cooling tube to prevent melting of the pyrex body.

Dimensions used for the atom beam source:  
 Gas delivery tube : 6 mm internal diameter  
 Nozzle of gas delivery tube : 0.5 mm  
 Cooling jacket - front section : 32 mm diameter

### 6.2.2 Nd:YAG and Dye Lasers

Two lasers were used to generate ultra-violet light with a wavelength of  $\sim 200$  nm, a Quantel actively Q-switched Nd:YAG laser and a Lambda Physik dye laser. The Nd:YAG laser starts with a fixed wavelength of 1064 nm which is generated by the  $\text{Nd}^{3+} \ ^4\text{F}_{3/2}$  to  $\ ^4\text{I}_{1/2}$  transition. This is frequency doubled through a potassium dihydrogen phosphate (KDP) crystal to give an output with a wavelength of 532 nm. This output has a pulse length of 6 ns, a repetition rate of 10 Hz and a maximum power of 400 mJ/pulse providing a peak intensity greater than 100 MW. The light of wavelength 532 nm passes into the pulsed dye laser which utilizes a grating tuned oscillator to provide an output between 570 and 635 nm due to the dye used in the system. For experiments mentioned here, a solution of dichloromethane (DCM) and rhodamine B in methanol was used to generate a wavelength of 600 nm. The efficiency of the dye used was approximately 25 %. The laser operates by means of a grating tuned oscillator and In order to prevent damage being caused to the grating, a maximum of 200 mJ/pulse was inputted resulting in outputs of approximately 50 mJ/pulse.

Harmonic generation allowed the 600 nm output to be frequency tripled. Frequency doubling was achieved using a KDP crystal (second harmonic generation) before directing the light through a  $\beta$ -barium borate (BBO) crystal (third harmonic generation). A polarization rotator between the KDP and BBO crystals was used to rotate the doubled (blue) light by  $90^\circ$  in order to make it parallel to the fundamental beam (red). Dynamic scanning of the light with a wavelength of  $\sim 200$  nm was achieved by housing the KDP and BBO crystals in INRAD auto-tracking systems to alter the phase matching angle as the wavelength of the output from the dye laser changed. The resultant output at  $\sim 200$  nm was directed to a Pellin-Broca prism to separate out the wavelengths and focus only the UV light into the chamber, reducing scattered light inside the experimental area. The UV light was initially aligned to the first of two dichroic mirrors positioned on an optical mount on the base of the UHV chamber. A second dichroic mirror was used to direct the light up into the chamber through a 125 mm focal lens to a point 12 mm in front of the Cu(111) crystal.

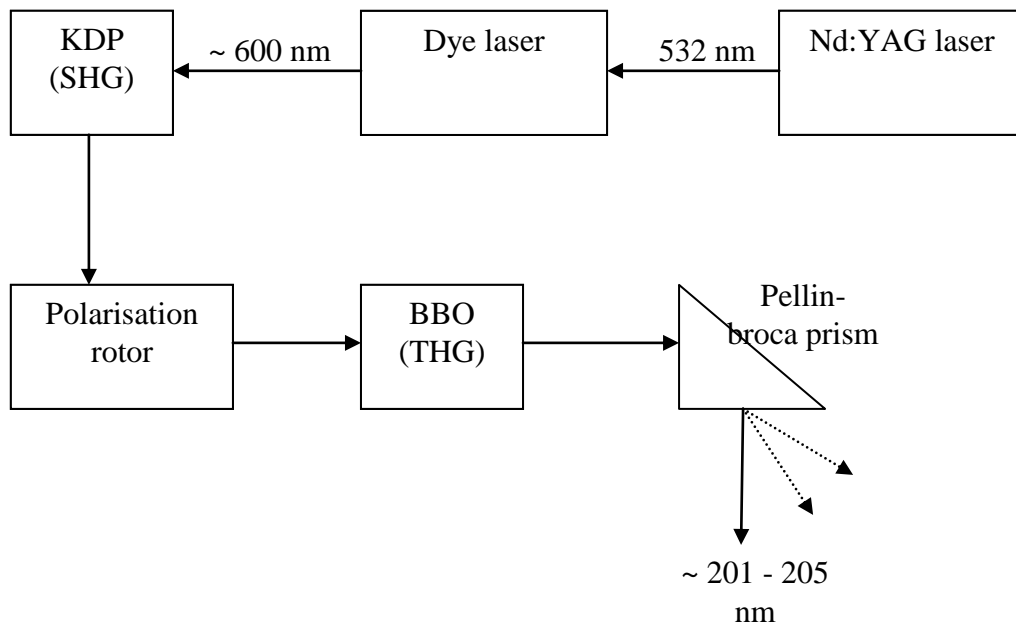


**Figure 6.8:** Schematic of the laser set-up used to generate VUV light with a wavelength of  $\sim 201 - 205$  nm.

### 6.2.3 Femtosecond Laser

For experiments described here, a Coherent Libra-S femtosecond laser was used. A range of optics were used in order to provide two beams from the femtosecond laser pulse for two pulse correlation (2PC) experiments. A schematic of the setup for the laser path to the main chamber is shown in figure 6.9.

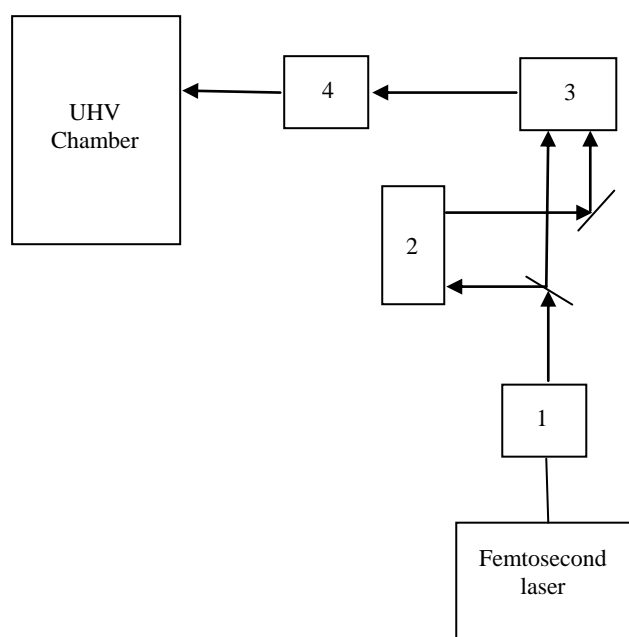


**Figure 6.9:** Schematic of the laser path from the femtosecond laser unit to the UHV chamber.

1. various prisms and mirrors used to direct the beam into the autocorrelator
2. Autocorrelator used to split the beam into two components for a 2PC experiment
3. Silver mirror used to direct the beam into the vacuum chamber through a window at the back of the chamber.
4. Gold mirror used to direct the beam into the vacuum chamber through a window at the back of the chamber.

The Libra femtosecond laser produces pulses in the order of  $10^{-15}$  s, which cannot be generated by a flash lamp based laser. There are five components to the laser set up which are the seed laser, pump laser, regenerative amplifier, stretcher/compressor and an electronics interface module. In order to produce ultrashort pulses with high peak power, chirped pulse amplification (CPA) and regenerative amplification (RA) are utilized. CPA reduces the chance of damage being caused due to the laser beam self focusing. Initially, a short pulse is generated which is stretched by up to 10,000 times using a single pulse stretcher to significantly reduce peak power. The pulse is then stretched and amplified by a Ti:sapphire regenerative amplifier which increases the energy by up to  $10^6$  times. The final step in CPA involves compressing the pulse resulting in a pulse duration close to the original time. Figure 6.10 shows a schematic of the CPA process. Regenerative amplification provides an efficient way of producing high energy laser pulses with high peak power. This is achieved by the amplification of a low energy pulse ( $\sim 3$  nJ) with a Ti:sapphire laser rod which has been optically excited by a frequency doubled Q-switched Nd:YLF laser. This produces pulses with an energy in excess of 1 mJ. A higher overall gain can be obtained by repeating the process and continuing to pass the pulse through the laser rod.

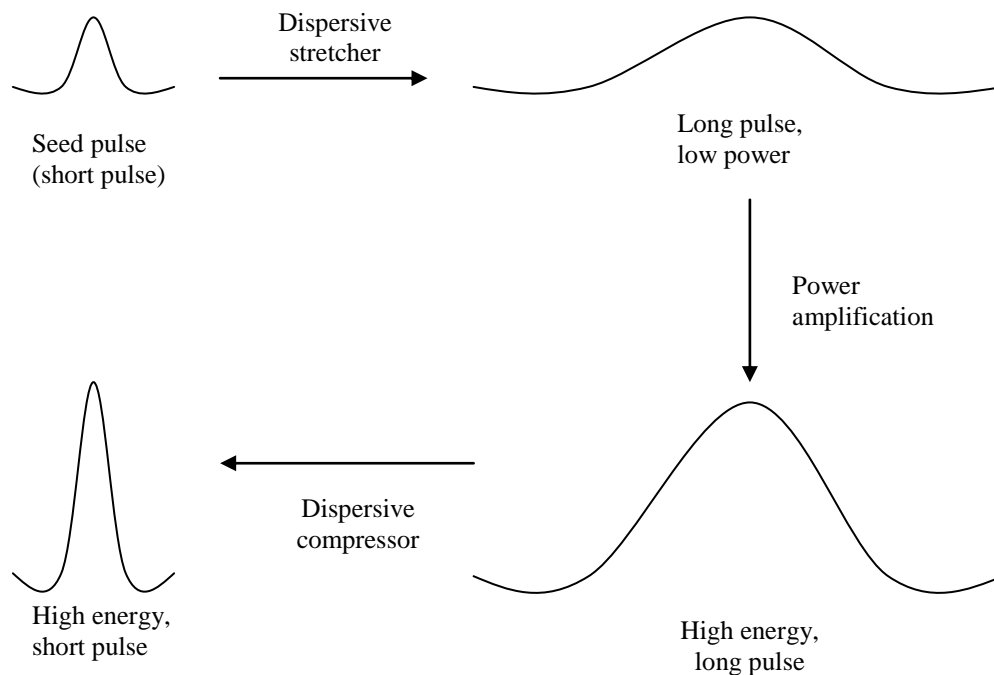


**Figure 6.10:** Schematic of the chirped pulse amplification technique. The seed pulse has low energy and a short wavelength. This is stretched and amplified before being compressed, resulting in a pulse with the same wavelength as the seed pulse but higher energy.

An autocorrelator is used to split the fs laser beam into two for two-pulse correlation (2PC) experiments to be carried out in order to differentiate between electron and phonon mediated processes. 2PC is carried out with two pulses, as close in intensity to each other as experimentally possible, incident on the adsorbate/substrate system with a variable delay between the two. A narrow full width half maximum (FWHM) on the scale of a few hundred fs is expected for reactions mediated by hot electrons, whereas a broader FWHM on the scale of approximately 100 ps is expected for processes mediated by phonons. The slower time expected for phonon mediated processes is due to the fact that phonons gain energy from the equilibration of hot electrons rather than from the laser pulse itself.

The autocorrelator was used to measure and then optimise the pulse width of the femtosecond laser pulse. The experimental data and fitted traces are shown in figure 6.11 at 1 kHz and 100 Hz. Despite the fact that the laser had been optimised to

operate at 1 kHz, a closer fit was observed at 100 Hz, although slight broadening can still be seen at the base of the trace in comparison to the fitted trendline.

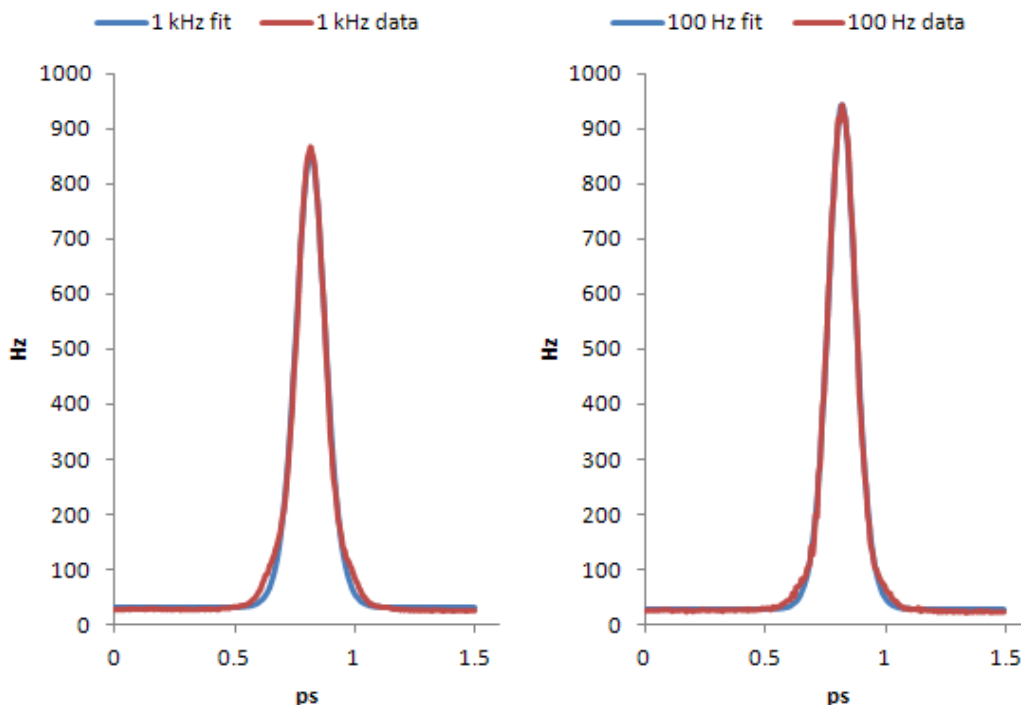


**Figure 6.11:** Autocorrelation traces of the femtosecond laser pulses at a) 1 kHz and b) 100 Hz.

#### 6.2.4 Ion Detection

Once molecules have been ionised using REMPI, they need to be detected and this was achieved with time-of-flight (TOF) measurements. The TOF optics (figure 6.12) had a Mo sheet at the front which was held at a negative voltage to attract positive ions towards it. The crystal was floated to the same voltage as the Mo sheet and positioned in front of the grid. Once ions were extracted from the chamber, they passed to a field free region inside the TOF tube and could be detected by a microchannel plate (MCP) with a gain of  $10^6$ . The MCP was supported on a ceramic mount in order to maintain electrical isolation from the grids inside the tube. The dispersion of ions through the TOF tube is due to the molecular velocities of the ions and therefore, ions

with higher velocities reach the MCP first. The signal from the MCP was amplified by an ten times ORTEC 90301 amplifier and collected by a 125 MHz LeCroy 9400 oscilloscope before being acquired by an Apple Mac II via a GPIB interface.

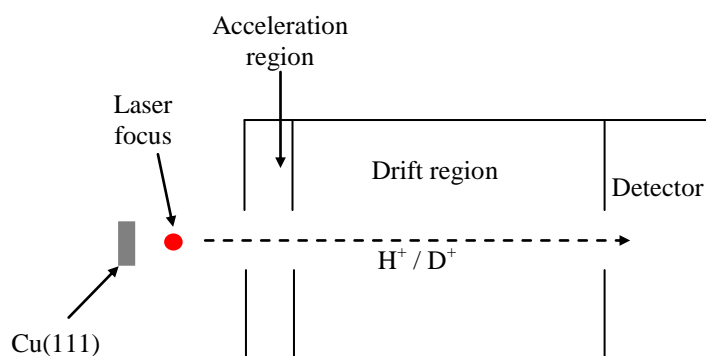


**Figure 6.12:** Schematic of the time-of-flight optics used for ion detection. The red spot represents the laser focal point, 12 mm in front of the Cu(111) crystal.

## 6.3 Results and Discussion

### 6.3.1 Deuterium

A series of TPDs were carried out for D<sub>2</sub> adsorbed on Cu(111). Deuterium was used for initial experience due to its absence in the background gases present in the chamber (unlike hydrogen). The crystal was cooled to 100 K before deuterium was dosed via the atom beam. After a fixed dose time (3 minutes), the beam was closed and excess deuterium pumped away. Figure 6.13 shows the TPD spectra obtained. A high temperature desorption peak appears at 350 K due to deuterium desorbing from the Cu(111) surface, followed by a lower temperature peak due to subsurface absorption. These findings are in agreement with previous studies carried which show that deuterium goes subsurface on Cu(111) at 170 – 180 K.

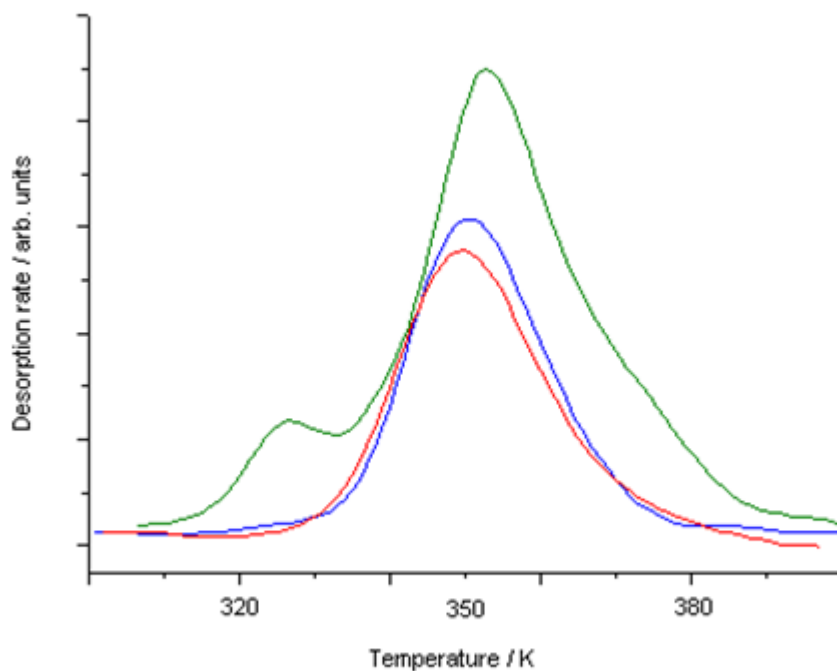
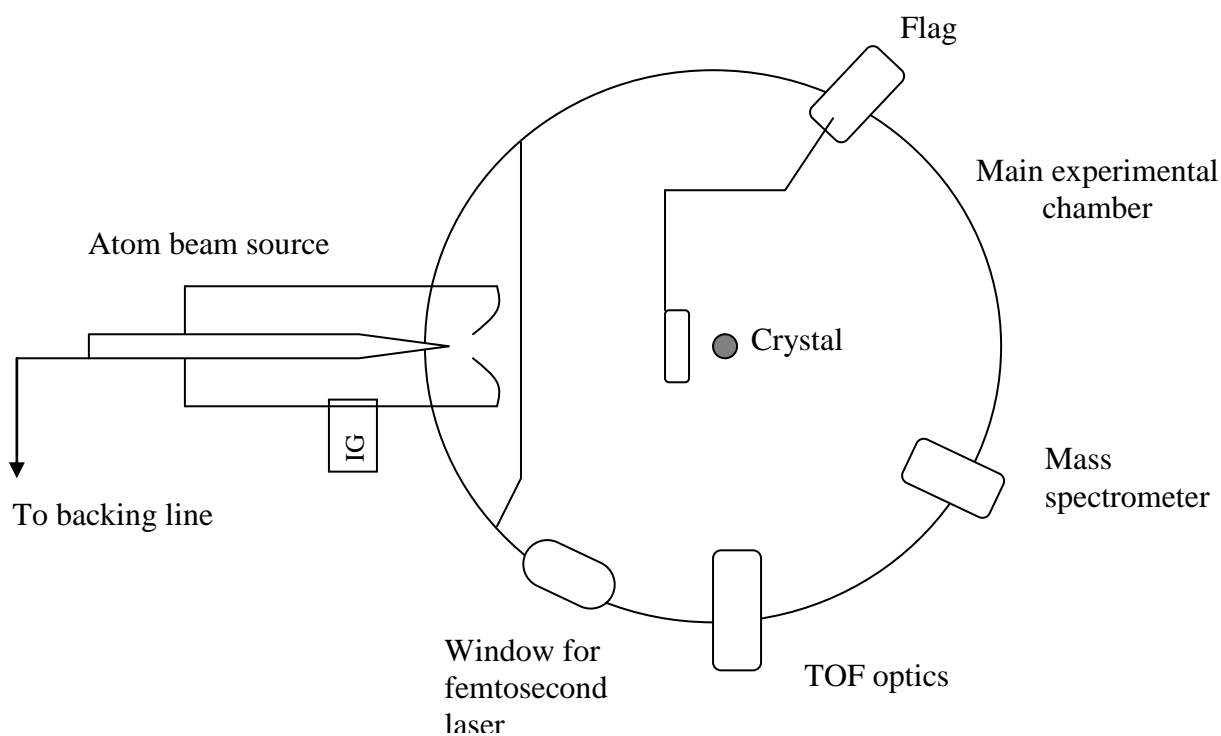


**Figure 6.13:** Temperature programmed desorption profiles for deuterium desorbing from Cu(111) by heating the sample. The peak on the right hand side corresponds to deuterium desorbing from the surface at  $\sim 350$  K. The lower temperature feature is due to subsurface D.

The Cu(111) sample was realigned so that deuterium could be dosed and a fs laser pulse could enter the chamber 12 mm in front of the front face of the crystal. A schematic of the set up is shown in figure 6.14. This allowed experiments to be carried out in the presence of a fs laser pulse. Deuterium TPDs were carried out as explained above and the traces showed no difference to the profiles shown in figure 6.13. This tells us that the femtosecond laser does not initiate recombinative desorption of deuterium from Cu(111) under the given conditions. Although no differences were observed in the desorption trace, this could have been as a result of the laser alignment not being precise enough.



Note, there is a window at the bottom of the UHV chamber and the UV light enters upwards through it.

**Figure 6.14:** Schematic of the experimental set-up.

### 6.3.2 Hydrogen REMPI

In order to acquire time-of-flight data, hydrogen was background dosed into the chamber at a pressure of  $1 \times 10^{-5}$  mbar. The wavelength for the output from the dye laser was set to the hydrogen  $Q_1$  line at  $\sim 605$  nm (605.196 – 605.221 depending on the temperature of the laboratory) resulting in a third harmonic beam with a wavelength of  $\sim 202$  nm. The laser light was aligned 12 mm in front of the sample and the hydrogen ions were ionised and attracted towards the negatively charged extract plates described in section 6.2.4. The signal was amplified and recorded but background noise was removed by setting a threshold limit required before ions would trigger the software to record the signal. The extract voltage was varied

between 0 – 60 V to give a plot of ion counts recorded as a function of flight time (figure 6.15). For each of the traces, long tails are observed as a result of  $H^+$  ions escaping into the field free region behind the crystal. This causes a longer flight time for the ions to reach the extract grid.

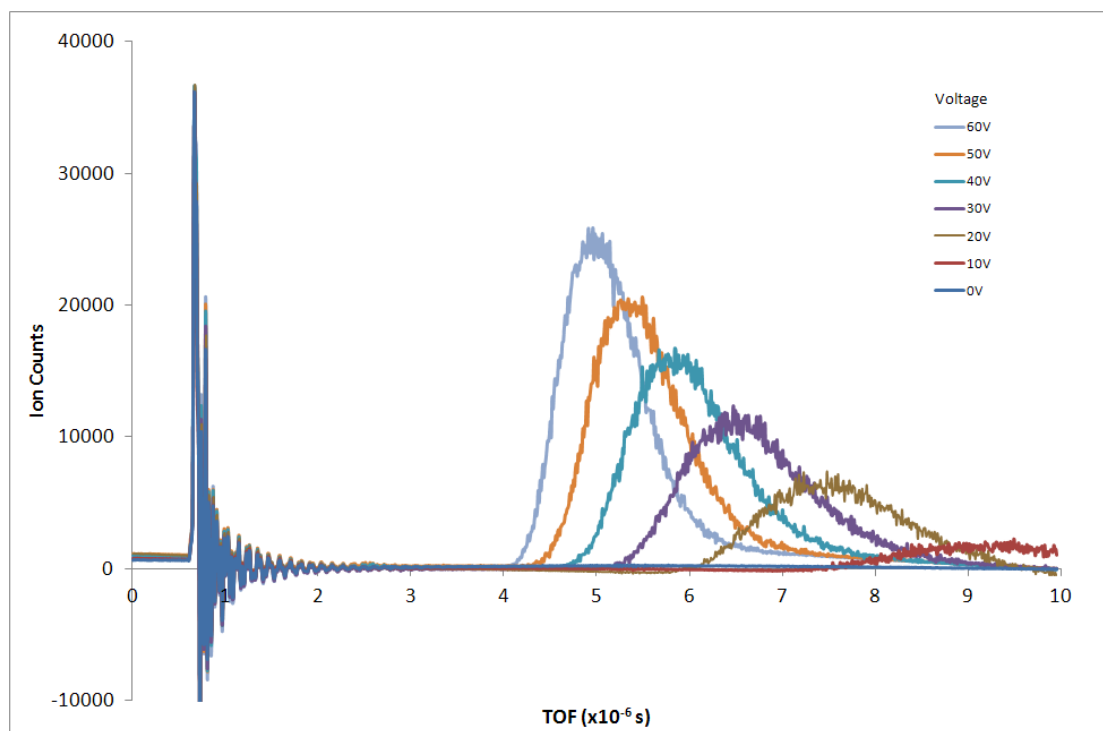


**Figure 6.15:** Recorded data showing the flight times of hydrogen ions with an applied extract voltage of 0 – 60 V.

The results shown in figure 6.15 can be compared to a model system in order to assess the accuracy of the REMPI experiments carried out. The model system can be calculated assuming constant acceleration using the equations given in equation 5.2 – 5.11.

<p>v = velocity  u = initial velocity  t = time  a = acceleration  F = force  m = mass  q = charge  E = electric field strength</p>
---

$$v = u + at \quad \text{Equation 6.2}$$

$$s = ut + \frac{1}{2}at^2 \quad \text{Equation 6.3}$$

$$F = ma = qE = q\frac{V}{x} \quad \text{Equation 6.4}$$

And therefore,

$$a = \frac{qV}{mx} \quad \text{Equation 6.5}$$

At peak maximum,  $V = 0$  and therefore  $x_0$  can be expressed as shown in equation 6.6.

$$x_0^2 = \frac{1}{2}at_0^2 \quad \text{Equation 6.6}$$

The time-of-flight can be calculated using the following equations:

$$t_u = t_1 - t_0 \quad \text{Equation 6.7}$$

Where,

$$t_1 = \frac{x_1}{u+at_0} \quad \text{Equation 6.8}$$

$$t_0 = \sqrt{\frac{(u^2+2ax_0)-u}{a}} \quad \text{Equation 6.9}$$

This allows  $\frac{P(u)}{du/dt}$  to be calculated,

$$\frac{du}{dt} = \frac{2u}{(u^2+2ax_0)^{1/2}} - 1 \quad \text{Equation 6.10}$$

And,

$$P(u) = \exp\left(\frac{-mu^2}{2k_B T}\right) \quad \text{Equation 6.11}$$

The data calculated is shown in figure 6.16.

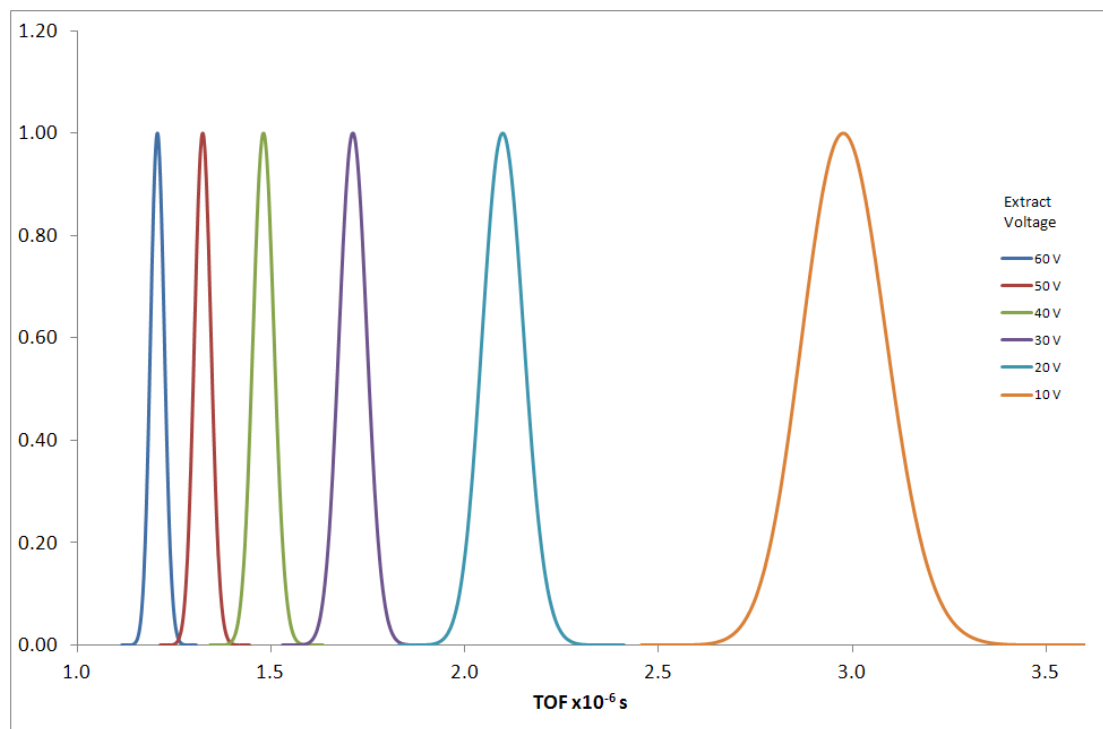


**Figure 6.16:** Ideal curves showing the calculated time scales for the flight times of hydrogen atoms with extract voltages of 10 – 60 V.

The values for the calculated flight times at different extract voltages are not the same as the initial experimental values. The calculated data shows symmetrical peaks whereas the real data forms asymmetric profiles with long trailing edges. The long tails can be explained by  $H^+$  ions escaping into a field free region behind the crystal and therefore taking a longer time to reach the detector. The real data is approximately an order of magnitude slower than the calculated times suggesting that the extract field is not linear. This also tells us that the effective voltage applied is only 75 % of the applied voltage and this therefore presents inaccuracies in the recorded data. The experimental set-up was probed and it was found that the VUV laser spot used for REMPI was slightly off to one side resulting in slower acceleration and therefore longer flight times to the detector. The misaligned laser spot will have also contributed to the long tails observed in the spectra in addition to the asymmetric symmetry of the peaks. In order to obtain results more comparable to the calculated data, the REMPI laser spot was realigned and the measurements were repeated. The data is shown in figure 6.10 and is in better agreement with the calculated data as the peaks recorded are more symmetrical. The difference in peak heights observed in

figure 6.17 is due to a change in intensity of the REMPI laser spot, which occurred as the temperature of the laboratory changed throughout the day.

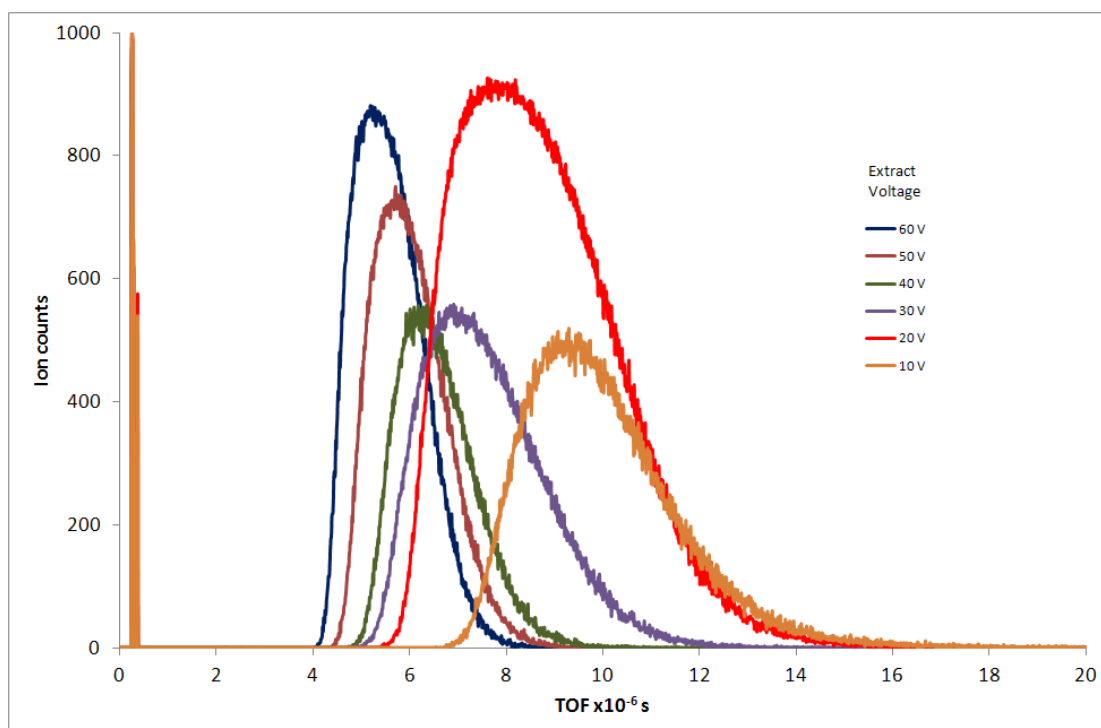


**Figure 6.17:** Time-of-flight recorded experimentally for hydrogen ions desorbing from Cu(111) with extract voltages of 10 – 60 V.

### 6.3.3 Hydrogen Recombination: Femtosecond Laser Excitation

TPD spectra were recorded for hydrogen desorbing from Cu(111) after being dosed at 100 K via the atom beam. Figure 6.18 shows a recorded spectrum. The peak at 40 counts is due to hydrogen desorbing from the surface, which occurs at 300 K according to various previous experiments carried out on the H<sub>2</sub>/Cu(111) system.

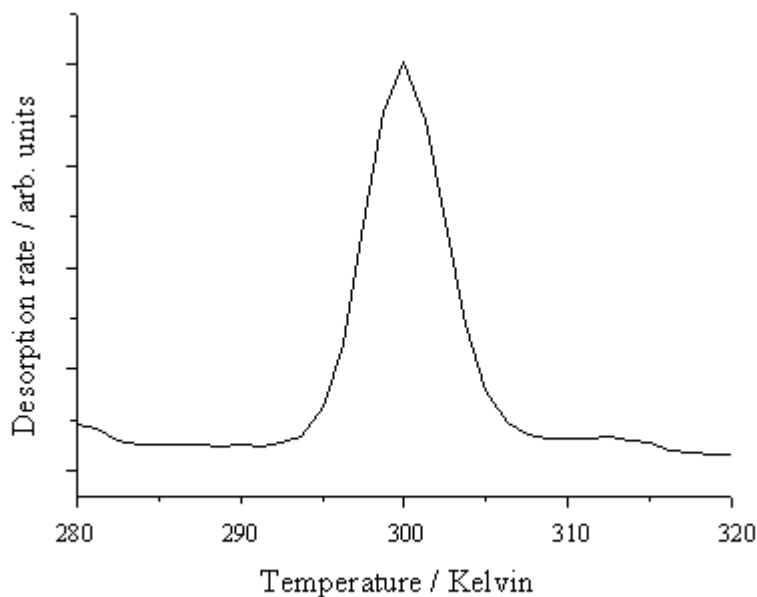


**Figure 6.18:** Temperature programmed desorption profile for hydrogen desorbing from Cu(111) at approximately 300 K.

A range of experiments were performed to determine whether the femtosecond laser pulse induced recombinative desorption. The data from each was compared to look for differences in the ion count under different conditions.

- a) A continuous beam of H atoms was dosed using the atom beam source and the fs laser pulse was positioned to a point 12 mm in front of the crystal. The REMPI-TOF set-up was used to detect ions during desorption. After running this set-up continuously, the atom beam was closed and excess hydrogen pumped away.
- b) Secondly, a continuous beam of H atoms was supplied by the atom beam source but only the UV light from the dye laser system was utilized to see if the fs laser had been producing ions in experiment a) above.
- c) Finally, only the UV light was let into the vacuum chamber without any hydrogen or light provided by the fs laser.

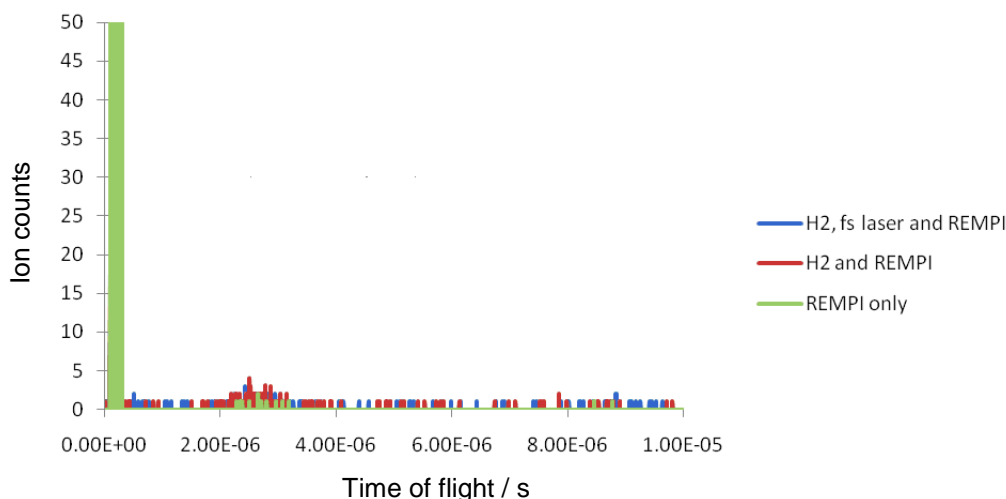


**Figure 6.19:** REMPI – TOF ion detection for experiments carried out using only the UV laser spot (green), hydrogen atom with the UV laser spot (red) and hydrogen, the UV laser and the femtosecond laser pulse (blue). This shows that there is no significant difference in the number of ions detected with the femtosecond laser pulse is used. No hydrogen recombination is induced by the femtosecond laser under the experimental conditions used. Ions are detected when the UV laser spot is used alone due to residual hydrogen in the chamber and the creation of ions as the laser spot scatters from objects inside the vacuum chamber.

As shown in figure 6.19 no significant differences were detected between the experiments carried out with hydrogen and VUV light with and without the fs laser pulses (a) and b) described above). The experiment using only UV light without a flux of hydrogen atoms or fs laser pulses sees a reduction in the total number of ions. The ions that were observed are due to residual hydrogen in the chamber and/or scattered light from the laser hitting surfaces inside the chamber. This set of experiments shows that the fs laser pulse did not initiate the recombinative desorption of hydrogen at Cu(111). During these experiments, the power of the fs laser pulses was maintained at a low value in order to avoid causing damage to the Cu(111) crystal. The pulse energy used was approximately 1 mJ/pulse (1.0 to 0.98 W peak power). In addition to this the beam had been deliberately de-focused, again to prevent causing damage to the surface. Overall it can be calculated that the fluence was  $8.8 \text{ J/m}^2$  due to a 6 mm spot diameter and an overall power of 0.25 mJ/pulse. Denzler *et al.* report a value of  $60 \text{ J/m}^2$  for recombinative desorption experiments carried out for deuterium on copper surfaces and therefore the fluence needed to be increased gradually in order to find a minimum value to allow the process to be initiated by the fs laser pulses.

The fluence was increased from  $8.8 \text{ J/m}^2$  until the damage threshold of the copper crystal was reached. No recombinative desorption induced by femtosecond laser pulses was detected and therefore further experiments are required for hydrogen desorption from Cu(111). In future experiments it will be important to use a fluence that does not damage the crystal but provides sufficient energy to induce the recombinative desorption of hydrogen.

#### 6.4 Concluding Remarks

Although it was not determined whether hydrogen recombination could be initiated by femtosecond laser pulses on Cu(111), experiments were carried out to determine the experimental procedures required to carry out the process. An atom beam source was successfully used to provide a continuous flow of H atoms into the vacuum chamber. The REMPI-TOF system was successfully synchronised to the femtosecond laser, resulting in a pump-probe set-up. It could be that hydrogen desorption is not initiated by fs-laser pulses and this could not be detected in the TPD because the spot size of the laser was 6 mm at low fluence, reducing to  $\sim 2$  mm at higher fluence, in comparison to a 10 mm copper crystal. In order to ensure desorption was induced, the beam should be scanned across the surface as it would be difficult to focus a small diameter beam on the exact point of on the crystal. A greater amount of experimentation is required to determine this.

It has been shown that thermal activation of hydrogen desorption occurs at the Cu(111) surface but femtosecond induced desorption did not occur. This can be attributed to the low fluence of  $8.84 \text{ J/m}^2$  initially used. As this was increased, the laser spot became more focused resulting in damage caused to the crystal.

Laser initiated desorption results in strongly forward peaked desorption and in order to initiate it, it is crucial that the REMPI laser beam is aligned precisely with the fs-laser beam. A drift of even 1-2 mm could make a large difference and result in the failure of the experiment. Great attention to detail needs to be taken when setting up the experiment in future.

Further experiments carried out on the H<sub>2</sub>/Cu(111) system would involve finding the correct fluence required to initiate the recombinative desorption reaction without damaging the surface. This would allow a two-pulse correlation experiment to be carried out to provide information on whether the desorption is mediated by phonons or electrons. The reader is referred to a reference by Denzler *et al.*<sup>11, 12</sup> and suggests that the experimental techniques employed by the group should be used to help with this experiment in the future. They employ the use of two quadrupole mass spectrometers. One QMS is situated at the bottom of the chamber for optical access through the cross beam analyser to record time-of-flight spectra of molecules desorbed by a laser pulse. The second QMS is mounted on a retractable translation stage, aligned radially to the center of the chamber. This system provides a higher collection efficiency as it utilises a 'home made' Feulner cup<sup>13</sup> which consists of a glass enclosure around the ionisation region as shown in figure 6.20. The sample is positioned directly in front of an orifice inside the enclosure and a fused silica window allows optical access. The desorbing molecules undergo multiple collisions with the glass walls inside the enclosure and are directed towards the QMS ioniser. Although the collection efficiency is greater, it should be noted that the compromise results in a loss of information about angular distribution and flight time. The high collection efficiency QMS enhances the signal – noise ratio and the example shown in figure 6.21 highlights the benefit of using the Feulner cup. This system would be beneficial to future hydrogen recombination studies on Cu(111) and would help to provide an indication as to whether atomic H desorption or recombinative hydrogen desorption occurs after excitation via a femtosecond laser pulse.

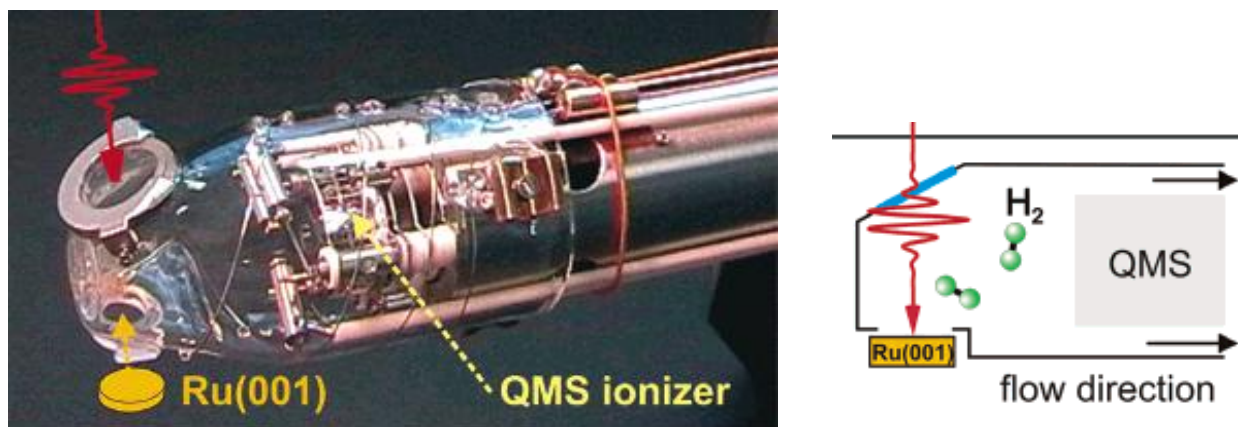


**Figure 6.20**<sup>12</sup>: High-collection efficiency quadrupole mass spectrometer. The photograph on the left shows the glass Feulner cup and the position of the crystal & fs laser pulse path. The figure on the right hand side shows a schematic of the set up. Reprinted (adapted) with permission from (D. N. Denzler, C. Frischkorn, M. Wolf and G. Ertl, *Journal of Physical Chemistry B*, 2004, 108, 14503-14510.). Copyright (2004) American Chemical Society.

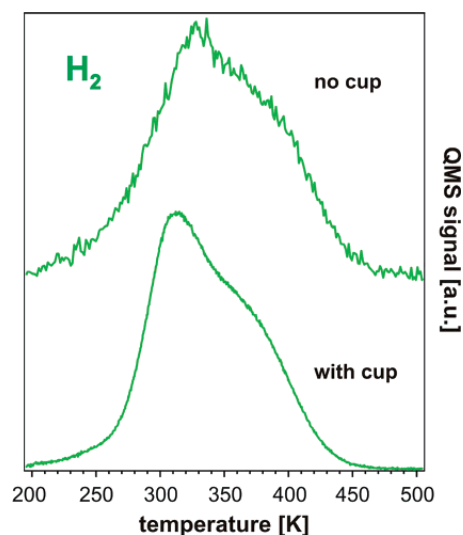


**Figure 6.21**<sup>12</sup>: Hydrogen TPD recorded with and without using the Feulner cup, highlighting the improvement in signal-noise ratio. Reprinted (adapted) with permission from (D. N. Denzler, C. Frischkorn, M. Wolf and G. Ertl, *Journal of Physical Chemistry B*, 2004, 108, 14503-14510.). Copyright (2004) American Chemical Society.

The set up of the laser system used by Denzler *et al.* is described in reference 14, and a schematic is shown in figure 6.22. The fs laser system is similar to the one described in this chapter; in summary, the group employ the use of an Ar<sup>+</sup> laser (Coherent Innova I-425) pumped Ti:sapphire oscillator (MIRA 9000) which is used as a seed for

a chirped pulse amplification system (Quantronix TitanII) consisting of two Nd:YLF pump lasers, a stretcher, a regenerative and a multipass amplifier and a compressor. As discussed in my description above, the pulse is firstly stretched to 200 ps before being amplified to 300  $\mu\text{J}$  in the regenerative stage (pumped by 6 mJ of frequency doubled Nd:YLF output). A pulse picker is used to clean the RGA output from pre- and post- pulses and the pulse is then sent through a two-stage Ti sapphire multipass amplifier. 800 nm pulses with 4.5 mJ pulse energy and a repetition rate of 400 Hz (adjustable down to 20 Hz) are produced after compression to 110 ps (FWHM).

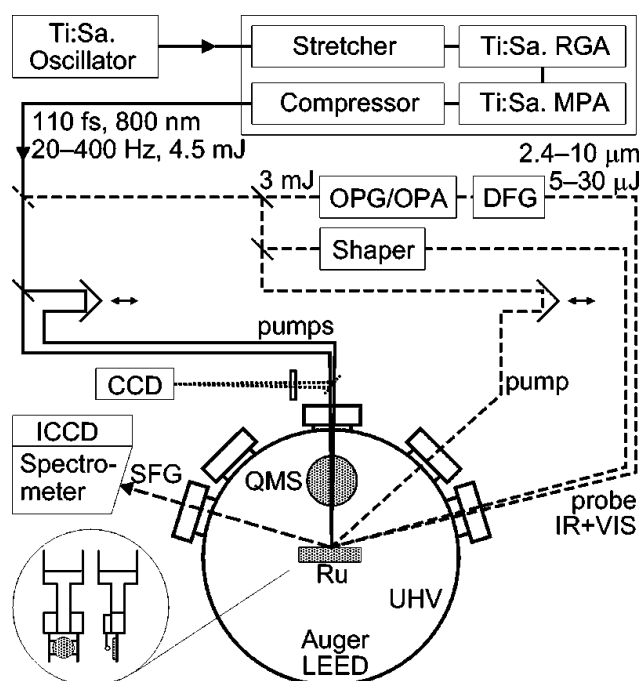


**Figure 6.22<sup>14</sup>:** Schematic of the experimental set up used by Funk *et al.*<sup>14</sup> and later by Denzler *et al.*<sup>12</sup>. Solid lines show the beam path for desorption experiments and dashed lines show the SFG setup.

Reprinted with permission from [S. Funk, M. Bonn, D. N. Denzler, Ch. Hess, M. Wolf, G. Ertl, *Journal of Chemical Physics*, 2000, 112, 9888-9897]. Copyright [2000], American Institute of Physics.

Funk *et al.*<sup>14</sup> successfully use the setup described above to characterise femtosecond laser induced desorption of CO from Ru(001). They show that irradiation with fs pulses (800 nm, 130 fs) causes desorption of CO with non-linear dependence of the yield on the absorbed fluence.

In summary, I would advise that someone carrying out these experiments in the future could learn from this and use more information from the literature to design the setup. Using the Feulner cup with the high collection-efficiency QMS would make the alignment of the lasers more achievable. It should be noted that the alignment is a crucial part of the experiment and small deviations could cause the experiment to fail, making it unclear whether the reaction does not take place or whether the setup is out of alignment.

## 6.5 References

1. J. S. Baskin and A. H. Zewail, *Journal of Chemical Education*, 2001, **78**, 737-751.
2. S. Pedersen, J. L. Herek and A. H. Zewail, *Science*, 1994, **266**, 1359-1364.
3. J. A. Prybyla, T. F. Heinz, J. A. Misewich, M. M. T. Loy and J. H. Glowia, *Physical Review Letters*, 1990, **64**, 1537.
4. C. Frischkorn and M. Wolf, *Chemical Reviews*, 2006, **106**, 4207-4233.
5. M. Bonn, S. Funk, C. Hess, D. N. Denzler, C. Stampfl, M. Scheffler, M. Wolf and G. Ertl, *Science*, 1999, **285**, 1042-1045.
6. M. Balooch, M. J. Cardillo, D. R. Miller and R. E. Stickney, *Surface Science*, 1974, **46**, 358-392.
7. H. A. Michelsen, C. T. Rettner and D. J. Auerbach, *Physical Review Letters*, 1992, **69**, 2678-2681.
8. C. T. Rettner, D. J. Auerbach and H. A. Michelsen, *Physical Review Letters*, 1992, **68**, 2547-2550.
9. E. E. Marinero, C. T. Rettner and R. N. Zare, *Physical Review Letters*, 1982, **48**, 1323-1326.
10. F. C. Fehsenfeld, K. M. Evenson and H. P. Broida, *Review of Scientific Instruments*, 1965, **36**, 294-298.
11. D. N. Denzler, C. Frischkorn, C. Hess, M. Wolf and G. Ertl, *Physical Review Letters*, 2003, **91**, 226102.
12. D. N. Denzler, C. Frischkorn, M. Wolf and G. Ertl, *Journal of Physical Chemistry B*, 2004, **108**, 14503-14510.
13. P. Feulner, D. Menzel, *Journal of Vacuum Science and Technology*, 1980, **17**, 662.
14. S. Funk, M. Bonn, D. N. Denzler, Ch. Hess, M. Wolf, G. Ertl, *Journal of Chemical Physics*, 2000, **112**, 9888-9897.